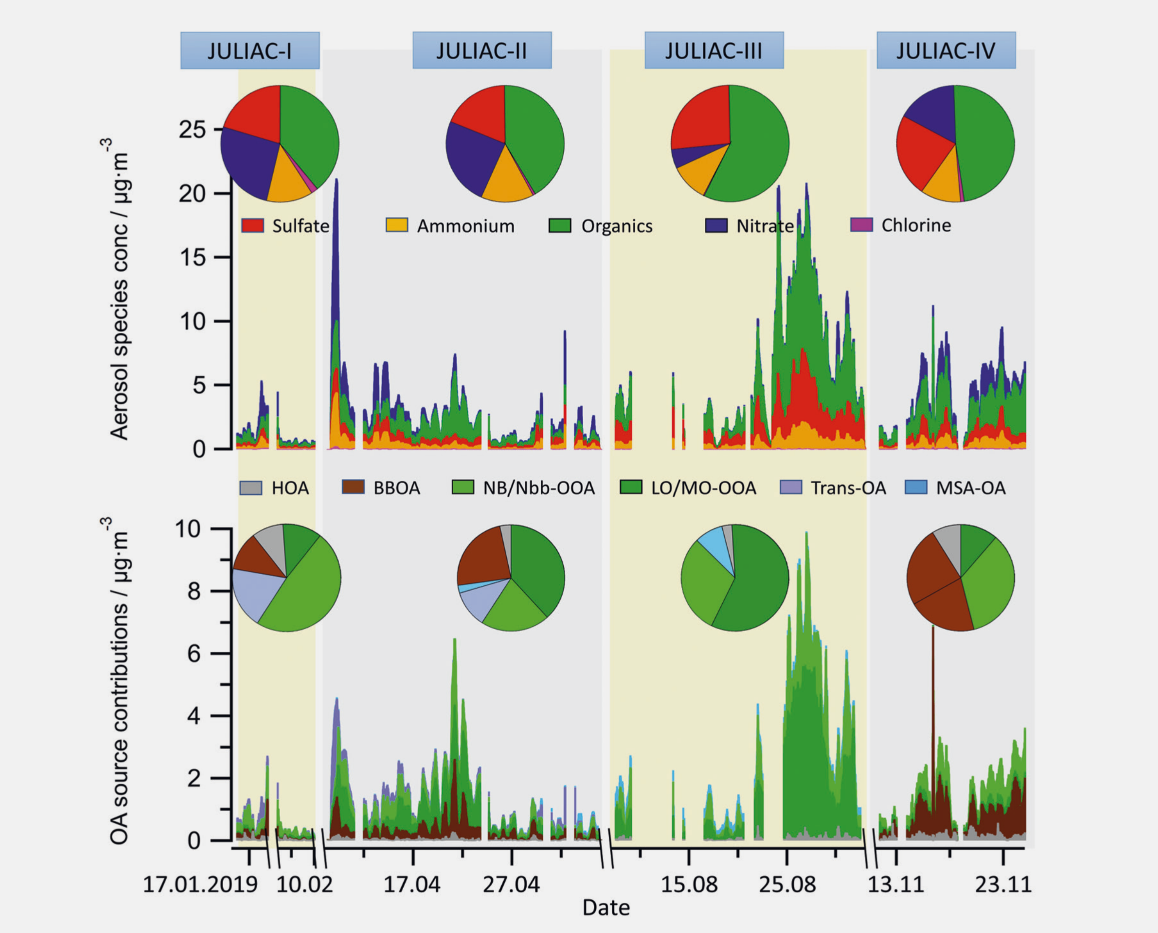

Seasonal Comparison of the Chemical Composition and Source Apportionment of Aerosols during the Year-Long JULIAC Campaign

Lu Liu

Energie & Umwelt / Energy & Environment
Band / Volume 595
ISBN 978-3-95806-668-7

Mitglied der Helmholtz-Gemeinschaft

JÜLICH
Forschungszentrum

Schriften des Forschungszentrums Jülich
Reihe Energie & Umwelt / Energy & Environment Band / Volume 595

Forschungszentrum Jülich GmbH
Institut für Energie- und Klimaforschung
Troposphäre (IEK-8)

Seasonal Comparison of the Chemical Composition and Source Apportionment of Aerosols during the Year-Long JULIAC Campaign

Lu Liu

Schriften des Forschungszentrums Jülich
Reihe Energie & Umwelt / Energy & Environment Band / Volume 595

ISSN 1866-1793 ISBN 978-3-95806-668-7

Bibliografische Information der Deutschen Nationalbibliothek.
Die Deutsche Nationalbibliothek verzeichnet diese Publikation in der
Deutschen Nationalbibliografie; detaillierte Bibliografische Daten
sind im Internet über http://dnb.d-nb.de abrufbar.

Herausgeber und Vertrieb: Forschungszentrum Jülich GmbH
Zentralbibliothek, Verlag
52425 Jülich
Tel.: +49 2461 61-5368
Fax: +49 2461 61-6103
zb-publikation@fz-juelich.de
www.fz-juelich.de/zb

Umschlaggestaltung: Grafische Medien, Forschungszentrum Jülich GmbH

Druck: Grafische Medien, Forschungszentrum Jülich GmbH

Schriften des Forschungszentrums Jülich
Reihe Energie & Umwelt / Energy & Environment, Band / Volume 595

D 468 (Diss. Wuppertal, Univ., 2022)

ISSN 1866-1793
ISBN 978-3-95806-668-7

Acknowledgments

Upon the completion of this thesis, I would like to express my gratitude and appreciation for my supervisors Prof. Peter Wiesen, Prof. Astrid Kiendler-Scharr as well as Dr. Thorsten Hohaus whose guidance, support, and encouragement has been invaluable throughout this study. Many thanks to Dr. Hohaus who has been an ideal mentor and advisor offering continuous assistance, inspiration, and enthusiasm all the time throughout the research project. With a special mention to Dr. Sören Zorn who always obligingly support and patiently instruct me all along with my project. I am deeply grateful to PD Dr. Thomas Mentel for his insightful comments and suggestions for my study.

This work would not have been possible without the fruitful collaboration of Dr. Birger Bohn, Dr. Frank Holland, Prof. Dr. Hendrik Fuchs, Dr. Ralf Tillmann, Stefanie Andres, Dr. Franz Rohrer, Vaishali Vardhan, Benjamin Winter, Dr. Sören Zorn and PD.Dr. Andreas Hofzumahaus during the JULIAC campaign. I would like to extend my sincere thanks to Donna Sueper, Bill Brooks of Aerodyne for their remote AMS technical support. Assistance provided by Dominik Raak and Kamil Kubik from the electronic workshop was very much appreciated. Technical support from Helga London, Michael Decker, and further analysis software support from Dr. Vlassis Karydis and Francesco Canonaco from PSI made the data treatment and in-depth analysis in this study possible. Also grateful to Dr. Georgios Gkatzelis and Dr. Changmin Cho who gave me countless academic inspiration in our fruitful discussion.

My sincere thanks also go to Dr. Zhaofeng Tan, Till Ziehm, Prof. Dr. Caiqing Yan, Marvin Glowania, Dr. Sungah Kang, Dr. Rongrong Wu who not only support and inspire me so much in the academic aspect but also assist me a lot to adapt and integrate the Ph.D. life in FZJ. I am proud of and grateful for my time working in IEK-8 FZJ where I met numerous opportunities and knew many excellent people throughout these four years.

Last but not the least, I would like to thank my family, friends, and my boyfriend Zhongfei Ren who accompany and support me so much in the past four years, especially the dark period of COVID.

Abstract

Atmospheric aerosols harm environmental air quality, atmospheric visibility, and play a critical role in climate-ecology interaction. Among aerosol compounds, organic aerosols (OA) contribute to 20 to 90% mass of total submicron particles, but their seasonally and regionally variable emissions and evolution processes are still unclear. Therefore, a year-long JULIAC (Jülich Atmospheric Chemistry Project) campaign has been conducted from Jan. 2019 to Nov. 2019 at the Forschungszentrum Jülich, Germany to better understand the seasonal variation of sources contributions and atmospheric evolutions of OA in this semi-rural site. During the JULIAC campaign, the submicron aerosol species concentration was continuously measured by a high-resolution time-of-flight aerosol mass spectrometer (HR-ToF-AMS) for one month of each season. For OA seasonal source apportionment, source factor analysis by positive matrix factorization (PMF) was utilized to resolve OA components into several source spectra. Moreover, concurrently measured comprehensive tracer gases (like volatile organic compounds (VOCs), radicals, NOx, O_3), the meteorological condition (like temperature, wind direction, wind speed), and the modeled air parcel back trajectories effectively support OA sources resolving and determination.

In this study, significant seasonal variations of submicron aerosol concentration and composition were observed. Aerosol nitrate shows the obvious seasonal trend related to temperature-dependence property. OA is the major component (mass fraction 39.0% of winter to 57.6% of summer) during the whole campaign. The annual averaged aerosol concentration (4.0 $\mu g/m^3$) is roughly keeping with aerosol levels reported in previous studies in Germany or other neighboring countries. The highest aerosol concentration (7.68 ± 4.82 $\mu g/m^3$), the largest mass fraction of OA (57.6%), and the lowest overall OA oxidation degree (O:C, 0.64 ± 0.08) were all observed at summer, which implies a strong biogenic VOCs derived secondary organic aerosol (SOA) formation.

For OA source apportionment, OA seasonal contributions from primary emissions (mainly traffic exhaust, biomass burning), secondary formation (mainly daytime oxidation, dark chemistry), and regional transport (consist of marine and continental plume transport) were revolved in this study. In terms of OA primary sources, Biomass Burning OA (BBOA) is the major anthropogenic primary source with OA contribution ranging from 11.7% to 45.2% of OA mass. BBOA factor concentrates at cold seasons and exhibits seasonal-dependent source characterization regarding seasonal changed biomass burning types. As for secondary sources, oxygenated organic aerosol (OOA) contribution from the daytime (Less Oxidized OOA, LO-OOA, and More Oxidized OOA, MO-OOA) and nighttime oxidation (Nocturnal Oxidation OOA, NO-OOA) processes were confirmed to be the major OA sources, accounting for 46% (autumn) to 88% (summer) of the total OA mass. Besides, OA contributions from regional transport (represented by Methanesulfonic Acid-Containing OA, MSA-OA, and Continental Regional Transport OA, Trans-OA) were resolved by PMF combined with meteorological and back-trajectory analysis, which contribute to 8.6% to 18.6% of total OA. In addition, the OA mass fraction contributed by the MSA-OA factor was demonstrated to be a good indicator of marine plume transport.

One major result of this study is the significant OA contribution from $NO_3\cdot$ dominated nocturnal chemistry resolved as NO-OOA factor. OA contribution from NO_3-initiated nocturnal oxidation accounts for 20.9% to 48.4% of total OA mass and even higher than that from daytime oxidation during winter and autumn, implying a possible night OA oxidation dominated environment during wintertime. In terms of precursors of NO_3-initiated nocturnal OA formation, NO-OOA splits to biogenic VOCs (BVOCs) dominated nocturnal oxidation OOA, NB-OOA (resolved at summer), and biomass burning VOCs (bbVOCs) dominated nocturnal oxidation OOA, Nbb-OOA (resolved at spring, autumn and winter). Overall, biomass burning-related OA, including primary emission BBOA and secondary dark formation Nbb-OOA accounts for 60.1% to 82.6% of total OA mass during autumn and winter. That implies NOx emission and biomass burning emission control are important for aerosol pollution mitigation during the cold period in this region. The resolving of the NO_3-initiated nocturnal OA contribution in this study not only completes field aerosol source apportionment analysis but also benefits the further understanding of nocturnal chemistry mechanism and improving the model for predicting global aerosol budget.

Contents

Chapter 1 Background and Motivation

1.1 Background

Atmospheric aerosols harm environmental air quality, atmospheric visibility, and play a significant role in climate-ecology interaction (Ramanathan et al., 2001, Boucher et al., 2013). Aerosol (mainly emitted from e.g., combustion and industrial activities) also could initiate many health-related problems, like respiratory diseases (Dockery et al., 1993, Pope et al., 2006, Dockery et al., 2007, Lelieveld et al., 2015). Differing chemical compositions and physicochemical properties of atmospheric aerosols relate to their emission sources, formation mechanisms, and aging processes.

Atmospheric aerosols, whether natural or anthropogenic, mainly originate from two processes: primary particles emissions and secondary particles formation from gaseous precursors as shown in Figure 1-1. In addition to primary emission and secondary formation, processes including oligomerization, condensation, aerosol aging, fragmentation, and cloud nucleation could dynamically affect the physical and chemical properties of organic aerosol (Jimenez et al., 2009, Canagaratna et al., 2010, Ng et al., 2010). Atmospheric aerosols mainly consist of black carbon (BC, mostly originate from incomplete combustion), mineral species, inorganic species (e.g., sea salt, sulfate, nitrate, ammonium), and organic species (also named organic aerosol or OA).

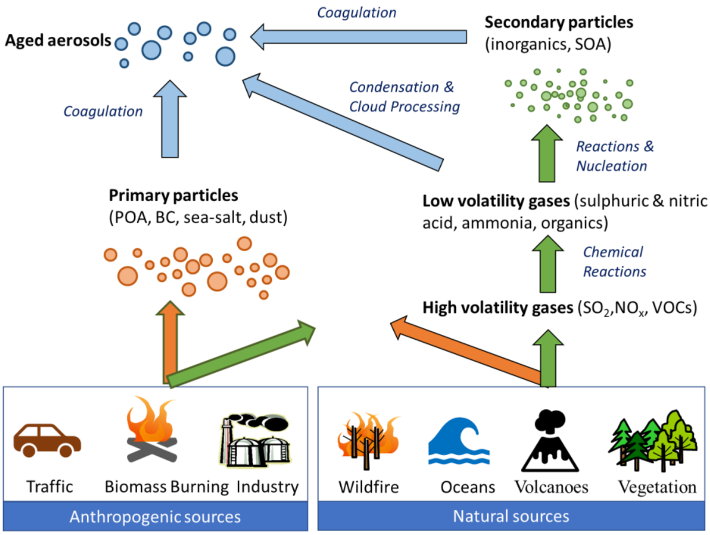

Figure 1-1: Overview of sources and evolutions process of aerosol particles in the atmosphere. Primary aerosols are emitted directly into the atmosphere, such as particles formed by sea spray, wildfire, and secondary aerosols are formed from gaseous precursors. Aged aerosols are formed from the coagulation of both primary and secondary particles and the condensation & cloud processing process of gaseous species.

Accordingly, variously originated aerosols cause changeable aerosol-related interference on Earth’s radiative balance through the direct effect of scattering and absorbing of radiation or through indirectly radiative forcing by modifying cloud properties and further precipitation (Myhre et al., 2013, Fanourgakis et al., 2019). The detailed radiative forcing of aerosol species related to their sources and precursors were illustrated in Figure 1-2 (quoted from (Stocker et al., 2013)). That graph also illustrates the importance of investigation of aerosol composition and sources on the study of aerosol net radiative forcing and hence aerosol climate effect.

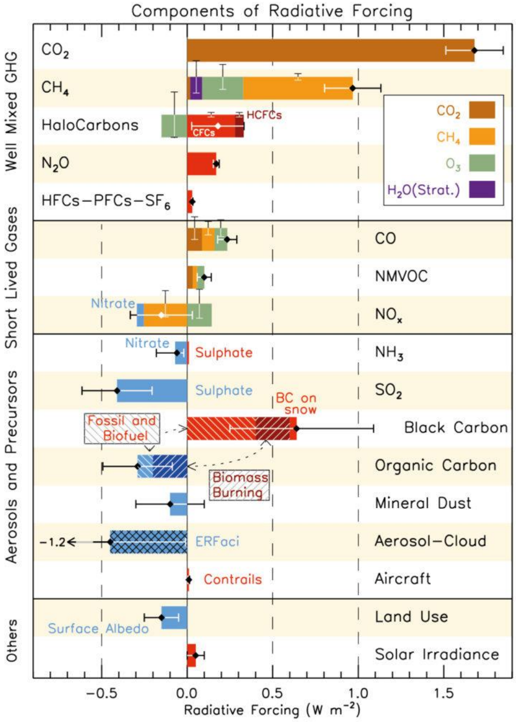

Figure 1-2: Radiative forcing bar chart for the period 1750–2011 based on emitted compounds (gases, aerosols, or aerosol precursors) or other changes. (Image credit: Figure 8.17 from AR5, WGI, Anthropogenic and natural radiative forcing, IPCC 2013)

For aerosol components, aerosol inorganic species: sulfate, nitrate, and ammonium are dominant compounds for submicron particles (PM1) and mainly originate from anthropogenic emission (Zhang et al., 2007a, Jimenez et al., 2009). Sulfur dioxide (SO_2) released from anthropogenic activities (like industry) and natural sources (mainly volcanic activities) are major aerosol sulfate precursors through reaction such as gas-phase oxidation and phase partitioning, and consequently affect the acidity of aerosols in the atmosphere (Tsigaridis et al., 2006, Zhang et al., 2007a). Gas-phase ammonia (NH_3) mainly originate from agricultural activities, like fertilizing and industrial activities, which could neutralize aerosol acidity (mainly sulfuric acid, nitric acid, and involving organic acid) and therefore commonly exist in aerosol as ammonium sulfate and ammonium nitrate. As for particulate nitrate, nitrogen oxides (like NO, NO_2) mainly emitted from car exhaust are major precursors of nitric acid and subsequently, affect aerosol nitrate mass loading.

Background and Motivation

Among aerosol compounds, organic aerosols (OA), have received considerable critical attention because they account for 20 to 90% mass of total submicron particles in the troposphere (Zhang et al., 2007b, Jimenez et al., 2009). As shown in Figure 1-1, the organic aerosol universal exists in ambient air and shows comprehensive primary emission sources (also named primary organic aerosol, POA) including both anthropogenic (such as traffic exhaust, industry emission) and natural sources (like wildfire, sea spray).

In addition, secondary organic aerosol (SOA) contributed by the reaction of gaseous precursors and further gas-particle phase partitioning is another important OA source (Hallquist et al., 2009). More specifically, gas-phase reactions are mainly oxidation between oxidants (like OH radical, O_3, NO_3 radicals, etc.) and volatile organic compounds (VOCs), semi-volatile, intermediate volatility organic compounds (S/IVOCs) from both biogenic and anthropogenic emissions (Jimenez et al., 2009). The physical and chemical characteristics of OA, such as volatility and hygroscopicity, are related to OA emissions and formation sources (Kanakidou et al., 2005, Goldstein et al., 2007, De Gouw et al., 2009).

Recently, SOA contribution from nocturnal chemistry (Atkinson et al., 2003, Brown et al., 2013) (mainly derived by oxidants NO_3 radical, O_3) draw more attention. Several previous labs (Ng et al., 2008, Fry et al., 2009) and ambient studies (Brown et al., 2009, Chen et al., 2015) found that significant contributions to SOA are from the reaction of $NO_3\cdot$ with biogenic VOCs (like isoprene and monoterpenes) during summertime. In addition, night-time oxidation of $NO_3\cdot$ with monoterpenes is suggested as a major reaction (Fry et al., 2014) and contributes up 30% or even 60% of total SOA based on several model results (Russell 2005, Hoyle et al., 2007, Pye et al., 2010). Recently, new lab research (Kodros et al., 2020) found that during winter-time rapid and significant secondary organic aerosol (SOA) could be formed through a dark reaction between NO_3 radical and fresh biomass burning emission, and it is suggested that over 70% of the biomass burning related organic aerosol to be related with nocturnal chemistry. Although the potential contribution to the aerosol phase from nocturnal oxidation has become the focus of an increasing amount of studies, there is still a lack of sufficient ambient data which supports the potential aerosol nocturnal chemistry contribution and implication in the real atmosphere.

As for SOA potential precursors, isoprene (C_5H_8) and monoterpenes ($C_{10}H_{16}$) are considered as most abundantly emitted BVOCs globally and made up of around 90% biogenic VOCs (BVOCs) emission (Guenther et al., 1995, Guenther et al., 2012). Ambient and laboratory research both imply that the oxidation of monoterpenes, isoprene made up of major biogenic derived SOA contribution (Yu et al., 1999, Volkamer et al., 2007, Ng et al., 2008, Tasoglou et al., 2015). Due to the high biogenic SOA production rate, around 2.86 and 97.5 Tg/yr (Henze et al., 2008, Farina et al., 2010, Hodzic et al., 2016), large amounts of global SOA models consider it as the only SOA source (Tsigaridis et al., 2014). However, there are also parts of researches that suggest a fraction of biogenic SOA to total SOA annual yield ranging from 74% (Hodzic et al., 2016) to 95% (Farina et al., 2010) considering anthropogenic SOA contribution or some other potential precursor contribution (Kelly et al., 2018). VOCs emitted from anthropogenic sources, such as biomass burning, and traffic exhaust as shown in Figure 1-1, consist of organic compounds with up to 30 carbon atoms or more, like aromatic (e.g. benzene, toluene), polycyclic aromatic (e.g. naphthalene), and furans (Schauer et al., 1999, Schauer et al., 2001, Kelly et al., 2018). Recent lab research (Kodros et al., 2020) and models studies (Shrivastava et al., 2015, Hodzic et al., 2016) suggest significant SOA contribution from the anthropogenic source, but the dominant precursors and potential SOA yield remain highly uncertain and need further investigation.

Organic aerosols, especially SOA, significantly contribute to total submicron particles in the troposphere, but the OA emission sources, evolution, and removal in the atmosphere are still under investigation. To well understand the complicated sources and evolution processes of organic aerosol, the concentration variations of organic aerosols were measured in amounts of field and laboratory studies mainly by real-time online high-resolution aerosol mass spectrometers, such as high-resolution time-of-flight aerosol mass spectrometer (HR-ToF-AMS) equipped with thermal desorption plus ionization techniques (Zhang et al., 2011, Pratt et al., 2012). Most commonly used aerosol mass spectrometers provide the concentration of bulk aerosol species and are utilized to distinguish mainly aerosol nitrate, sulfate, ammonium, organics, and chlorine (Canagaratna et al., 2007a). There are more advanced techniques that could provide more detailed chemical information of aerosol composition, such as soft-ionization aerosol mass spectrometers (SI-AMS), often at the expense of measuring only part of the PM mass.

Although AMS spectra contain limited molecular tracers, it's sufficient to further investigate aerosol source apportionments through factor analysis (Jimenez et al., 2009, Sun et al., 2011). Factor analysis is a mathematical technique to resolve the variability of ions intensities as a function of time measured by AMS as the linear combination of limited static OA contribution source factor profiles and their corresponding time variation (Jimenez et al., 2009) (Sun et al., 2012). Factor analysis converts extremely complicated OA composition into several chemically and physically meaningful source spectra. Moreover, factor analysis also realizes the global comparison of the chemistry, variability, and evolution characteristics of atmospheric submicron OA (Jimenez et al., 2009). With the universal usage of high time resolution online aerosol spectroscopy (like AMS and ACSM), factor analysis (like Positive matrix factorization/PMF), is commonly utilized in ambient aerosol field studies to investigate the aerosol sources and corresponding source contribution variations (Jimenez et al., 2009, Zhang et al., 2011, Sun et al., 2012, Crippa et al., 2014, Dai et al., 2019).

Numerous studies conducted in many different environments and parts of the globe show that an oxygenated organic aerosol (OOA) factor derived by utilizing PMF to identify the contribution of different sources, is dominated by processes of atmospheric oxidation of gas-phase species and accounts for a significant fraction of total OA mass concentration. In earlier studies of aerosol PMF factor analysis, two-OOA systems are widely utilized to describe the non-primary organic aerosol source. The most common OOA factor pairs are semi-volatility oxygenated OA (SV-OOA) and low-volatility oxygenated OA (LV-OOA), in which SV-OOA represents less-photochemically oxidized OA (fresh secondary organic aerosol) while LV-OOA represents significantly more oxidized OA (Jimenez et al., 2009).

With the continuous improvement of PMF analysis of high-resolution mass spectra, more distinctive types and sources of the general OOA profiles are resolved. For example, based on the oxidation state and elemental ratios (like O:C ratio), a less oxidized OOA (LO-OOA) factor and a more oxidized OOA (MO-OOA) factor are then introduced by (Sun et al., 2012) to subdivide the traditional SV-OOA factor. With further researches of OOA volatility, previous studies point out that LV-OOA and SV-OOA consist of compounds with broad and overlapping volatilities (effective saturation concentration C^* in the range of 10^{-7} to 10^{-3} µg m^{-3}, and 10^{-4} to 10 µg m^{-3} respectively)(Paciga et al., 2016), and overall show similar volatilities in general (Hildebrandt et al., 2010). For example, around 42% SV-OOA mass concentration is reported to consist of low-volatile organic compounds (LVOCs, with effective saturation concentration C^* of 10^{-3} to 0.1 µg m^{-3}) while the rest half was mainly semi-volatile organic compounds (SVOCs, with C^* of 1 to 100 μg m^{-3}) (Paciga et al., 2016). Based on these results, some studies propose that the naming of LV-OOA and SV-OOA factors could be misleading, and it would be more reasonable to describe the OOA factors based on the level of the photochemical age. Therefore, LV-OOA and SV-OOA might be better described as e.g. very oxygenated OA (V-OOA) and moderately oxygenated OA (M-OOA) (Kostenidou et al., 2015), or LO-OOA and MO-OOA (Sun et al., 2012). Although factors defined by levels of oxidation derived from the elemental composition are argued as "source factors" which are not assigned to a specific source (Zhang et al., 2018), it provides a universal and relative reliable factor to illustrate the determined OOA factors.

More source factors, such as primary source Hydrocarbon-Like Organic Aerosol (HOA) and Biomass Burning Organic Aerosol (BBOA) are commonly identified by PMF analysis in previous studies. Fossil fuel combustion and other urban sources are usually defined as the primary organic aerosol source, hydrocarbon-like OA (HOA). As one major type of fossil fuel combustion, the mobile exhaust is mainly contributed by partially burned fuel and recondensed engine lubricating oil, mainly consisting of n-alkanes, cycloalkanes, branched alkanes, and aromatics (Canagaratna et al., 2004, Chirico et al., 2010). Therefore, the spectrum of the HOA factor is dominated by C_nH_{2n+1} (m/z 29, 43, 57, 71) and C_nH_{2n-1} (m/z 41, 55, 69) ion groups, with the signal at $C_4H_9^+$ (m/z 57) being usually the major ion and can be considered as the tracer ion of HOA (Mohr et al., 2012).

Biomass burning OA (BBOA) resolved by PMF is suggested to be dominated by monosaccharide derivatives from the pyrolysis of cellulose, but also slightly contributed by straight-chain aliphatic, oxygenated compounds (like cellulose and lignin) and terpenoids (Crippa et al., 2013b). Therefore, characteristic fragments $C_2H_4O_2^+$ (m/z 60) and $C_3H_5O_2^+$ (m/z 73) mainly contributed by levoglucosan which is produced by cellulose pyrolysis (Simoneit et al., 1999, Alfarra et al., 2007) are commonly considered as the biomass burning tracer ions in the AMS mass spectrum.

Moreover, regional transport, such as marine plume transport is also possible to be resolve by PMF analysis. Methanesulfonic acid (MSA, CH_3SO_3H) is a secondary product from oxidation of dimethyl sulfide (DMS) (Zorn et al., 2008, Ge et al., 2012), and could affect cloud condensation nuclei (CCN) activity and consequently affect radiation budget then climate (Yan et al., 2019). Methanesulfonic acid (MSA) is commonly considered as the tracer of marine air plume regional transport because the precursor DMS is mainly produced by phytoplankton and anaerobe bacteria in the ocean and is the main natural source of sulfur containing compounds (Charlson et al., 1987).

MSA-containing organic aerosol source factor (commonly derived by PMF factor analysis) is commonly named as methanesulfonic acid-containing organic aerosol (MSA-OA) and has been detected in previous studies not only in the coastal and oceanic environment (Schmale et al., 2013) but also in megacities, like Paris (Crippa et al., 2014).

1.2 Motivation and Tasks

Ambient aerosols chemical composition and concentration commonly show significant seasonal variation due to not only seasonal dependent primary emissions (like agricultural burning, residential heating) but also secondary aerosol formation with seasonal changed dominant precursors (like biogenic VOCs, and biomass burning VOCs) and oxidants (like OH radical, O_3, and $NO_3^{\cdot}$ radical). Therefore, obvious seasonal differences in aerosol mass concentration and chemical composition are expected to be observed during the annual field campaign. In addition to the study of the variation of aerosol concentration and composition (mainly ammonium (NH_4), nitrate (NO_3), sulfate (SO_4), chloride (Cl), and organic compounds), seasonal source apportionment study of mainly organic aerosol (OA) would like to reveal seasonal changed aerosol contributions from different sources. Furthermore, potential seasonal changes of contributions and properties (e.g., source factors spectra, oxidation degree) of OA sources, especially secondary OA sources, can be used to enhance the understanding of the aerosol evolution process.

Accordingly, a year-long observation campaign JULIAC (Jülich Atmospheric Chemistry Project) has been done at a semi-rural site, Forschungszentrum Jülich, from Jan. 2019 to Nov. 2019. Seasonal variations of the chemical composition of submicron aerosols were measured during the JULIAC campaign by the high-resolution time-of-flight aerosol mass spectrometer (HR-ToF-AMS) and were discussed in section 4.1. Seasonal source apportionment of mainly organic aerosol during the JULIAC was investigated by statistical methods (PMF/ME-2) combined with comprehensive gas phases species measured concurrently (mainly in sections 4.2, 4.3, and 4.4). Moreover, seasonal contribution and source properties of OA sources factor resolved by PMF were mainly discussed in section 4.5.

Chapter 2 Campaign and Instruments

In this chapter, the JULIAC campaign is detailed introduced in section 2.1 mainly regarding location site and basic setup. The simulation chamber SAPHIR (Simulation of Atmospheric Photochemistry in a Large Reaction Chamber), one core part of the hardware setup of the JULIAC is briefly presented in section 2.2. The introduction of all instruments involved in the JULIAC campaign could be found in sections 2.3, 2.4, and 2.5.

2.1 JULIAC campaign

In this section, the location and surrounding environment of the JULIAC campaign is firstly described. And then the introduction concentrates on the basic hardware setup and design target of the JULIAC campaign.

2.1.1Campaign location and characteristics

To better understand the annual variation and source contribution of the radical budget, gas-phase composition, and organic aerosols, the year-long JULIAC (Jülich Atmospheric Chemistry Project) campaign has been conducted from Jan. 2019 to Nov. 2019 at the Forschungszentrum Jülich (50.909227N, 6.412235E), North Rhine-Westphalia, Germany, as shown in Figure 1-3 left). The location of the JULIAC campaign is surrounded by a forest mainly comprised of mixed deciduous forest and located about 5 km southeast of Jülich (population size about 34,000) and 30 km northeast of Aachen. In addition, as shown in Figure 1-3 right panel, there is one sugar factory located around 4 km northwestern, and two coal mines are located in the eastern and southwestern direction of the measuring site, respectively. And one eight-unit coal-fired power plant, the Weisweiler power station is located around 12km southwestern of the campaign location. Due to the surrounding environment, the JULIAC campaign site could be affected by both anthropogenic and biogenic emission sources.

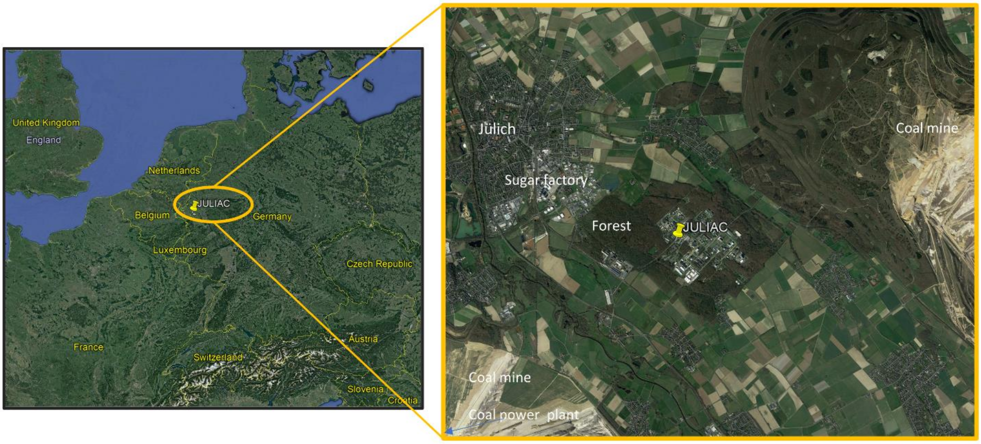

Figure 1-3: left) Location of the JULIAC campaign and right) zoom-in map for the geographical environment around the JULIAC campaign site. Major anthropogenic sources (like sugar factory, coal mines, and power plants) and biogenic sources (e.g. forest) around the site are all marked on the map.

2.1.2 Campaign setup

Intensive measurements (each 4-6 weeks) of comprehensive instrumentations were done in four different seasons and were named as the JULIAC-I (Jan. 15th to Feb. 10th, Winter), the JULIAC-II (Apr. 8th to May 5th, Spring), the JULIAC-III (Aug. 7th to Sep. 1st, Summer), and the JULIAC-IV (Oct. 28th to Nov. 24th, Autumn) in order. An overview of all available data collected during the JULIAC campaign could be found in appendix A. 12. As shown in Figure 1-4 left), the basic setup of the JULIAC measurement is sampling ambient air through an inlet line held by a 50 m high tower into the atmosphere simulation chamber SAPHIR (detailed information given in section 2.2). The purpose of that inlet system is to focus on regional atmospheric composition and meteorological effect and to reduce local interference from near-ground emission and forest canopy. A comprehensive setup of instrumentation was directly connected with the SAPHIR chamber to measure metrological parameters, radicals, OH reactivity, trace gases like CO, CO_2, NO_X, volatile organic compounds (VOCs), and chemical and physical properties of submicron aerosols. That setup ensures that the sampled ambient air plumes are consistently detected by all involved measurements during the JULIAC campaign, and by then could be utilized to further understand atmospheric processes and mechanisms. In particular, using the SAPHIR chamber in this campaign setup as a flow-through reactor shared by all sampling lines provides an ideal tool to characterize atmospheric trace gases, like OH, HO_2, NO_3, N_2O_5, and OH reactivity (Cho et al., 2021). In this work the focus is on the physical and chemical characterization of ambient aerosols measured with an Aerodyne aerosol high-resolution time-of-flight aerosol mass spectrometer (HR-ToF-AMS, see section 2.3.1), a Scanning Mobility Particle Sizer (SMPS, see section 2.4), and condensation particle counter (CPC, see section 2.4) during the JULIAC campaign.

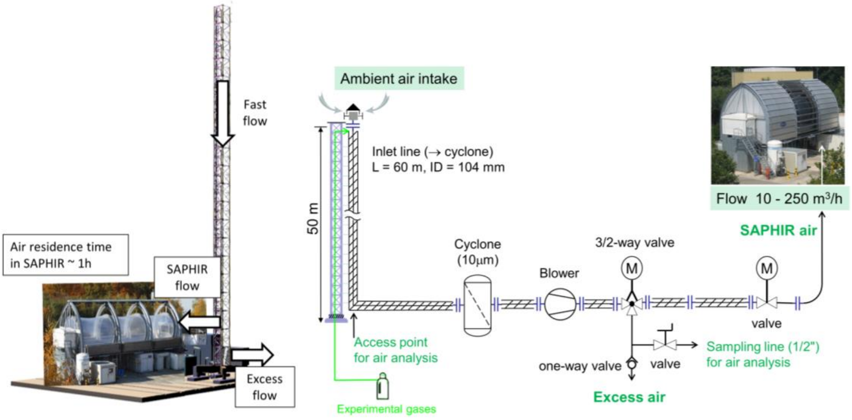

Figure 1-4: left) Concise concept map for basic setup of JULIAC campaign. Major air flow directions are marked in the graph. Right) Schematic diagram of JULIAC inlet system. (Image credit: IEK-8, Forschungszentrum Jülich). The core part's name and corresponding basic parameters are all marked.

The core parts of the inlet system of the JULIAC campaign are displayed in Figure 1-4 and a detailed introduction are given below from left to right in Figure 1-4 right):

(1) a 50-meter high tower that holds a sampling line. The sampling line is made from stainless steel tube with an inner diameter of 104 mm and inner surfaces coated with non-reactive SilcoNert 2000 (SilcoTek) to minimize losses of trace gases to the surfaces of the sampling line. Considering changing weather situations, the top opening of the tube is shielded by a roof to avoid precipitation entering the tube which could cause interference and uncertainties for determining water-soluble trace gases.

Multiple sensors are mounted on the top opening of the tube: an ultrasonic anemometer for 3D wind and temperature data (METEK, USA-1), two relative humidity/temperature sensors, and a barometric pressure sensor (Driesen + Kern, DKP102X, DKRF473) to real-time monitor the ambient pressure, temperature, relative humidity, and 3D wind data at 50 m as well as temperature, relative humidity, pressure, and volume flow of the sampling air. A separate heating circuitry, consisting of the heating element and two thermocouples, was mounted on the outer surface of the tube to maintain a constant tube temperature in case of adiabatic cooling of the air.

(2) A cyclone (LTG, ZSB-6) was used to remove coarse particles from the sampling air. The cyclone could efficiently remove 90% of 6 – 10 µm size particles and around 50% of 2 – 3 µm size particles from the sampling air. Inner surfaces of the cyclone are coated with SilcoNert® 2000 (SilcoTek) and heated to 2 degrees higher temperature compared to ambient to compensate the adiabatic cooling of the air. Upstream of the cyclone sensors capture temperature and relative humidity (Driesen + Kern, DKRF473) as well as the differential pressure to ambient (ABB, 266GST) in the airflow.

(3) the blower (Aerzener Maschinenfabrik, AERZEN Turbo G3 Type: TB 50-0.6 S) is mounted behind the cyclone which pushes sampling air through the whole JULIAC inlet system with a constant flow of 660 m^3/h during the entire JULIAC campaign. Inner surfaces of connecting flanges are coated with SilcoNert® 2000 (SilcoTek).

(4) A 3/2-way valve (GEMÜ, P600M) connects the inlet system with the SAPHIR chamber and is used to sample airflow separation between the SAPHIR chamber and vent excess air (connect to atmosphere). For the most period of the JULIAC campaign, 250 m^3/h sampling airflow is directed to the SAPHIR chamber.

(5) A bypass sampling line is installed at the vent tube for excess air which over the designed flow of SAPHIR. Several T-piece connectors are equipped at end of the bypass sampling line to provide access for sampling air directly from the JULIAC tower sampling line without the need to introduce the air prior into the SAPHIR chamber and allow for direct measurements from the sample ambient air at 50 meters height. This setup could be used to estimate the effect (like wall loss, a smoothing effect due to the resistance time of the air sample in the SAPHIR chamber, etc.) of the SAPHIR chamber, and could be used as an alternative and supporting measurements as well. During JULIAC tower sampling (break times among intensive JULIAC phases), instruments directly measured air from the bypass sampling line for additional measurements.

During the JULIAC campaign, 3 working modes, flow mode, batch mode, and perturbation mode were designed for the JULIAC campaign. Instruments involved in the campaign measure air sampled from the SAPHIR chamber:

(1) Flow mode. During this mode, ambient air sampled from the JULIAC tower goes through the SAPHIR chamber continuously with a flow rate of 250 m^3/h, which means sampling air has 1 hour residence time in the chamber. This mode is utilized for long-term continuous ambient measurement and all submicron aerosol data for the JULIAC intensive phases in this study are collected under this mode.

(2) Batch mode. In this mode, the inside and outside flow of the chamber turn off after sampling ambient air and then inject reactants (like O_3, NO_2, seed, etc.) into the chamber to initialize the designed reaction for hours. Instrument connected with SAPHIR keeps recoding the chemical variation that happened in the chamber, and mostly for one day boosting simulation.

(3) Perturbation mode. This mode is designed to explore the changes of atmospheric species (e.g. particle formation, chemical composition) under perturbation such as addition biogenic VOC (PLUS) (simulate increased influence on vegetation emissions) and NOx (simulate anthropogenic influence on forest emission). This mode only is planned but not run in the JULIAC campaign.

As discussed above, the JULIAC campaign setup significantly improves the data comparability of all instruments due to the same sampled air, benefit effective data comparability, broaden and improve detection for several trace gases. In addition, the aerosol transmission loss and changes of chemical and physical properties caused by the JULIAC setup were tested before the JULIAC campaign. The results are discussed in detail in appendix A. 1. In brief, the results illustrate that the JULIAC inlet line system show a slight effect on aerosol organics and does not change aerosol size-dependent chemical composition in evidence. Therefore, the main analysis, aerosol organics source apportionment analysis used in this study should be less affected by the aerosol loss.

2.2 Atmospheric simulation chamber SAPHIR

Figure 1-5: photo of the atmosphere simulation chamber SAPHIR located in the Forschungszentrum Jülich. (Image credit: IEK-8, Forschungszentrum Jülich)

The SAPHIR (Simulation of Atmospheric Photochemistry in a Large Reaction Chamber) chamber is a large-scale outdoor atmospheric simulation chamber located in the Forschungszentrum Jülich. The SAPHIR chamber is constructed as a cylindrical-shaped Teflon chamber with length, diameter, and volume of 18 m, 5 m, and 270 m^3, respectively. The chamber consists of double-wall fluorinated ethylene propylene (FEP) Teflon film, and the interspace between two films is flushed continuously with high purity air or nitrogen to minimize contamination with outside air due to diffusion. The pressure inside the chamber is slightly higher than ambient pressure, on average at about 80 Pa.

During the JULIAC campaign, synthetic air was used as a replenishing flow (flow rate of approximately 20 m^3/h) to compensate for the loss from instrument sampling and chamber leaks. Two fans (rotation speed 1200 rpm) are mounted inner chamber to make sure a homogeneous mixing of the sampled air. More details about the SAPHIR chamber can be found elsewhere (Bohn et al., 2005b, Bohn et al., 2005a). The dilution rate constant caused by replenishing flow and the aerosol wall loss caused by turbulence in the chamber are both small enough (with a loss ratio of

10^{-5}) to be neglectable (detailed discussion in appendix A. 2). Detailed calculations and discussions can be found in appendix section A. 2.

2.3HR-ToF-AMS

2.3.1 HR-ToF-AMS introduction

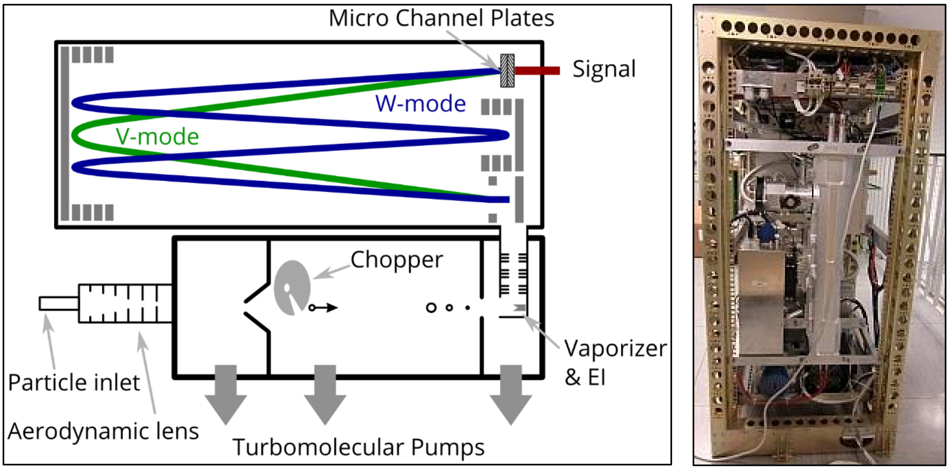

Figure 1-6: left) Schematic of the high-resolution time-of-flight aerosol mass spectrometer (Image credit: (DeCarlo et al., 2006)). Right) Photo of high-resolution time-of-flight aerosol mass spectrometer utilized during the JULIAC-I and the JULIAC-II

In this study, the high-resolution time-of-flight aerosol mass spectrometer (HR-TOF-AMS) is used to continuously measure mass concentrations and size distribution of non-refractory chemical compositions (mainly ammonium (NH_4), nitrate (NO_3), sulfate (SO_4), chloride (Cl), and organic compounds) of the submicron particle during the whole JULIAC campaign. Two same version HR-TOF-AMS were alternately used during the JULIAC campaign, and therefore named the one utilized during the JULIAC-I and II as AMS_1 in this thesis, and the other used for the JULIAC-III and IV as AMS_2.

Ambient aerosol sampled into HR-TOF-AMS firstly goes through a 100 µm diameter critical orifice with an average flow rate around 1.3-1.5 cm^3/s, and then passes an aerodynamic lens (Zhang et al., 2002). The aerodynamic lens focuses aerosols ranging from 50 nm to 600 nm into a narrow aerosol beam (diameter around 100 µm) with almost 100% transmission efficiency. Bigger and smaller aerosols in the range of 20-2000 nm also could be transmitted but with decreased efficiency (Heberlein et al., 2001).

The particle beam then leaves the aerosol sampling chamber and goes through a channel skimmer (diameter 1mm) to skim off most air entry inlet pumped by a 280 l/s turbo molecular pump (VarianV-301NAV) and a backed diaphragm pump (Vacuubrand MD1-Vario). Then particles enter the high vacuum particle sizing chamber pumped by 70 l/s TwisTorr84fs turbo molecular pump. Particles fly through this chamber with an aerodynamic size-related terminal velocity acquired in the aerodynamic lens. During PTOF mode of AMS, particle beams then are effectively chopped by chopper mounted in front of the terminal of sizing chamber with 0.5% chopper circumference, and then the particle size information could be determined based on the particle flight time inside sizing chamber.

For AMS working modes, the position and operating mode of the chopper determine the AMS working mode (MS or PTOF). For MS mode, the chopper position switches between open positions (where aerosol beam could continuously be transported into next chamber) and close positions (where no particle is transmitted into detection region instead of cutting particle beam). More mechanism introduction of TOF-AMS basic working mode could be found in a previous paper (Drewnick et al., 2005). Particles transmitted into the evaporation and ionization chamber impact on 600˚C porous tungsten vaporizer (Canagaratna et al., 2007b). A micro thermocouple is mounted in the front of the vaporizer to concurrently monitor the status of the vaporizer. The vaporizer is located at the center and downstream of an electron-ion source, hence the vaporized non-refractory species could be efficiently ionized by 70 eV electrons emitted from a tungsten filament and then enter orthogonal TOF extractor through electrostatic lenses.

After drifting through the TOF extractor at 50 eV, ions are orthogonally extracted into the TOF chamber by a high voltage pulse. Then ions fly in the TOF chamber in V or W shape path reflected by gridded ion reflector mounted at one end of TOF chamber, and then go through post acceleration and finally detecte by microchannel plate (MCP, DR-4200 Tofwerk). A more detailed introduction of the TOF chamber could be found in a previous publication (Steiner et al., 2001). The electronic signal from MCP is then detected by an analog-to-digital conversion data acquisition card (AP240, Acqiris, Geneva, Switzerland) and further transferred to and stored in one personal laptop.

2.3.2 HR-ToF-AMS maintenance and data treatment

To visualized illustrate the whole instrument maintenance process, workflow chart of complicated HR-ToF-AMS software operations, output data treatments, storage of corresponding data and recording of the JULIAC are firstly displayed in Figure 1-7. These diagnostics parameters during AMS operation are important indicator to evaluate instrument stability and support possibly needed data correction.

For AMS raw data treatment, the basic principle for converting detected ion intensity (I, in Hz) at specific charge ratio (m/z) to mass concentration (C, in μg/m^3) is shown in Eq. 1(Jimenez et al., 2003). MW means the species molecular weight (g.mol^{-1}), Q represents the flow rate of AMS (cm^3 s^{-1}), N_A is Avogadro’s number, and IE is the ionization efficiency (see section 2.3.2.3). In practice, relative ionization efficiency of species (RIEs, see section 2.3.2.4) is introduced to obtain reference IE/MW from a well characterized calibrant species (normally nitrate). Collection efficiency of aerosol species is also used to correct deviation of AMS detection due to the transmission loss (details in section 2.3.2.5). A detailed flow chart that mainly focuses on raw AMS data treatment like correction and calibration, could be found in Figure 1-8.

$$C_S = \frac{10^{12} MW}{IE\, Q\, N_A} I \qquad \text{Eq. 1}$$

$$C_S = \frac{10^{12} MW_{NO3}}{CE_s RIE_s IE_{NO3} Q N_A} \sum_{all,i} I_{s,i} \qquad \text{Eq. 2}$$

2.3.2.1 HR-ToF-AMS operation data

In terms of instrument operation and corresponding data, ToF Power Supply (TPS) voltage tuning by Tofwerk TPS controller software is necessary once the vacuum chamber is open for maintenance, and the old voltage setting menu needs to be backup for the revert. ToF-AMS Instrument Control and Data Acquisition Software, ToF-AMS DAQ of Aerodyne (more details could be found in https://sites.google.com/site/tofamsdaq/) is the application used for HR-ToF-AMS instrument operation such as data acquisition and storage, hardware parameter control. All operation data monitored by TPS and DAQ are all important referred values to evaluate instrument stability and data quality. For example, the diagnostic parameters (like baseline, MCP voltage, single ion, filament emission, airbeam, flowrate, etc.) detected by ToF-AMS DAQ are automatically stored in Hierarchical Data Format (.hdf) and Igor Text (.itx) format of output data of AMS, and are initial checking step after raw data loading by AMS data analysis software, SQUIRREL (DeCarlo et al., 2006, Sueper et al., 2009) as shown in Figure 1-8.

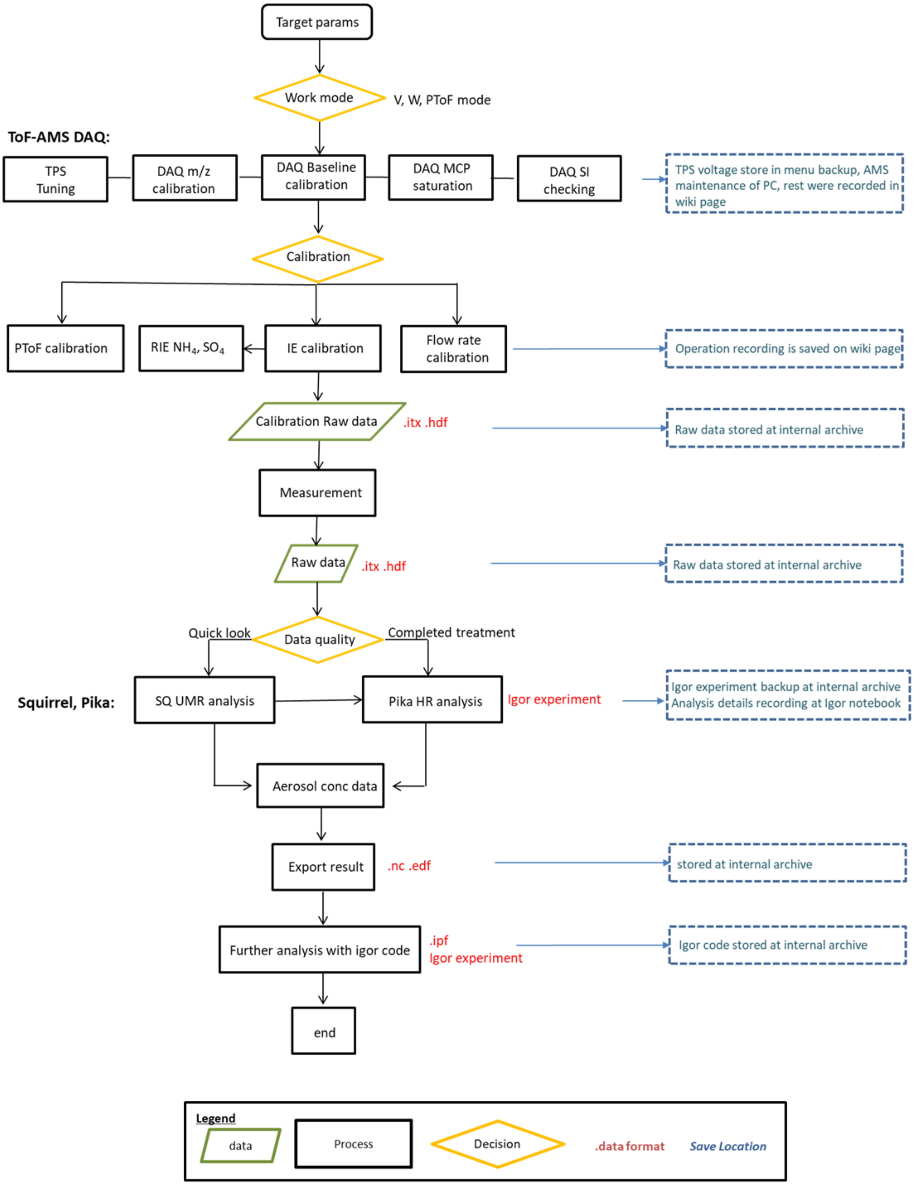

Figure 1-7 Flow chart for HR-ToF-AMS maintenance during the campaign and raw data treatment process by software Squirrel and Pika. Instrument parameters during maintenance, raw data, processed data of AMS, utilized Igor procedures and corresponding data process recording were all backed up online, and the stored locations were also listed in flowchart. Simplified AMS data process of Squirrel and Pika in this flowchart will be detailed displayed in Figure 1-8.

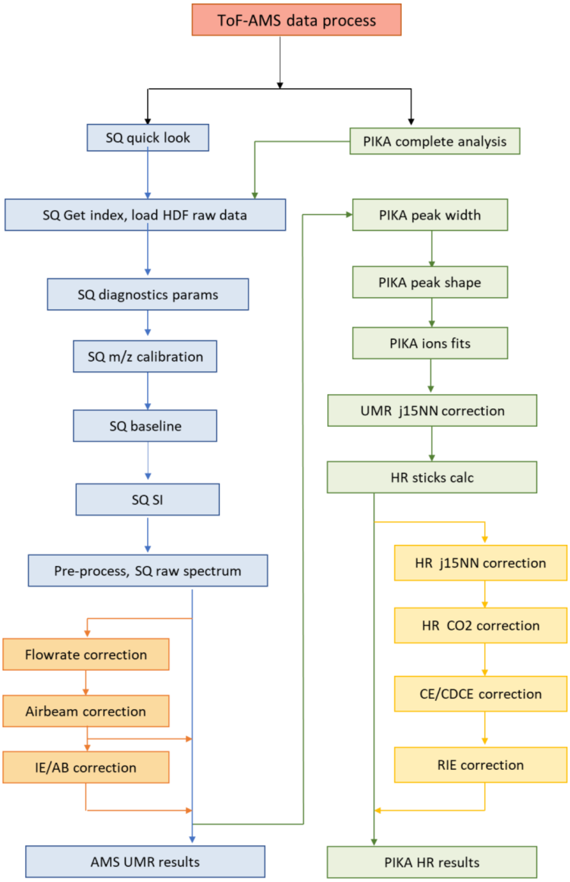

Figure 1-8: Detailed flow chart for AMS UMR and HR data treatment, including the major calibration and correction steps applied during the JULIAC data treatment.

2.3.2.2 Flowrate calibration

The flow rate of AMS sampling air is an important parameter to convert signal intensity to mass concentration. The value of flow rate is not directly detected but derived from inlet lens pressure (saved as analog input #3) and converted using a static linear equation. During the JULIAC-II, 0.1 to 0.25 cm^3/s positive bias of AMS logged flow rate was observed in comparison with inlet flow rate measured by Gillian Gilibrator 2 (Bubble Generator Standard Flow Cell, Flow range 20 cc- 6 LPM, P/N 800286). Therefore, one flow rate calibration has been done at the 20.03.2019 the JULIAC-II to correct logged flow rate. One flow control valve was equipped in the front of the

AMS inlet line to create gradient inlet flow rates. At each flow rate during calibration, at least one run in MS mode of HR-ToF-AMS was saved to record analog input lens pressure, and the corresponding real inlet flow rate was measured by gilibrator and recorded. The new flow rate can be derived using the parameters below (which is derived from flow rate calibration data). Flowrate calibration data analysis has been shown in Figure 1-9, with flow rate slope 2.33 and flowrate intercept -2.09.

New flow rate=flowrate intercept + flow rate slope *(lens pressure)

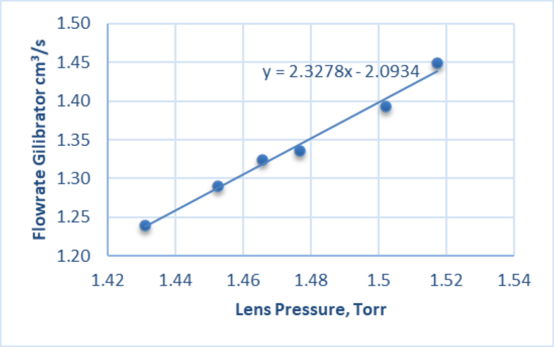

Figure 1-9: Flowrate calibration results analysis for AMS during the JULIAC-II with gilibrator detected flowrate as y-axis and Lens pressure as x-axis

2.3.2.3 Ion efficiency calibration

Ionization efficiency (IE) is a core parameter to convert signal ion intensity to species mass concentration. Therefore, IE calibration was regularly done around every two weeks to reduce the uncertainty caused by IE variation during the JULIAC campaign. IE is estimated based on ions per particle (IPP) divided molecules per particle (MPP), and ammonium nitrate is usually used as calibration species for IE calibration because of its high evaporation efficiency (close to 100%). During the JULIAC campaign calibration, gradient NH_4NO_3 standard solutions carried by synthetic air going through an atomizer and then a silicone dryer was utilized to generate gradient pure NH_4NO_3 particles flow. 350 nm NH_4NO_3 particle was then selected by DMA (Differential Mobility Analyzer, TSI, Model 3080), and then split the flow into HR-ToF-AMS and CPC in parallel (TSI, Model 3785) to detect ion intensity and count particle number respectively. More details of ionization calibration and calculation principles could be found in a previous publication

(Drewnick et al., 2005). One sample result of ionization efficiency calibration calculation has been shown in Figure 1-10, illustrating the correlation between AMS measured bulk nitrate mass concentration calculated by initial IE value, and nitrate mass concentrations calculated by particle number concentration measured by CPC and particle size detected by PToF mode of AMS. Liner fitting was done in the graph, and correction coefficient (b, 1.0534) based on original IE and updated new ionization coefficient is displayed. Th overview of diagnostic and IE parameters archived during the whole JULIAC campaign is displayed in appendix Table A 2.

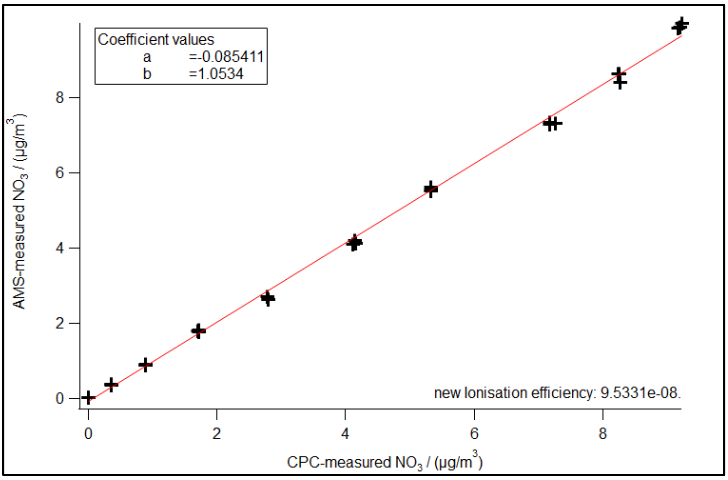

Figure 1-10: Result example of the ionization efficiency (IE) calibration. Y-axis represents the AMS measured bulk nitrate mass concentration correlates with X-axis stands for nitrate mass concentrations calculated by particle number concentration measured by CPC and particle size detected by PToF mode of AMS

2.3.2.4 RIE correction

As introduced in section 2.3.2.3, pure ammonium nitrate is normally used as ionization calibration species because of the high evaporation ratio (almost 100%). However, IE value calibrated by NH_4NO_3 could not be directly used to convert all aerosol species intensity to mass concentration, but need a relative ionization efficiency of the species (RIEs) in comparison to NH_4NO_3 as introduced by (Jimenez et al., 2003, Alfarra et al., 2004, Canagaratna et al., 2007b).In addition, RIE_{NO3} value is usually used as 1.1 instead of 1 because only fragments NO^+ (m/z 30) and NO_2^+

(m/z 46) are counted during NH_4NO_3 IE calibration instead of total ion fragments of NO_3. In the JULIAC study, standard NH_4NO_3 and $(NH_4)_2SO_4$ are measured during IE calibration. Therefore, RIE_{NH4} and RIE_{SO4} are calculated based on standard measurement during IE calibrations and applied for all AMS data collected during four intensive phases. Detailed calculation steps are given below.

The basic mechanism for RIE_{NH4} and RIE_{SO4} correction is the aerosol ion balance principle for AMS data. In detail, the ideally molecular ratio of high-resolution bulk NH_4 to bulk NO_3 ($HRNH_4/HRNO_3$) should equal 1 for standard NH_4NO_3 measurement and the molecular ratio of high-resolution bulk NH_4 to bulk SO_4 ($HRNH_4/HRSO_4$) should equal 2 for standard $(NH_4)_2SO_4$ measurement by AMS. Based on that, here introduce two RIE correction parameters R_{NH4} and R_{SO4} for representing the initial measured molecular ratio of $HRNH_4/HRNO_3$ of NH_4NO_3 and $HRNH_4/HRSO_4$ of $(NH_4)_2SO_4$ measurement before RIE correction as shown in Eq. 3 and Eq. 4. C_{NH4}, C_{NO3} and C_{SO4} used in these formulas represents corresponding aerosol bulk species HR concentration (in $\mu g/m^3$) calculated by PIKA with default RIE, $RIE_{NH4,def}=4$, $RIE_{NO3,def}=1.1$ and $RIE_{SO4,def}=1.2$. MW used in formulas is the molecular weight of corresponding species in g/mol. To connect the correction factor R with RIE, the basic formula for transferring the AMS detected ion intensity (I, in counts per second or Hz) of one aerosol species (S) to a mass concentration (C, in $\mu g/m^3$) introduced by (Jimenez et al., 2003) is used as shown in Eq. 5. After replacing Cs in Eq. 3 and Eq. 4 by Eq. 5, a new equation for RIE correction could be converted as shown in Eq. 6 and Eq. 7. Therefore, based on the ion balance principle introduced, new RIE_{NH4_corr} and $RIE_{SO4,corr}$ after RIE correction could be calculated by Eq. 8 and Eq. 9.

$$R_{NH4} = \frac{C_{NH4}/MW_{NH4}}{C_{NO3}/MW_{NO3}} \qquad \text{Eq. 3}$$

$$R_{SO4} = \frac{C_{NH4}/MW_{NH4}}{C_{SO4}/MW_{SO4}} \qquad \text{Eq. 4}$$

$$Cs = \frac{10^{12} MW_{NO3}}{RIE_s IE_{NO3} Q\, N_A} \sum\nolimits_{all,i} I_{s,i} \qquad \text{Eq. 5}$$

$$R_{NH4} = \frac{RIE_{NO3} \sum_{all,i} I_{NO3,i} MW_{NO3}}{RIE_{NH4} \sum_{all,i} I_{NH4,i} MW_{NH4}} \qquad \text{Eq. 6}$$

$$R_{SO4} = \frac{RIE_{SO4} \sum_{all,i} I_{SO4,i} MW_{SO4}}{RIE_{NH4} \sum_{all,i} I_{NH4,i} MW_{NH4}} \qquad \text{Eq. 7}$$

$$RIE_{NH4\_corr} = R_{NH4} \times R_{NH4\_def} \qquad \text{Eq. 8}$$

$$RIE_{SO4\_corr} = (2/R_{SO4}) \times R_{SO4\_def} \qquad \text{Eq. 9}$$

Because RIE_{NH4} is also involved in RIE_{SO4} correction, the order of RIE_{NH4} correction should be earlier than RIE_{SO4}. Moreover, RIE_{NH4_corr} should be applied to PIKA and recalculate NH_4 and SO_4 species HR concentration before R_{SO4} calculation.

Table 1-1: The overview of the value of applied RIE_{NH4} and RIE_{SO4} for all four JULIAC intensive phases.

Phases	RIE_NH$_4$	RIE_SO$_4$
JULIAC-I	3.84	0.98
JULIAC-II	3.52	1.06
JULIAC-III	4.41	1.18
JULIAC-IV	3.84	1.18

2.3.2.5 AMS collection efficiency

Collection efficiency (CE) of AMS means the particle transmission and detection efficiency and is mainly affected by 1) transmission loss in the aerodynamic lens as a function of particle size, 2) shape-related collection loss at the vaporizer due to particle beam broaden, 3) particle bouncing loss when impact vaporizer as a function of particle phases. An empirical algorithm called composition-dependent collection efficiency (CDCE) was introduced by (Middlebrook et al., 2012) to improve the determination of CE. Constant collection efficiency (CE) equal to 0.96 for AMS_1 was applied for the JULIAC-I and the JULIAC-II, while Composition-dependent collection efficiency (CDCE) (Middlebrook et al., 2012) was estimated and applied with setting default CE value of 0.57 for AMS_2 during the JULIAC-III and the JULIAC-IV. Default CE value was the averaged ratio of an aerosol total mass detected by AMS and SMPS, and the SMPS total mass of aerosol SMPS was calculated with the averaged aerosol density of 1.4 g cm^{-3} (Cross et al., 2007) and aerosol total volume detected by SMPS. The variation of collection efficiencies among different AMS is common, and CE values estimated in this study is comparable to previously reported CE values of AMS (Lanz et al., 2010).

2.4 SMPS and CPC

The size distribution of particles in the diameter range of 10 to 1000 nm could be detected by Scanning Mobility Particle Sizer (SMPS, TSI). But during the JULIAC campaign, around 10-750 nm diameter scan range was set for SMPS, and the maximum and minimum scanned range of aerosol has been slightly adjusted to balance the high time resolution and high coverage of total fine particle. The time resolution of SMPS data used during the JULIAC was 7 min. The SMPS is made up of an Electrostatic Classifier (TSI Classifier model 3080, TSI DMA 3081) and a Condensation Particle Counter (TSI Water CPC 3786). Inlet aerosol is firstly charged by passing through a Model 3077 Krypton-85 neutralizer and then enter a Differential Mobility Analyzer (DMA) where the electrical field of the DMA together with the electrical mobility of the particles defines the particle size exiting the DMA. The size selected monodisperse particles existing from DMA then go through the CPC to be counted the number concentration. The size distribution of particle number, surface, and mass concentration could be estimated based on the selected size by DMA, detected number concentration of each size range, and averaged aerosol density of 1.4 g cm^{-3}(Cross et al., 2007). Instead of illustrating particle size distribution, SMPS data is also used to estimate the collection efficiency of AMS during the JULIAC campaign. A stand-alone condensation particle counter (TSI water CPC 3788) was also used to record the total number concentration of particles (diameter>5nm). The operation, maintenance, and data treatment of the SMPS were supported by Stefanie Andres.

2.5 Supporting measurements and instrumentations

In terms of the rest atmospheric species involved in this study, N_2O_5 were measured by custom-built cavity ring-down spectroscopy (FZJ-CRDS) and a similar design in details could be found in

(Wagner et al., 2011). Photolysis frequencies were estimated based on spectral actinic flux densities detected by a spectroradiometer (Bohn et al., 2005b, Bohn and Zilken 2005a). Carbon monoxide (CO), carbon dioxide (CO_2), and methane (CH_4) concentrations were continuously detected by a cavity ring-down instrument (Picarro). nitrogen dioxide (NO_2) and nitric oxide (NO) were monitored by a chemiluminescence (CL) instrument with a photolytic converter (ECO PHYSICS); O_3 was monitored by two UV photometers (Ansyco 41M and Thermo Scientific 49i) which agree with each within 5 %. Comprehensive VOCs concentration is supplied by both proton transfer reaction-time of the flight-mass spectrometer (PTR-ToF-MS) and Vocus PTR-ToF.

Chapter 3 Methodologies

Data analysis methodologies utilized in this study are centrally introduced in this chapter. The mechanism of source factor analysis, positive matrix factorization (PMF) is detailed presented. Calculation methods and formular for aerosol components (e.g. organic nitrate), elemental ratio (e.g., O:C) are also displayed here. In addition, meteorological analysis (such as wind rose), modelling (e.g., ISORROPIA) and chemical kinetics calculation involved in this study are also briefly introduced in this chapter.

3.1 Positive matrix factorization/PMF

3.1.1 PMF mechanism

Positive matrix factorization (PMF) is a mathematical technique to treat bilinear unmixing problems (Paatero et al., 1994) and has been extensively applied in aerosol source apportionment studies (Jimenez et al., 2009, Zhang et al., 2011, Sun et al., 2012, Crippa et al., 2014, Dai et al., 2019). As shown in Eq. 10, PMF resolves the variability of a multivariate database X (variables m/z intensities as a function of time measured by HR-ToF-AMS in this case) as the linear combination of limited factor profiles matrix F (each row i of F represent static factor mass spectrum) and their corresponding time series matrix G (each column j represent corresponding factor time series) as shown in Figure 3-1. Factor profile could not only illustrate the ion attribution from same source but also ion fragments distribution from same species (e.g., organic nitrate fragment NO_2^+, NO^+). Matrix E represents the model residual and is calculated by summing up the squared model residuals e_{ij} weighted by the uncertainty σ_{ij} for all input points in matrix X as shown in Eq. 11. Objective function Q represents the total sum of the squared model residuals e_{ij} weighted by the uncertainty σ_{ij} for all into data ij as shown in Eq. 11, which is minimized during PMF algorithm.

$$X = G \times F + E \qquad \text{Eq. 10}$$

$$Q = \sum_{i=1}^{m} \sum_{j=1}^{n} \left(\frac{e_{ij}}{\sigma_{ij}}\right)^2 \qquad \text{Eq. 11}$$

For understanding the source's contribution and their seasonal variation of organic aerosol, PMF analysis was utilized to resolve high-resolution aerosol organics matrix (m/z 12-160) detected by HR-ToF-AMS for four JULIAC intensive phases. In this study, the software Source Finder (SoFi Pro 8.0.3.1) (Canonaco et al., 2013), Igor-based interface for initiating and controlling the multilinear engine (ME-2) (Paatero 1999) algorithm, was applied for resolving seasonal aerosol organics source apportionments. ME-2 solver could constrain priori mass spectral information or time series and accordingly reduce the rotational ambiguity (Paatero et al., 2003). More details setting of PMF/ME-2 modeling was given below.

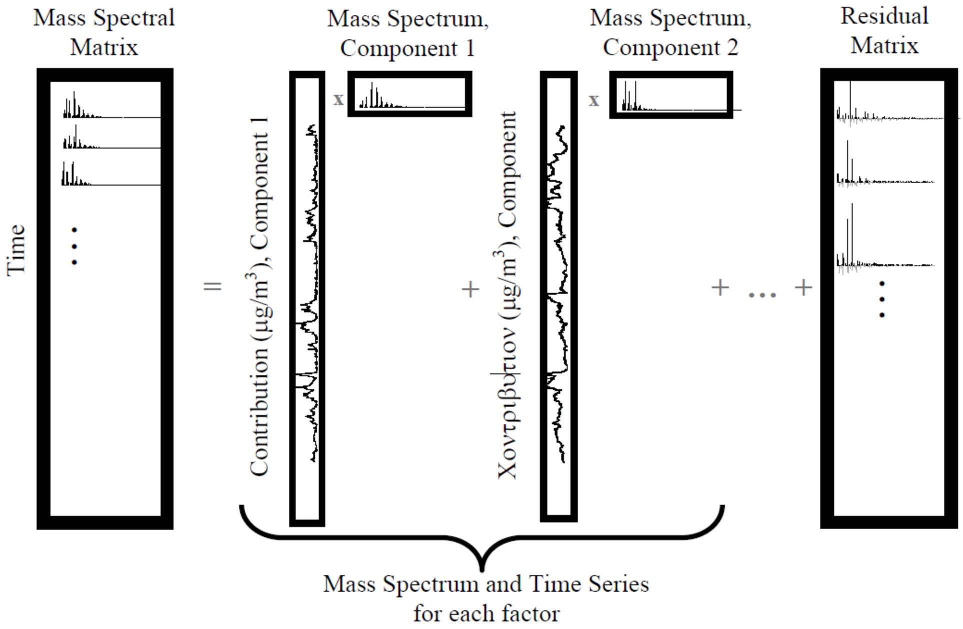

Figure 3-1: Schematic of PMF analysis of an AMS dataset. The matrix of time series of the factors corresponds to matrix G and the matrix of factors mass spectra represents matrix F in Eq. 10 (image credit: Fig. 1. (Ulbrich et al., 2009))

3.1.2 Unconstrained and constrained PMF

The non-negative aerosol organics matrix (m/z 12-160, without isotopes) detected by HR-ToF-AMS and the corresponding error matrix were prepared and extracted by the PIKA tool kit according to the algorithm introduced by (Ulbrich et al., 2009). For the main setting of PMF analysis, the signal to noise (S/N) threshold of the unexplained variation was set to be 2. S/N down weight function for cell-wise data was applied to downweigh error of each cell separately which S/N lower than 1 (Visser et al., 2015). Downweighing is executed by enlarging the error of weaker signals by multiplying a factor of 2 to reduce the influence of these points in the PMF algorithm (Paatero and Hopke 2003, Crippa et al., 2013b). CO_2^+ related ions (O^+, HO^+, H_2O^+, and CO^+) were also downweighed with a weight factor of 2.24 in case of the excessive weighting of CO_2^+. Unconstrained PMF runs were firstly performed for the organic matrix of each JULIAC phase in ME-2 by rotational techniques, Seed and Fpeak with a scan range of 2-10 factors to evaluate appropriate factor numbers. In this step, Q normalized to the expected value of Q (Q/Qexp), unexplained variation (UEV, unexplained real signal+nosie), and residual variation (as shown in Figure 3-2) were mainly monitored and compared. The expected Q (Qexp) equals the degrees of freedom of the fitted data as shown in Eq. 12, with m, n representing columns and rows number of the input matrix and p representing factors number (Paatero et al., 2002). For the AMS data set, p(n+m) is ignorable compared to n*m. Therefore, Qexp could be estimated as n*m which corresponds to the data point number of the input matrix. If all data in the input matrix are fit to within their expected error, then $(\frac{e_{ij}}{\sigma_{ij}})^2$ equal to 1 and then obtained Q/Qexp should close to 1(Ulbrich et al., 2009)

$$Qexp = n \cdot m - p \cdot (n + m) \qquad \text{Eq. 12}$$

Factor numbers satisfy low and stable Q/Qexp value (previously reported between 1-5), low UEV (around 20% to 50% for big ambient datasets), and low value of residual without regular diurnal and overall variation could be preliminarily considered as proper factor number and applied in further compile constrained PMF analysis. Factors (mainly primary factors in this study) with typical spectrum features and interpretable diurnal and overall variations could be firstly exported as preliminary factor spectrum, which could be used as a prior factor for the next constrained PMF analysis.

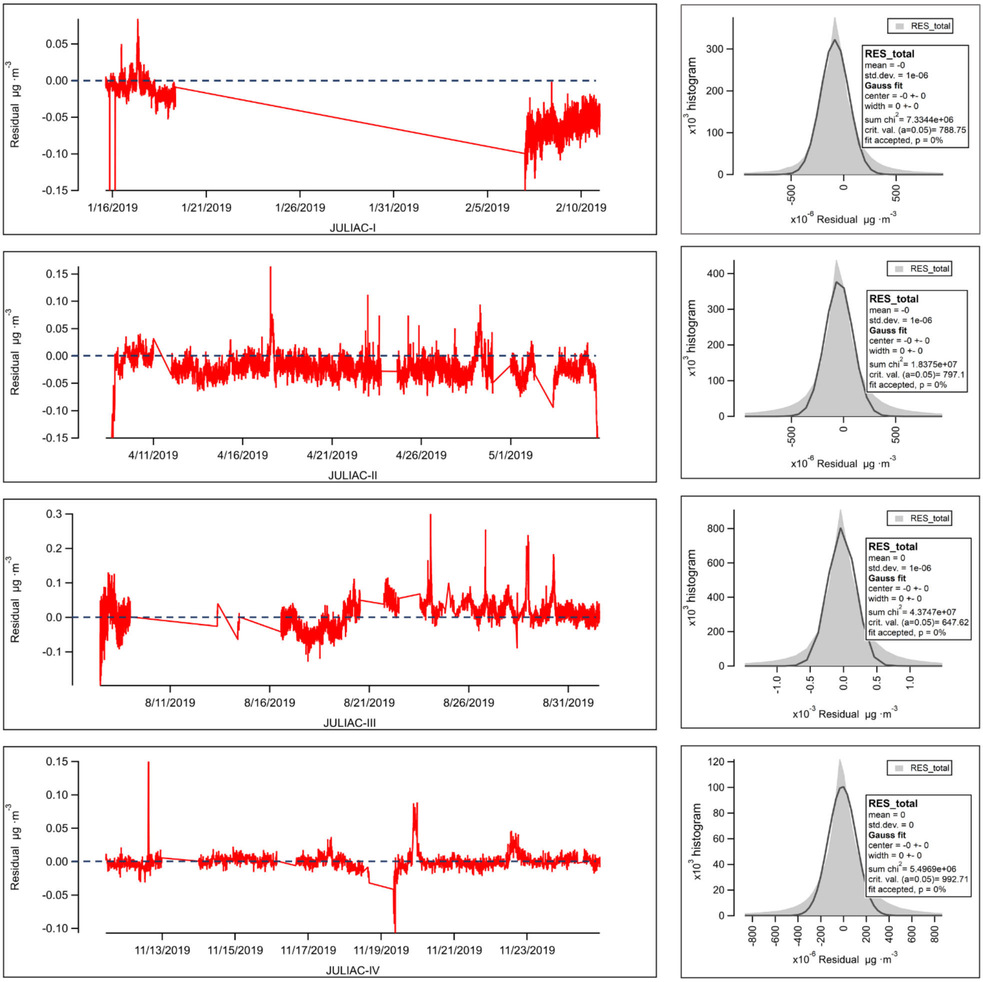

Figure 3-2: time series (left) and histogram (right) of the OA PMF residual for final selected PMF run for four intensive phases of the JULIAC campaign. Zero lines are marked for all residual time series as reference

Constrained PMF analysis, mainly by a-value approach, was then executed with assumed proper factor numbers and constrained factor profiles (normally primary factor, like HOA) from previous similar filed organic aerosol source apportionment studies or preliminary factors determined by unconstrained analysis of this study. Multiple prior factors (maximum 5) could be constrained at the same time, and a proper a-value should be tested by dimension sensitivity scanning. In terms of the scanning range of a value, 0.6 is suggested as a good compromise for allowing flexibility in resolved constrained factors while still keeping high similarity between resolved factors with constrained reference profiles (Lanz et al., 2008). Huge amounts of PMF run will be generated with similar modeled quality (means the similar value of Q/Qexp, UEV, etc.) after the above unconstrained and constrained PMF analysis, which were burdens if manually explore all runs properties. Therefore, criteria-based selection supported by Sofi was used to automatically explore large numbers of runs once by inspecting the scores of user-defined criteria. For example, as shown in Figure 3-3, one-dimensional plot of the score for user setting criteria (factor time-series correlation coefficient with organic nitrate variation) was displayed over all PMF runs, and then in this visualized graph proper runs could be easily selected. More than one criteria could be applied for proper runs exploration, which could efficiently narrow down the run number for detailed interpretability investigation as discussed below.

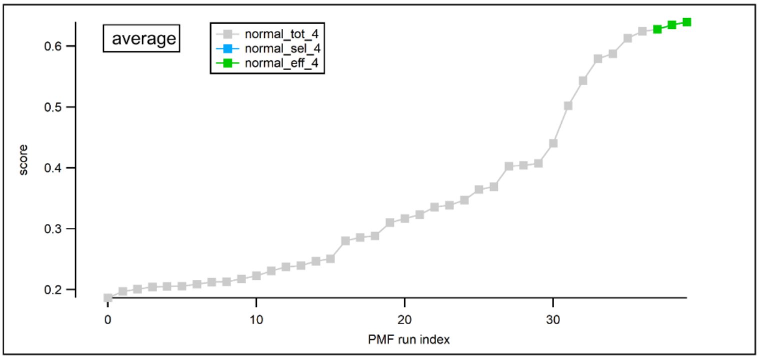

Figure 3-3: Auto criteria-based selection function based on the user-defined criteria (named score in the graph). In this example, the score represents the correlation coefficient organic nitrate variation during the JULIAC-II with factor time-series resolved in several PMF runs.

After the criteria-based selection, limited runs were selected and could be detailed explored in terms of spectra overall features, and diurnal and overall variation patterns. To support that exploration, large amounts of referred profiles from previous research and comprehensive atmospheric species data sets detected during the JULIAC were utilized. As shown in Figure 3-4, correlation analysis overview of profile and time series generated in Sofi panel efficiently search the potential connection. In addition to that powerful and quick scan supplied by Sofi, more interpretation and arguments about the proper PMF runs selection will be given in section 4.2.

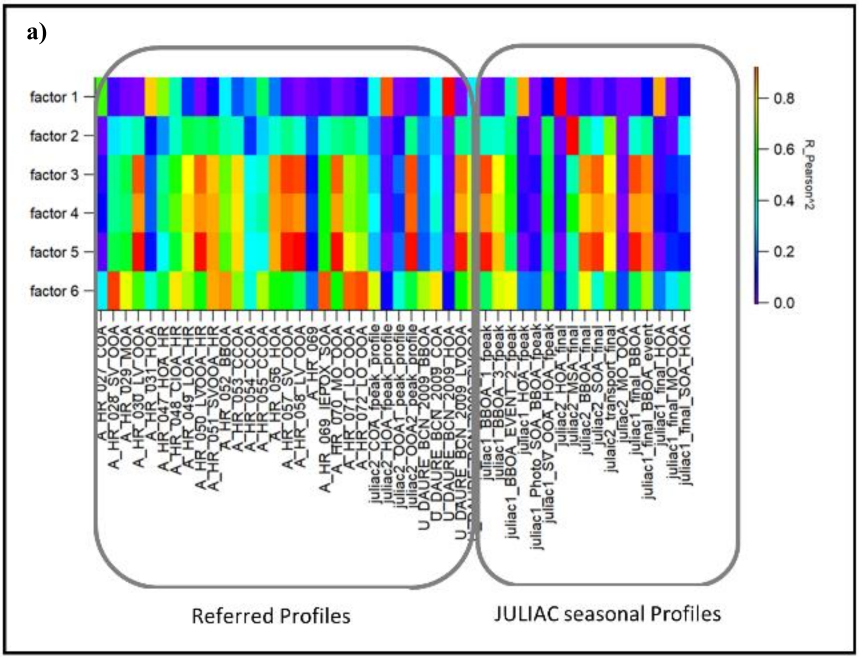
a)
factor 1
factor 2
factor 3
factor 4
factor 5
factor 6
A_HR_027_COA
A_HR_028_SV_OOA
A_HR_029_MOA
A_HR_030_LV_OOA
A_HR_031_HOA
A_HR_047_HOA_HR
A_HR_048_CIOA_HR
A_HR_049_LOOA_HR
A_HR_050_LVOOA_HR
A_HR_051_SVOOA_HR
A_HR_052_BBOA
A_HR_053_CCOA
A_HR_054_CCOA
A_HR_055_CCOA
A_HR_056_HOA
A_HR_057_SV_OOA
A_HR_058_LV_OOA
A_HR_069
A_HR_069_IEPOX_SOA
A_HR_070_MO_OOA
A_HR_071_LO_OOA
A_HR_072_LO_OOA
juliac2_COA_fpeak_profile
juliac2_HOA_fpeak_profile
juliac2_OOA1_peak_profile
juliac2_OOA2_peak_profile
U_DAURE_BCN_2009_BBOA
U_DAURE_BCN_2009_COA
U_DAURE_BCN_2009_HOA
U_DAURE_BCN_2009_LVOOA
juliac1_BBOA_1_fpeak
juliac1_BBOA_3_fpeak
juliac1_BBOA_EVENT_2_fpeak
juliac1_HOA_fpeak
juliac1_Photo_SOA_BBOA_fpeak
juliac1_SV_OOA_HOA_fpeak
juliac2_HOA_final
juliac2_MSA_final
juliac2_BBOA_final
juliac2_SOA_final
juliac2_transport_final
juliac2_MO_OOA
juliac1_final_BBOA
juliac1_final_BBOA_event
juliac1_final_HOA
juliac1_final_MO_OOA
juliac1_final_SOA_HOA
0.8
0.6
0.4
0.2
0.0
R_Pearson^2
Referred Profiles
JULIAC seasonal Profiles

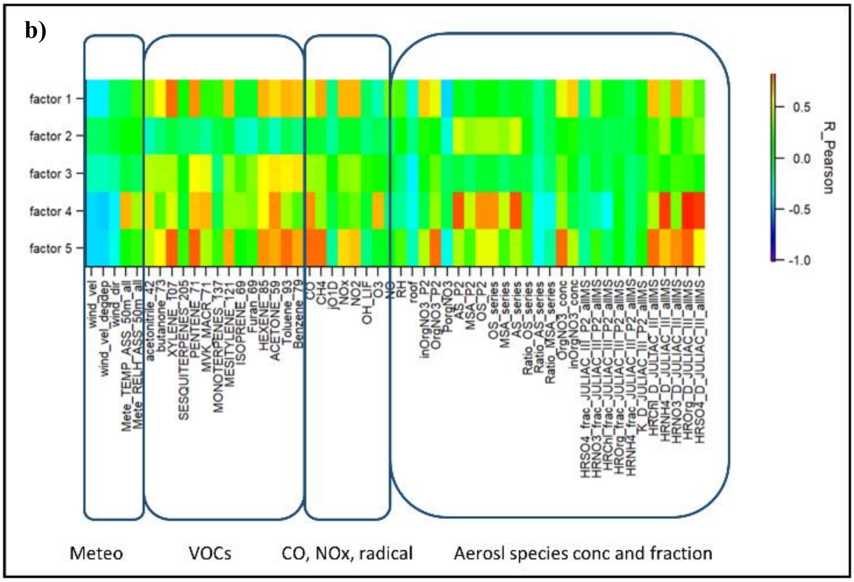
b)
factor 1
factor 2
factor 3
factor 4
factor 5
wind_vel
wind_vel_degdep
wind_dir
Mete_TEMP_ASS_50m_all
Mete_RELH_ASS_50m_all
acetonitrile_42
butanone_73
XYLENE_107
SESQUITERPENES_205
PENTENE_71
MVK_MACR_71
MONOTERPENES_137
MESITYLENE_121
ISOPRENE_69
Furan_69
HEXENE_85
ACETONE_59
Toluene_93
Benzene_79
CO
CH4
jO1D
NOx
NO2
OH_LIF
O3
NO
RH
roof
inOrgNO3_P2
OrgNO3_P2
PorgNO3
AS_P2
MSA_P2
OS_P2
OS_series
MSA_series
AS_series
Ratio_OS_series
Ratio_AS_series
Ratio_MSA_series
OrgNO3_conc
inOrgNO3_conc
HRSO4_frac_JULIAC_III_P2_allMS
HRNO3_frac_JULIAC_III_P2_allMS
HRChl_frac_JULIAC_III_P2_allMS
HROrg_frac_JULIAC_III_P2_allMS
HRNH4_frac_JULIAC_III_P2_allMS
K_D_JULIAC_III_P2_allMS
HRChl_D_JULIAC_III_allMS
HRNH4_D_JULIAC_III_allMS
HRNO3_D_JULIAC_III_allMS
HROrg_D_JULIAC_III_allMS
HRSO4_D_JULIAC_III_allMS
0.5
0.0
-0.5
-1.0
R_Pearson
Meteo
VOCs
CO, NOx, radical
Aerosl species conc and fraction

Figure 3-4: Correlation analysis overview of (a)factor profiles and (b) factor time series of the JULIAC-III constrained PMF analysis. For profile correlations, large amounts of referred profiles from previous research and other JULIAC phases seasonal PMF results were included. For time-series correlation, comprehensive atmospheric species data sets were included, like wind direction and speed, VOCs, trace gases.

In conclusion, the optimal PMF solution was finally selected after checking the evaluation parameters, the residuals, the overall features and tracer ions of factor spectrum, the correlation, and interpretability of factor's variation (including diurnal pattern) accordance with external tracer (like VOCs, radicals, photolysis frequency, wind direction speed, etc.).

3.1.3 Nitrate added PMF analysis

In this study, PMF analysis and corresponding results normally mean PMF with non-negative aerosol organics matrix as input if there is no specific note. In addition, nitrate ions added PMF analysis was also utilized in this study by manually combining intensity and error variation of fragment NO^+ and NO_2^+ into the organic matrix and corresponding error matrix respectively. That nitrate added PMF analysis is designed to study the sources attribution of organic nitrate and further support the development of night OA formation. Corresponding results will be mainly discussed in section 4.4 and detailed PMF results overview could be found in section A. 11. More inorganics ions added PMF methods (like sulfate ions added PMF) could be found in website: http://cires1.colorado.edu/jimenez-group/wiki/index.php/PMF-AMS_Analysis_Guide#For_AMS_Organics_.2B_Other_Signals_including_AMS_Inorganics, but won't be mentioned in this study.

The determination of all source factors of nitrate+organic PMF analysis mainly rely on the similarity of factor spectra and time series with organic PMF results, and full overview of nitrate+organic PMF during the JULIAC are displayed in appendix A. 11. Overall, nitrate fragments are barely attributed to HOA, BBOA, and LO/MO-OOA factors, and therefore their overall factor time series, diurnal pattern, and profile characteristics (such as elemental ratio) of nitrate+organic PMF analysis are almost the same with organic PMF results and easily to be determined. And for NO-OOA and regional transport factor determined by nitrate+organic PMF, their factor spectrum show obvious changes due to nitrate fragments distribution, but their time series still show high similarity with them in organic PMF results. In addition, one more nitrate factor (called NO_3-OA) is determined during nitrate+organic PMF analysis and mainly illustrate aerosol inorganic nitrate variation. NO_3-OA factor is found during the JULIAC-III and the JULIAC-IV, while during the JULIAC-I and the JULIAC-II it mixed with regional transport factor, so called Trans-NO_3-OA to imply a possible ammonium nitrate abundant plume regional transport.

3.2 Aerosol components and elemental ratio calculation

3.2.1 Aerosol organic nitrate estimation

Organic nitrate is formed through oxidation of VOCs in the presence of NOx and could subsequently distribute between gas-particle phases. A considerable amount of researches has pointed out that, Particle-phase organic nitrate ($pRONO_2$) not only play a key role in secondary organic aerosol formation (Xu et al., 2015b, Lee et al., 2016) and dynamic partitioning between gas-particle phases (Pye et al., 2015) but also take account of significant contribution to total organic aerosol mass (Kiendler-Scharr et al., 2016, Ng et al., 2017). Therefore, in this study concentration tendency of aerosol organic nitrate is estimated for the whole JULIAC intensive phases by an approach that mainly relied on the relative intensity of NO^+ and NO_2^+ detected by AMS (Farmer et al., 2010, Fry et al., 2013, Xu et al., 2015a, Kiendler-Scharr et al., 2016). The ratio of NO_2^+/NO^+ for all AMS measured data sets, marked as $R_{measured}$ in below Eq. 13, is used to determine the fractional contribution variation of aerosol organic nitrate ($pOrgNO_{3,frac}$) normalized to the bulk aerosol nitrate ($NO_{3,total}$) measured by AMS as shown in Eq. 13. And then the concentration variation of organic nitrate could be calculated by multiply $pOrgNO_{3,frac}$ and bulk aerosol nitrate ($NO_{3,total}$) as shown in Eq. 14, and the difference between bulk aerosol nitrate and organic nitrate is then considered as aerosol inorganic nitrate.To estimate the mass fraction of organic nitrate in measured dataset, the ratio of NO_2^+/NO^+ for pure organic nitrate (R_{OrgNO3}) and for pure ammonium nitrate (R_{calib}) are also required in Eq. 13 as parametric of standards of aerosol organic and inorganic nitrate. That ion ratio for pure ammonium nitrate is marked as R_{calib} because ammonium nitrate particle is normally used for all ionization calibration of AMS, and thus R_{calib} could be determined at each AMS IE calibration experiment.

The R_{calib} of NO_2^+/NO^+ for pure ammonium nitrate for AMS_1 (for the JULIAC-I and the JULIAC-II) and AMS_2 (for the JULIAC-III and the JULIAC-IV) measured by all IE calibrations are displayed in Figure 3-5 and Figure 3-6 respectively. Overall, the variations of R_{calib} for AMS_1 and AMS_2 are both stable, ranging from 0.51-0.58 and 0.38-0.44 respectively, and therefore averaged R_{calib}, 0.54 for AMS_1 and 0.41 for AMS_2, are applied into aerosol organic nitrate estimation during corresponding JULIAC phases in this study. For more details, the variability of calibration ratio of NO_2^+/NO^+ among different AMS has been reported and summarized in several studies (Kulmala et al., 2011, Crippa et al., 2014, Kiendler-Scharr et al., 2016) with R_{calib} variate between 0.29 and 0.85. For the ratio of NO_2^+/NO^+ for pure organic nitrate (R_{OrgNO3}), amounts of lab simulation based on oxidation reaction between volatile organic compounds (VOCs) and NO_3 radical has been done to investigate R_{OrgNO3} and suggest a possible range value of 0.2 to 0.08. Here, the fixed value (0.1) of R_{OrgNO3} suggested by Kiendler-Scharr et al 2016, is applied for all JULIAC intensive phases. Based on all the above assumptions, this methodology supplies a lower limits estimation of aerosol organic nitrate with around ± 20% uncertainty (Xu et al., 2015a, Kiendler-Scharr et al., 2016). The time series of aerosol organic nitrate for all four JULIAC intensive phases has been estimated by the approach introduced here and displayed in Figure 4-5, as well as the corresponding variation of total aerosol nitrate and inorganic nitrate.

$$pOrgNO_{3,frac} = \frac{(1+R_{OrgNO3})\times(R_{measured}-R_{calib})}{(1+R_{measured})\times(R_{OrgNO3}-R_{calib})} \quad \text{Eq. 13}$$

$$pOrgNO_{3,conc} = pOrgNO_{3,frac} \times NO_{3,total} \quad \text{Eq. 14}$$

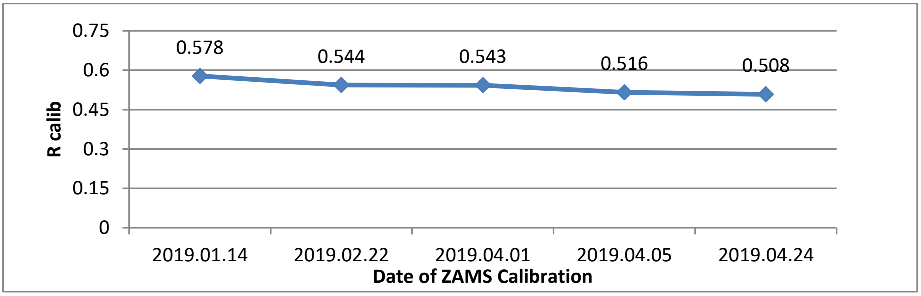

Figure 3-5: The variation of the fragment ratio of NO_2^+/NO^+ for pure NH_4NO_3 measured at AMS_1 ionization calibration during the JULIAC-I and the JULIAC-II.

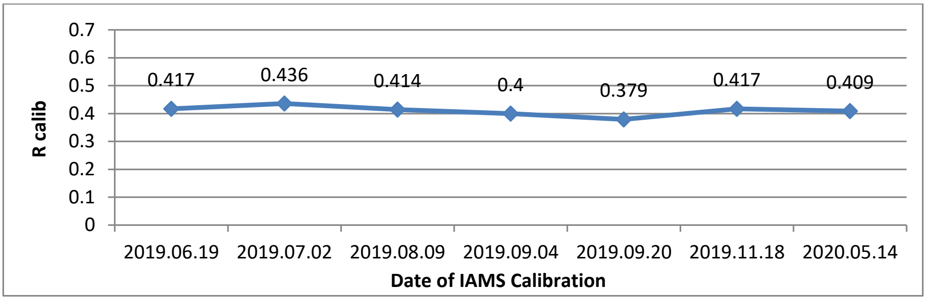

Figure 3-6: the variation of the ratio of NO_2^+/NO^+ of pure NH_4NO_3 measured at AMS_2 ionization calibrations during the JULIAC-III and the JULIAC-IV.

3.2.2 Aerosol methanesulfonic acid estimation

Methanesulfonic acid (MSA, chemical formula CH_3SO_3H) mainly derived by dimethylsulfide (DMS) oxidation, could affect cloud condensation nuclei (CCN) formation and consequentially alter radiation budget and climate (Lovelock et al., 1972, Charlson et al., 1987, Stefels et al., 2007).

To improve the understanding of the effects of MSA and potentially corresponding marine plume transport, accurate quantification methodologies of MSA mass concentration in aerosols are required. This section will introduce two major fragment methods to estimate the concentration of MSA based on AMS high-resolution data.

Ge Method (Ge et al., 2012) is shown in Eq. 15. The principle of this method is using the concentration of three characteristic ions of MSA: $CH_2SO_2^+$ (m/z 78), $CH_3SO_2^+$ (m/z 79), and $CH_4SO_3^+$ (m/z 96), to estimate the mass concentration of MSA. The ratio of 0.147 used in Eq. 15 is based on calibration with standard compounds measured in a laboratory setup.

$$[MSA] = \frac{[CH_2SO_2^+]+[CH_3SO_2^+]+[CH_4SO_3^+]}{0.147} \qquad \text{Eq. 15}$$

The HKUST method (Huang et al., 2015) is introduced in Eq. 16 and Eq. 17. $\sum_k I_{MSA,k}$, $\sum_n I_{Org,n}$, $\sum_t I_{SO4,t}$ represent the total ion intensities corresponding to MSA, organics and sulfate respectively, where k, n, and t are the number of ions of their related species.

$I_{MSA,\ CH3SO2}$ is the intensity of a typical ion $CH_3SO_2^+$ of MSA. RIE_{MSA} is the relative ionization efficiency of MSA and the empirical value of 1.3 is used for the analysis of the whole AMS data set during the JULIAC campaign. The determination method for $\mathrm{RIE}_{\mathrm{org}}$ and $\mathrm{RIE}_{\mathrm{SO4}}$ and their corresponding value during the whole JULIAC is introduced in section 2.3.2.4.

$$\sum\nolimits_k I_{MSA,k} = \frac{I_{MSA,CH3SO2}}{0.097} \qquad \text{Eq. 16}$$

$$[MSA] = \frac{\frac{\sum_k I_{MSA,k}}{RIE_{MSA}}}{\frac{\sum_n I_{Org,n}}{RIE_{Org}} + \frac{\sum_t I_{SO4,t}}{RIE_{SO4}}} \times ([Org] + [SO_4]) \qquad \text{Eq. 17}$$

3.2.3 Elemental ratio of organic compounds

Elemental ratios (mainly H:C, O:C, N:C, S:C and OM:OC) are important characteristics of organic aerosol and provide key information for understanding aerosol origination, impact, and fate in the atmosphere (Aiken et al., 2007, Aiken et al., 2008). In this study, elemental ratios of organic aerosol (OA) and OA factors are calculated by the improved-ambient method introduced by (Canagaratna et al., 2015).

3.3 Meteorological and modeling analysis

3.3.1 Back trajectory analysis

24-h back trajectories with 2 hours resolution ending in sampling site were executed during four JULIAC intensive phases by PC-based Hybrid Single-Particle Lagrangian Integrated Trajectory (HYSPLIT) model (Version 5.0.0) based on Global Data Assimilation System (GDAS) meteorological data supplied by National Oceanic and Atmospheric Administration (NOAA) Air Resources Laboratory (ARL). The arriving time of trajectories corresponds to the detection time of instruments involved in the JULIAC campaign and the arrival height corresponding 50 m sampling height of the JULIAC tower. Further exploration of trajectories, like cluster analysis, concentration field (CF) statistics (Seibert et al., 1994, Debevec et al., 2017) was implemented by a powerful Igor Pro graphical interface, ZeFir (version 3.7, https://sites.google.com/site/zefirproject/home)(Petit et al., 2017). More applications and a detailed introduction about ZeFir trajectories exploration could be found in previous studies (Debevec et al., 2021).

3.3.2 Polar analysis

The polar analysis normally means displaying pollutant concentration (mean concentration for one wind speed-direction bin) in polar coordinates to investigate the correlation of pollutants with wind speed and direction (or another numeric variable). In this study, the wind speed and direction dependence of aerosol species detected by HR-ToF-AMS during the JULIAC, and the organic aerosol source factors resolved by PMF were mainly developed by non-parametric wind regressions (NRW) polar plots (Henry et al., 2009). Since the algorithm of the polar graph does not consider the frequencies of wind direction and wind speed, the traditional wind rose, and joint probability graphs were also made to illustrate the likelihood of each combination of wind direction and wind speed. All the above polar plots utilized in this study were also produced by the ZeFir tool. The meteological data used for polar analysis is detected in 50 m height. To synchronize the measurements in the SAPHIR chamber, the time line of all meteorological data are back-shifted for half hour to compensate the 1 hour residence time of sampled air in the SAPHIR chamber.

3.3.3 Atmospheric layer estimation and effect

Surface inversion, also called radiational inversion, is produced by terrestrial radiational cooling of near-ground air during the night. Surface inversion could enhance the stability of the near-ground atmosphere and can enhance the accumulation of near-ground emissions at night. Therefore, to reduce or mostly eliminate the potential surface layer interference, the sampling setup of the JULIAC campaign is designed to collect sampling air from a 50-meter height. Based on previous studies of surface layer height at the same site, a 50 m sampling height should be through the year most of the time higher than the near-ground inversion layer and located at the nocturnal boundary layer. The surface layer is also estimated based on the potential temperatures (θ) calculated by gradient measurements of ambient temperature at height 2-m, 10-m, 20-m, 30-m, 50-m, 80-m, 100-m, and 120-m during the whole JULIAC campaign. The potential temperature (θ) is estimated by Eq. 18, in which T represents absolute temperature (in K), P is ambient pressure, P_0 stands for standard reference pressure (1013.25 hPa), R means the gas constant of air and $c_p$is the specific heat capacity (Bolton 1980, Moore 1999). For this study the constant value of R/c_p 0.286 is used for all calculations, and the pressure measured at the ground during campaign is used as P for all heights which neglects pressure changes with height. Pressure changes between the surface and 120 m are estimated to be 14.3 hPa and are reasonably small for this study to avoid large uncertainties in the determined layer height.

$$\theta = T(\frac{P_0}{P})^{R/c_p} \qquad \text{Eq. 18}$$

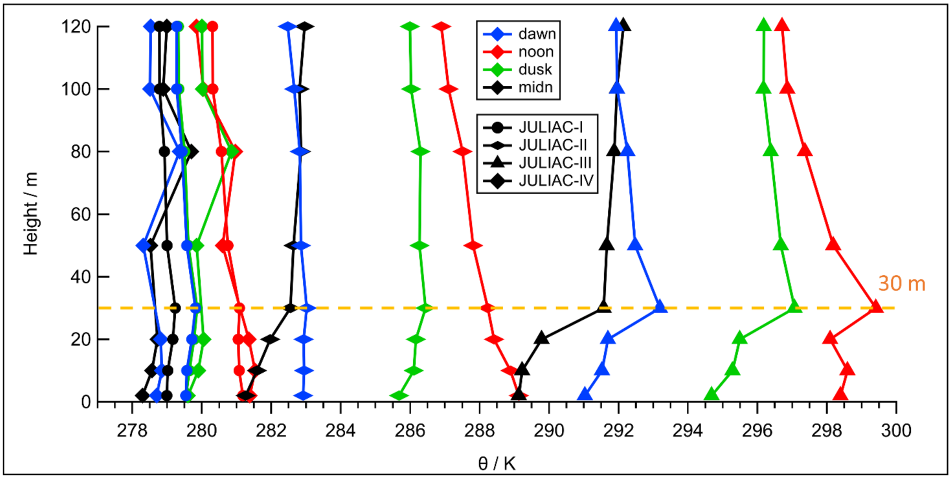

Figure 3-7: Potential temperatures estimation of four JULIAC phases based on gradient measurements of ambient temperature at height 2 m, 10 m, 20 m, 30 m, 50 m, 80 m, 100 m, and 120 m. Daily variation of potential temperature are sorted into four main period: midnight (22:00-3:00 UTC); dawn (4:00-9:00 UTC); noon (10:00-15:00 UTC) and dusk (16:00-21:00 UTC).

The potential temperatures variations versus the height at four time periods (midnight, dawn, noon, and dusk) during the whole JULIAC campaign are displayed in Figure 3-7. As an indicator of atmospheric stability, $d\theta/dH$ implies stable atmosphere when its show a positive value otherwise indicates an unstable atmosphere (Moore 1999). A well-mixed atmospheric layer should ideally show constant potential temperature along with the vertical height (Batchvarova et al., 1994). During night, the vertical structure of atmosphere is normally made up of a surface layer (normally <20 m), a nocturnal boundary layer (NBL, 20 m-200 m), and a residual layer (>200 m) due to temperature inversion (Brown et al., 2007). The surface inversion layer during the whole JULIAC campaign is around 30 meters high for all seasons based on potential temperature profiles shown in Figure 3-7, meaning that the ambient air sampled at 50-meter height by the JULIAC tower should be located almost all of the time in the nocturnal boundary layer. In conclusion, 50-m sampling setup design of the JULIAC campaign correspond to nocturnal boundary layer measurement during night.

Compared to the boundary layer, the nocturnal boundary layer is often relatively stable due to the radiative cooling of the ground surface. Therefore, the turbulence in NBL could be suppressed and subsequently cause aerosol accumulation in the near-ground height, which is called NBL driven accumulation in this study. For boundary lay effect during the daytime, numbers research have reported that boundary layer could continuously expand from a few hundred meters from sunrise to 1-2km height at around noon (local 14:00-17:00)(Martin et al., 2010, McGrath-Spangler et al., 2013, Xu et al., 2015a). That continuous boundary height expansion consequently causes the dilution effect of aerosol species, which is called boundary layer height (BLH) driven dilution here.

Although there is no direct measurement to estimate the stability status of NBL and boundary layer height variation, the possible nighttime NBL driven accumulation and BLH driven dilution could be roughly deduced by the diurnal behavior of aerosol species, especially aerosol sulfate. Compared to semi-volatile aerosol species (such as nitrate), low volatile aerosol sulfate has no temperature-dependent evaporation and could be considered as a better tracer of layer effect. As shown in Figure 3-8, the diurnal variation of aerosol bulk species organics (Org), nitrate (NO_3), ammonium (NH_4), chlorine (Chl), and sulfate (SO_4) mass concentration normalized to corresponding diurnal maximum concentration are displayed for all JULIAC intensive phases. And the corresponding diurnal maximum of all aerosol species is also marked in the graph with unit $\mu g/m^3$.

About possible NBL driven accumulation during night, the enhancement from sunset and sharp decrease at daybreak of aerosol sulfate will be the typical phenomenon of strong NBL driven accumulation. However, in Figure 3-8, nighttime sulfate increasing only be observed during the JULIAC-I and no obvious sulfate concentration decrease during daybreak of the whole JULIAC. These support that there is no strong aerosol night accumulation caused by NBL during the JULIAC.

In terms of possible BLH driven dilution during the daytime, a significantly decrease of aerosol sulfate during daytime from morning to noon is the typical aerosol behavior dominated by BLH driven dilution. In Figure 3-8, during daytime, sulfate concentration only decreases during the

JULIAC-I but increase during the rest phases. That daytime enhancement of sulfate concentration could be secondary sulfate formation from photochemistry and possible SO_4 entrainment from aloft (Weber 2003). Overall, it suggests the BLH dilution effect does not dominate aerosol species daytime variation during most time of the JULIAC.

In conclusion, the JULIAC campaign setup corresponds to the nocturnal boundary layer (NBL) measurement during night. The dynamics of the atmospheric boundary layer have limited but not dominated effect on aerosol variation and subsequently OA source contribution during the JULIAC campaign.

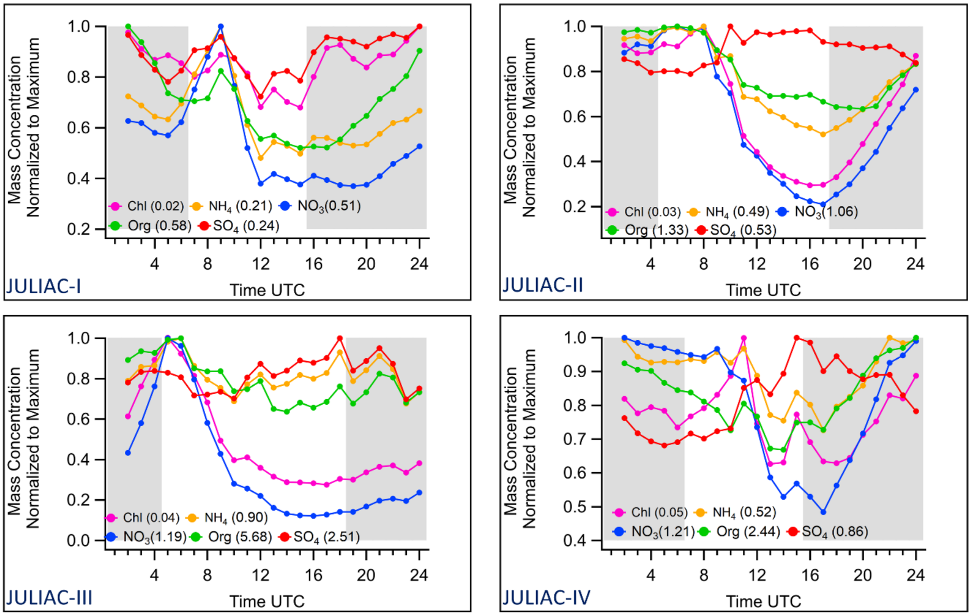

Figure 3-8: Diurnal variation of aerosol bulk species organics (Org), nitrate (NO_3), ammonium (NH_4), chlorine (Chl), and sulfate (SO_4) mass concentration normalized to corresponding diurnal maximum concentration for all JULIAC intensive phases. The corresponding diurnal maximum of all aerosol species are marked in the graph with unit µg/m^3.

3.3.4 ISORROPIA simulation

ISORROPIA-II is a computationally efficient and rigorous thermodynamic model that predicts the physical state and composition of inorganic atmospheric aerosol (Fountoukis et al., 2007). In this study, the liquid water content of aerosol is calculated by ISORROPIA-II based on the observed ambient relative humidity (RH), temperature (T), and aerosol concentration of nitrate (NO_3^-), sulfate (SO_4^{-2}), chloride (Cl^-), ammonium (NH_4^+), sodium (Na^+), and potassium (K^+). The advantage of ISORROPIA over the other thermodynamic equilibrium coded has been investigated with numerous in-situ data sets (Nowak et al., 2006, Fountoukis et al., 2009). The aerosol liquid water content data simulated by ISORROPIA-II in this study was supplied by Dr. Vlassis Karydis.

3.4 Chemical kinetics calculation

3.4.1 NO_3 radical estimation

Ambient N_2O_5 concentration variation was measured by a custom-built cavity ring-down spectroscopy (FZJ-CRDS) instrument during the JULIAC campaign (except the JULIAC-I). Based on the reversible reaction shown in Eq. 19, NO_3 radical concentration could be estimated through the thermal equilibrium Eq. 20 with the ambient concentration of N_2O_5 and NO_2(Brown et al., 2003). The equilibrium constant k(T) is estimated by the formula in Eq. 21 and the value of parameters A and B used in this study are $3.0\times10^{-27}/cm^3$ $molecule^{-1}$ and 10990/K respectively (recommended by NASA-JPL https://jpldataeval.jpl.nasa.gov/pdf/JPL_02-25_4_equil_rev01.pdf).

$$NO_3 + NO_2 \rightleftarrows N_2O_5 \qquad \text{Eq. 19}$$

$$[NO_3] = [N_2O_5]/(k(T) \times [NO_2]) \qquad \text{Eq. 20}$$

$$k(T)/cm^3 \cdot molecule^{-1} = A \cdot exp(B/T)\ \ (200 < T < 300K) \qquad \text{Eq. 21}$$

3.4.2 Branching ratio

The branching ratio was defined to be the fraction of the overall reaction that proceed via different channels (Cleaves 2011). In this study, the branching ratio is used to describe the consuming ratio of VOCs in dark oxidation for different dark oxidants. Major dark oxidants $NO_3\cdot$ and O_3 are mainly considered in this study, and the branching ratio of NO_3 radical during nocturnal oxidation was given in Eq. 22 as an example. Same branching ratio calculation and application could be found in the previous study (Xu et al., 2015).

$$Branching\ ratio_{species\ i+NO_3\cdot} = \frac{k_{[species\ i+NO_3\cdot]} \times [NO_3\cdot]}{k_{[species\ i+NO_3\cdot]} \times [NO_3\cdot] + k_{[species\ i+O_3\cdot]} \times [O_3]} \qquad \text{Eq. 22}$$

Chapter 4 Results and Discussion

In this chapter, submicron aerosol species (mainly aerosol organics (Org), nitrate (NO_3), ammonium (NH_4), chlorine (Chl), and sulfate (SO_4)) seasonal concentration variations during the year-long JULIAC campaign are displayed and discussed in section 4.1. For organic aerosol, the seasonal source apportionment result overview of OA during the JULIAC campaign is exhibited in section 4.2 with detailed determination discussions. Specific OA sources (the marine OA transport and nocturnal OA contribution) resolved in this study are concentrated discussed in detail in section 4.3 and 4.4, respectively. Moreover, seasonal comparisons of OA properties (e.g. oxidation degree) and OA factors source contributions and source properties are discussed in section 4.5.

4.1 Aerosol chemical composition overview

The averaged mass concentration of total non-refractory submicron particles (NF-PM1) and the averaged bulk concentration of major aerosol species (organics, nitrate, ammonium, chlorine, and sulfate) during four intensive phases of the JULIAC campaign (from Jan. 2019 to Nov. 2019) measured by HR-ToF-AMS are concluded in Table 4-1 in comparison with previous ambient aerosol studies. As shown in Table 4-1, the average total mass concentrations of aerosol during the JULIAC-I (winter), the JULIAC-II (spring), the JULIAC-III (summer), and the JULIAC-IV (autumn) are 1.05 ± 0.98 $\mu g/m^3$, 2.56 ± 2.61 $\mu g/m^3$, 7.68 ± 4.82 $\mu g/m^3$, and 4.24 ± 2.27 $\mu g/m^3$, respectively, which are comparable to previous aerosol seasonal observations listed in Table 4-1. And the overall average of aerosol mass concentration measured in this semi-rural site is 4.0 $\mu g/m^3$, roughly keeping with the aerosol levels reported in previous studies in Germany or other contiguous countries (Allan et al., 2003, Vester et al., 2007, Jimenez et al., 2009, Raatikainen et al., 2010).

Table 4-1: the overview and comparison of averaged aerosol species concentration and averaged total aerosol concentration measured by AMS, total aerosol number and volume measured by SPMS and atmospheric condition parameters (relative humidity RH, and ambient temperature temp) among four JULIAC intensive phases and other previous aerosol observations.

Campaign	Period	Total aerosol µg/m^3	Nitrate µg/m^3	Sulfate µg/m^3	Ammonium µg/m^3	Chlorine µg/m^3	Organics µg/m^3	Total volume nm^3/cm^3	Total number cm^{-3}	RH %	Temp °C	Reference
JULIAC-I	Jan.15th--Feb.10th, 2019, Winter	1.05 ± 0.98	0.27±0.41	0.21±0.16	0.13±0.17	0.02±0.02	0.41±0.31	3.07±2.78 e^9	2.45±1.53 e^3	66.6±17.9	4.9±3.5	This study
JULIAC-II	Apr. 8th--May 5th, 2019, Spring	2.56 ± 2.61	0.63±1.29	0.48±0.35	0.37±0.51	0.02±0.02	1.07±0.87	2.15± 1.58 e^9	2.78±1.32 e^3	44.0±21.4	11.5±5.5	This study
JULIAC-III	Aug. 7th--Sep. 1st, 2019, Summer	7.68 ±4.82	0.31±0.46	1.65±1.18	0.66±0.47	0.02±0.01	3.46±2.97	1.60± 1.85 e^9	4.02±1.89 e^3	44.9±21.1	20.7±5.0	This study
JULIAC-IV	Nov. 11th--Nov. 24th, 2019, Autumn	4.24 ± 2.27	0.98±0.78	0.70±0.41	0.47±0.31	0.04±0.03	2.04±1.11	1.13±0.74 e^9	2.41±1.28 e^3	64.8±15.3	14.9±4.6	This study
Cabauw, the Netherlands	Jul. 2012—Jun. 2013	6.2	1.86	0.93	0.89	0.06	2.17	---	---	82.2	9.2	(Schlag et al., 2016)
Hyytiälä, Finland	Mar. 31th—Apr. 15th 2005, spring	2.02	0.25	0.33	0.2	---	1.24	---	---	---	---	(Raatikainen et al., 2010)
Texas, Houston, USA	Feb. 3th—17th, 2014, winter.	6.06±4.29	1.4±1.4	1.4±0.8	0.9±0.6	0.06±0.09	2.3±1.4	---	---	76±18	9.3±6.0	(Dai et al., 2019)
Texas, Houston, USA	May 1st—31th, 2014, summer	3.6±2.32	0.08±0.1	1.3±0.6	0.5±0.2	0.02±0.02	1.7±1.4	---	---	72±19	23.6±3.8	(Dai et al., 2019)
SGP site, Oklahoma, USA	Nov. 2010—Jul. 2012	7.0±9.3	1.5±3.0	0.8±1.0	0.66±1.2	0.02±0.04	4.0±6.2	---	---	---	---	(Parworth et al., 2015)

Concerning aerosol seasonal variation, time series of aerosol organics (Org), nitrate (NO_3), ammonium (NH_4), chlorine (Chl), and sulfate (SO_4) bulk concentration has been displayed for each JULIAC intensive measurement in Figure 4-1. The gap in these aerosol variation curves represents the lack of valid aerosol data mainly due to instrument failure. As shown in Figure 4-1, the maximum of total aerosol mass concentration appears at the JULIAC-III (summer). That might be facilitated by the abundant biogenic VOCs (BVOCs) emissions and strong photochemistry during summer and is further discussed with source apportionment results in section 4.2. In contrast, the aerosol mass concentration of the JULIAC-I (winter) is the lowest during the whole year.

Regarding seasonality of aerosol composition, aerosol nitrate and ammonium mass concentration both reach a yearly maximum of 11.08 μg/m^3 and 4.24 μg/m^3 at the JULIAC-II (spring), and that higher level of ammonium nitrate is shown to be strongly affected by regional transport based on meteorological and source factor analysis results (see section 4.2). Aerosol organics and sulfate both reach their yearly maximum, 13.60 μg/m^3 and 5.97 μg/m^3, respectively during the JULIAC-III (summer). And based on the PMF analysis shown in Figure 4-39 and section 4.2, around 88% of organic aerosol during the JULIAC-III is contributed by biogenic derived SOA, which illustrates that the biogenic emission is the major OA source during the JULIAC-III. The high concentration of aerosol sulfate in the JULIAC-III is probably related to local formation, but the formation paths or mechanism are still not clear and needs further investigation. Aerosol chlorine concentration is low during the whole JULIAC campaign with an average value ranging from 0.02 - 0.04 μg/m^3.

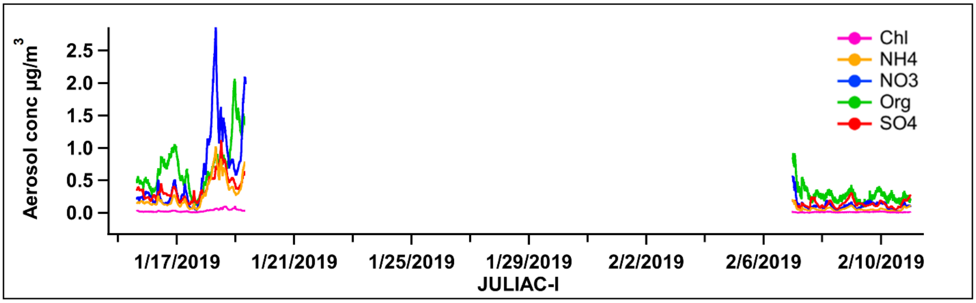

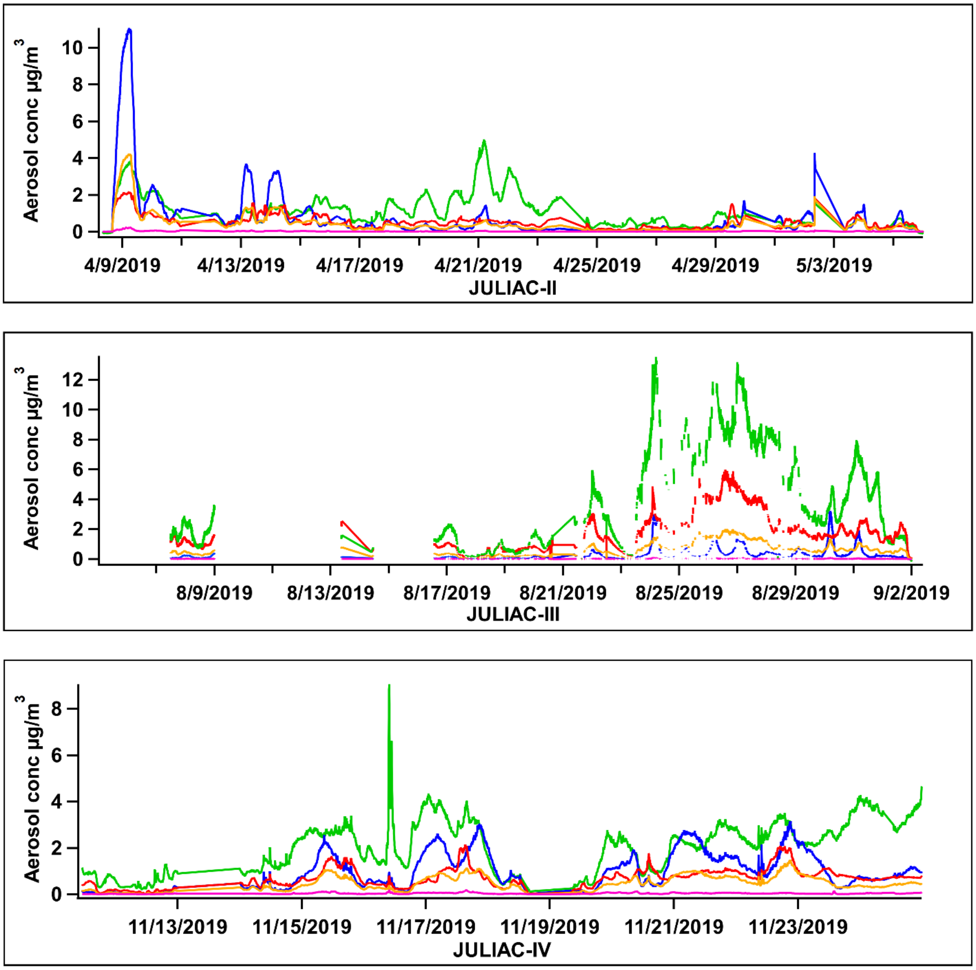

Figure 4-1: the time series of aerosol organics (Org), nitrate (NO_3), ammonium (NH_4), chlorine (Chl), and sulfate (SO_4) bulk concentration during the whole year-long JULIAC campaign

For aerosol composition, obvious seasonal differences of aerosol species fractions could be found when compared among four intensive JULIAC phases. As shown in Figure 4-2, the averaged aerosol species' mass concentrations are relatively similar during three intensive phases, namely JULIAC-I, JULIAC-II, and JULIAC-IV consisting mainly of organics (39%-48%) and followed by sulfate (19%-23%) and nitrate (17%-26%). In contrast, the JULIAC-III shows an obvious enhancement in organics (58%) and sulfate (26%) and a decrease in nitrate (5%). Overall, aerosol nitrate fraction shows obvious seasonal variation, ranging from 5.3% in the JULIAC-III to 25.9% in the JULIAC-I, and organics were the major components of aerosol during the whole JULIAC campaign accounting for 39.0% in the JULIAC-I to 57.6% in the JULIAC-III of aerosol total mass, which has been numerous times also found in both previous urban and remote site studies in Europe (Jimenez et al., 2009, Zhang et al., 2011, Crippa et al., 2014).

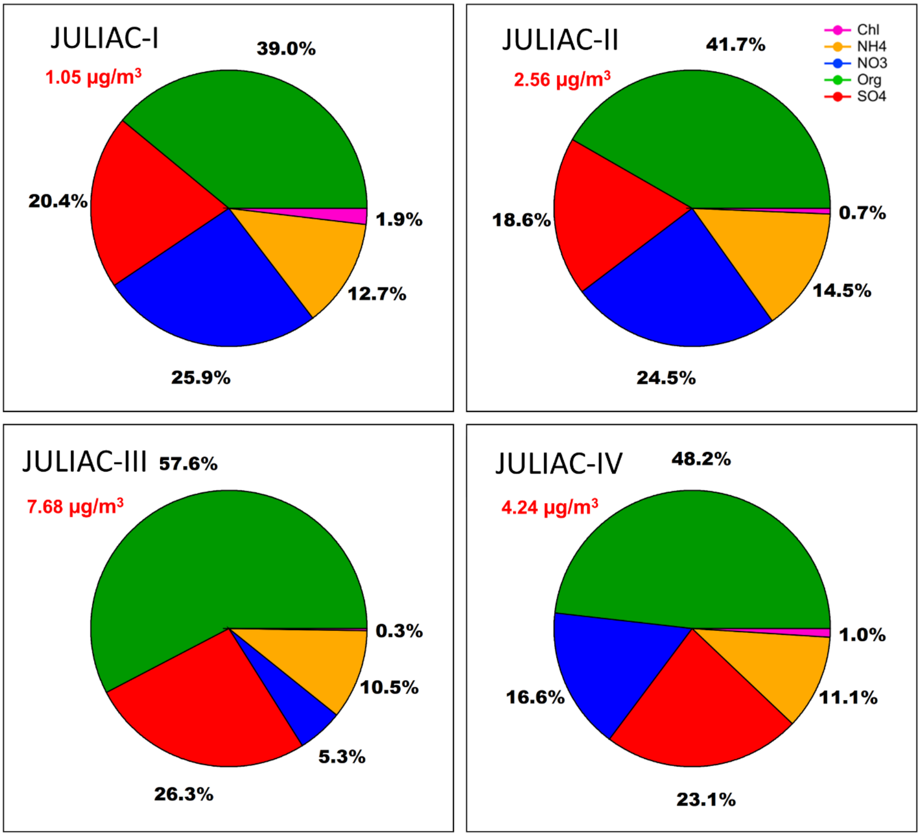

Figure 4-2: Seasonal difference of the aerosol composition with pie charts of averaged aerosol composition for all JULIAC intensive measurements. The averaged total aerosol mass concentration is also displayed for each season and marked in red.

In addition, the seasonal meteorological condition could affect aerosol concentration and composition due to regional transport. Therefore, the detailed polar graph of aerosol species (see Figure 4-3) during four JULIAC intensive phases could preliminarily show aerosol species source regions and more aerosol regional transport discussion will be given in section 4.2.3 combined with wind rose plots (see Figure 4-16), back trajectory analysis, and aerosol source appointment results.

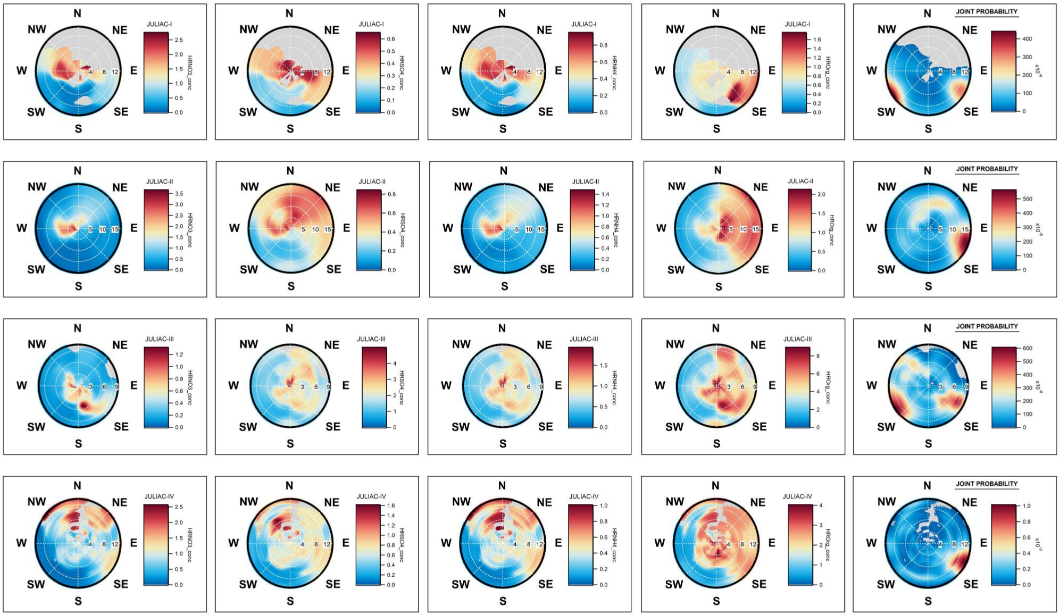

Figure 4-3: Polar diagram of aerosol species during four JULIAC intensive phases based on non-parametric wind regressions (NRW). From left to right, there are the NRW graphs colored by the concentration of aerosol nitrate, sulfate, ammonium, organics, and the corresponding joint probability graph. The polar graph is created based on the wind direction and wind speed measured in 50-m height. The concentration of aerosol species are utilized as the color code in the polar graph to illustrate the potential regional source.

With respect to diurnal variation of aerosol species shown in Figure 4-4, aerosol nitrate shows strong diurnal variation during the whole year with a maximal night-day difference of 1.04 µg/m^3. Aerosol nitrates build up until sunrise which may be related to the possible accumulation effect of the nocturnal boundary layer (see section 3.3.3), traffic emissions, and NO_3· dark oxidation (details discussed in section 4.4). The obvious downtrend of aerosol nitrate concentrations during the daytime starting around 4:00-8:00 (UTC)until 11:00-16:00 (UTC) is likely related to the dilution effect caused by the daytime expansion of the boundary layer (see section 3.3.3) and volatility-dependent nitrate evaporation. The slight enhancement of aerosol organic around mid-day in diurnal variation implies the OA contribution from photooxidation. Moreover, the significant night enhancement of organics concentration is possibly contributed by primary emission (like biomass burning, discussed in 4.2), dark oxidation (introduced in section 4.4), and possible accumulation effect caused by nocturnal boundary layer (details in 3.3.3). The concentration of aerosol sulfate increases during the day at almost all the JULIAC measurement periods with maximal day enhancement equal to 0.5 µg/m^3 (the JULIAC-III), which could be explained by photooxidation SO_2 or SO_4 entrainment from aloft (Weber 2003).

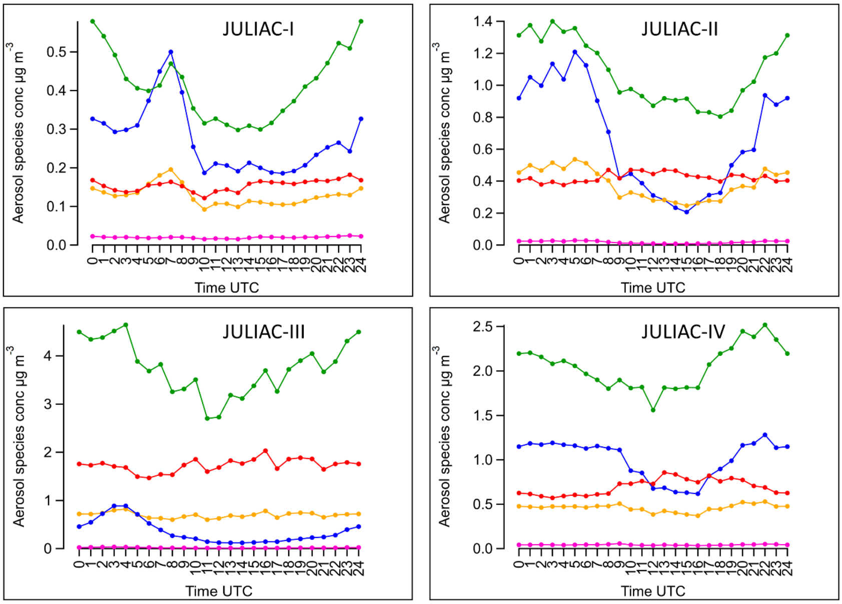

Figure 4-4: the averaged diurnal variation of aerosol organics (Org), nitrate (NO_3), ammonium (NH_4), chlorine (Chl), and sulfate (SO_4) bulk concentration for four intensive phases of the JULIAC campaign. Be aware that the Y-axis scale is different for four phases.

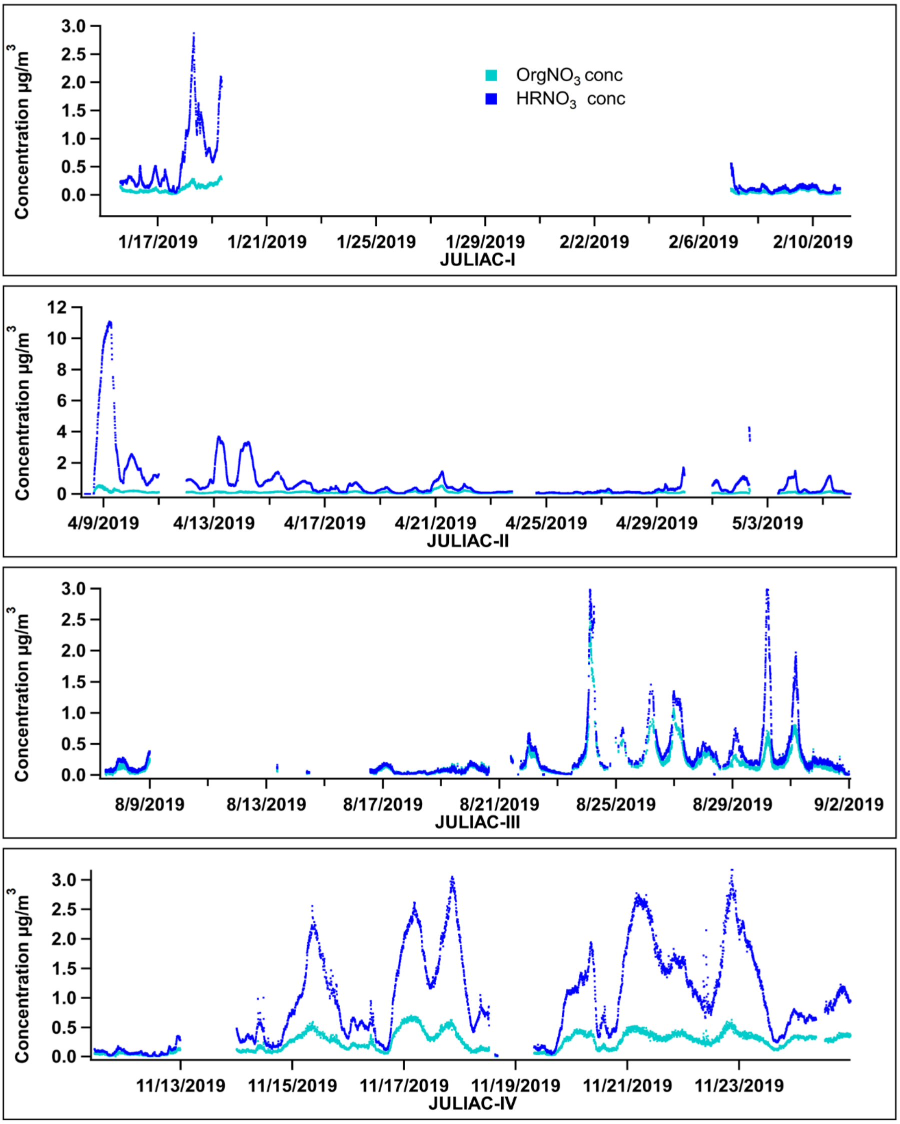

Figure 4-5: Seasonal comparison of time series for aerosol high-resolution bulk nitrate and organic nitrate mass concentration among four intensive phases of the JULIAC campaign.

As introduced in section 3.2.1, aerosol organic nitrate (ON) can have significant meaning in understanding the secondary aerosol formation and gas-particle phase dynamic partitioning, and also shows the apparent contribution to total organic aerosol (Pye et al., 2015, Xu et al., 2015b, Kiendler-Scharr et al., 2016, Lee et al., 2016, Ng et al., 2017). Therefore, the variations of aerosol organic nitrate for four intensive phases of the JULIAC campaign are calculated based on the approach introduced in section 3.2.1 and displayed in Figure 4-5. As shown in Figure 4-5, the most significant aerosol organic nitrate mass concentration is found during the JULIAC-III with the maximum concentration of 2.6 μg/m^3 reached at 2:30 (UTC). For the rest three JULIAC phases aerosol organic nitrate level is relatively low and below 0.7 μg/m^3. In addition, aerosol organic nitrate not only shows a significant high concentration but also shows a significant night-time enhancement during the JULIAC-III. That phenomenon may reveal potential dark oxidation of BVOCs and NO_3 radicals, which has been observed in previous field studies in different regions (Ng et al., 2008, Brown et al., 2009, Fry et al., 2009, Ayres et al., 2015, Chen et al., 2015, Fisher et al., 2016, Kiendler-Scharr et al., 2016). Although organic nitrate shows relatively low concentrations in the rest of three intensive phases compared to the JULIAC-III, the possible nighttime secondary organic aerosol (SOA) formation and seasonal dependent dark oxidation mechanism is focused discussed in section 4.4.

In conclusion, significant seasonal variations of both aerosol concentration and composition are found during the year-long JULIAC campaign. The average concentration of total aerosol in summer (7.68± 4.82 μg/m^3) is seven times higher than that in winter (1.05±0.98 μg/m^3), which implies the significant OA contribution from biogenic source (possibly SOA formation through photochemical path) in contrast to anthropogenic contribution in this site. For aerosol species, the mass fraction of aerosol nitrate shows the most obvious seasonal variation, which might be related to volatility-dependent evaporation and regional transport. The concentration of aerosol sulfate shows the biggest seasonal differences and peaked in summer with active local contribution (probably photochemical paths). Aerosol organics are the major aerosol species during the whole JULIAC campaign, and OA reach the maximal concentration in summer which is possibly related to fresh biogenic derived secondary organic compounds formation during summer.

4.2 Seasonal OA source apportionment overview

The significant contribution and various origination of organic aerosols have been introduced in section 1.1. Therefore, to increase the understanding of the complex sources of organic aerosol and the seasonal variation of these sources, source apportionment analysis using PMF/ME-2 (for details see section 3.1) for aerosol organics detected by HR-ToF-AMS has been conducted for four JULIAC intensive phases.

The final source factors resolved by seasonal PMF analysis and corresponding evaluation parameters for the JULIAC campaign are displayed in Table 4-2. The final optimal PMF solutions show Q/Qexp equal to 1.04, 1.03, 3.20, and 3.30 respectively for the JULIAC-I to IV, with corresponding unexplained variation (UEV) equal to 0.37, 0.31, 0.28, and 0.25. The UEV shown in Table 4-2 is comprised of unexplained noise and unexplained real signals, with the S/N threshold for the unexplained variation setting as 2.

The higher level of Q/Qexp of PMF results of the JULIAC-III and the JULIAC-IV compared to the JULIAC-I and the JULIAC-II is likely related to the stability and the sensitivity difference between the two different HR-ToF-AMS instruments used during the campaign. In other words, the same S/N threshold setting during PMF analysis but the different noise levels of AMS_1 and AMS_2 might cause that slight discrepancy of Q/Qexp values. Q/Qexp>>1 for the JULIAC-III and the JULIAC-IV indicate the possible underestimation of the errors of the AMS_2(Ulbrich et al., 2009), which also correspond to the pronounced lower unexplained noise ratio of AMS_2 data.

Overall, the Q/Qexp values (1.03 to 3.30) in this study compared to previous AMS studies (normally Q/Qexp ranges 1 to 5) (Canonaco et al., 2013, Zhang et al., 2015a) are small enough to illustrate the good quality of PMF resolving.

Table 4-2: The source factors and diagnostic parameters overview of final selected optimal PMF run for four JULIAC intensive phases. All source factors resolved in this study are displayed: Hydrocarbon-Like Organic Aerosol (HOA), Biomass Burning Organic Aerosol (BBOA), Less Oxidized Oxygenated Organic Aerosol (LO-OOA), More Oxidized Oxygenated Organic Aerosol (MO-OOA), Nocturnal Oxidation Oxygenated Organic Aerosol (NO-OOA), Methanesulfonic Acid-Containing Organic Aerosol (MSA-OA), Continental Regional Transport Organic Aerosol (Trans-OA).

JULIAC Phases	Q/Qexp	UEV (Unexplained noise+Unexplained real signals)	Resolved factors numbers	Resolved PMF factors
JULIAC-I	1.04	0.37 (0.29+0.08)	5	HOA, BBOA, Trans-OA, MO-OOA, NO-OOA
JULIAC-II	1.03	0.31 (0.22+0.09)	6	HOA, BBOA, Trans-OA, MSA-OA, LO-OOA, NO-OOA
JULIAC-III	3.20	0.28 (0.14+0.14)	4	HOA, MSA-OA, LO-OOA, NO-OOA
JULIAC-IV	3.30	0.25 (0.11+0.14)	5	HOA, BBOA, BBOA2, MO-OOA, NO-OOA

In terms of optimal PMF results, 7 types of source factors in total were resolved during the JULIAC campaign for all seasons. The detailed resolved factors for each JULIAC phase are in Table 4-2. These resolved PMF source factors could be divided into three main categories: Primary source (hydrocarbon-like OA (HOA), biomass burning OA (BBOA)), oxygenated organic aerosol source (less oxidized oxygenated OA (LO-OOA), more oxidized oxygenated OA (MO-OOA), and nocturnal oxidation oxygenated OA (NO-OOA)), and regional transport source (continental OA transport (Trans-OA) and marine OA transport (MSA-OA)). Regional OA transport resolved by PMF analysis in this study mainly refers to intensive aerosol transport events with obvious aerosol composition changes.

An example of PMF results overview including OA source factor profile, factor contribution overall variation, and diurnal variation of the JULIAC-II are displayed in Figure 4-6, and the overall PMF results for the rest phases are given in appendix A. 7. In addition, a detailed discussion of interpretability and implications of these factors will be given in the following sections 4.2.1, 4.2.2, and 4.2.3, respectively.

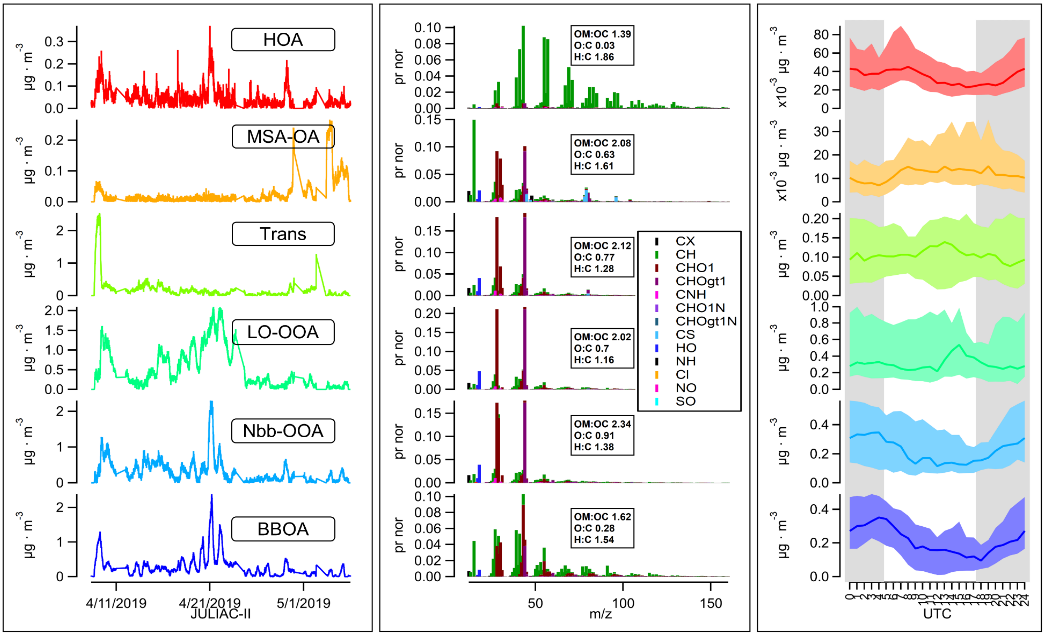

Figure 4-6: The organic aerosol source apportionment results overview resolved by PMF for the JULIAC-II. From left to right, the overview of OA contribution variations of source factors, high-resolution source factors spectra colored by ions family group, and corresponding source factor contribution diurnal pattern (median+IQR). For factor spectra overview, elemental ratio (OM:OC, O:C, H:C) of all OA factors are marked in the graph. The y-axis presents the ion signal intensity fraction while x-axis range is m/z (mass to charge) 12-160.

4.2.1 Primary sources

4.2.1.1 Hydrocarbon-like organic aerosol, HOA

As the HOA introduction in section 1.1, the spectrum of the HOA factor is dominated by C_nH_{2n+1} (m/z 29, 43, 57, 71) and C_nH_{2n-1} (m/z 41, 55, 69) ion groups, with the signal at $C_4H_9^+$ (m/z 57) being usually the major ion and can be considered as the tracer ion of HOA (Mohr et al., 2012). As shown in HOA factor spectrum in Figure 4-7, the CH family dominates the whole spectrum and shows a significant contribution of fragment $C_4H_9^+$ (m/z 57) which all match reported HOA features.

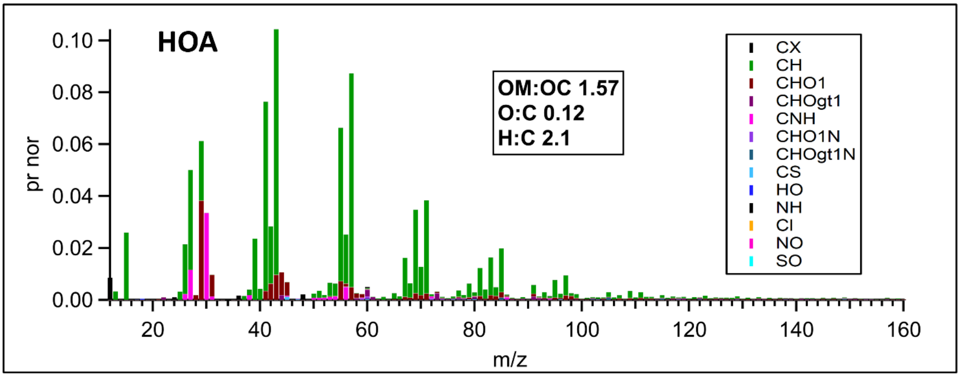

Figure 4-7: high-resolution HOA factor spectra colored by family groups for the JULIAC-I. Elemental ratio (OM:OC, O:C, H:C) of this OA factor has been displayed. The y-axis presents the ion signal intensity fraction while x-axis range is m/z (mass to charge) 12-160.

The corresponding O:C ratio (see elemental ratio introduction in section 3.2.3), ranging from 0.03 to 0.13, of all four HOA factors, is the lowest compared to all other factors derived for all JULIAC phases (as shown in Figure 4-6), and the H:C ratio (see section 3.2.3), ranging from 1.61 to 2.1 is the highest. That elemental ratios range of HOA factors determined in this study is also consistent with previous studies (DeCarlo et al., 2010, Mohr et al., 2012, Crippa et al., 2013b, Sun et al., 2016). In addition, several HOA spectra reported by previous studies (Mohr et al., 2012, Crippa et al., 2013b, Hayes et al., 2013) are utilized for spectrum comparison as shown in Table 4-3. The high correlation coefficient R^2 ranging from 0.72 to 0.99 and theta angle (Kostenidou et al., 2009) ranging from 12.80° to 33.08° further confirms the identification of the HOA factor in this study. The seasonal comparison of the HOA factor will be discussed in section 4.5.

Table 4-3: the cross-correlation analysis (R^2 and theta angle) of HOA spectrum among seasonal HOA resolved in four JULIAC phases and HOA factor reported in previous PMF studies (referred HOA factor data supported by high-resolution AMS spectral database, [High Resolution AMS Spectral Database (colorado.edu)](colorado.edu)). The background colors of coefficient cell are color scales following the value of R^2, and utilize red represent the highest value 1 and green as the lowest value 0.

R^2 / Theta	HOA_JULIAC-I	HOA_JULIAC-II	HOA_JULIAC-III	HOA_JULIAC-IV	Reference
U_DAURE_BCN_2009_HOA	0.81 / 23.71°	0.99 / 12.80°	0.98 / 12.80°	0.72 / 33.08°	(Mohr et al., 2012)
A_HR_031_HOA	0.82 / 23.93°	0.83 / 24.02°	0.82 / 24.02°	0.82 / 24.34°	(Crippa et al., 2013a)
HOA_JULIAC-I	1.00 / 0°	0.83 / 21.97°	0.85 / 21.97°	0.88 / 20.01°	JULIAC-I
HOA_JULIAC-II	0.83 / 21.97°	1.00 / 0°	0.99 / 0°	0.75 / 28.87°	JULIAC-II
HOA_JULIAC-III	0.85 / 21.97°	0.99 / 0°	1.00 / 0°	0.75 / 28.87°	JULIAC-III
HOA_JULIAC-IV	0.88 / 20.01°	0.75 / 28.87°	0.75 / 28.87°	1.00 / 0°	JULIAC-IV

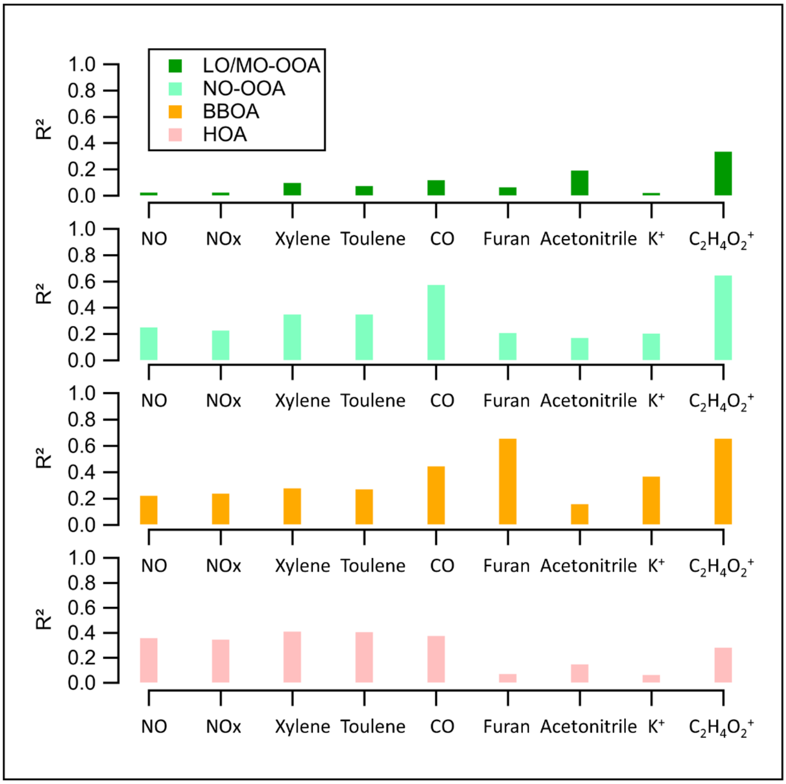

Figure 4-8: Cross-correlation R^2 overview of major source factors (LO/MO-OOA, NO-OOA, HOA, BBOA) in this study among car exhaust tracer gas (NO, NOx, Xylene, Toluene), biomass burning trace gas (CO, Furan, Acetonitrile) and biomass burning aerosol tracer fragments (K^+, $C_2H_4O_2^+$). OA regional transport factors are not involved due to their extremely low correlation with all primary emission tracers.

Concerning the diurnal characteristic of the HOA factor contribution, the pronounced peak at morning rush hour as shown in Figure 4-9 indicates that traffic exhaust is the main source contributor. The continuous decrease of HOA during noon may be caused by the reduction of traffic during daytime and the dilution effect of the expansion of the boundary layer, and a detailed discussion of the effect of atmospheric dynamics can be found in section 3.3.3. And that dilution effect might also vague the HOA enhancement during evening rush hour.

The concurrent measurement of traffic emission tracer gas, mainly NO, NOx, Toluene, Xylene, were also utilized to further analyze HOA factor determination. As shown in Figure 4-8, the averaged time-series correlation of HOA with NO, NOx, Toluene, and Xylene during the whole JULIAC campaign shows the maximal correlation coefficient compared to the rest factors with an averaged R^2 equal to 0.36, 0.35, 0.41, 0.40, respectively, which further supports that the HOA factor in this study mainly results from traffic emission. Moreover, the consistent diurnal behavior of typical traffic emission tracer gases and HOA contribution as shown in Figure 4-9 also supports the above HOA identification. Overall, the HOA factor resolved by PMF analysis during all JULIAC phases is demonstrated from both spectra features and diurnal behavior characteristics by referred factors and comprehensive tracer gases variation, and mainly represents the organic aerosol contribution from traffic sources in this study. The seasonal variation of HOA contribution during the whole JULIAC is displayed in Table 4-10.

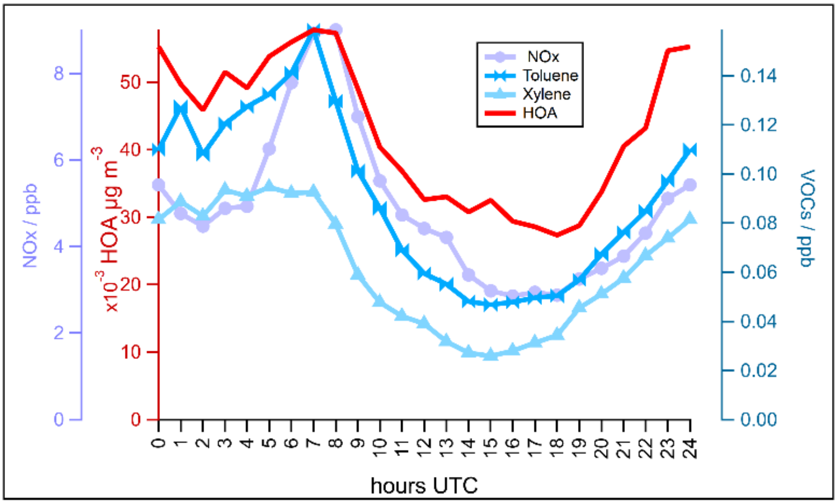

Figure 4-9: Diurnal variation comparison between the OA contribution of HOA factor, the concentration of NOx, toluene, and xylene during the JULIAC-II. Toluene and Xylene use the same y-axis named VOCs.

4.2.1.2 Biomass burning emission, BBOA

As the introduction in section 1.1, characteristic fragments $C_2H_4O_2^+$ (m/z 60) and $C_3H_5O_2^+$ (m/z 73) are commonly considered as the biomass burning tracer ions in the AMS mass spectrum (Simoneit et al., 1999, Alfarra et al., 2007). In this study, the significant signal of $C_2H_4O_2^+$ (m/z

60) and $C_3H_5O_2^+$ (m/z 73) could also be found in the BBOA factors spectrum as shown as an example for the JULIAC-I (see Figure 4-10). Complete factors spectrum overview of the JULIAC-I could be found in Appendix A. 7. These typical fragments are also one important marker for BBOA factor determination in this study. In addition, the time series of fragment $C_2H_4O_2^+$ (m/z 60) closely follow BBOA variation for all JULIAC phases and show the maximum value of averaged correlation coefficient R^2 equal to 0.85 compared to the other source factors as displayed in Figure 4-8, which also strongly support the determination of the BBOA factor.

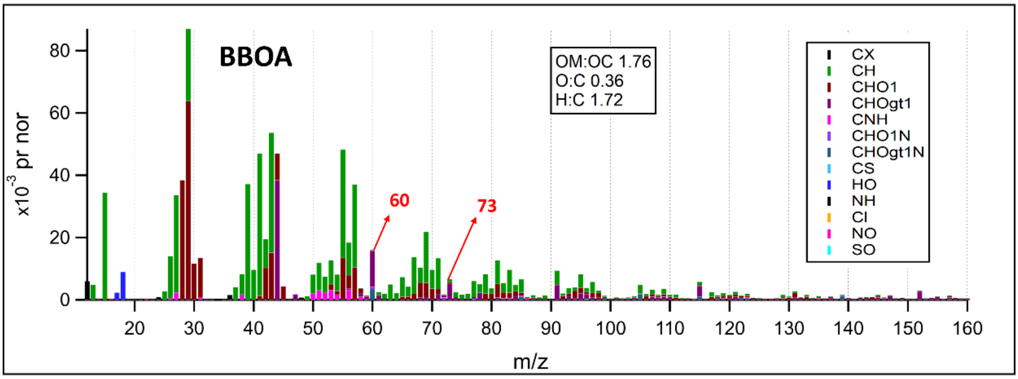

Figure 4-10: high-resolution BBOA factor spectra colored by family groups for JULIAC-I. Elemental ratio (OM:OC, O:C, H:C) of this OA factor has been displayed. The y-axis presents the ion signal intensity fraction while x-axis range is m/z (mass to charge) 12-160. The position of characteristics ion for BBOA factor, $C_2H_4O_2^+$ (m/z 60) and $C_3H_5O_2^+$ (m/z 73) are marked in the graph

In terms of overall features of factor spectrum, the O:C ratio of the BBOA factor spectrum, ranging from 0.28 to 0.36 during the JULIAC campaign, is lower than corresponding OOA factors and higher than HOA factors, which is comparable to the oxidation level of BBOA reported in previous studies (Aiken et al., 2009, DeCarlo et al., 2010, Mohr et al., 2012). Moreover, the high-resolution BBOA factor spectrum reported in previous PMF analysis of AMS data (Mohr et al., 2012, Hu et al., 2013) are used to compare with the BBOA factor spectrum determined during each JULIAC phase as shown in Table 4-4. In addition, the obvious seasonal difference of BBOA factors resolved during different JULIAC phases shown in Table 4-4 is discussed in section 4.5.3. Overall, BBOA resolved in our study is closer to referred BBOA factor reported by Hu et al with R^2 ranging from 0.76 to 0.94 and theta ranging from 14.23° to 27.92°. And the high similarity of BBOA spectrum with previously referred factor also confirm the determination of BBOA factor in this study.

Table 4-4: the cross-correlation analysis (R^2 and theta angle) of BBOA spectrum among seasonal BBOA resolved in four JULIAC phases and BBOA, CCOA factors reported in previous PMF studies (referred BBOA+CCOA factor data supported by high-resolution AMS spectral database, High Resolution AMS Spectral Database (colorado.edu)). The background colors of the coefficient cell are color scales following the value of R^2, and utilize red represents the highest value 1 and green as the lowest value 0

R^2 / Theta	BBOA _JULIAC-I	BBOA _JULIAC-II	BBOA _JULIAC-IV	BBOA2 _JULIAC-IV	Reference
U_DAURE_BCN_2009_BBOA	0.44 / 46.80°	0.79 / 34.73°	0.26 / 56.13°	0.59 / 40.61°	(Mohr et al., 2012)
A_HR_052_BBOA	0.84 / 22.74°	0.76 / 27.92°	0.82 / 24.58°	0.94 / 14.23°	(Hu et al., 2013)
A_HR_053_CCOA	0.64 / 34.92°	0.53 / 40.97°	0.92 / 16.23°	0.80 / 24.83°	(Hu et al., 2013)
BBOA_JULIAC-I	1.00 / 0°	0.58 / 38.87°	0.63 / 36.32°	0.76 / 28.17°	JULIAC-I
BBOA_JULIAC-II	0.58 / 38.87°	1.00 / 0°	0.49 / 43.83°	0.81 / 24.62°	JULIAC-II
BBOA_JULIAC-IV	0.63 / 36.32°	0.49 / 43.83°	1.00 / 0°	0.81 / 24.79°	JULIAC-IV
BBOA2_JULIAC-IV	0.76 / 28.17°	0.81 / 24.62°	0.81 / 24.79°	1.00 / 0°	JULIAC-IV

In addition to characteristic fragments $C_2H_4O_2^+$, more gas/particle-phase tracers of biomass burning, or combustion emissions are measured and utilized to further verify the BBOA factor determination. As shown in Figure 4-8, the averaged correlation coefficient during the whole JULIAC campaign between the overall variation of biomass burning tracers furan (Coggon et al., 2016, Akherati et al., 2020), acetonitrile (de Gouw et al., 2003, Wang et al., 2016), aerosol potassium (K^+) (Li et al., 2003, Zhang et al., 2013, Tao et al., 2014, Yu et al., 2018), combustion tracer CO and seasonal PMF source factors time series are displayed. BBOA factor shows a significantly higher R^2 value of all above tracers compared to the other primary source (HOA) and secondary source factors (LO-OOA and MO-OOA), which sustain the determination of BBOA. NO-OOA also shows good agreement with the above tracers and implies the possible biomass burning-related formation mechanism of NO-OOA. Detailed analysis of the NO-OOA factor will be discussed in section 4.4.

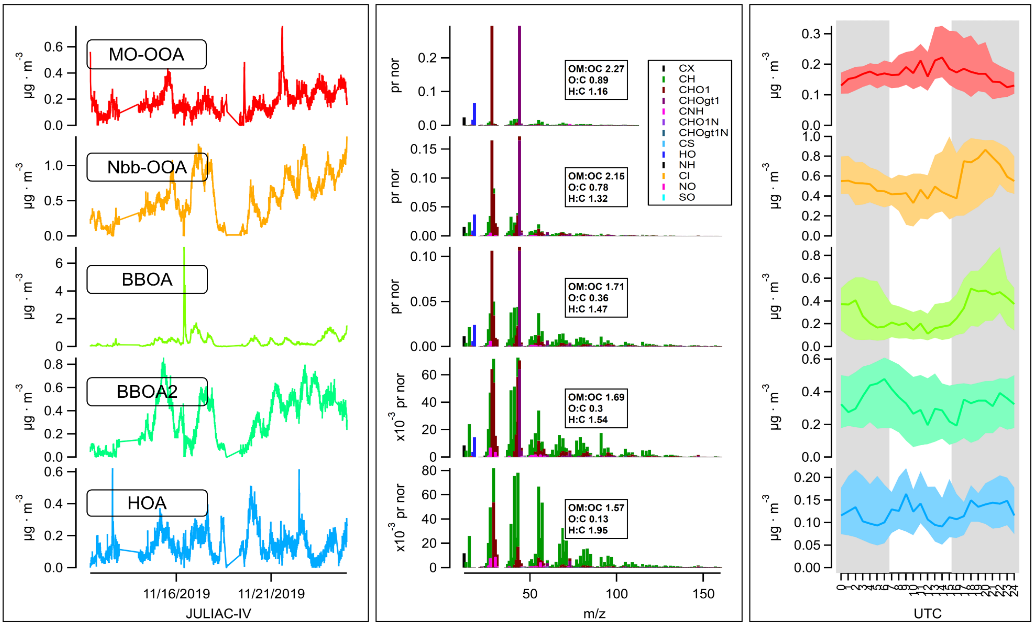

Figure 4-11: The organic aerosol source apportionment results overview resolved by PMF for the JULIAC-IV. From left to right, the overview of OA contribution variations of source factors, high-resolution source factors spectra colored by ions family group, and corresponding source factor contribution diurnal pattern (median+IQR). For factor spectra overview, elemental ratio (OM:OC, O:C, H:C) of all OA factors are marked in the graph. The y-axis presents the ion signal intensity fraction while x-axis range is m/z (mass to charge) 12-160.

In terms of possible BBOA regional transport, regional aerosol transport is discussed in section 4.2.3 based on OA source attribution combined with back trajectory analysis (introduced in section 3.3.1) and wind polar analysis (see section 3.3.2). Overall, possible biomass burning regional transport is founded during both the JULIAC-I and the JULIAC-IV, while the BBOA factor is dominated by local emission during the JULIAC-II. For example, the BBOA factor resolved at the JULIAC-I is proved to be dominated by regional transport based on the focused distribution of high BBOA contributions at bigger wind speed zoon in the polar graph as shown in Figure 4-15 and the distinct back trajectory for BBOA peak as shown in Figure A 9. The significant BBOA peak appeared at the JULIAC-I (18th Nov. 2019) following the sudden wind direction changing with around 200 degrees. That suggests a strong regional effect on that BBOA peak instead of the local emission.

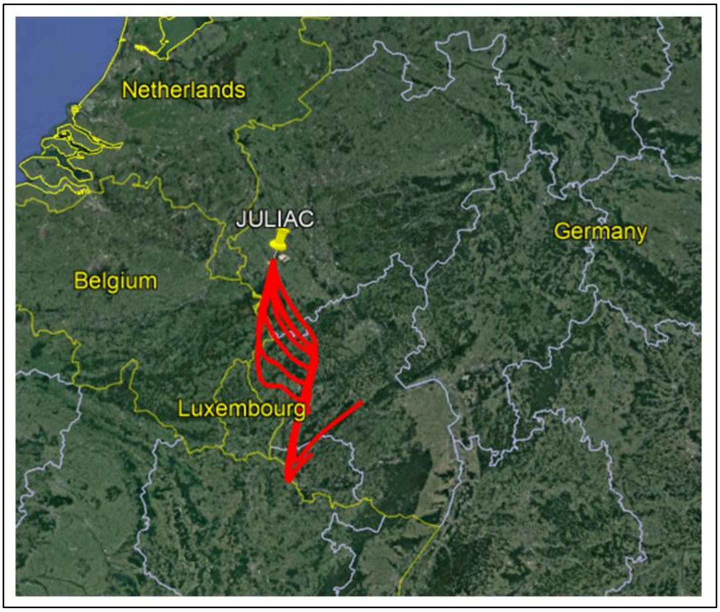

Figure 4-12: 2-hours resolution back trajectory lines of 24-hours back-trajectory simulated by HYSPLIT4 (Version 5.0.0) during 2:00-14:00 UTC of 16th Nov. 2019 of JULIAC-IV to investigate the potential plume transportation effect on sharp BBOA peak. JULIAC site position is marked by the yellow pin.

In addition, one typical intensive biomass burning emission and a controversial source resembling biomass burning are founded during the JULIAC-IV. Firstly, an intensive local biomass burning emission event could be observed during the JULIAC-IV at 7:00-13:00 UTC 16th Nov. 2019 as shown in the factor time series overview in Figure 4-11. Considering sharp peak of the BBOA factor variation, corresponding sudden changing of aerosol composition (as shown in Figure A 3), concurrent stable air parcel trajectory (as shown in Figure 4-12), and the relative steady meteorological condition (reflected by stable wind speed and wind velocity), that event is classified as an intensive local emission of biomass burning.

A polar graph colored by concurrent BBOA concentration during the JULIAC-IV is displayed in Figure 4-15. The centralized distribution of the high level of BBOA at the low wind speed region further highlights the significant local biomass burning contribution during the JULIAC-IV campaign.

Moreover, two BBOA factors have been resolved during the JULIAC-IV, but their factor spectrum shows a clear seasonal difference when compared with the BBOA spectrum determined at the rest seasons. As shown in Table 4-4, these spectra of two BBOA factors of the JULIAC-IV both show good agreement with reference coal combustion (CCOA) factor spectrum (R^2 0.80-0.92 and theta 16.23°-24.83°) as well as reference BBOA factors spectra (R^2 0.82-0.94 and theta 14.23°-24.58°), while the rest of the BBOA factor determined during the other JULIAC phases show less spectrum similarity with CCOA factor with R^2 0.53-0.64. The special BBOA spectrum during the JULIAC-IV high possibly related to the enhancement emission of coal combustion during the cold season, like Jülich sugar factory emission (compact working during November and December). Detailed seasonal differences of factors will be focused discussed in section 4.5.3.1.

As shown in Figure 4-11, although BBOA2 is classified as a biomass burning emission source, it contains less contribution of characteristic ions $C_2H_4O_2^+$ (0.12%) which might be caused by the aging process of biomass burning plume during regional transport (DeCarlo et al., 2010). The relative flat diurnal variation of BBOA2 compared to BBOA and polar graph distribution as shown in Figure 4-15 also imply BBOA2 could be affected by regional transport (Mohr et al., 2012). However, there are still other possibilities of BBOA2. However incomplete VOCs data during the JULIAC-IV at this semi-rural site limit the further precise investigation of BBOA2. Therefore, BBOA2 factor is considered as one primary OA emission source and is high possible contributed by biomass burning emission and affected by regional transport.

In conclusion, BBOA factors were widely resolved by PMF during the JULIAC-I, the JULIAC-II, and the JULIAC-IV, and are supported by correlations with biomass burning tracers, reference BBOA spectra, and meteorological analysis. The source properties and contribution of BBOA show the clear seasonal difference which might relate to seasonal varied biomass burning type, and that seasonal comparison is discussed in sections 4.5.2 and 4.5.3.

4.2.2 Secondary sources

As OOA factor introduction in section 1.1, less oxidized LO-OOA and more oxidized MO-OOA factors are mainly identified in this study by the typical OOA factor spectrum and diurnal pattern of factor contribution. The LO-OOA was resolved during the JULIAC-II and III while MO-OOA was resolved during the JULIAC-I and IV. As shown in Figure 4-13, LO-OOA and MO-OOA factor spectrum both exhibit the strongest contribution from fragments m/z 44 (signal at m/z 28 assumed equal to m/z 44(Aiken et al., 2008)) with dominant families CxHyO, CxHyOz (z>1). The oxidation degree of LO-OOA and MO-OOA are almost the biggest for all seasons with spectrum O:C ratio ranging from 0.7 to 1.0, which is comparable to previous studies (Hu et al., 2013, Xu et al., 2015b, Sun et al., 2016, Dai et al., 2019).

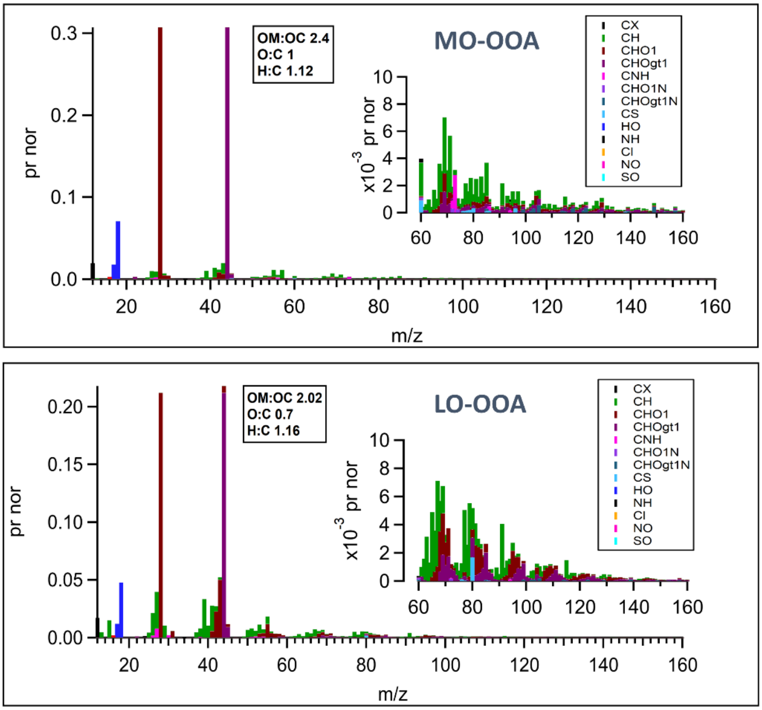

Figure 4-13: high-resolution MO-OOA factor spectrum for the JULIAC-I and LO-OOA factor spectrum for the JULIAC-II. Normalized ions attribution in factor profile are colored by corresponding ion family groups and elemental ratio (OM:OC, O:C, H:C) of OA factors has been displayed. Factor spectrum in the range of m/z 60-160 is displayed in the zoom-in window. The y-axis presents the ion signal intensity fraction while x-axis range is m/z (mass to charge) 12-160.

Plenty of high-resolution OOA factors spectra determined by previous source apportionment studies (Mohr et al., 2012, Crippa et al., 2013a, Hayes et al., 2013, Hu et al., 2013, Hu et al., 2015) are utilized to further support LO-OOA and MO-OOA determination in this study. As shown in Table 4-5, the overall spectra of LO-OOA and MO-OOA factors in this study are most close to the LV-OOA factor reported by (Hu et al., 2013) with R^2 ranging from 0.93 to 0.99 and theta angle (Kostenidou et al., 2009) ranging from 5.9° to 15.72°, and followed by LV-OOA (Hayes et al., 2013) and then SV-OOA (Hu et al., 2013) MO-OOA (Hu et al., 2015). That high correlation between LO-OOA and MO-OOA in this study with referred OOA factors further confirmed the OOA resolving and determination in this study.

Table 4-5: the cross-correlation analysis (R^2 and theta angle) of OOA spectrum among seasonal OOA resolved in four JULIAC phases and OOA factors reported in previous PMF studies (referred OOA factor data supported by high-resolution AMS spectral database, High Resolution AMS Spectral Database (colorado.edu)). The background colors of coefficient cell are color scales following the value of R^2, and utilize red represent the highest value 1 and green as the lowest value 0

R^2	MO-OOA _JULIAC-I	LO-OOA _JULIAC-II	LO-OOA _JULIAC-III	MO-OOA _JULIAC-IV	Reference
U_DAURE_BCN_2009_SVOOA	0.55 / 42.84°	0.64 / 37.43°	0.70 / 34.10°	0.57 / 42.11°	(Mohr et al., 2012)
A_HR_057_SV_OOA	0.88 / 20.62°	0.95 / 13.02°	0.97 / 9.43°	0.89 / 19.90°	(Hu et al., 2013)
A_HR_051_SVOOA_HR	0.63 / 37.46°	0.81 / 25.67°	0.85 / 23.89°	0.65 / 36.44°	(Hayes et al., 2013)
U_DAURE_BCN_2009_LVOOA	0.85 / 23.20°	0.92 / 17.59°	0.96 / 13.22°	0.85 / 22.99°	(Mohr et al., 2012)
A_HR_030_LV_OOA	0.82 / 26.12°	0.93 / 16.94°	0.97 / 12.49°	0.83 / 25.58°	(Crippa et al., 2013a)
A_HR_050_LVOOA_HR	0.90 / 18.42°	0.98 / 7.70°	0.98 / 10.74°	0.91 / 17.84°	(Hayes et al., 2013)
A_HR_058_LV_OOA	0.93 / 15.72°	0.98 / 8.80°	0.99 / 5.90°	0.93 / 15.24°	(Hu et al., 2013)
A_HR_029_MOA	0.30 / 55.34°	0.38 / 49.96°	0.50 / 42.98°	0.31 / 54.95°	(Crippa et al., 2013a)
A_HR_070_MO_OOA	0.85 / 22.93°	0.94 / 14.48°	0.97 / 10.03°	0.86 / 22.59°	(Hu et al., 2015)
A_HR_049_LOA_HR	0.59 / 39.76°	0.71 / 32.00°	0.74 / 30.65°	0.61 / 38.88°	(Hayes et al., 2013)
A_HR_071_LO_OOA	0.46 / 47.32°	0.63 / 36.66°	0.72 / 31.56°	0.47 / 46.57°	(Hu et al., 2015)
A_HR_072_LO_OOA	0.39 / 51.19°	0.58 / 39.88°	0.66 / 35.05°	0.40 / 50.35°	(Hu et al., 2015)
MO_OOA_JULIAC-I	1.00 / 0°	0.95 / 13.30°	0.91 / 17.82°	1.00 / 1.72°	JULIAC-I
LO_OOA_JULIAC-II	0.95 / 13.30°	1.00 / 0°	0.98 / 8.42°	0.95 / 12.53°	JULIAC-II
LO_OOA_JULIAC-III	0.91 / 17.82°	0.98 / 8.42°	1.00 / 0°	0.91 / 17.16°	JULIAC-III
MO_OOA_JULIAC-IV	1.00 / 1.72°	0.95 / 12.53°	0.91 / 17.16°	1.00 / 0°	JULIAC-IV

In terms of diurnal pattern, LO-OOA and MO-OOA are the only two source factors with pronounced noon peaks which are mainly related to secondary organic compounds formation from photochemistry. The diurnal variation of photolysis frequency of NO and O_3 concentration also shows good accordance with LO-OOA and MO-OOA diurnal behavior, and high overall time series correlations between O_3 and LO-OOA and MO-OOA are found during warm season the JULIAC-II and the JULIAC-III with R^2 equal to 0.56 and 0.71 respectively. Therefore, LO-OOA and MO-OOA factors determined during the JULIAC campaign could be considered as OA sources mainly contributed by the daytime oxidation process based on source spectrum properties and typical diurnal pattern. More seasonal comparison discussion, like the seasonal difference (such as oxidation degree) of LO-OOA and MO-OOA, will be given in section 4.5.3.

In general, LO-OOA and MO-OOA are representing the oxidized organic compounds usually formed by photochemistry processes, while the potential contributions from dark oxidation mechanisms, such as NO_3 radical derived dark chemistry, are not included. More and more previous aerosol apportionment studies found unresolved factors which seemed to represent some form of an OOA factor with an increase in or a maximum concentration reached during the night which potentially indicate significant nocturnal chemistry contribution (Saarikoski et al., 2012, Crippa et al., 2013b, Florou et al., 2017, Cheng et al., 2021). However, a specific PMF factor indicative and dominated by the night-time oxidation process, such as oxidation by NO_3 radicals, has not been clearly separated and identified yet. In this study nocturnal oxidation oxygenated organic aerosol factor, NO-OOA is defined as a new source factor for the first time to further complement the OOA source factors system. Detailed discussions and potential implications of the NO-OOA factor are given in section 4.4.

4.2.3Regional transport

As introduced before, two types of regional transport factors, one for marine plume transport called methanesulfonic acid-containing OA (MSA-OA) factor, the other for continental regional transport (Trans-OA) factor were resolved during the JULIAC campaign. The MSA-OA has been found in the previous coastal, oceanic environment study (Schmale et al., 2013) and also at rural (Schlag et al., 2016) and megacities researches (Crippa et al., 2014), which is considered to be the OA contribution from marine plume regional transport. Detailed investigation and implications of the MSA-OA factor are given in section 4.3. The trans-OA stands for the continental OA regional transport events resolved by PMF analysis but without a fixed transport origination.

The meteorological analysis is mainly utilized to support regional transport factor determination for both MSA-OA and trans-OA factors, such as the factor contribution dependent back trajectories analysis and polar analysis. For example, as shown in Figure 4-14, the time of the enhancement of trans-OA contribution during the JULIAC-II shows good accordance with the period of SW direction air parcel regional transport (represented by mean cluster 1 colored by blue). The dominant southwestern distribution of Trans-OA in polar coordinates as shown in Figure 4-15 further confirms that regional transport OA factor determination. Based on seasonal PMF results listed in Table 4-2, regional transport OA (MSA-OA+Trans-OA) has been resolved at the JULIAC-I, the JULIAC-II, and the JULIAC-III, accounting for 18.6%, 13.7%, and 8.6%

mass fraction of corresponding total aerosol organics. The strongest OA regional transport effect appears at the JULIAC-I, which is also supported by the concentrated OA distribution at high wind speed zone in the aerosol organic dependent polar graph of the JULIAC-I in Figure 4-3.

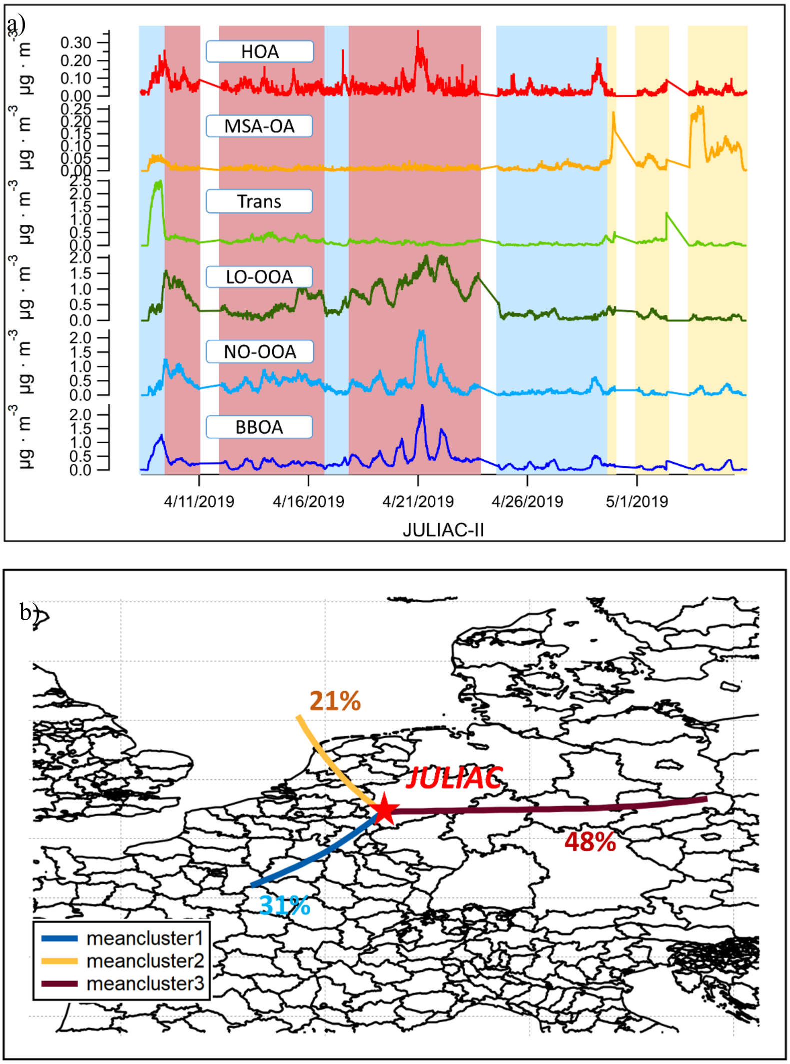

Figure 4-14: a) Concentration time series of PMF source factors of the JULIAC-II phase with the background color of trajectory clusters; b) Three trajectory clusters of the JULIAC-II 24-hours back-trajectory simulated by HYSPLIT4. Corresponding time coverage proportion of the averaged clusters are marked in the graph.

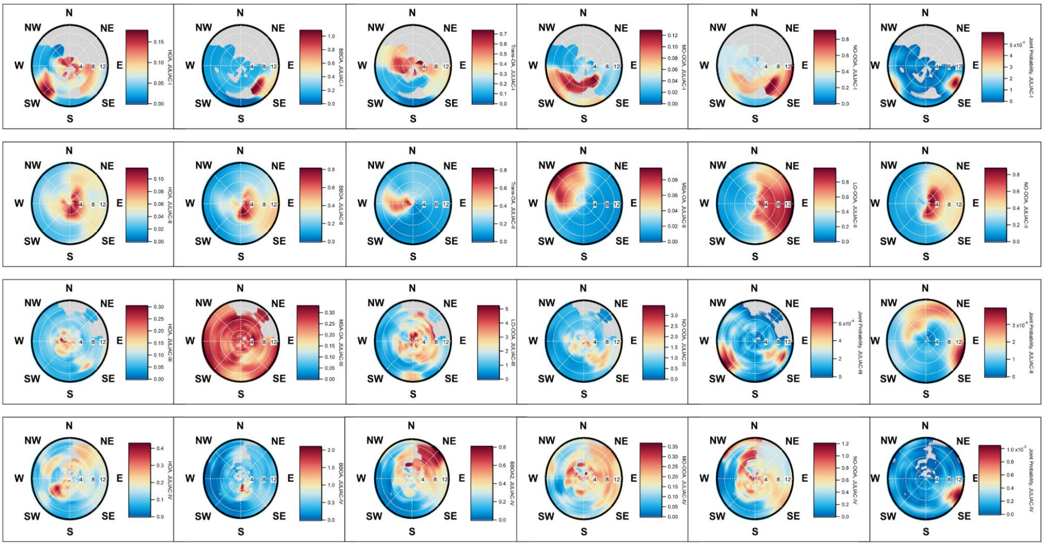

Figure 4-15: Source factors contribution dependent polar diagram and joint possibility for all JULIAC intensive phases based on non-parametric wind regressions. The polar graph is created based on the wind direction and wind speed measured in 50-m height. The OA contribution from all OA sources are utilized as color code in the polar graph to illustrate the potential regional source.

Although no distinct regional transport OA factor was resolved at the JULIAC-IV, OA distribution of the JULIAC-IV in the polar coordinates in Figure 4-3 compared to the JULIAC-I, the JULIAC-II and the JULIAC-III implies a possible OA regional transport. To investigate that contradiction between results of PMF and meteorological analysis, the organic aerosol concentration-dependent wind rose graph for all JULIAC phases and OA area contribution graph for the JULIAC-IV are shown in Figure 4-16 and Figure 4-17 to further illustrate the meteorological condition and potential OA regional transport during the JULIAC-IV.

Compared to the other three phases, the JULIAC-IV shows the most compact wind direction distribution, with SE direction frequency over 50% as shown in Figure 4-16 and corresponding high wind speed (>10km/h) as shown in Figure 4-3. Therefore, one could conclude that the sampling site is affected by SE direction wind during most of the time of the JULIAC-IV. Moreover, the OA area contribution of the JULIAC-IV estimated by concentration field (CF) statistics analysis (introduced in section 3.3.1) based on 24-hours back trajectory lines shows that the SE direction trajectory area corresponds to the relatively high OA concentration during the JULIAC-IV.

Overall, the sampling site is dominated by the southeastern wind, and OA is possibly continuously affected by SE direction regional plume regional transport during most of the time of the JULIAC-IV. OA regional transport contribution is difficult to be resolved unambiguously by PMF analysis to be a distinct source factor during the JULIAC-IV. One reason might be related to the similarity of OA properties between SE inland transported plumes and local atmosphere, and no characteristic peak of the variation of regional transport OA under continuous directional plume transport. This limitation of PMF analysis should be noticed in further OA regional transport studies.

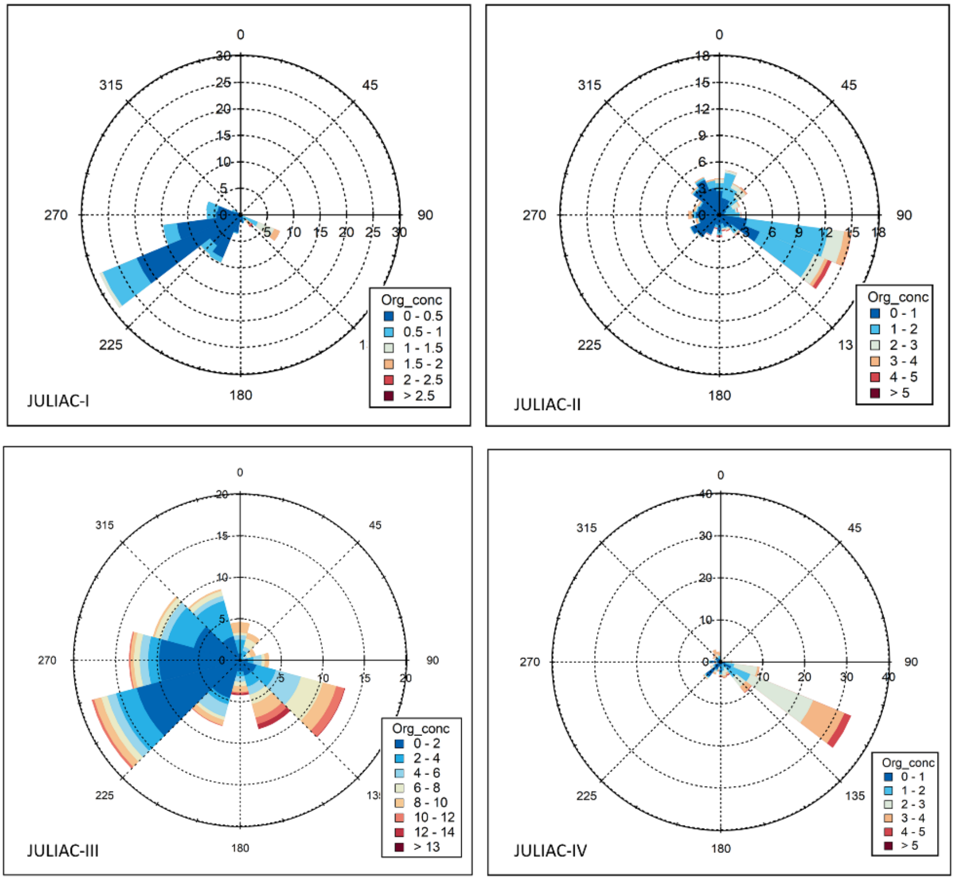

Figure 4-16: Wind rose graph colored by corresponding organic aerosol concentration for four intensive phases of the JULIAC campaign. The polar graph is created based on the wind direction and wind speed measured in 50-m height.

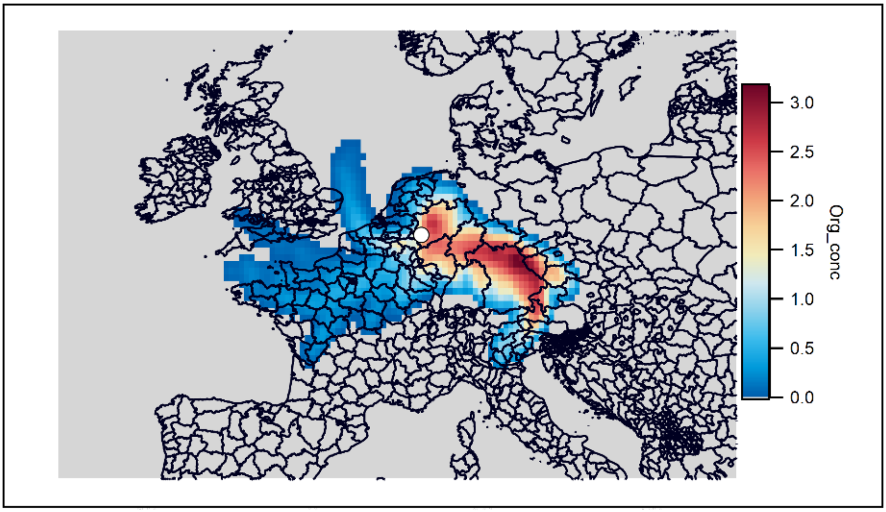

Figure 4-17: Potential area contribution of aerosol organics during the JULIAC-IV processed by concentration field (CF) statistics in ZeFir. Trajectory data used for CF analysis are 2-hours resolution back trajectory lines of 24-hours back-trajectory simulated by HYSPLIT4 (Version 5.0.0).

In conclusion, OA regional transport resolved by PMF analysis combining trajectory and meteorological analysis in this study shows clear marine source OA regional transport during the JULIAC-II and JULIAC-III mainly from the North Sea and the Celtic Sea direction respectively. In addition to the marine source, regional transport event from the western and southwestern direction has been discovered during the JULIAC-I and JULIAC-III. In total, regional transport OA contributes 8.6% to 18.6% of total OA mass. That implies the importance of regional transport on OA source and properties understanding especially in cold weather in this study. The OA regional transport during the JULIAC-IV is illustrated by trajectory and meteorological analysis but not parsed as a distinct regional transport OA factor by PMF analysis. In conclusion, PMF could effectively resolve the OA contribution of regional transport with characteristic plume components but show limitations in resolving continuous and directional plume transport with analogous species.

4.3 Marine source factor: Methanesulfonic acid-containing organic aerosol/MSA-OA factor

This study determined the MSA-OA factor (introduction see section 1.1) based on PMF methods in the JULIAC-II and the JULIAC-III. Good agreement is found between the MSA-OA factor's concentration/fraction and marine plume trajectory simulated by NOAA HYSPLIT (Hybrid Single-Particle Lagrangian Integrated Trajectory (Cohen et al., 2015)). Meanwhile, MSA concentration is estimated by two characteristic ions methods as a comparison to further investigate the reliability of the time series of the MSA-OA factor. Detailed discussions are given below.

In Figure 4-18, the MSA-OA factor profile detected from the JULIAC-II is shown and compared with the factor profile from a previous study (Schlag et al., 2017). The y-axis represents the factor profile normalized to 1, and the x-axis is the mass-to-charge ratio (m/z) in unit mass resolution. The profile's elemental composition of the MSA-OA factor in this study (O:C=0.63 and H:C=1.61) are similar to those reported in the study by (Schlag et al., 2017) (O/C=0.55 and H/C=1.70). The two MSA-OA factors mentioned above both contain typical MSA-OA marker fragments: CHS^+ (m/z 44.98), $CH_2SO_2^+$ (m/z 77.98), $CH_3SO_2^+$ (m/z 78.99), and $CH_4SO_3^+$ (m/z 95.99). $CH_3SO_2^+$ is regarded as a characteristic fragment for MSA containing ambient aerosols (Zorn et al., 2008, Huang et al., 2017) and is the most abundant ion of the CS family in the MSA-OA factor profile. The high consistency of marker fragments of two MSA-OA factors supports that the resolved MSA-OA factor during the JULIAC campaign is indeed strongly influenced by DMS oxidation products.

Except above four fragment ions, the MSA-OA profile of this study also contains one more ion belonging to the CS family, CH_3S^+ (m/z 47.00). Although CH_3S^+ is not in this reference factor, it has been included in the MSA-OA factor in a previous study (Schmale et al., 2013). The low-intensity level of CH_3S^+ (m/z 47.00) may one possible reason to explain why it's not a stable maker ion in MSA-OA profiles.

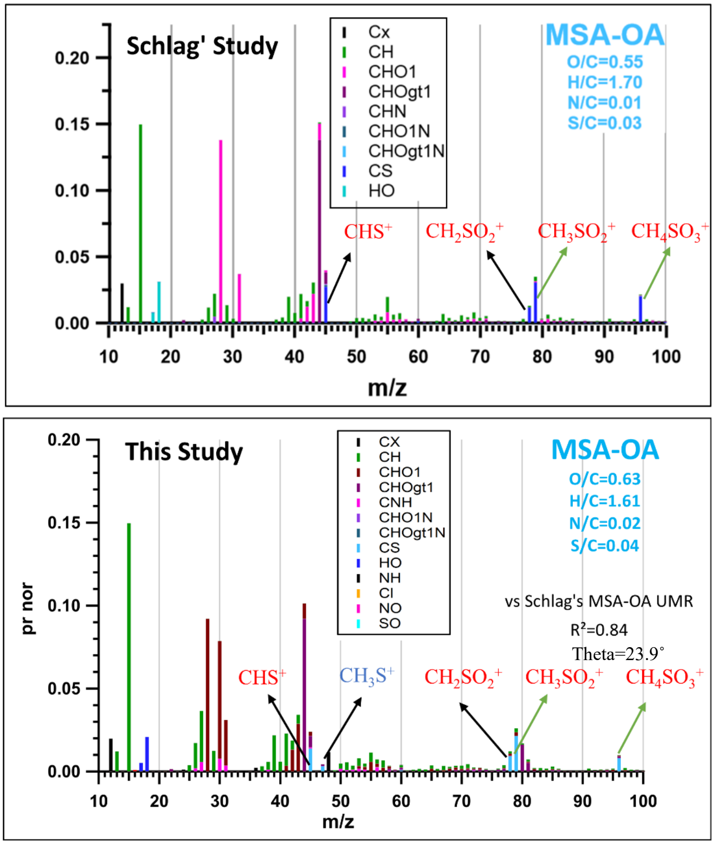

Figure 4-18: MSA-OA factor profile comparison between the study by Schlag et al., 2017 (upper), and this study the JULIAC-II (bottom). Typical MSA marker fragments: CHS^+ (m/z 44.98), CH_3S^+ (m/z 47.00), $CH_2SO_2^+$ (m/z 77.98), $CH_3SO_2^+$ (m/z 78.99), and $CH_4SO_3^+$ (m/z 95.99) are highlighted in factor profile. Normalized ions attribution in factor profile are colored by corresponding ion family groups, and elemental ratios (O/C. H/C. N/C, S/C) of MSA-OA factor are also marked in the graph. The y-axis presents the ion signal intensity fraction while the x-axis range is m/z (mass to charge) 10-100.

The overall MSA-OA spectrum comparison is also made among this study and previous studies (see Table A 3). The highest spectra similarity of MSA-OA is found between this study and study by Schlag et al., 2017 with R^2=0.70-0.84 and theta=23.9˚-30.0˚. However, the overall poor spectrum similarity of MSA-OA among previous studies implies that the MSA-OA factor, as a regional transport factor, could be identified by characteristic MSA ions but show variable overall factor spectrum might be related to the distance of plume transport. That variable overall MSA-OA spectrum is discussed in seasonal comparison of MSA-OA spectrum in section 4.5.3.

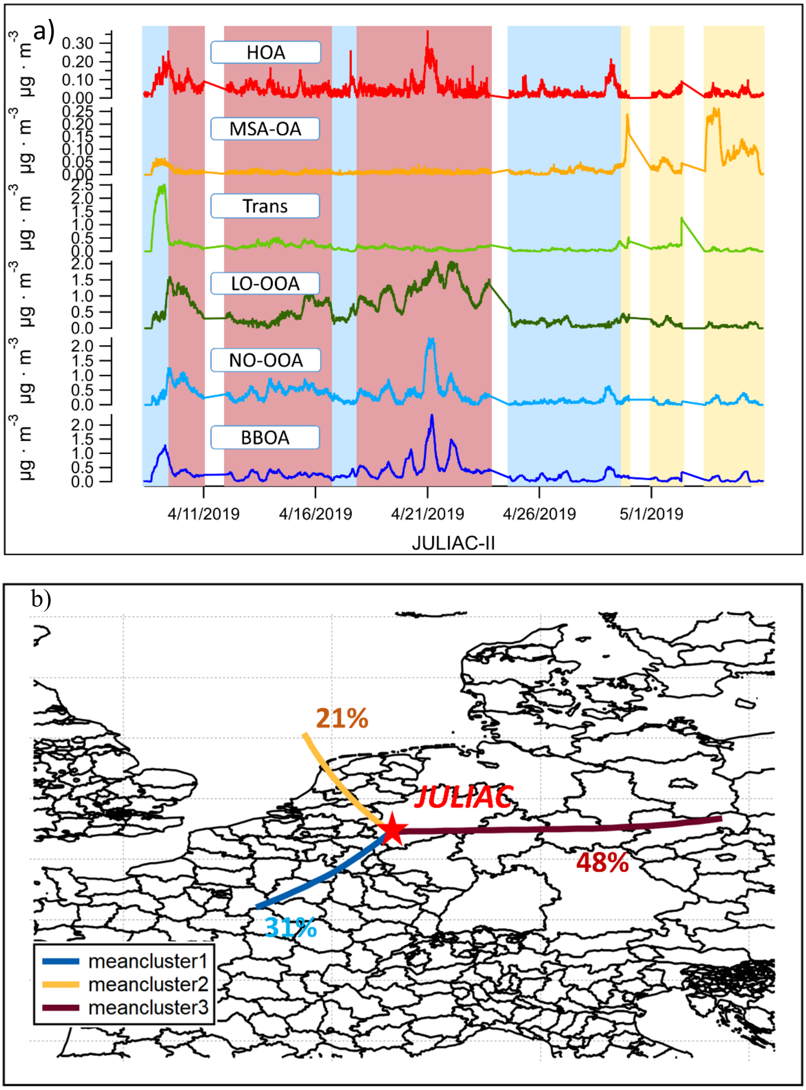

Figure 4-19: a) Concentration time series of PMF source factors of the JULIAC-II phase with the background color of trajectory clusters; b) Three trajectory clusters of the JULIAC-II 24-hours back-trajectory simulated by HYSPLIT4.

To further validate the MSA-OA factor in this study, polar graph and back-trajectory analyses are combined to investigate the marine regional transport characterization of the MSA-OA factor. In Figure 4-19 a), all PMF source factors' time series during the JULIAC-II are displayed and the background color corresponds to the color of the clusters of the 24-hours back-trajectory shown in Figure 4-19 b). The cluster 1 (cover 31% of total time) colored by blue and cluster 3 (account for 48% of period) colored by red represent the averaged plume trajectory transported from the southwestern and eastern continents, respectively. The trajectory line of mean cluster 2 (yellow line, time ratio of 21%) in Figure 4-19 b) is dominated by marine air parcel regional transport towards the measurement site. During the corresponding marine plume period, the concentration of factor MSA-OA shows a significant increase while other factors' concentration time series are comparably low in concentration and do not show any large variations. The correlation between the MSA-OA and the back-trajectory originating from the marine area implies that the MSA-OA factor is significantly dominated by the marine plume and could be considered as a marine transport indicator.

In addition, the polar diagram in Figure 4-20 shows that almost all high MSA-OA concentrations (>0.1 $\mu g/m^3$) are distributed in a high-wind-speed radius (>10 km/h) of NW direction, which supports the interpretation of the strong influence of northwestern direction marine transport which accompanies the occurrence of the MSA-OA factor at the measurement site. The MSA-OA factor mass concentrations trends, marine trajectory analysis, and wind pattern confirm that the MSA-OA factor separated by PMF is correctly attributed and could be considered as a tracer of marine transport. In this study, the MSA-OA factor is mainly transported from the northwestern direction where the North Sea is located.

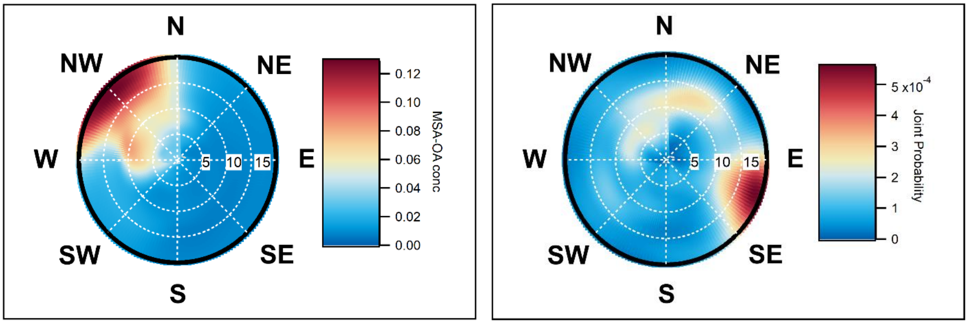

Figure 4-20: Polar diagram of MSA-OA concentration (left) and joint possibility (right) during the JULIAC-II phase based on non-parametric wind regressions. The polar graph is created based on the wind direction and wind speed measured in 50-m height. OA contribution of MSA-OA factor is utilized as color code in the polar graph to illustrate the potential regional source and the joint graph shows the wind frequency.

In the above discussion, the MSA-OA factor has been verified by comparison and correlation of previously determined factor profiles and marine transport events. To further examine and validate the reliability of the MSA-OA factor, the mass concentration of aerosol MSA calculated by two characteristic ion methodologies (introduced in section 3.2.2) were utilized as comparison. As shown in Figure 4-21, the time series correlation between the MSA-OA factor (x-axis) and two aerosol MSA concentration (calculated by the Ge method (red) and HKUST method (blue) are displayed. The difference of the MSA and MSA-OA concentration need to be emphasized here: MSA concentration consist of organic fragments (such as $CH_3SO_2^+$) and inorganic fragments (such as SO_2^+). However, MSA-OA factor represent aerosol organics contribution from marine regional transport, which concentration only contain organic part of aerosol MSA and some other organics fragments (e.g. CH_2O^+, CO_2^+) attributed to marine source. Therefore, it's reasonable to see the concentration level of the MSA-OA factor is different with pure aerosol MSA concentration. The high correlation coefficient, R^2 0.95 for MSA-OA vs MSA (Ge method) and 0.94 for MSA-OA vs MSA (HKUST method) respectively, strongly support the resolving of MSA-OA factor. Overall, this comparison further promotes the accuracy of the MSA-OA factor derived by the PMF analysis.

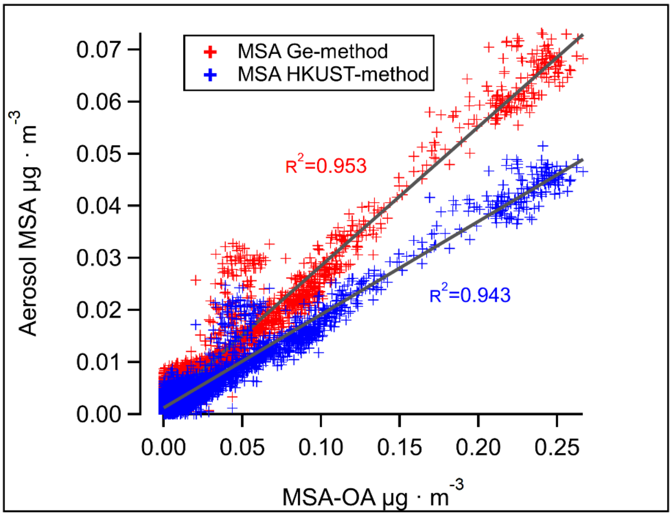

Figure 4-21: Time series correlation among the concentration of aerosol MSA calculated by Ge, HKUST methods, and the OA contribution of MSA-OA source factor during the JULIAC-II campaign. Correlation coefficients R^2 are marked in the graph.

An MSA-OA factor is identified for the JULIAC-III intensive phase by unconstrained PMF analysis as well, and its spectrum (as shown in Figure A 4) contains the same MSA-OA characteristic ions as the JULIAC-II and show correlation R^2=0.6 with the MSA-OA spectrum of the JULIAC-II. It also shows the same marine transport properties as in the JULIAC-II. In Figure 4-22 a) the time series of mass fraction of MSA-OA factor (calculated by OA contribution of MSA-OA factor divided by the total OA mass concentration) and the aerosol MSA mass fraction for both Ge and HKUST methods (calculated by each aerosol MSA mass concentration divided by the total aerosol mass concentration) are given and background colored by 72h back-trajectory clusters (back longer than JULIAC-II 24h for clear marine origination). The mass fraction time series of MSA-OA and aerosol MSA show a high correlation, with coefficient R^2 0.76 and 0.72 for the Ge method and HKUST method, respectively. And almost all peaks of MSA-OA and aerosol MSA mass fraction appeared at the marine plume transport period. The above analysis not only confirms the determination of the MSA-OA factor by PMF analysis but also illustrates that MSA-OA could be regarded as a marine transport indicator.

However, during the JULIAC-III the correlation with marine transport is not apparent from the mass concentration time series of MSA and MSA-OA factor alone. In contrast, the time series of the mass fraction of MSA normalized to total aerosol and MSA-OA normalized to total organic show an obvious increase during the marine regional transport period. In comparison, the mass concentration time series of MSA-OA and aerosol MSA are also given in Figure 4-22 b), and at dark-red background regime (corresponding to slow plume movement, or relative steady conditions of local atmosphere) aerosol MSA mass concentration reaches the maximum for both Ge and HKUST methods, while MSA-OA factor also shows relatively high concentration here. In addition, the mass concentration time-series correlation between MSA-OA with aerosol MSA during the JULIAC-III are also poor, with correlation coefficient R^2 0.20 and 0.23 for Ge and HKUST methods respectively. One possibility is there might exist other unknown terrestrial sources for aerosol MSA formation which has been suggested by previous studies (Ge et al., 2012, Young et al., 2016, Zhou et al., 2017) but the possible mechanism still needs further investigation. Overall, the OA contribution mass fraction of MSA-OA factor or aerosol MSA mass fraction still clearly indicate marine transport.

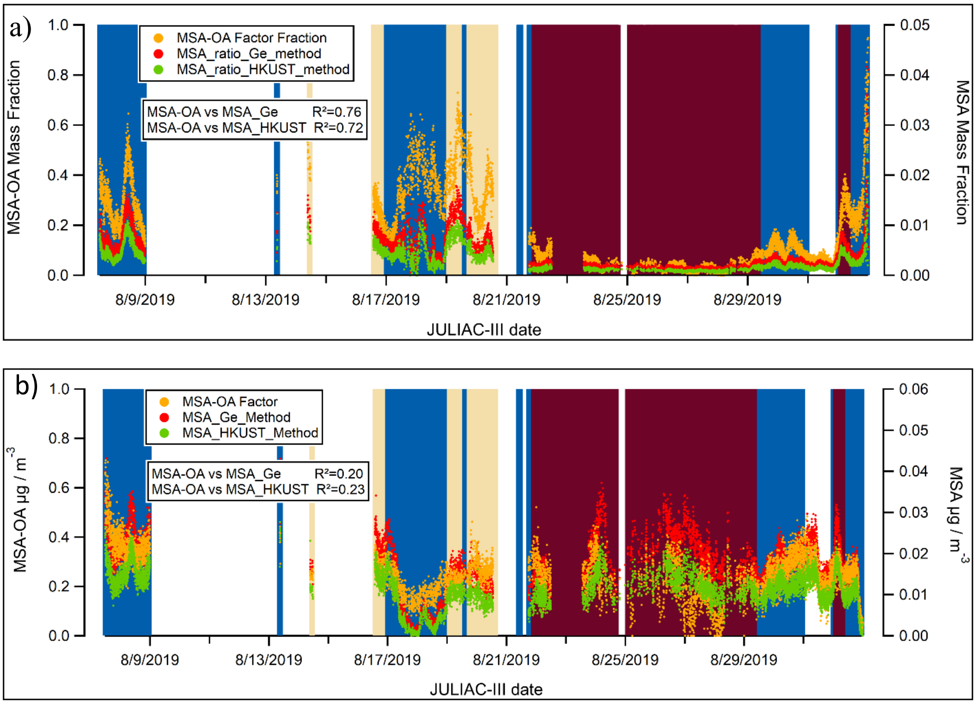

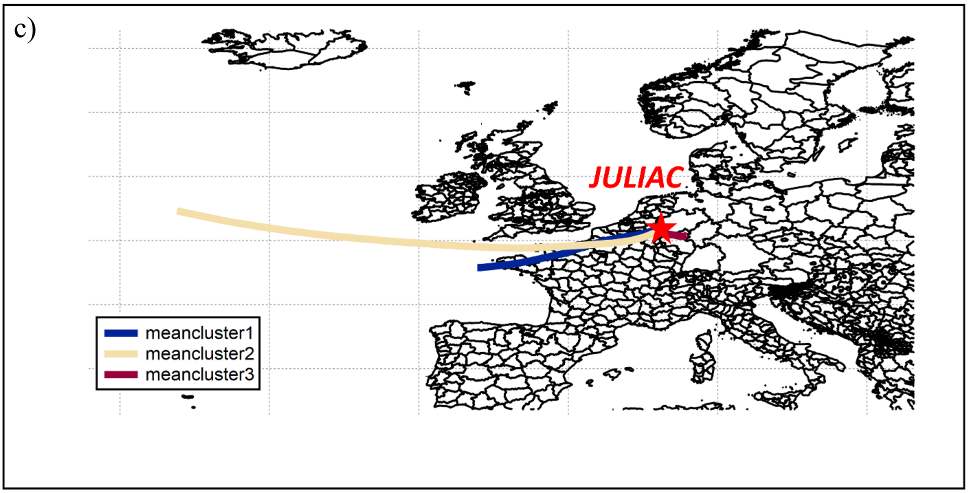

Figure 4-22: a) OA contribution mass fraction of MSA-OA factor (normalized to the mass of aerosol organics) and aerosol MSA mass fraction (normalized to the mass of total aerosol) calculated by Ge and HKUST methods during the JULIAC-III phase with the background color of back-trajectory clusters; b) Mass concentration time series of MSA-OA factor and aerosol MSA calculated by Ge and HKUST methods during the JULIAC-III phase with the background color of back-trajectory clusters; c) Three mean trajectory clusters of the JULIAC-III 72-hours back-trajectory simulated by HYSPLIT4.

In summary, this study verified the MSA-OA factor determined by PMF analysis in terms of the factor's profile and time series. Additionally, the MSA-OA factor and corresponding OA contribution mass fraction (especially for summer) are demonstrated to be the indicator of marine transport according to meteorological and back-trajectory analysis. That unsolved high local aerosol MSA concentration still deserves further investigation to interpret whether it's an overestimation caused by methodologies or unknown local aerosol MSA formation. MSA-OA factor found at the JULIAC-II and the JULIAC-III contain the same characteristic fragments but show a slight difference in ions contribution of factor profile (detailed MSA-OA factor profile of the JULIAC-III could be found in Figure A 4) and all seasonality of OA source factors are discussed in detail in section 4.5.

4.4 Nocturnal oxidation oxygenated organic aerosol/NO-OOA factor

In this study, the nocturnal oxidation oxygenated organic aerosol factor, denoted from here as NO-OOA factor, is resolved by PMF analysis for the first time and introduced as a distinct nocturnal OOA factor mainly derived by NO_3-initiated oxidation for all seasons. In this study, an independent NO-OOA factor illustrates the contribution variation and proportion of nocturnal OA in parallel with OA daytime contribution mainly from photo-oxidation reactions (represented by LO-OOA and MO-OOA in this study). In addition, the seasonal comparison of NO-OOA properties and mass contribution also reveals mechanism changes and the significance of nocturnal chemistry.

$$\boldsymbol{NB-OOA}\text{: } \mathit{Biogenic\ VOCs} + NO_3\cdot \xrightarrow{\mathit{Gas-phase\ reaction}} \xrightarrow{\mathit{Phases\ partitioning}} \mathit{Night\ oxidation\ OOA} \qquad \text{Eq. 23}$$

$$\boldsymbol{Nbb-OOA}\text{: } \mathit{Biomass\ burning\ VOCs} + NO_3\cdot \xrightarrow{\mathit{Gas-phase\ reaction}} \xrightarrow{\mathit{Phases\ partitioning}} \mathit{Night\ oxidation\ OOA} \qquad \text{Eq. 24}$$

As shown in Eq. 23 and Eq. 24, NO-OOA further split into two sub-OOA factors based on seasonal major precursors, biogenic VOCs (BVOCs) dominated nocturnal oxidation OOA (NB-OOA), and biomass burning VOCs (bbVOCs) dominated nocturnal oxidation OOA (Nbb-OOA). The Nbb-OOA factor was resolved in the JULIAC-I, II, IV accompanied by significant biomass burning emission (conclude from the concentration CO and VOCs such as acetonitrile and furan, see Figure A 10, and BBOA contribution) and obvious contribution of biomass burning tracer ions $C_2H_4O_2^+$ (m/z 60) in factor profile. In contrast, NB-OOA is only observed at the JULIAC-III (summertime) in this study when BVOCs (such as isoprene, monoterpene, see Figure A 10) emission was strong, and a significant contribution of m/z 91 is observed (commonly founded in biogenic emission dominate OOA (Budisulistiorini et al., 2015, Chen et al., 2015)) in factor spectrum. A more detailed discussion is given below to investigate the feasibility and implications of the NO-OOA (Nbb-OOA and NB-OOA) factor.

4.4.1 Nocturnal aerosol oxidation

As shown in Figure 4-23, aerosol oxidation degree represented by the aerosol O:C elemental ratio and $fCO_2^+/fC_2H_3O^+$ fragment ratio of organic aerosol for all seasons have been displayed. In Figure

4-23, day and night time are distinguished by the seasonally averaged value of photolysis frequency of NO_2 (jNO_2) measured by a spectroradiometer (Bohn et al., 2005b, Bohn and Zilken 2005a) during the JULIAC campaign. More specifically, periods with jNO_2 equal to zero represents nigh-time and are marked by grey background, on the contrary daytime are marked by the white background. An obvious OA oxidation degree increasing during daytime (between 11:00-17:00 UTC) is observed during the whole JULIAC campaign and is mainly derived by photooxidation. In addition, night enhancement of OA oxidation degree is also observed during 0:00 to 2:00 UTC, which implies noticeable aerosol nocturnal oxidation throughout the year. In addition, that significant OA oxidation degree enhancement during nighttime at all seasons has already been reported in previous ambient aerosol research (Li et al., 2015). That illustrates seasonal apparent nocturnal oxidation is not just a unique phenomenon during the JULIAC campaign.

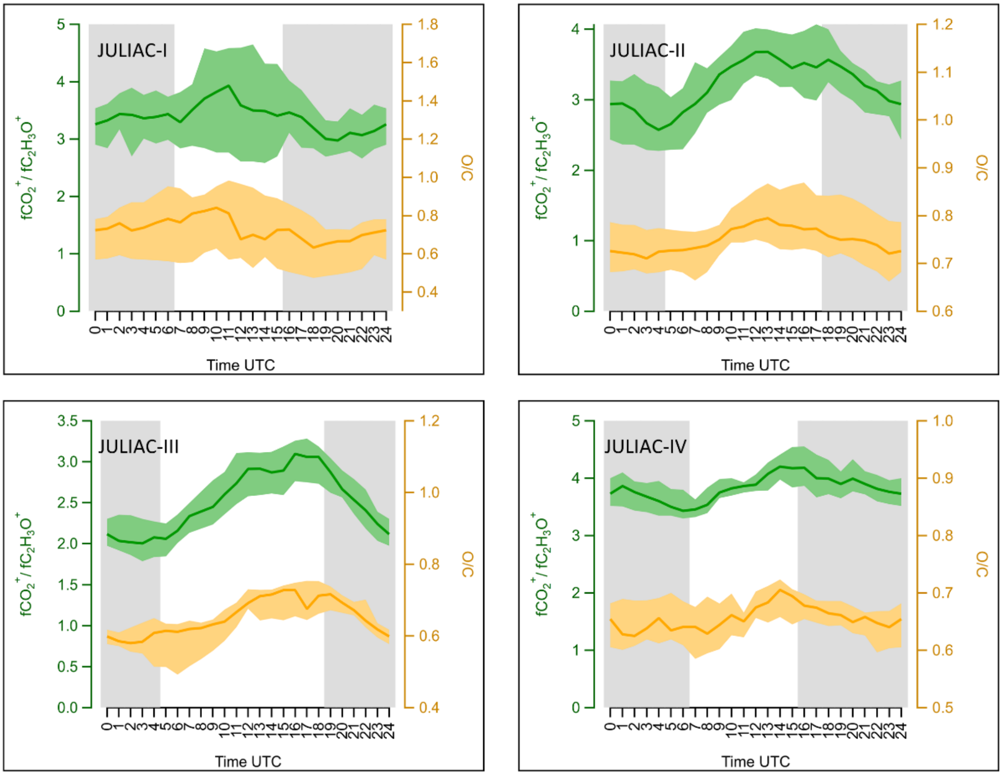

Figure 4-23: diurnal variation of the median and interquartile range (IQR) of organic aerosol O:C elemental ratio and $fCO_2^+/fC_2H_3O^+$ fragment ratio for all four seasons of the JULIAC campaign. Solid lines correspond to median variation and color regions represent the IQR. Grey background indicates nigh-time and white background marks day-time calculated by corresponding photolysis frequency data measured during the JULIAC campaign. Note that the scale of the Y-axis is inconsistent among four JULIAC phases.

Therefore, the nocturnal oxidation oxygenated organic aerosol factor (NO-OOA) resolved by PMF should represents the OA contribution from that apparent OA nocturnal oxidation confirmed above. NO-OOA factors spectra for all the JULIAC phases are displayed in Figure 4-24 a) and are colored by corresponding ion family groups. A high contribution of the signal at m/z 44 (normalized intensity fraction 0.08-0.18) implies NO-OOA as an oxygenated OA in comparison with that of SV-OOA (0.05) and LV-OOA (0.16) reported by study by (NG 2011). The CHOx dominant ions pattern (mainly CO^+ (m/z 28), CHO^+ (m/z 29), $C_2H_3O^+$ (m/z 43) and CO_2^+ (m/z 44)) and the oxidation degree (O:C 0.39 for NB-OOA and 0.76-0.91 for Nbb-OOA) of the factor spectra further support that the NO-OOA factor represent secondary organic compounds contribution instead of

OA primary emission. The diurnal variation of the averaged concentration of NO-OOA factors for all the JULIAC intensive phases are shown in Figure 4-24 b). The apparent peak of the NO-OOA contribution appearing at night during all the JULIAC intensive phases strongly indicates NO-OOA as a potential night OOA source.

In terms of factor spectrum characteristics of Nbb-OOA and NB-OOA, Nbb-OOA factors spectra (for the JULIAC-I, II, and IV) consist of the same major ions and similar contributions of tracer ions $C_2H_4O_2^+$ (m/z 60) of biomass burning. Moreover, the overall similarity of Nbb-OOA spectra is illustrated by the high value of correlation coefficient R^2 of factor profiles which are all over 0.9 (as shown in Table 4-11). For NB-OOA, the ion fraction of $C_2H_4O_2^+$ (m/z 60) equaling to 1.8‰ is weaker in comparison to that of Nbb-OOA spectra (ranging from 3.7‰ to 5.2‰). The intense signal at m/z 91 (mainly due to the contribution of the signal from the ion $C_7H_7^+$) in the spectrum range of m/z > 80 of the NB-OOA factor is reported to be mainly detected in aged aerosol, especially OOA formed by oxidation of BVOCs (Chirico et al., 2010, He et al., 2010, Ortega et al., 2013, Chen et al., 2015).In addition to tracer ions, the overall oxidation degree illustrated by O:C of Nbb-OOA (ranging from 0.76 to 0.91) and NB-OOA (0.39) also show an apparent difference.

Overall, yearly obvious OA nocturnal oxidation is observed based on the night peak of organic aerosol oxidation degree, and that corresponds to the nocturnal OA source resolved as NO-OOA factor during all seasons of the JULIAC campaign. For sub-NO-OOA factors, the tracer ions attribution and overall oxidation degree of factor spectrum are different between Nbb-OOA (resolved during the JULIAC-I, II, and IV) and NB-OOA (resolved at the JULIAC-III), which strongly suggest the seasonal-dependent precursors of NO-OOA. More discussions are given to further investigate the determination and formation mechanism of NO-OOA, such as dominant nocturnal oxidant (see section 4.4.2) and seasonal precursors (see section 4.4.3).

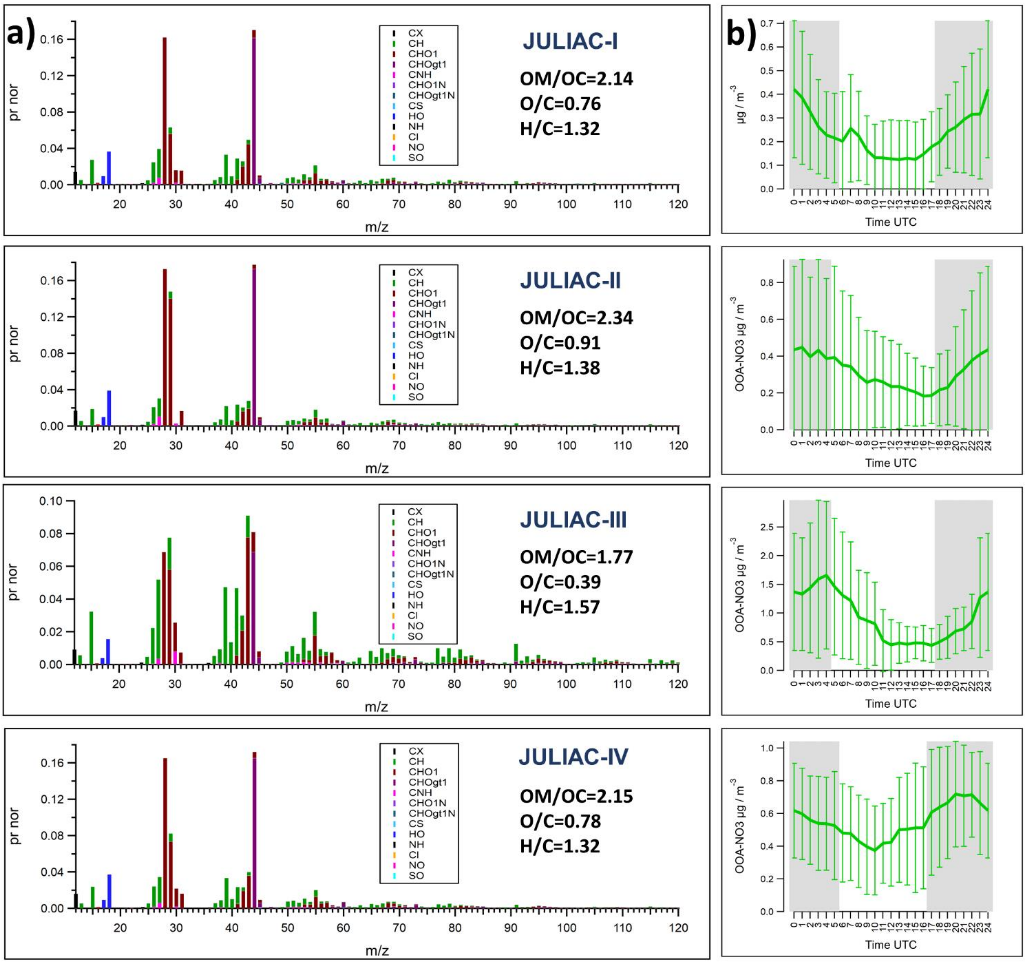

Figure 4-24: a) high-resolution NO-OOA factor spectra colored by family groups for the whole JULIAC campaign. The y-axis presents the ion signal intensity fraction while the x-axis range is m/z (mass to charge) 12-160. Elemental ratio (OM:OC, O:C, H:C) of this OA factor has been displayed. b) Diurnal variation of means concentration with a standard deviation error bar of NO-OOA factors during the whole JULIAC campaign. Grey background means nigh-time and white background stand for day-time calculated by corresponding photolysis frequency measurements.

4.4.2 NO_3 radical as dominant oxidant of nocturnal OA oxidation

Yearly obvious nocturnal OA oxidation has been observed in OA oxidation degree diurnal variation, and that corresponds to the nocturnal OA contribution resolved as NO-OOA factor by PMF. In this section, the possible mechanism, mainly about the major oxidants (NO_3 radical and O_3) of that nocturnal OA oxidation is further discussed.

Previous studies have reported that NO_3-initiated nocturnal oxidation in the atmosphere is commonly accompanied by a significant enhancement of aerosol organic nitrate (Boyd et al., 2017, Brownwood et al., 2021). In this case, the concentration variation of aerosol organic nitrate could illustrate the intensity of NO_3-initiated nocturnal oxidation, and likely associate with NO-OOA contribution variation if NO_3 radical is the dominate nocturnal oxidant. To analyze the relation between aerosol organic nitrate and NO-OOA factor, the combined matrix of aerosol organics and nitrate fragments are evaluated by PMF source apportionment analysis (methods and factor determination introduced in section 3.1.3).

As shown in Figure 4-25, the NO-OOA factor spectra determined by nitrate+organics PMF consist of significant nitrate fragments distribution, mainly NO^+ and NO_2^+ (completed PMF results in appendix A. 11). The aerosol organic nitrate concentration originated from NO-OOA source could be estimated by NO^+, NO_2^+ fragments' distribution pattern introduced by several studies (Farmer et al., 2010, Fry et al., 2013, Xu et al., 2015a, Kiendler-Scharr et al., 2016) and briefly introduced in section 3.2.1. The fraction of NO_2^+/NO^+ for NO-OOA factors, ranging from 0.09 to 0.3, is significantly lower than that for pure inorganic nitrate (detected during NH_4NO_3 IE calibration), ranging from 0.41 to 0.54 as shown in Figure 4-26, which means a significant fraction of organic nitrate formed from NO-OOA source.

Overall, the significant NO^+ and NO_2^+ fragment contribution and their distribution pattern in NO-OOA factors' spectra determined by NO_3 +Organics PMF analysis show obvious aerosol organic nitrate forms from the nocturnal oxidation source, which imply NO_3 radical as the dominant oxidant for the nocturnal OA formation.

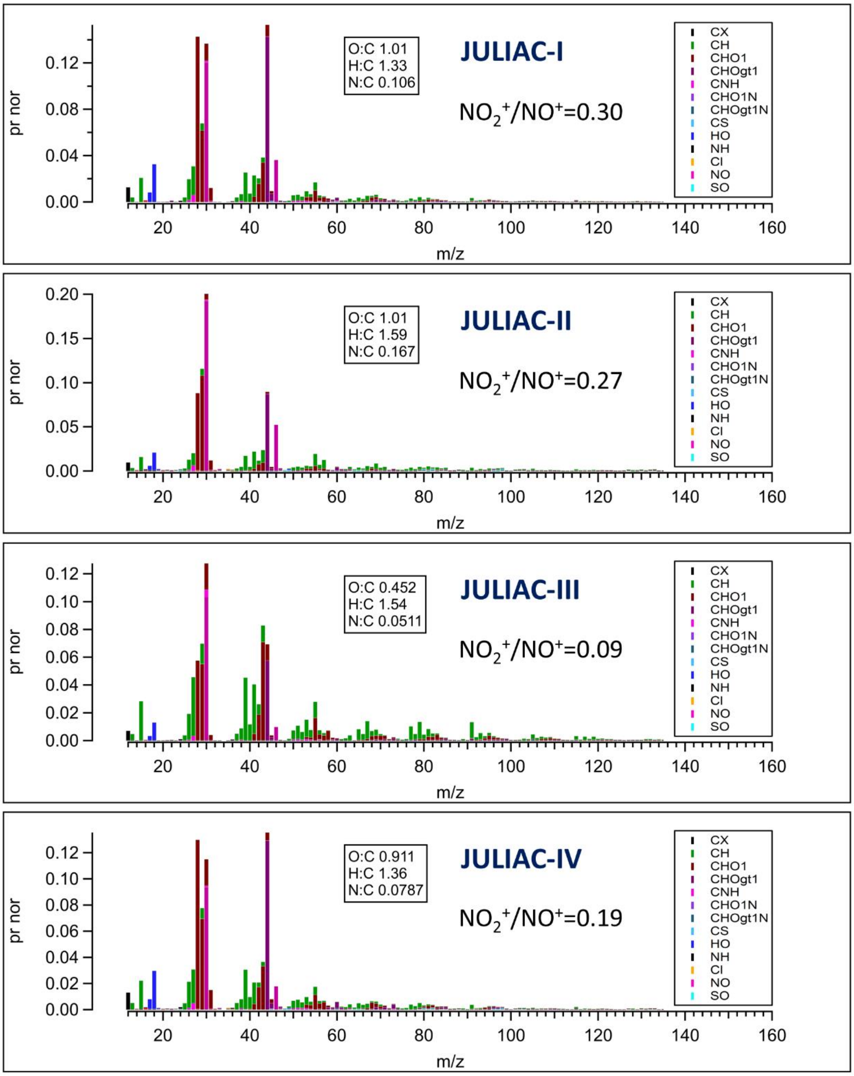

Figure 4-25: NO-OOA factors spectrum determined by NO_3 +Organics PMF analysis for the whole JULIAC campaign. Factor spectra colored by family groups. Fractions of NO_2^+/NO^+ and elemental ratio (O:C, H:C and N:C) of NO-OOA factor are displayed for each JULIAC phase. The y-axis presents the ion signal intensity fraction while the x-axis range is m/z (mass to charge) 12-160.

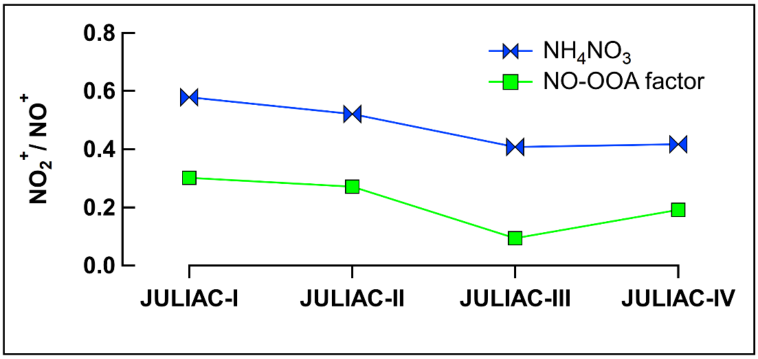

Figure 4-26: The ion fraction of NO_2^+/ NO^+ comparison between NO-OOA factors' spectrum determined by NO_3 +Organics PMF analysis and pure inorganic nitrate (NH_4NO_3) measured during IE calibration for the whole JULIAC campaign.

In addition to the above nitrate added PMF analysis, the time-series correlation between the concentration of aerosol organic nitrate ($OrgNO_3$) (methodology details could be found in section 3.2.1) and OA contribution of NO-OOA source is utilized to further investigate the nocturnal oxidation mechanism. In case of potential misattribution of consistent behavior caused by the accumulation effect of the nocturnal boundary layer (see section 3.3.3), aerosol bulk nitrate concentration is also correlated with the contribution of NO-OOA factors as a comparison. More specifically, a high correlation between the NO-OOA factor contribution and $OrgNO_3$ concentration is only well-grounded when the correlation coefficient of NO-OOA vs $OrgNO_3$ is higher than NO-OOA vs aerosol bulk nitrate.

As shown in Figure 4-27, the correlation coefficient R^2_{OrgNO3} (NO-OOA vs $OrgNO_3$), and R^2_{NO3} (NO-OOA vs aerosol bulk nitrate) are 0.28 and 0.22 for the JULIAC-I, 0.59 and 0.04 for the JULIAC-II, 0.83 and 0.48 for the JULIAC-III, and 0.60 and 0.37 for the JULIAC-IV. The R^2_{OrgNO3} for most JULIAC phases are obvious higher than the corresponding R^2_{NO3} only except the JULIAC-I. For the low value of R^2_{OrgNO3} and R^2_{NO3} observed at the JULIAC-I, that could be related to less effective PMF factor analysis for the discontinuous and incomplete AMS dataset (only 9 days valid AMS data set) during the JULIAC-I. The high value of R^2_{OrgNO3} (ranging from 0.59 to 0.83) during the JULIAC-II to IV, could effectively demonstrate that nocturnal OA oxidation is accompanied by obvious organic nitrate formation, which further supports NO_3 radical as the dominant oxidant for the nocturnal OA formation.

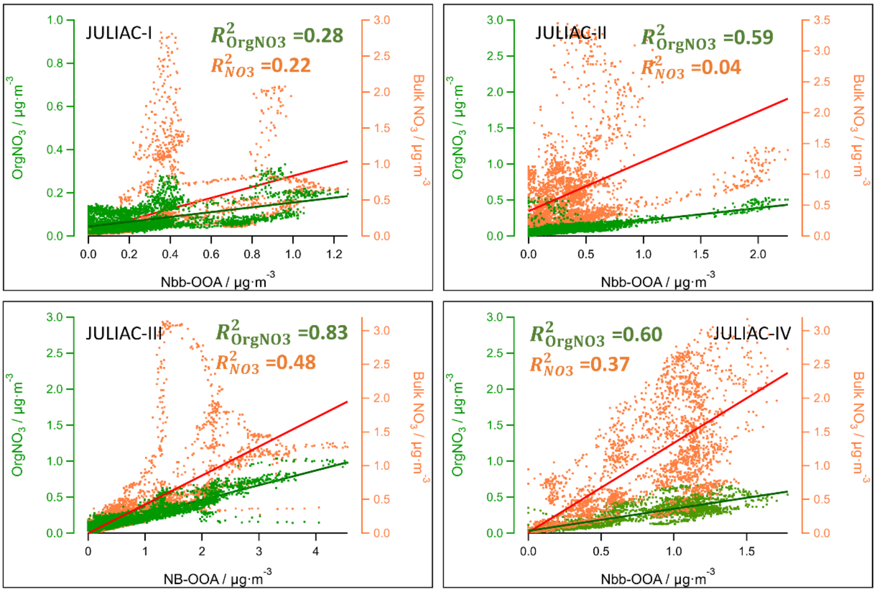

Figure 4-27: Time series correlation analysis between NO-OOA factor contribution with aerosol bulk nitrate concentration (NO_3, right Y-axis) and organic nitrate concentration ($OrgNO_3$, left Y-axis). Note that for better-comparing trends the Y-axis scale of bulk nitrate, $OrgNO_3$, and NO-OOA are different. The red and green solid lines are linear regression fitting lines for NO-OOA vs aerosol NO_3 and NO-OOA vs aerosol OrgNO3 respectively.

In addition to NO_3-initiated oxidation, dark ozonolysis is also a potential aerosol nocturnal oxidation path that need to be discussed. The reaction rate of dark ozonolysis and NO_3-initiated oxidation are compared to further investigate the dominant nocturnal oxidant. In this study, the branching ratios (introduced in section 3.4.2) for night time oxidation of representative biogenic VOCs (BVOCs) and biomass burning VOCs (bbVOCs) are calculated by the reaction rate derived separately for either $NO_3\cdot$ or O_3 normalized to the combined reaction rate (see Eq. 22). NO_3 radical concentration used here is calculated by measured N_2O_5 and NO_2 concentrations based on thermal equilibrium (see section 3.4.1). Furan and naphthalene (Kelly et al., 2018) reaction rates are selected to represent bbVOCs potential oxidation while isoprene, α-pinene, β-pinene, and limonene reaction rate are utilized to show biogenic derived oxidation. As shown in Table 4-6, the night averaged concentrations of $NO_3\cdot$ and O_3 correspond to an average concentration between 18:00 and 5:00 UTC. Temperature-dependent reaction rate constants k(T) are calculated based on the averaged night temperature (UTC 18:00-5:00) and NIST kinetics database (https://kinetics.nist.gov/kinetics/KineticsSearchForm.jsp), and detailed calculation is given in section A. 9. Based on the yearly averaged branching ratio, over 96% bbVOCs and over 75% BVOCs possibly react with NO_3 radical during the night. Moreover, even higher fractions, over 88%, of BVOCs tend to react with $NO_3\cdot$ at night during the JULIAC-III when strong biogenic emission and potential nocturnal oxidation possibly happen.

For SOA yield, although studies of dark oxidation SOA yield for bbVOCs is still sparse, related studies for BVOCs are extensive and corresponding results are displayed in Table 4-6. In general, the BVOCs (except α-pinene) SOA yield of $NO_3\cdot$ derived dark oxidation is around 2 to 10 times higher than that of O_3 derived dark oxidation. Therefore, based on the comparison of reaction rate and SOA yield between NO_3 radicals and O_3, one could conclude that NO_3 radical is the dominant oxidant for nocturnal OA oxidation in this study.

Table 4-6: Estimated reaction branching ratio of furan, naphthalene, isoprene, α-pinene, β-pinene, and limonene with respect to different oxidants ($NO_3\cdot$ and O_3). Temperature-dependent reaction rate constants listed here are calculated based on averaged night temperature (UTC 18:00-5:00) and NIST kinetics database (https://kinetics.nist.gov/kinetics/KineticsSearchForm.jsp), and detailed calculation is given in section A. 9. Averaged night concentration of O_3 and estimated $NO_3\cdot$ between 18:00 and 5:00 UTC are used to estimate oxidants' branching ratio of biogenic and biomass burning VOCs

Species	JULIAC Phases	Averaged Night Conc (UTC 18:00-5:00)		Rate Constant cm^3 mole·c^{-1} s^{-1}		Branching Ratio		Dark SOA yield from literature	
		$NO_3\cdot$ppt	O_3 ppb	$NO_3\cdot$	O_3	$NO_3\cdot$	O_3	$NO_3\cdot$	O_3
Furan	JULIAC-I	0.7	28.2	1.51E-12	2.42E-18	0.94	0.06	0.016-0.024 (Joo et al., 2019)	---
	JULIAC-II	1.7	38.5	1.47E-12	2.42E-18	0.96	0.04		
	JULIAC-III	4.7	36.6	1.39E-12	2.42E-18	0.99	0.01		
	JULIAC-IV	0.7	17.3	1.51E-12	2.42E-18	0.96	0.04		
Naphthalene	JULIAC-I	0.7	28.2	2E-11	2.81E-19	1.00	0.00	---	0.23-0.37(Riva et al., 2016)
	JULIAC-II	1.7	38.5	2E-11	2.81E-19	1.00	0.00		
	JULIAC-III	4.7	36.6	2E-11	2.81E-19	1.00	0.00		
	JULIAC-IV	0.7	17.3	2E-11	2.81E-19	1.00	0.00		
isoprene	JULIAC-I	0.7	28.2	5.65E-13	7.73E-18	0.64	0.36	0.05-0.15 (Brownwood et al., 2021) (Ng et al., 2008, Rollins et al., 2009)	0.01-0.09 (Clark et al., 2016)
	JULIAC-II	1.7	38.5	5.92E-13	8.83E-18	0.75	0.25		
	JULIAC-III	4.7	36.6	6.5E-13	1.15E-17	0.88	0.12		
	JULIAC-IV	0.7	17.3	5.62E-13	7.62E-18	0.74	0.26		
α-pinene	JULIAC-I	0.7	28.2	6.46E-12	6.63E-17	0.71	0.29	0.007-0.07 (Hallquist et al., 1999) (Mutzel et al., 2021)	0.15 (Shilling et al., 2008)
	JULIAC-II	1.7	38.5	6.38E-12	6.98E-17	0.80	0.20		
	JULIAC-III	4.7	36.6	6.21E-12	7.75E-17	0.91	0.09		
	JULIAC-IV	0.7	17.3	6.47E-12	6.59E-17	0.79	0.21		
β-pinene	JULIAC-I	0.7	28.2	2.51E-12	1.53E-17	0.80	0.20	0.5-0.55	0.03-0.05

	JULIAC-II	1.7	38.5	2.51E-12	1.69E-17	0.87	0.13	(Xu et al., 2015b) (Fry et al., 2009) (Boyd et al., 2017)	(Griffin et al., 1999) (Zhao et al., 2015)
	JULIAC-III	4.7	36.6	2.51E-12	2.06E-17	0.94	0.06		
	JULIAC-IV	0.7	17.3	2.51E-12	1.51E-17	0.87	0.13		
limonene	JULIAC-I	0.7	28.2	1.22E-11	1.64E-16	0.65	0.35	0.44-2.31 (Boyd et al., 2017) (Fry et al., 2014)	0.24-0.55 (Zhang et al., 2006, Zhao et al., 2015)
	JULIAC-II	1.7	38.5	1.22E-11	1.76E-16	0.75	0.25		
	JULIAC-III	4.7	36.6	1.22E-11	2.01E-16	0.89	0.11		
	JULIAC-IV	0.7	17.3	1.22E-11	1.63E-16	0.74	0.26		

The above discussion demonstrates that NO_3-initiated dark VOCs oxidation can be regarded as a major source contributing to the nocturnal OA formation resolved as NO-OOA factor. However, what kinds of VOCs species dominate that NO_3 radical derived oxidation, and whether dominant VOCs shows the seasonal variations are still unclear. Therefore, in the subsequent analysis, the NO-OOA factor is sub-divided into $NO_3\cdot$ derived BVOCs oxidation dominated nocturnal oxidation OOA (NB-OOA), and $NO_3\cdot$ derived bbVOCs oxidation dominated nocturnal oxidation OOA (Nbb-OOA) to further investigate the seasonally potential dominant precursors.

4.4.3 Seasonal dominant precursors for NO_3-initiated dark oxidation

4.4.3.1 Biomass burning VOCs

As shown in the brief introduction of factor spectrum characteristics in section 4.4.2, Nbb-OOA is subclassified and defined as a sub-NO-OOA factor and possibly contributed by NO_3-initiated dark oxidation of biomass burning VOCs (bbVOCs). In this section, the possibility of bbVOCs working as dominant precursors for $NO_3\cdot$ derived dark OA oxidation during the JULIAC-I, II, and IV are detailed discussed.

Firstly, $C_2H_4O_2^+$ ion fragment attribution in the Nbb-OOA factor spectrum is concerned since $C_2H_4O_2^+$ is commonly considered as biomass burning tracer ions in the AMS spectrum (Simoneit et al., 1999, Alfarra et al., 2007). As displayed in Figure 4-24, the relatively high ion intensity fraction of $C_2H_4O_2^+$ in Nbb-OOA factor spectra (3.6 ‰ for the JULIAC-I, 4.9 ‰ for the JULIAC-II, and 5.2 ‰ for the JULIAC-IV) demonstrate that bbVOCs contributes to the Nbb-OOA factor. In addition, the high correlation between the BBOA and Nbb-OOA time series (R^2 ranging from 0.48 to 0.62) as shown in Figure 4-29a) further supports that Nbb-OOA is closely related to biomass burning sources compared to other OOA factors. As shown in Figure 4-29 b), the concentration variation of combustion tracer gas CO and aerosol tracer ion $C_2H_4O_2^+$ are correlated with the OA contribution variation of Nbb-OOA factor. Their high correlation coefficient (R^2 0.44 to 0.75 for Nbb-OOA vs CO, and R^2 0.68 to 0.82 for Nbb-OOA vs $C_2H_4O_2^+$) indicate again that close relationship of Nbb-OOA factor and biomass burning emission.

In addition to CO and $C_2H_4O_2^+$ mentioned above, more biomass burning tracers and representative bbVOCs measured by AMS, VOCUS, and PTR-MS during the JULIAC campaign are involved in the discussion (see Figure 4-8). For example, furan is a heterocyclic compound commonly found in biomass burning plumes which plays an important role in SOA formation from oxidation in the gas or aqueous phase (Akherati et al., 2020). For aerosol potassium, it was used as biomass burning tracer in amounts of studies (Li et al., 2003, Zhang et al., 2013, Tao et al., 2014, Yu et al., 2018), but also was reported has obvious contributions from non-biomass burning sources (Aiken et al., 2010, Zhang et al., 2010). Here K^+ represents the bulk potassium concentration of non-refractory potassium salts (mainly KNO_3) detected by AMS (Drewnick et al., 2006, Kobayashi et al., 2022) and is considered as a possible biomass burning tracer ion.

For the diurnal behavior (one-hour resolution), the concentration of NO_3 radical, aerosol K^+, furan, and the OA contribution of Nbb-OOA factors during JULIAC-II are shown in Figure 4-28 a). In general, NO_3 radical concentration reaches the maximum in two hours after sunset, followed by an increase of the Nbb-OOA factor contribution which peaks in six hours after sunset. Both K^+ and Furan concentration time series peak during the night at the same time with Nbb-OOA implies the abundant biomass burning emitted bbVOCs during nocturnal OA formation. To further investigate the potential bbVOCs contribution to Nbb-OOA, the reaction rates of NO_3-initiated Furan oxidation are calculated and displayed in diurnal pattern Figure 4-28 b). Kinetics rate constants utilized in reaction rate calculation are all listed in Table A 5, and the value of reaction rate of Furan+NO_3 radical are converted to mass concentration using the corresponding molar weight of Furan+$NO_3\cdot$ for easier comparison. The high reaction rate all coincides with the enhancement of Nbb-OOA contribution. Overall, the diurnal behavior of biomass burning precursors concentration and corresponding reaction rate of NO_3-initiated oxidation agree and support that bbVOCs derived NO_3-initiated nocturnal OA formation mainly contribute to the Nbb-OOA factor.

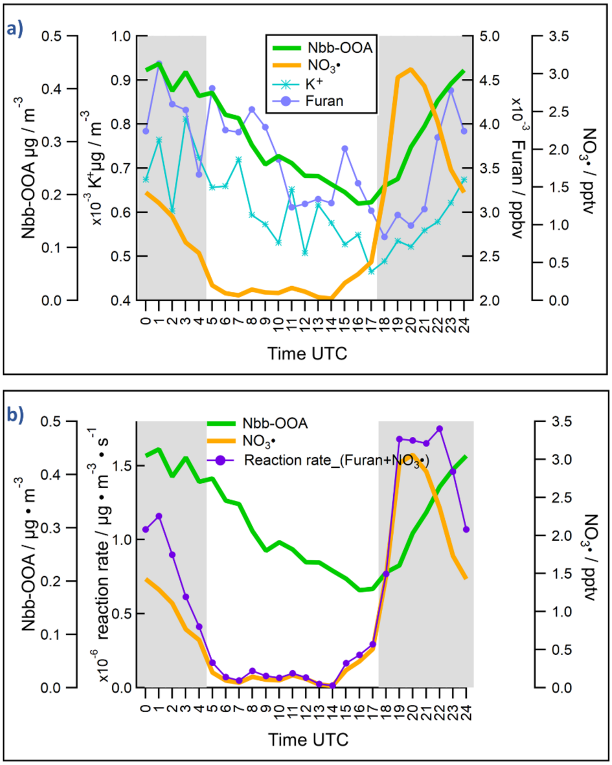

Figure 4-28: Diurnal variation of the OA contribution of Nbb-OOA factor, the concentration of $NO_3^{\cdot}$ radical (calculated by N_2O_5+NO_2), aerosol potassium (K^+, potential tracer of biomass burning), representative biomass burning VOCs (Furan), and corresponding reaction rate for Furan+NO_3 radical during JULIAC-II. Kinetics rate constants for reaction rate calculation are listed in Table A 5. For a better comparison between Nbb-OOA contribution and reaction rate of Furan+NO_3 radical, reaction rate values are converted to mass concentration using corresponding Furan+NO_3 molar weight. Grey background means nigh-time and white background stand for day-time calculated by corresponding photolysis frequency data. For the Nbb-OOA study, only JULIAC-II intensive phase has both valid NO_3 radical data and VOCs data, therefore was used as an example.

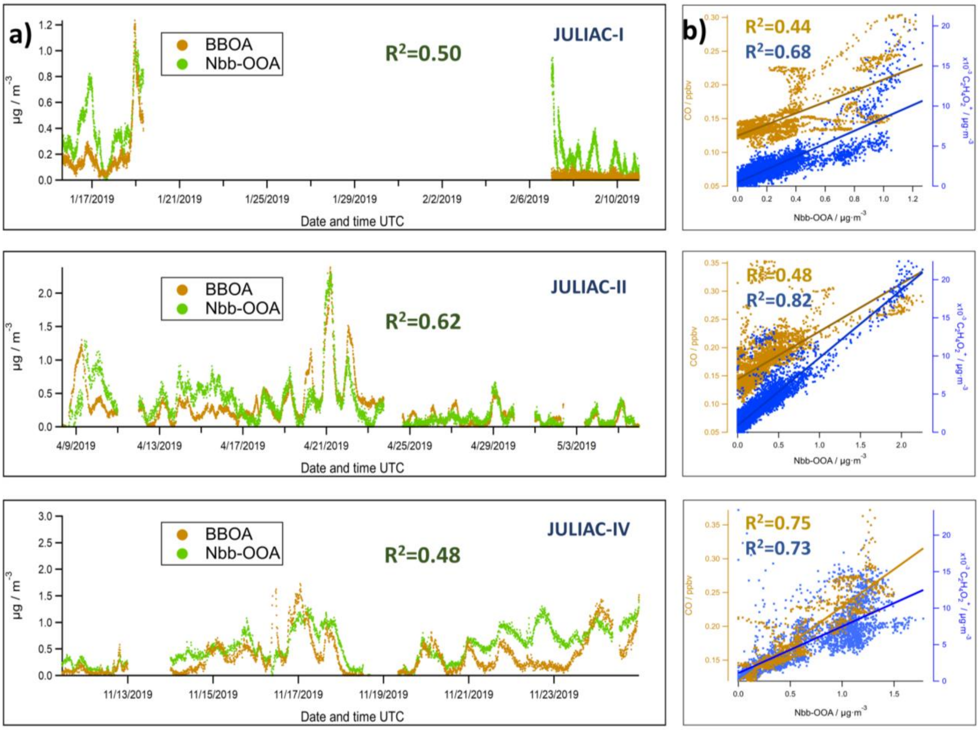

Figure 4-29: a) OA contribution time series and correlation analysis of Nbb-OOA factor and BBOA factor for the JULIAC-I, JULIAC-II, and JULIAC-IV. The corresponding correlation coefficients R^2 of time-series correlation are marked in the graph b) Time series correlation analysis of NO-OOA factor contribution (x-axis) with the concentration of gas CO (left y-axis) and aerosol fragments $C_2H_4O_2^+$ (right y-axis) for the JULIAC-I, JULIAC-II, and JULIAC-IV. Correlation coefficients R^2 are marked in graphs.

As shown in Figure 4-39, the Nbb-OOA factor defined in this research accounts for 20.9% to 48.4% of the total OA mass. The OA contribution of the Nbb-OOA factor at the JULIAC-I and JULIAC-IV even exceeded the average OA contribution of the BBOA factor. That substantial Nbb-OOA proportion means significant dark aging of biomass burning emissions, which has been observed and proved in a recent NO_3 radical dark oxidation chamber experiment (Kodros et al., 2020). The chamber experiment by Kodros et al., 2020 was designed to investigate dark oxidation of bbVOCs by exposing fresh biomass burning emission to NO_2 and O_3 (precursors of NO_3 radical). That study found a quick and significant increase of organic aerosol mass concentrations during NO_3-initiated dark oxidation (over 40% OA mass increase happened during the first one hour of the experiment). That chamber study also reported that over 70% of organic aerosol related to biomass burning emission could be affected by dark oxidation and further highlights the importance of nocturnal OA contribution. In Figure 4-30, the chamber OOA factor (bbVOCs + $NO_3\cdot$) derived by Kodros et al., 2020 is compared with the averaged spectrum of the Nbb-OOA factor (the average of Nbb-OOA factors of the JULIAC-I II and IV). Overall, the averaged Nbb-OOA factor shows a close agreement with the spectrum of chamber-produced OA with a high correlation coefficient R^2 0.92 and theta angle (Kostenidou et al., 2009) of 15.3°.

Moreover, as shown in Figure 4-31, two ambient unresolved OOA factors with a single night peak in previous winter experiments (Saarikoski et al., 2012, Florou et al., 2017) also show a high spectrum similarity (R^2 0.94 and 0.81, Theta 13.7° and 24.1° respectively) with the Nbb-OOA factor derived in this work. More unresolved or arguable OOA factors with significant night peaks observed in previous studies are listed and grouped by seasons in Table 4-8, which will be compared and discussed in section 4.4.4. In conclusion, previous lab and ambient experiments not only support the determination of a resolvable Nbb-OOA factor but also support bbVOCs are the major precursors of nocturnal OA formation based on high spectra similarity.

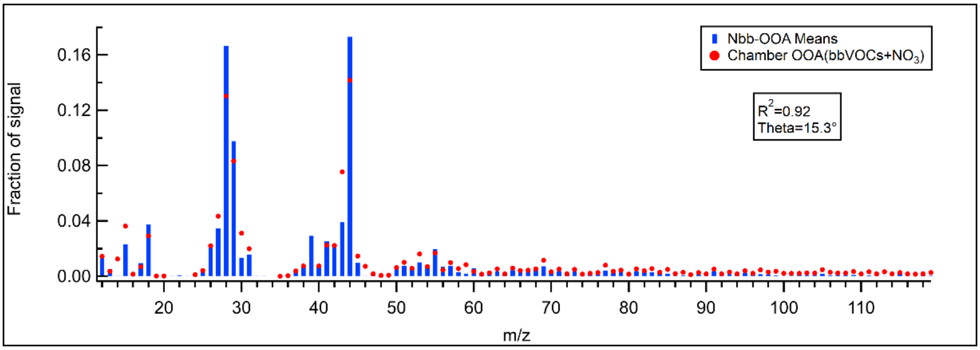

Figure 4-30: Factor spectra comparison between the averaged factor profile of Nbb-OOA of the JULIAC campaign and the chamber simulated OOA factor based on biomass burning emission and NO_3 radical (precursor NO_2+O_3) dark oxidation (Kodros et al., 2020). Correlation coefficient R^2 and theta angle are marked in the graph to illustrate the spectrum similarity. The y-axis presents the ion signal intensity fraction while the x-axis ranges from m/z (mass to charge) 10 to m/z 119.

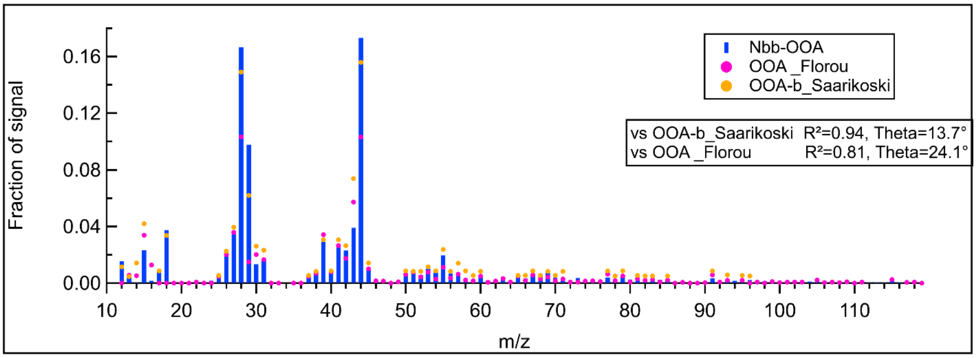

Figure 4-31: Factor spectra comparison between the averaged factor profile of Nbb-OOA of the JULIAC campaign and ambient unsolved OOA factors spectra in previous winter experiments (Saarikoski et al., 2012, Florou et al., 2017). A clear single night peak was found in these two ambient OOA without clear evident explanation. Correlation coefficient R^2 and theta angle are marked in the graph to illustrate the spectrum similarity. The y-axis presents the ion signal intensity fraction while the x-axis ranges from m/z (mass to charge) 10 to m/z 119.

Chamber studies have shown that the signal of fragment $C_2H_4O_2^+$ (or m/z 60 for UMR data) gradually decrease during both photo-oxidization (OH radical exposure) (DeCarlo et al., 2010) and dark aging experiments (NO_3 radical exposure with precursors NO_2+O_3, see insert in Figure 4-32) (Kodros et al., 2020) of fresh biomass burning emission. Aircraft measurement also found reduced levoglucosan concentrations during the aging of fresh biomass burning plumes in the atmosphere (Capes et al., 2008). Therefore, as shown in Figure 4-32, the increasing tendency of fCO_2^+ and decreasing tendency of $fC_2H_4O_2^+$ among BBOA, Nbb-OOA, and MO-OOA factors show an evident oxidation evolution of ambient biomass burning through $NO_3\cdot$ dominated dark oxidation. That factors gradient distribution in $fC_2H_4O_2^+$ vs fCO_2^+ space effectively confirm bbVOCs as the dominant precursors for nocturnal OA contribution resolved as Nbb-OOA factor.

In addition, the insert in Figure 4-32 illustrates the oxidation evolution of OA in f60 (corresponding HR $fC_2H_4O_2^+$) and f44 (corresponding HR fCO_2^+) space during 3-hours biomass burning dark aging experiment by Kodros et al. 2020, resulting in OA with f44=0.11 and f60=0.013. In contrast to the values for f44 and f60 reached in the chamber study, the Nbb-OOA factor (fCO_2^+ 0.17 and $fC_2H_4O_2^+$ 0.005) resolved during the JULIAC showed a relative higher OA oxidation degree, which may relate to the difference of biomass burning type, the variable biomass burning contribution at sampling sites, and the other minor precursors for Nbb-OOA factor, like biogenic or traffic emission.

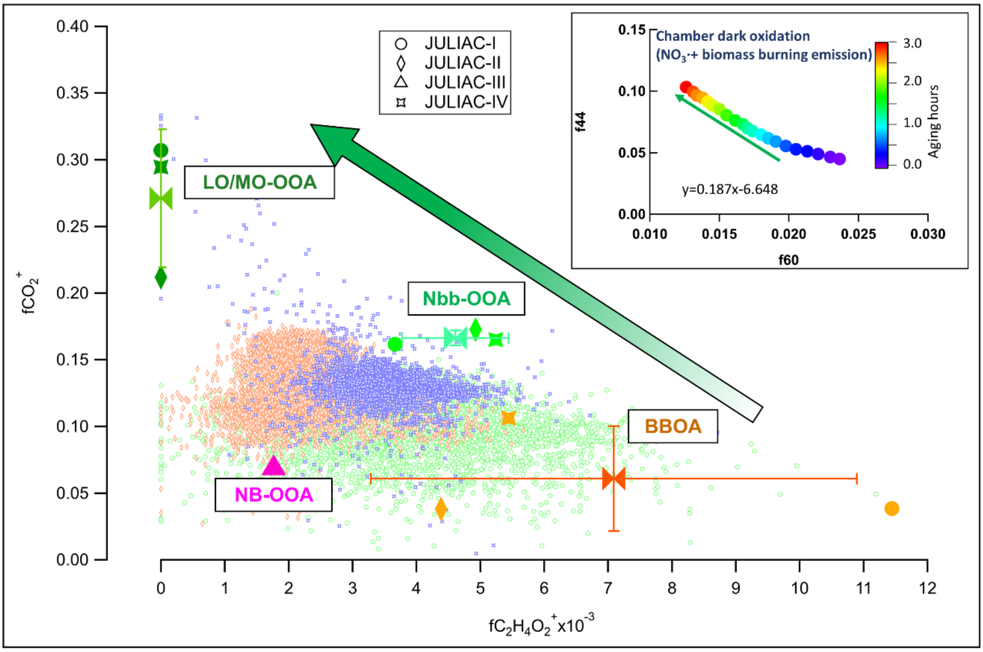

Figure 4-32: fCO$_2^+$ (fraction of fragment CO$_2^+$ in OA) vs fC$_2$H$_4$O$_2^+$ (fraction of fragment C$_2$H$_4$O$_2^+$ in OA) for raw organic aerosols, and MO-OOA, Nbb-OOA, and BBOA factors' profile during the JULIAC-I, JULIAC-II, and JULIAC-IV are given. Means value and stand derivation error bar for these three types of source factors are also displayed. fCO$_2^+$ vs fC$_2$H$_4$O$_2^+$ for NB-OOA of JULIAC-III is also added here to show the difference between Nbb-OOA and NB-OOA. A small window at the upper right corner displays the evolution of HR-ToF-AMS measured OA through f60 vs f44 space for 3 hours' biomass burning dark aging laboratory experiments (Kodros et al., 2020).

Based on the above discussion, the OA contribution of the Nbb-OOA factor mainly represents nocturnal secondary OA formed from bbVOCs derived dark NO$_3$-initiated oxidation. Therefore, the potential relationship between the primary OA emission (means BBOA) and secondary OA dark formation (means Nbb-OOA) both from biomass burning sources is explored here. As shown in Figure 4-33, the correlation analysis between the OA contribution variation of BBOA factor (x-axis) and Nbb-OOA factor (y-axis) during the JULIAC-I, II, and IV is displayed and linear fitted. Concerning the potential effect of nocturnal OA formation from aqueous-phase chemistry (Dai et al., 2019), aerosol water liquid content (ALWC, simulated by ISORROPIA-II ,see section 3.3.4) is also considered and utilized as dots gradient color in Figure 4-33. The slope of linear fit means the proportion of biomass burning related OA between dark secondary formation and primary emission. That high proportion value (0.88) illustrate that the dark secondary paths (mainly NO_3 oxidation) is equally important as primary emission in terms of biomass burning related OA contribution.

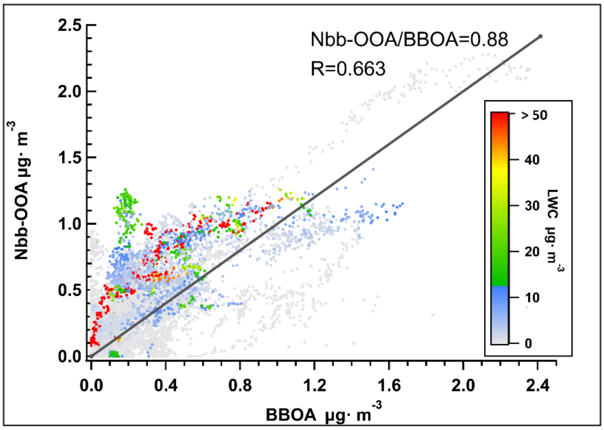

Figure 4-33: Correlation analysis between the OA contribution of BBOA factor (x-axis) and Nbb-OOA factor (y-axis) during the JULIAC-I, II, and IV. The color of the dots is marked by the corresponding ALWC concentration. Linear fitting was done for all dots with a slope of 0.88 and a correlation coefficient R=0.663.

In addition, as shown in Table 4-7, the OA contribution proportion between Nbb-OOA and BBOA increases accompanied by ALWC enhancement, which possibly relates to potential aqueous-phase chemistry OA contribution for the Nbb-OOA factor. However, considering the complicated mutual influence between aerosol composition (especially nitrate) and ALWC (Wang et al., 2020), that aqueous-phase chemistry hypothesis is not investigated yet which needs further lab simulation support.

Table 4-7: Correlation analysis between the OA contribution of BBOA factor and Nbb-OOA factor during the JULIAC-I, II, and IV for gradient aerosol liquid water content. Nbb-OOA/BBOA is the slope of the linear fit, and R^2 is the correlation coefficient of the linear fit. The data number fraction represents the raw data number located in the corresponding ALWC range normalized to total raw data number.

ALWC µg/m³	**Nbb-OOA/BBOA**	**R^2**	**Data number fraction**	**Error Y-axis** µg/m³
0-10	0.83	0.63	90.3%	0.005
10-20	1.27	0.72	3.1%	0.038
20-30	1.62	0.71	1.1%	0.079
30-40	1.36	0.93	0.5%	0.045
40-50	1.31	0.95	0.5%	0.034
>50	1.72	0.90	4.5%	0.044

In conclusion, the Nbb-OOA factor displays the shared characteristics of the high oxidation level of OOA factor and the significant tracer ions contribution of BBOA factor. The accordant diurnal behavior analysis and high overall time-series correlation among Nbb-OOA factor contribution and the concentration of NO_3 radical, biomass burning/combustion tracers ($C_2H_4O_2^+$ and gas-phase CO), aerosol organic nitrate strongly confirm that Nbb-OOA factor determined during the JULIAC-I, JULIAC-II, and JULIAC-IV present the OA formation from bbVOCs dominated NO_3-initiated nocturnal oxidation. In addition, the high similarity of factor spectra between Nbb-OOA and lab OOA factor (NO_3 radical dominated dark oxidation experiment of fresh biomass burning emission) further confirms that bbVOCs as major precursors of Nbb-OOA. Moreover, the remarkable characteristics of the distinct source of Nbb-OOA compared with BBOA and LO/MO-OOA are demonstrated in fCO_2^+ vs $fC_2H_4O_2^+$ space, which could be an indicator of Nbb-OOA factor determination in further studies.

4.4.3.2 Biogenic VOCs

As mentioned in section 1.1, significant secondary organic aerosol (SOA) production from NO_3 radical reaction with biogenic VOCs (BVOCs) has been widely investigated not only in chamber studies (Ng et al., 2008, Fry et al., 2009) but also in ambient measurements (Brown et al., 2009, Chen et al., 2015, Xu et al., 2015a, Kiendler-Scharr et al., 2016, Fry et al., 2018). In terms of major precursors of BVOCs for night SOA formation, isoprene (C_5H_8) and monoterpenes ($C_{10}H_{16}$) are mainly studied because they are the most abundant emitted BVOCs globally and account for around 90% of total BVOCs emission in the atmosphere (Guenther et al., 1995, Lathière et al., 2006, Guenther et al., 2012).

As mentioned in section 4.4.1, NB-OOA factor is introduced as a sub-NO-OOA factor which is only resolved during the JULIAC-III (during summertime). The different spectrum of the NB-OOA (as displayed in Figure 4-24) and the distinct attribution of marker ions in contrast to the Nbb-OOA factor in fCO_2^+vs $fC_2H_4O_2^+$ space (as shown in Figure 4-32) suggest different major precursors of nocturnal OA formation during the JULIAC-III. In addition, no significant OA contribution of BBOA factor determined during the JULIAC-III also confirmed that biomass burning should not be the dominant precursor contribute to NB-OOA factor. For ions larger than m/z 80 in the NB-OOA spectrum, the most significant ion is m/z 91 which is commonly observed in biogenic emission dominated OOA source (Budisulistiorini et al., 2015, Chen et al., 2015).

Overall, the noticeable spectra discrepancy of NB-OOA factor compared with Nbb-OOA factor, especially a smaller contribution of m/z 60 and enhanced intensity of m/z 91 in NB-OOA spectrum, and seasonal variation of primary emission (anthropogenic and biogenic emission) both suggest different dominated VOCs precursors (high possible BVOCs) of NO_3-initiated nocturnal OA formation during JULIAC-III (summer). The following discussion further investigates whether BVOCs and which type BVOCs (mainly about monoterpenes and isoprene) can dominate the formation of nocturnal $NO_3\cdot$ derived OA formation.

The averaged diurnal pattern of the concentration of monoterpenes and isoprene during the JULIAC-III are displayed in Figure 4-34 a) in correlation with that of NB-OOA factor and NO_3 radical. The daily averaged concentration of isoprene and monoterpenes variate from 0.10-0.35 ppbv and 0.02-0.05 ppbv respectively. The concentration of isoprene shows a continuous decrease since sunset with an average loss of 0.21 ppbv followed by an OA contribution increase of NB-OOA factor of 1.2 $\mu g.m^{-3}$, while the concentration of monoterpenes is relatively stable during night time ranging from 0.03 to 0.04 ppbv.

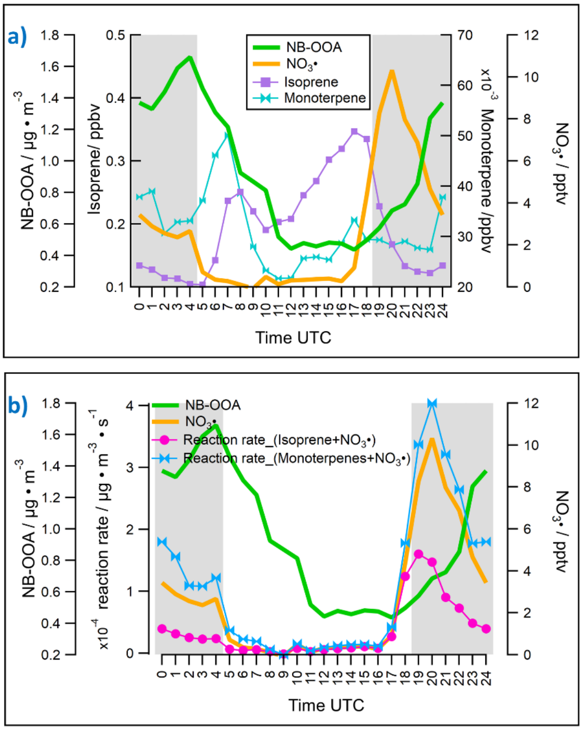

Figure 4-34: Diurnal variation of the OA contribution of NB-OOA factors, the concentration of NO_3 radical (calculated by N_2O_5+NO_2), representative biogenic VOCs (isoprene and monoterpenes), and corresponding reaction rate for BVOCs+NO_3 radical. Kinetics rate constants for reaction rate calculation are listed in Table A 5. For a better comparison between NB-OOA contribution and reaction rate of BVOCs+NO_3 radical, reaction rate values are converted to mass concentration using corresponding BVOCs+NO_3 molar weight. Grey background means nigh-time and white background stand for daytime calculated by corresponding photolysis frequency data. For a clarified illustration of potential precursors, BVOCs variation during the JULIAC-III, the diurnal concentration variations of aerosol potassium and furan during the JULIAC-III are given in appendix A. 14.

To further investigate the major BVOCs contributing to the NB-OOA factor, the reaction rates of NO_3-initiated BVOCs oxidation (mainly for isoprene and monoterpenes) are calculated and displayed in diurnal pattern in Figure 4-34 b). Kinetics rate constants utilized in reaction rate calculation are all listed in Table A 5, and the averaged rate constant of α-pinene, β-pinene, and limonene is used as the rate constant of monoterpenes. For a better comparison between NB-OOA contribution and reaction rate of BVOCs+NO_3 radical, reaction rate values are converted to mass concentration using the corresponding molar weight of BVOCs+NO_3·. As shown in Figure 4-34 b), the maximal reaction rate of monoterpenes+ NO_3 radical (4.04 e^{-4} µg·m^{-3}·s^{-1}) appears at 20:00

UTC, which is over 2.5 times of maximal reaction rate of isoprene+ NO_3 radical (1.60 e^{-4} $\mu g \cdot m^{-3} \cdot s^{-1}$) appearing at 19:00 UTC. Based on the overall diurnal variation of reaction rate, monoterpenes show an obvious advantage in nocturnal NO_3-initiated oxidation compared to isoprene.

In addition to reaction rate, the SOA yield of BVOCs+$NO_3\cdot$ oxidation is also an important indicator to investigate major BVOCs precursors for nocturnal NO_3-initiated OA contribution during summer. Amount of chamber studies have reported relatively low SOA yield (normally mass fraction of SOA normalized to that of consumed VOCs mass), ranging from 2% to 15% for the NO_3-initiated oxidation of isoprene (Ng et al., 2008, Rollins et al., 2009, Brownwood et al., 2021). That low SOA yield is possibly related to the semi-volatile or intermediate-volatile property of its major product, isoprene monomers (account for around 80% of product signals) and consequently cause weak partitioning of product to aerosol phase (Brownwood et al., 2021, Wu et al., 2021).

On the contrary, monoterpenes are commonly suggested as the dominant VOCs contribution to biogenic derived night OA formation (Fry et al., 2014) (Russell 2005, Hoyle et al., 2007, Pye et al., 2010) with SOA yield ranging from around 20% to 230% under different simulated condition (like injected reactant ratio, monoterpenes species, and RH) (Boyd et al., 2017, Mutzel et al., 2021). If using the lowest SOA yield of monoterpenes (20%) and the night averaged reaction rate of monoterpenes+ NO_3 radical (2.14 e^{-4} $\mu g \cdot m^{-3} \cdot s^{-1}$) to estimate the nocturnal OA production, around 1.16 $\mu g \cdot m^{-3}$ OA are produced which is comparable to the averaged night enhancement of NB-OOA 1.20 $\mu g.m^{-3}$. Therefore, the comparison and calculation of reaction rate and SOA yield of NO_3-initiated BVOCs oxidation further confirm that BVOCs, especially monoterpene, dominate the summer-time nocturnal OA contribution.

As an additional analysis, the factor spectrum of NB-OOA is compared with that of ambient biogenic derived OOA factors which are suggested contributed by $NO_3\cdot$ oxidation and have significant night enhancement reported in previous studies (Paglione et al., 2014, Chen et al., 2015, Xu et al., 2015b). As shown in Figure 4-35, factor spectra of three ambient OOA factors, OOA-3 (Chen et al., 2015), LO-OOA (Xu et al., 2015b), and SV-OOA (Paglione et al., 2014) is compared with that of NB-OOA factor and high spectra similarity is found with R^2 equal to 0.92, 0.96, 0.78, and theta 14.3°, 22.9°, 27.7° respectively. OOA-3 (Chen et al., 2015) and LO-OOA (Xu et al., 2015b) were suggested to be associated with the fresh production of biogenic derived secondary

OA with a significant increase during the night. Potential nighttime $NO_3\cdot$ chemistry contribution to LO-OOA has been suggested and discussed regarding the concurrent concentration variation of aerosol organic nitrate (LO-OOA vs ON R^2=0.81) and biogenic derived SOA yield simulation by (Xu et al., 2015b). That study concludes that 64% of total nighttime OA production should originate from $NO_3\cdot$ oxidation path, in which monoterpenes derived SOA account for over 80% of the contribution. The SV-OOA (Paglione et al., 2014) was proved to be contributed by nighttime NO_3 chemistry with high time-series correlation of SV-OOA contribution with aerosol organic nitrate concentration (R^2=0.58) and modeled SOA from NO_3 oxidation during May of 2008 (Kiendler-Scharr et al., 2016).

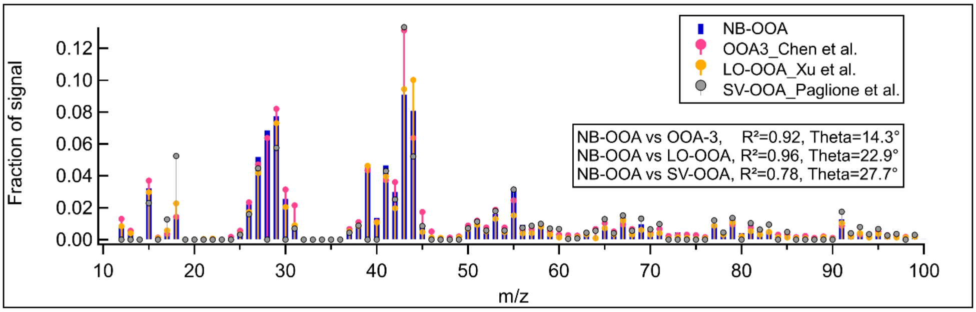

Figure 4-35: Unit mass resolution spectrum comparison between NB-OOA of the JULIAC campaign and ambient biogenic derived OOA factor, OOA3 by (Chen et al., 2015), LO-OOA by (Xu et al., 2015b), and SV-OOA (Paglione et al., 2014) with clear night enhancement. Only m/z ≤ 100 of spectra are considered because the contribution of ions at m/z > 100 is negligible. Linear correlation analysis between UMR spectrum of NB-OOA and biogenic derived OOA factors of ambient experiment has been made and correlation coefficients are also displayed in the graph. Correlation coefficient R^2 and theta angle are marked in the graph to illustrate the spectrum similarity.

Moreover, two OOA factors from β-pinene+$NO_3\cdot$ and limonene+$NO_3\cdot$ chamber experiment determined by Boyd et al. are also compared with the NB-OOA factor as shown in Figure 4-36. The NB-OOA factor shows similar ions distribution, especially at the range of m/z>50, with two chamber-OOA factors, with correlation coefficient R^2=0.71 and theta=27.8° for β-pinene+$NO_3\cdot$, and R^2=0.64 and theta=34.3° for limonene+$NO_3\cdot$ respectively. Therefore, the high spectra similarity with monoterpenes+$NO_3\cdot$ chamber OOA factor further confirms that monoterpenes likely dominate $NO_3\cdot$ derived night OA formation during summertime.

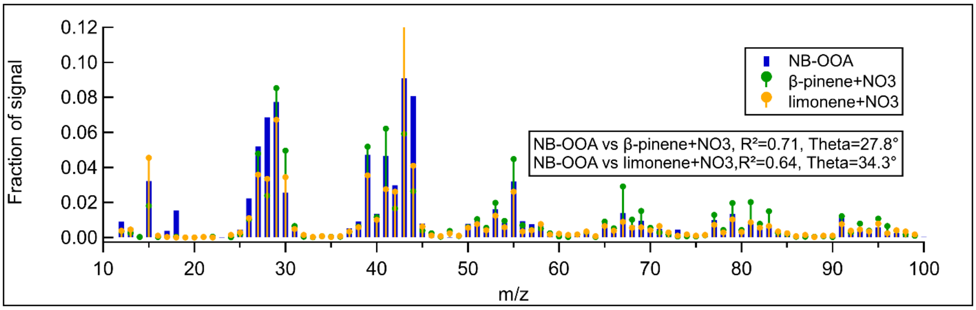

Figure 4-36: Comparison of the unit mass resolution spectrum between NB-OOA of the JULIAC-III and the mass spectra of OOA factors determined by NO_3 radical oxidation in chamber experiments (limonene+$NO_3\cdot$ and β-pinene+$NO_3\cdot$)(Boyd et al., 2017). Only $m/z \leq 100$ of spectra are considered due to negligible contribution of ions at $m/z > 100$. Linear correlation coefficient between the UMR spectrum of NB-OOA and the OOA of lab simulation has been made and displayed. Correlation coefficient R^2 and theta angle are marked in the graph to illustrate the spectrum similarity.

In summary, the reaction rate and SOA yield calculation of NO_3-initiated BVOCs oxidation (mainly for monoterpenes and isoprene) illustrate that BVOCs, especially monoterpenes, dominate the $NO_3\cdot$ derived night OA contribution during summertime. Moreover, high similarity of factor spectra between NB-OOA factor and ambient biogenic derived OOA factors, and chamber derived OOA factor ($NO_3\cdot$+monoterpenes) further support that conclusion.

4.4.4 Perspectives

Because of the significant NO-OOA formation during the whole JULIAC campaign, the potential OA contribution from $NO_3\cdot$ derived nocturnal chemistry probably also exists in previous aerosol source apportionment research but may be defined as unexplained OOA with night enhancement or as common OOA factors with unresolved features, like BBOA factors with high oxidation degree. In several studies, BBOA factors with significantly high oxidation degree (DeCarlo et al., 2010, Crippa et al., 2013b, Cheng et al., 2021), LO/MO-OOA factors and unresolved OOA factors with significant nighttime enhancement of OA contribution (Budisulistiorini et al., 2015, Chen et al., 2015, Xu et al., 2015b, Florou et al., 2017, Dai et al., 2019) has been found in previous aerosol PMF analysis.

Regarding the characteristics of maximal OA contribution at night and high oxidation degree, these previous ambiguous source factor to a certain extend could be explained by an unresolved NO-

OOA factor or mixed NO-OOA with BBOA or MO/LO-OOA factors. For these untypical factors, night chemistry (especially $NO_3\cdot$ derived BVOCs oxidation), nocturnal boundary layer effect, and aqueous chemistry are suggested to explain the night enhancement of OA contribution of these OOA. The three types explanations given in these studies concerning higher oxidized BBOA factors are, (1) sustain photo-oxidation of biomass burning plume during the evening (DeCarlo et al., 2010, Cheng et al., 2021), (2) interference of background OOA (Crippa et al., 2013b), and (3) aqueous phase chemistry (Dai et al., 2019). For example, BBOA factor with a high f44 and O:C ratio (0.42) has been found in the study by (DeCarlo et al., 2010) and reported that potential secondary BBOA effect as a possible explanation. However, the fraction between primary BBOA and secondary BBOA is difficult to estimate. Further tracer-based source apportionment analysis (Cheng et al., 2021) determines a mixing factor, biomass burning (BB)/SOA, based on levoglucosan, 4-nitrocatechol and benzenetricarboxylic acids (tracers of aging of biomass burning plume) measurements. That study further confirms SOA formation in biomass burning plume but concluded that photo-oxidation during evening dominated that biomass burning derived SOA formation.

Table 4-8: Brief overview of potential Nbb-OOA and NB-OOA factors or their related mixing factors observed in previous ambient aerosol source factors results. Major analysis methodologies and conclusions for unknown factors are also given as a reference.

Index	Ambiguous factors	Season and sites	Analysis methods	Conclusion	Reference
1	OOA2-BBOA	Winter, Paris	Levoglucosan time series correlation	Primary BBOA and background OOA	(Crippa et al., 2013b)
2	BBOA	Spring, Mexican Plateau	Profile correlation with photochemical aged BBOA in smog chamber aging experiment	Indicate that this factor probably contains some S-BBOA (secondary BBOA), although the fraction of P-BBOA (Primary BBOA) vs. S-BBOA is difficult to estimate.	(DeCarlo et al., 2010)
3	Mixing factor biomass burning (BB)/SOA	Whole year, Hong Kong	Levoglucosan and 4-nitrocatechol, benzenetricarboxylic acids time series correlation	Photo-oxidation of BB, formation of BB SOA should be even fastly achieved during the regional transport	(Cheng et al., 2021)
4	Mixing factor LO-OOA/, MO-OOA	Whole year, Houston, Texas	Profile correlation of aqOOA factor, R=0.96	Aqueous-phase chemistry suggested by relationships with Ox and LWC,	(Dai et al., 2019)
5	OOA	Winter, Athens	O:C 0.46, Clear midnight peak of OOA, Organic nitrate mass ratio diurnal pattern	Night nitrate is major contributed by inorganic nitrate. Deny the possibility of nitrate radical derived oxidation and mentioned unsolved OOA night peak.	(Florou et al., 2017)

6	Aged-BBOA	Winter, Dongguan	Time-series correlation with $C_2H_4O_2^+$, R^2=0.71, O:C=0.60	Biomass burning aging.	(Zhu et al., 2018)
7	Mixing factor LO-OOA	Whloe year, Houston, Texas	Time-series correlation with ON, R=0.73, Profile correlation of aqOOA factor profile.	Nocturnal NO_3-initiated oxidation of anthropogenic and biogenic VOCs. Possible aqueous phase chemistry.	(Dai et al., 2019)
8	Mixing factor LO-OOA	Summer, Southeastern United States	Time-series correlation with ON, R=0.81	Speculation of $NO_3\cdot$ derived oxidation of BVOCs	(Xu et al., 2015b)
9	91factor	Summer, Tennessee	----	Photochemistry and nighttime chemistry	(Budisulistiorini et al., 2015)
10	OOA-3	Sping, Amazon Basin,	----	Nocturnal boundary layer effect. Fresh SOA by BVOCs oxidation.	(Chen et al., 2015)

Overall, OA contribution from $NO_3\cdot$ derived nocturnal chemistry, represented by NO-OOA, could widely exist in an atmosphere not only in this study but possibly make a significant OA contribution to the number of previous studies. In addition, the proportion of biomass burning related OA between dark secondary formation and primary emission Nbb-OOA/BBOA (0.88) determined in this study could be used as a reference proportion for determination or estimation the OA contribution from bbVOC derived dark NO_3 oxidation in other filed studies.

4.4.5 Conclusion

The significant OA contribution from NO_3-initiated nocturnal chemistry is resolved as separated nocturnal oxidation oxygenated organic aerosol factor, NO-OOA factor, by PMF analysis for the first time in this study for all seasons during the JULIAC campaign. The high OA contribution of NO-OOA factor, ranging from 20.9% to 48.4% mass fraction of organic aerosol, is comparable to the estimated OA contribution of $NO_3\cdot$ derived oxidation by lab and model research (Russell 2005, Pye et al., 2010, Xu et al., 2015b, Kodros et al., 2020). Two sub-NO-OOA factors, NB-OOA and Nbb-OOA illustrate the seasonal-dependent precursors of NO_3-initiated dark oxidation. The Nbb-OOA factor determined during the JULIAC-I, JULIAC-II, and JULIAC-IV present the OA formation from bbVOCs dominated NO_3-initiated nocturnal oxidation, while the OA contribution of NB-OOA determined during the JULIAC-III (summer) is mainly contributed by BVOCs (especially monoterpene) derived NO_3-initiated nocturnal oxidation.

4.5 Seasonal comparisons of OA.

Because of the impact of aerosol on air quality, climate, and human health, large amounts of field studies in megacities and rural areas have been done all over the world to understand the aerosol characteristics and evolution mechanism (Chen et al., 2015, Schlag et al., 2016, Sun et al., 2016, Lalchandani et al., 2021, Mahilang et al., 2021). In this study, the concentration variation of aerosol species measured by HR-ToF-AMS during four seasons of the JULIAC campaign supply an opportunity to investigate the seasonal variation of aerosol properties and seasonal dependent sources contribution. The seasonal variation of aerosol composition and aerosol bulk species concentration has been mainly discussed in section 4.1. Aerosol organics is confirmed as the major components of aerosol during the whole JULIAC campaign accounting for 39.0% to 57.6% of the aerosol total mass. Detailed determination and demonstration of seasonal source apportionment of organic aerosol are given in section 4.2 to 4.4, but the seasonal comparison of organics aerosol properties, like oxidation degree and OA factor contribution and characteristics are still missing. Therefore, to further understand seasonal evolution of organic aerosol, below discussion will be mainly revolved around the seasonal comparison of oxidation degree of OA, OA source contribution, and source properties variation.

4.5.1 The oxidation degree of OA

The oxidation degree of organic aerosol for each intensive JULIAC phase are displayed in the Van Krevelen triangle (Ng et al., 2011) with x-axis O:C and y-axis H:C as shown in Figure 4-37. The elemental ratio (O:C, H:C, OS_C) of aerosol organics was calculated by the improved-ambient method (Canagaratna et al., 2015) see section 3.2.3. In addition, the concentration of oxidant Ox (O_3+NO_2) measured concurrently is utilized as color-code in the graph to roughly illustrate the intensity of the secondary source (especially photochemistry) in the atmosphere (Canonaco et al., 2015, Li et al., 2015). The averaged elemental ratio O:C, H:C, OS_C with corresponding standard derivation for four JULIAC intensive phases are displayed in Table 4-9.

The overall organic aerosol oxidation degree reaches to the minimum during summer (the JULIAC-III) in this study with the lowest averaged O:C value of 0.64. That seasonal variation of OA oxidation is opposite to what observed at urban site where OA oxidation degree reach to yearly peak during summer (Li et al., 2015). As discussed in section 4.1, the site in this study is a typical semi-rural site where aerosol mass reaches the maximum during summer and aerosol organics are yearly major species. In the contrast, the referred urban field study shows comparable aerosol levels during the whole year and found aerosol sulfate as a yearly dominated aerosol species. Therefore, the opposite seasonal characteristics of the oxidation degree of OA are possibly related to the different major emission sources.

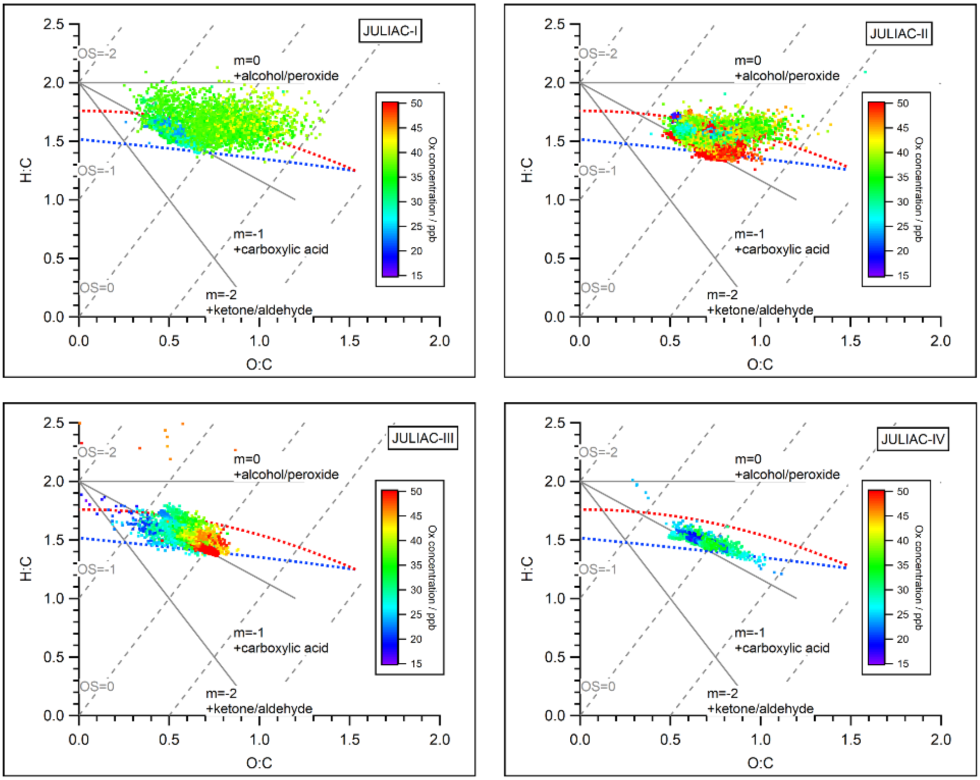

Figure 4-37: Van Krevelen triangle graph (Ng et al., 2011) for all raw organic aerosol collected during four intensive phases of the JULIAC campaign. Atomic ratio regions of standard groups: alcohol/peroxide, carboxylic acid, and ketone/aldehyde introduced by (Aiken et al., 2007) were marked in graphs as reference. Dots in all graphs were colored-coded by the concentration of an oxidant Ox (NO_2+O_3) detected during the JULIAC campaign to roughly represent the intensity of secondary source, especially photochemistry. The red and blue dash line corresponds to the right and left lines of the f44/f43 triangle introduced in (Ng et al., 2010). The estimated carbon oxidation states (OSc≈2O/C-H/C) were marked as gray dash lines.

Table 4-9: Overview of the averaged elemental ratio O:C, H:C, OS_C with corresponding standard variation of total organic aerosol for four JULIAC intensive phases.

Averaged elemental ratio	JULIAC campaign			
	JULIAC-I/Winter	JULIAC-II/Spring	JULIAC-III/summer	JULIAC-IV/autumn
O:C	0.71±0.20	0.76±0.12	0.64±0.08	0.66±0.09
H:C	1.63±0.11	1.50±0.10	1.50±0.08	1.50±0.06
OSc	-0.21±0.41	0.01±0.26	-0.23±0.23	-0.18±0.23

The accordance of O:C increasing with the enhancement of Ox concentration shown at the JULIAC-III in Figure 4-37 supports fresh OA from mainly photooxidation path dominate OA contribution during summer and that agree with the high mass fraction of LO-OOA (58.2%) determined during the JULIAC-III. No clear relationship could be found between OA oxidation degree with Ox level during the rest seasons. That also confirmed the OA source appointment results that OA is mainly contributed by nocturnal oxidation (Nbb-OOA) and anthropogenic emission (HOA, BBOA) during JULIAC-I, II, and IV (see Table 4-10). That seasonal oxidation variation of OA is also reflected in PMF OOA source factors seasonal properties, such as highly oxidized OOA during wintertime (displayed in Table 4-10), and is detailed in discussed in section 4.5.

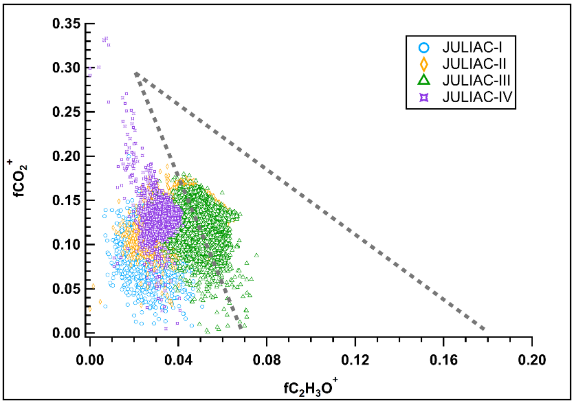

Figure 4-38: fCO_2^+ (fraction of fragment CO_2^+ in OA) vs $fC_2H_3O^+$ (fraction of fragment $C_2H_3O^+$ in OA) for all raw organic aerosols detected during the JULIAC campaign. Each intensive phase was marked by different color markers to show seasonal variation. . The coarser dash lines represent the f44/f43 distribution triangular region of ambient OOA factors reported in (Ng et al., 2010)

In addition to the elemental ratio discussed above, fCO_2^+ (fraction of fragment CO_2^+ in OA) and $fC_2H_3O^+$ (fraction of fragment $C_2H_3O^+$ in OA), corresponding to f44 and f43 for UMR data (Ng et al., 2010) respectively, are also commonly used as diagnostic parameters to illustrate the oxidation degree and OA evolution path. Clear season difference of $fC_2H_3O^+$ was displayed in Figure 4-38 with maximum appearing at the JULIAC-III and minimum showed at the JULIAC-I. High $fC_2H_3O^+$ was normally considered as an indicator of fresh SOA formation while fCO_2^+ value represents the contribution of highly oxidized aerosol or aged aerosol (Sun et al., 2012). Therefore, the OA seasonal difference displayed in $fC_2H_3O^+$ vs fCO_2^+ analysis and elemental analysis both support a yearly strongest fresh SOA formation during summer and weakest of that during winter, which is consistent with seasonal source contribution discussion as shown in section 4.5.

4.5.2 Seasonal variations of source contributions

Organic aerosol source apportionment has been conducted separately for each intensive phase of the JULIAC campaign, and detailed methodology introduction of PMF analysis and interpretation of seasonal optimal source factors could be found in sections 3.1 and section 4.2 to 4.4 respectively. In this chapter, the seasonal variation of source properties and contribution during the JULIAC campaign is focused discussed.

As shown in Figure 4-39, the averaged concentration of bulk aerosol species and the averaged OA contribution of PMF-resolved source factors has been displayed for four intensive JULIAC phases. The detailed mass and mass fractions values of that overview pie chart are concluded in Table 4-10. As introduced in section 4.2.1, the HOA factor determined in this study mainly represents the OA contribution from traffic exhaust and accounts for a minor mass fraction of total OA, ranging from 3% to 9.5% during the whole year. Primary biomass burning emission (possibly including coal combustion) shows enhanced OA emission during cold seasons contributing to 11.7% to 45.2% of total OA, but no obvious BBOA contribution was resolved during summertime.

The OA from secondary sources is mainly resolved as OOA (LO-OOA, MO-OOA, NO-OOA) factors and accounting for 46% to 88% of total OA mass during the whole JULIAC campaign. Moreover, the significant OA formation from the NO_3-initiated nocturnal oxidation during each season is illustrated by the high OA mass fraction of NO-OOA ranging from 20.9% to 48.4%. LO-OOA and MO-OOA are distinguished mainly by the oxidation degree, but both represent OOA from daytime oxidation, especially photooxidation path. The relative OA contributions of daytime (LO-OOA, MO-OOA) and nighttime (NO-OOA) oxidation paths show the seasonal variation of the dominant formation mechanism of OOA. OA contribution during summer is mainly contributed by daytime oxidation path, especially biogenic emission oxidation and accounts for over half total OA mass. But during the JULIAC-I and the JULIAC-IV, OA contribution of nocturnal oxidation (Nbb-OOA) even over that of daytime oxidation (MO-OOA) which implies nocturnal oxidation dominated OA formation environment during cold weather in this study. Moreover, all biomass burning-related OA (BBOA+Nbb-OOA) accounts for 82.6% of total OA mass during JULIAC-IV, which implies the biomass burning sources control (like residential heating, industry) is the core part for autumn or the whole wintertime air pollution control.

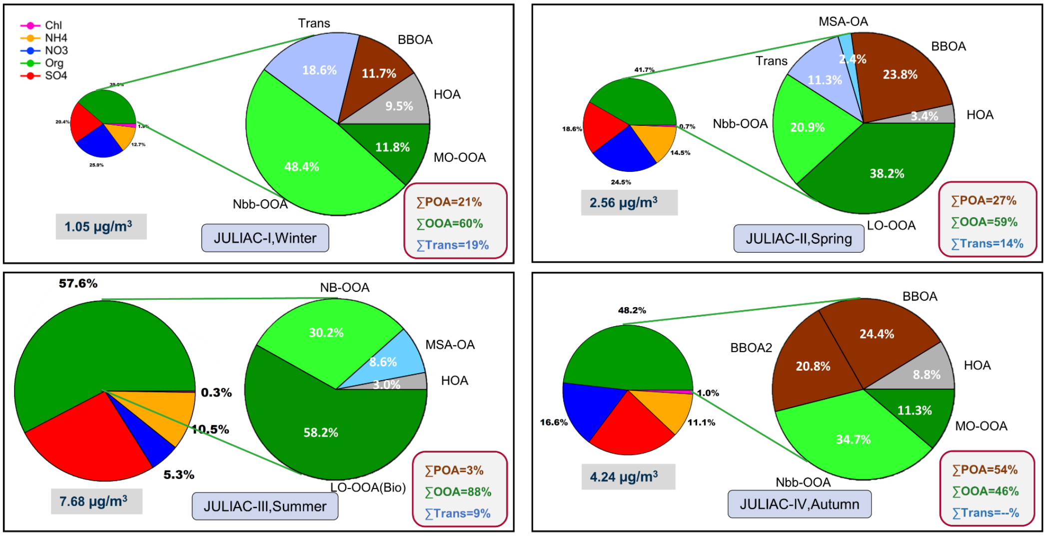

Figure 4-39: Seasonal comparison of the average mass of total aerosol mass concentration, aerosol composition fraction of bulk species (NO_3, SO_4, Chl, NH_4, Org), and source factors (HOA, BBOA, LO-OOA, MO-OOA, NO-OOA, Trans-OA, MSA-OA) contribution for aerosol organics for four intensive phases of the JULIAC campaign. Primary OA emission (HOA+BBOA), secondary OA formation (LO-OOA+MO-OOA+NO-OOA) and regional transport (Trans-OA+MSA-OA) are calculated and compared among four seasons.

Table 4-10: the summary of total OA mass concentration and corresponding mass contribution fraction and oxidation degree of OA source factors resolved by PMF analysis during four intensive phases of the JULIAC campaign.

		JULIAC campaign			
		JULIAC-I/Winter	JULIAC-II/Spring	JULIAC-III/summer	JULIAC-IV/autumn
Concentration	Total OA mass, µg/m^3	0.41	1.07	4.42	2.04
OA factors OA contribution µg/m^3 and OA contribution mass fraction	HOA	9.50%, 0.04	3.40%, 0.04	3%, 0.13	8.80%, 0.18
	BBOA	11.70%, 0.05	23.80%, 0.25	--	45.20%, 0.92
	MSA-OA	--	2.40%, 0.03	8.60%, 0.38	--
	Trans-OA	18.60%, 0.08	11.30%, 0.12	--	--
	LO-OOA	--	38.20%, 0.41	58.20%, 2.57	--
	MO-OOA	11.80%, 0.05	--	--	11.30%, 0.23
	NO-OOA	48.40%, 0.20	20.90%, 0.22	30.20%, 1.33	34.70%, 0.71
OA factors oxidation degree H/C; O/C	HOA	2.1; 0.12	1.86; 0.03	1.93; 0.03	1.95; 0.13
	BBOA	1.72; 0.36	1.54; 0.28	--	1.54;0.3 1.47;0.36
	MSA-OA	--	1.61; 0.63	1.47; 0.49	--
	Trans-OA	1.76; 0.54	1.28; 0.77	--	--
	LO-OOA	--	1.16; 0.70	1.29; 0.70	--
	MO-OOA	1.12; 1.00	--	--	1.16; 0.89
	NO-OOA	1.32; 0.75	1.38; 0.91	1.57; 0.39	1.32; 0.78

In addition to the primary and secondary sources of OA, regional transport also play an important role in OA contribution (9%-19%) and shows clear seasonal variation related to the meteorological condition. As discussed in sections 4.2.3 and 4.3, regional transport OA contribution could be separated by PMF as a distinct regional transport factor because of the obvious changed organic aerosol composition of the transported plume, like the high content of MSA in the marine plume. However, no distinct regional transport OA factor was resolved during the JULIAC-IV by PMF analysis, though the regional OA effect could be recognized by meteorological analysis. For that matter, the limitation of PMF analysis in OA regional transport separation has been mentioned and discussed in section 4.2.3. Anyhow, OA regional transport contribution separated by PMF during the JULIAC campaign is consistent with back trajectory analysis and meteorological analysis and plays a significant impact in understanding OA inter-regional influence and model improvement.

4.5.3 Seasonal variations of source properties

4.5.3.1 Seasonal variations of OA factors spectrum

The factor analysis method of organic aerosol resolves different sources' contributions by sorting complex OA composition into several types of OA source factors with static mass spectrum. However, the factor spectrum of the same type of source could show variation due to seasonal-dependent emissions (like biomass burning type) and seasonally changed reaction mechanisms (mainly for OOA). Therefore, the organic aerosol source apportionment has been conducted separately for each intensive phase of the JULIAC campaign and the potential variation of one type of factor source could be investigated in this study. In above section 4.2.1, seasonal comparison of the overall spectrum of primary source factors HOA and BBOA has been exhibited in Table 4-3 and Table 4-4. The HOA factors show less seasonal variation with spectrum correlation R^2 ranging from 0.75 to 0.99 and theta ranging from 0° to 28.87°, while the pronounced seasonal variation of factor spectrum of biomass burning could be observed with spectrum R^2 ranging from 0.49 to 0.81 and theta ranging from 24.62° to 43.83°. That seasonal behavior of source factor spectrum means traffic exhausts emission represented by HOA factor is compositionally stable during the whole JULIAC year.

On the contrary, the source property of biomass burning shows a clear seasonal variation which might be related to seasonal changed biomass burning types. As shown in wildfire counts map Figure A 15, the densest wildfire counts around the site were observed by satellite during spring, and enhanced wildfire emission might be related to the low spectra similarity of BBOA factors between the spring and the rest seasons. As introduced in section 2.1.1, the Jülich sugar factory compact works during November and December every year which might cause different BBOA spectrum during autumn. In addition, increase residential heating during winter and autumn might also contribute to different BBOA spectra.

In terms of OOA seasonal variation, LO-OOA and MO-OOA factor spectra resolved at each season have been compared in Table 4-5 and show high overall similarity with spectrum R^2 equal to 0.91 to 0.98 and theta ranging from 1.72° to 17.82°. However, that spectrum consistency of LO-OOA and MO-OOA doesn't mean a consistent reaction mechanism but is more related to the same dominated fragments m/z 44 and m/z 28 of LO-OOA and MO-OOA.

And for the OA from NO_3-initiated nocturnal oxidation resolved as NO-OOA factor, the detailed discussion of seasonal changes of VOCs precursors has been given in section 4.4.3, which conclude BVOCs leads NO_3-initiated nocturnal oxidation during summer and bbVOCs dominate NO_3-initiated nocturnal oxidation during the rest seasons. That seasonal-dependent precursor of NO-OOA is also reflected in the overall factor spectrum as shown in Table 4-11. The spectra of Nbb-OOA factors determined at different JULIAC phases show high similarity with cross-correlation R^2 ranging from 0.90 to 0.99 and theta ranging from 5.18° to 17.33° while showing less similarity with NB-OOA with R^2 ranging from 0.60 to 0.70 and theta ranging from 32.00° to 35.97°.

Table 4-11: Overview of amounts of cross-correlation analysis (R^2 and theta angle) between NO-OOA factors of the JULIAC campaign, chamber simulated OOA based on biomass burning emission and NO_3 (NO_2+O_3) dark oxidation, and ambient OOA factor with clear night enhancement. The background colors of the coefficient cell are color scales following the value of R^2, and utilize red represents the highest value 1 and green as the lowest value 0

R^2 / Theta	**Nbb-OOA _JULIAC-I**	**Nbb-OOA _JULIAC-II**	**Nbb-OOA _JULIAC-IV**	**NB-OOA _JULIAC-III**	**Reference**
Nbb-OOA_JULIAC-I	1.00 / 0°	0.90 / 17.33°	0.99 / 5.18°	0.70 / 32.00°	this study
Nbb-OOA_JULIAC-II	0.90 / 17.33°	1.00 / 0°	0.94 / 13.19°	0.60 / 35.97°	this study
Nbb-OOA_JULIAC-IV	0.99 / 5.18°	0.94 / 13.19°	1.00 / 0°	0.68 / 33.03°	this study
NB-OOA_JULIAC-III	0.70 / 32.00°	0.60 / 35.97°	0.68 / 33.03°	1.00 / 0°	this study
Chamber OOA (bbOA+NO_3·)	0.92 / 15.07°	0.87 / 19.88°	0.92 / 15.32°	0.76 / 26.50°	(Kodros et al., 2020)
Athens OOA	0.89 / 18.10°	0.68 / 32.45°	0.84 / 21.78°	0.72 / 29.30°	(Florou et al., 2017)
OOA-b Saarikoski	0.97 / 9.57°	0.85 / 21.62°	0.95 / 12.01°	0.71 / 26.79°	(Saarikoski et al., 2012)

In conclusion, primary emission source HOA shows seasonal stable source property, while biomass burning source BBOA exhibits seasonal dependent source characterization mainly due to seasonal changed emission types. Secondary daytime oxidation OA source, LO-OOA (for the JULIAC-II and III) and MO-OOA (for the JULIAC-I and IV) shows a similar factor spectrum of all seasons with the same major fragments of m/z 44 and m/z 28. The NO_3-initiated nocturnal oxidation OA source NO-OOA shows clear factor spectrum difference related to the seasonal variation of dominant VOCs precursors of nocturnal oxidation.

4.5.3.2 Seasonal variations of oxidation degree of OA factors

In the above section, the seasonal variation of the overall factor spectrum has been discussed. To further investigate the seasonal difference of OA source factors and OA evolution paths, the oxidation degree of all PMF source factors determined in this study has been displayed in fCO_2^+ (fraction of fragment CO_2^+ in OA) vs $fC_2H_3O^+$ (fraction of fragment $C_2H_3O^+$ in OA) space as shown in Figure 4-40 and Figure 4-41.

For primary emission, the HOA and BBOA are located at the left corner of fCO_2^+ vs $fC_2H_3O^+$ space with both lower values of fCO_2^+ and $fC_2H_3O^+$, which is comparable to the features of primary source factors reported in previous studies (Sun et al., 2012, Crippa et al., 2013b, Chen et al., 2015, Zhang et al., 2015b). The seasonal variation of biomass burning emission is also shown by the relatively scattered distribution of BBOA factors in this graph. BBOA factor resolved at JULIAC-II shows a distinct location in fCO_2^+ vs $fC_2H_3O^+$ space with the highest $fC_2H_3O^+$ compared to the rest BBOA which also supports the speculation in 4.5.3.1 about different biomass burning types (possible increased wildfire) during spring.

For LO-OOA and MO-OOA factors, even though no clear seasonal difference of overall factor spectra was found in section 4.2.2, clear seasonal variation of source factor oxidation degree could be illustrated in Figure 4-40. LO-OOA factors of the JULIAC-II and the JULIAC-III located at a position with relatively higher $fC_2H_3O^+$ but lower fCO_2^+ compared to MO-OOA factors of the JULIAC-I and the JULIAC-IV, which imply a stronger fresh SOA formation during the JULIAC-II and III compared to the JULIAC-I and IV. That lowest oxidation degree of LO-OOA appearing during the JULIAC-III is consistent with the lowest overall organic aerosol oxidation degree discussed in section 4.5.1.

Concerning the nocturnal oxidation OA source, NO-OOA (Nbb-OOA) factor during the JULIAC-I, II, and IV located in space close to each other but only NO-OOA (NB-OOA) during the JULIAC-III show a remarkable difference with the lowest $fC_2H_3O^+$ and fCO_2^+ compared to the rest JULIAC phases. That distinct oxidation degree of NB-OOA compared to Nbb-OOA factor agree with the conclusion of seasonal dependent precursors for NO_3-initiated dark oxidation in section 4.4.3. The horizontal movement of OOA data in this fCO_2^+ vs $fC_2H_3O^+$ space was reported to be mainly driven by biogenic emissions (Canonaco et al., 2015), which further supports that nocturnal oxidation during summer was mainly dominated by BVOCs.

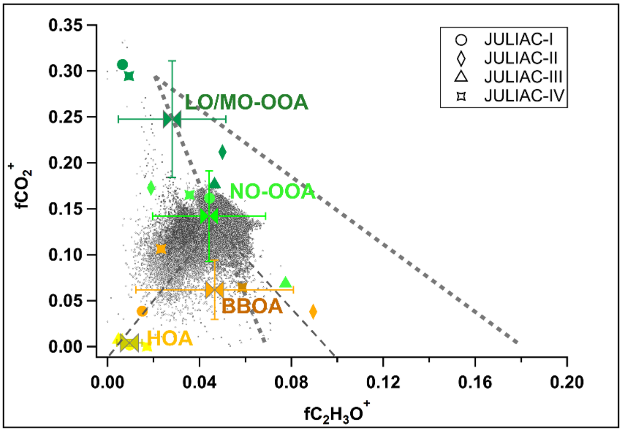

Figure 4-40: fCO_2^+ (fraction of fragment CO_2^+ in OA) vs $fC_2H_3O^+$ (fraction of fragment $C_2H_3O^+$ in OA) for all raw organic aerosols during the JULIAC campaign were displayed by the gray dots. And the OA source factors (including LO/MO-OOA, NO-OOA, BBOA, HOA, except regional transport factors) resolved by PMF during each JULIAC phase were also exhibited in fCO_2^+ vs $fC_2H_3O^+$ space with marker type representing phases and marker color standing for factor type. Means value and stand derivation error bar for these four types of source factors are also displayed. The coarser dash lines represent the f44/f43 distribution triangular region of ambient OOA factors reported in (Ng et al., 2010)

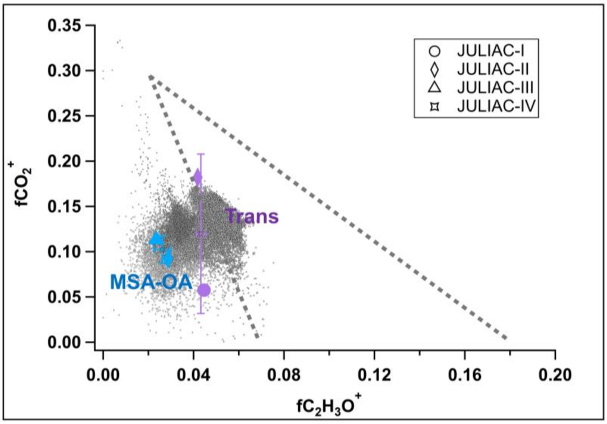

Figure 4-41: fCO_2^+ (fraction of fragment CO_2^+ in OA) vs $fC_2H_3O^+$ (fraction of fragment $C_2H_3O^+$ in OA) for all raw organic aerosols during the JULIAC campaign were displayed by the gray dots. And two types of regional transport OA source factors (MSA-OA and Trans-OA factors) resolved by PMF during each JULIAC phase were also exhibited in fCO_2^+ vs $fC_2H_3O^+$ space with marker type representing phases and marker color standing for factor type. Means value and stand derivation error bar for these four types of source factors are also displayed. The coarser dash lines represent the f44/f43 distribution triangular region of ambient OOA factors reported in (Ng et al., 2010)

As shown in Figure 4-41, the scattered distribution of all regional transport OA factors in fCO_2^+ vs $fC_2H_3O^+$ space show pronounced seasonal differences. But for the regional transport OA factor, that seasonal difference is less related to seasonal dependent emission or reaction path but mainly related to the meteorological condition (as shown in Figure 4-11) and the trajectory of the transported plume. For example, although OA of the JULIAC-II and the JULIAC-III show an apparent seasonal difference in both local primary emission and secondary sources as discussed above, two MSA-OA factors found during these two phases still show close location in fCO_2^+ vs $fC_2H_3O^+$ space because of the same marine plume regional transport. Therefore, the source properties of regional transport OA are more origin-dependent rather than seasonal-dependent. As mentioned in 4.3, although the MSA-OA factor is defined as the marine plume transport factor, the overall source factors still can vary to some degree because of changed plume transport parameters (like regional transport time, ambient temperature). Therefore, characteristic ions of the MSA-OA factor could be commonly used to determine the MSA-OA factor but the whole MSA-OA spectrum correlation or prior MSA-OA factor constrain PMF analysis are not suggested to be utilized to determine marine OA transport.

In conclusion, the seasonal differences of OA are mainly investigated in terms of the OA oxidation degree, OA source contribution, and OA sources spectrum properties. For primary sources, the traffic exhaust source represented by HOA shows stable source properties and minor OA contributions. In the contrast, the OA contribution fraction and source spectrum of biomass burning sources (BBOA) are both show clear seasonal variations which are related to seasonal-dependent biomass burning types (like industry, residential heating). For secondary OOA sources, daytime (LO-OOA and MO-OOA) and nighttime oxidation (NO-OOA) are major OA sources in this study. And their seasonal variation of source properties is mainly related to the major precursors and formation mechanisms. For regional transport OA (MSA-OA+Trans-OA), the source properties of regional transport OA are more origin-dependent rather than seasonal-dependent.

Chapter 5 Summary and Outlook

During the year-long JULIAC campaign, pronounced seasonal variations of submicron particles (PM1) concentration and composition were measured and investigated. In this study, submicron aerosol mass concentrations show the yearly average of 4.0 μg/m^3 and reach the maximum (7.68± 4.82 μg/m^3) in summer and the minimum (1.05±0.98 μg/m^3) in winter. That overall aerosol level is lower than the annual mean value of 5 μg/m^3 of WHO PMF$_{2.5}$ air quality guidelines (Organization et al., 2021), which means the relatively low health risk from aerosols in this region.

For seasonal comparison of aerosol inorganic species, the mass fractions of aerosol nitrate range from 5.3 % in summer to 25.9 % in winter, which might relate to volatility-dependent evaporation and regional transport. The concentration of aerosol sulfate shows the biggest seasonal differences and peaked in summer with active local contribution (probably photochemical paths).

Aerosol organics are the major aerosol species during the whole JULIAC campaign accounting for 39.0% (winter) to 57.6% (summer) of total aerosol mass. The yearly lowest oxidation degree (averaged O:C value of 0.64) of OA is observed during summer and suggests a strong biogenic derived SOA formation. OA seasonal source appointment analysis shows that biomass burning emission is the major anthropogenic OA source in this site, and biomass burning related OA (primary and secondary) accounts for 60.1% to 82.6% of total OA mass during autumn and winter. That implies during the cold period, the biomass burning sources control (like residential heating, industry) should be the core part for air pollution mitigation, and the risk of respiratory and cardiovascular diseases due to biomass burning emission might increase (Karanasiou et al., 2021). In addition, the other primary anthropogenic emission, traffic emission (HOA) only makes a minor OA contribution (3%-9.5%) during the whole year.

For OA secondary sources, OA originated from daytime oxidation (LO-OOA, MO-OOA) and nocturnal oxidation (NO-OOA) accounts for 46% to 88% of the total OA mass during the whole JULIAC year. OA contribution from daytime oxidation especially photooxidation path was resolved as LO-OOA factor for the JULIAC-II and III accounting from 38.2%-58.2% of OA mass and as MO-OOA for the JULIAC-I and IV contributing 11.3% -11.8% of OA mass. The seasonal difference of OA contribution and factor characteristics between LO-OOA and MO-OOA imply a stronger daytime OOA formation during spring and summer due to abundant biogenic emissions.

Appendix

The NO-OOA was resolved by PMF analysis for the first time and illustrates the significant OA contribution from NO_3-initiated dark oxidation. The nocturnal OA formed from NO_3-initiated oxidation contribute to 20.9% to 48.4% of the total OA mass, and that fraction is comparable to the suggested dark OA contribution proportion in previous lab and model studies (Russell 2005, Pye et al., 2010, Xu et al., 2015b, Kodros et al., 2020). A stronger OA contribution of NO_3-initiated dark oxidation compared to that of daytime oxidation is found during winter and autumn, which implies NO_3-initiated dark oxidation possibly dominate OOA formation during the cold period. The resolving of the NO_3-initiated nocturnal OA contribution in this study has significance not only in completing the missing OA contribution of nocturnal chemistry for field aerosol source apportionment analysis but also in benefiting the further understanding of nocturnal chemistry mechanism, modeling and predicting global aerosol budget and SOA yield.

For a detailed dark oxidation mechanism, $NO_3\cdot$ is confirmed to be the major oxidant for dark OA formation instead of O_3 due to chemical components (e.g., aerosol organic nitrate) and reaction kinetics discussion. In addition, two sub-NO-OOA factors, NB-OOA and Nbb-OOA are introduced to illustrate the seasonal-dependent precursors of NO_3-initiated dark oxidation. The Nbb-OOA factor determined during the JULIAC-I, JULIAC-II, and JULIAC-IV present the OA formation mainly from bbVOCs dominated NO_3-initiated nocturnal oxidation, while the OA contribution of NB-OOA determined during the JULIAC-III (summer) is mainly contributed by BVOCs (especially monoterpene) derived NO_3-initiated nocturnal chemistry. In addition, the high value (0.88) of biomass burning related OA contribution proportion between dark secondary formation (Nbb-OOA) and primary emission (BBOA) illustrate that the dark secondary path is equally important as primary emission in terms of biomass burning related OA contribution. Therefore, NOx emission and biomass burning emission control, especially during the cold period, possibly benefit the mitigation of secondary aerosol formed from NO_3-initiated dark oxidation.

Regional OA transports from both marine (MSA-OA) and continental regions (Trans-OA) have been resolved during the JULIAC campaign and account for 8.6%-18.6% mass fractions of OA. Marine OA transport (MSA-OA) is found at this non-coastal site during the JULIAC-II, and III, and OA mass fraction contributed by MSA-OA is demonstrated to be a good indicator for marine transport. However, PMF algorithms could effectively resolve plume transport with characteristic components (like MSA, HN_4NO_3) in this study but show limitations in parsing continuous and directional plume transport with analogous species (compared to local background). The unresolved high local aerosol MSA concentration during summer still deserves further investigation to interpret unknown local MSA formation mechanisms.

For OA sources seasonal comparison, the traffic exhaust source (resolved as HOA) shows stable source properties while biomass burning source (BBOA) shows clear seasonal changed factor spectra and OA contribution probably related to seasonal-dependent biomass burning types (like industry, residential heating). For secondary sources, the source properties of daytime (LO-OOA and MO-OOA) and nighttime oxidation (NO-OOA) are mainly related to formation mechanisms, such as oxidant and VOCs precursors. For regional transport OA (MSA-OA+Trans-OA), the source properties of regional transport OA are more origin-dependent rather than seasonal-dependent.

For future aerosol sources study, more attention should be drawn to the potential aerosol contribution from NO_3-initiated nocturnal oxidation. The resolving and comparison of the NO-OOA factor in diverse aerosol field measurements will be valuable to investigate the potential contribution and implication of nocturnal chemistry in the real atmosphere. More chamber experiments for NO_3 derived dark oxidation with various precursors (including both anthropogenic VOCs and BVOCs) under different conditions (e.g., RH, temperature) will be helpful to further investigate the mechanism of NO_3-initiated nocturnal OA formation. The comparison between NO_3-initiated SOA yield between model and filed measurements also deserves to be explored for further model improvement.

Appendix

Appendix A

A. 1 Aerosol transmission loss of the JULIAC inlet system

Inlet system of the JULIAC campaign (like 50-meter tower, blower) would inevitably cause particle loss to some degree. Therefore, the JULIAC inlet system testing was done to well determine the potential effect of the JULIAC inlet system on atmospheric chemical composition before the JULIAC campaign started. The basic setup of inlet system testing is switching all instruments sampling lines between the JULIAC inlet line and 2-m ambient air sampling line every half hour and comparing results' difference detected from these two inlet lines. The aerosol concentration and chemical composition comparison between the JULIAC inlet system and the 2-m ambient inlet was displayed in Figure A 1. Higher particle concentration was detected from the 2-m ambient inlet compared to that from the JULIAC inlet system, which may relate to transition loss in the JULIAC inlet system. For aerosol chemical composition comparison, nitrate and ammonium were significantly higher in 2-m ambient inlet detection, while organics and sulfate concentration were quite comparable between two inlet systems detections. That different behavior of aerosol species in inlet system tests may be caused by the high loss ratio of nitrate and ammonium or related to near ground emission of ammonium nitrate.

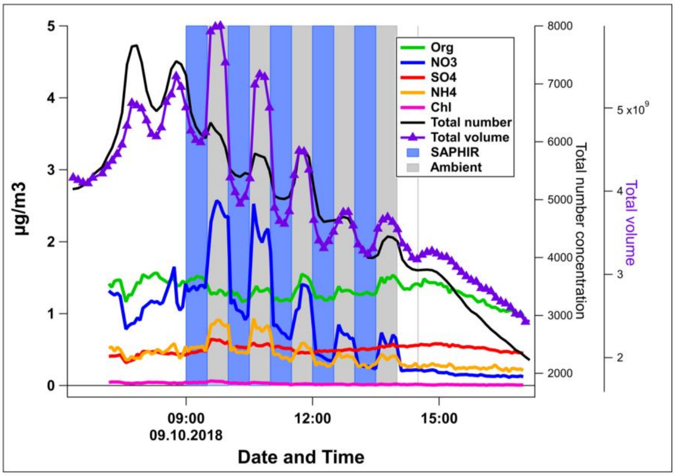

Figure A 1: Comparison of chemical composition and physical properties of aerosol between 2- meters-height ambient air measurement and SAPHIR measurement under the JULIAC setup

For further developing the inlet system effect on aerosol properties, the size-dependent chemical composition of aerosol between 2-meters ambient inlet and the JULIAC inlet system were compared in Figure A 2. Similar particle size distributions were found for aerosol species between two inlet systems' detection. Based on that, one could estimate that the JULIAC inlet line did not seem to generate extra particles. In conclusion, the JULIAC inlet line system showed a slight effect on aerosol organics and sulfate concentration and did not significantly change aerosol size-dependent chemical composition. However, aerosol nitrate and ammonium difference between two inlets measurement still can't be distinguished from aerosol loss in the inlet system and near-ground emission effect yet.

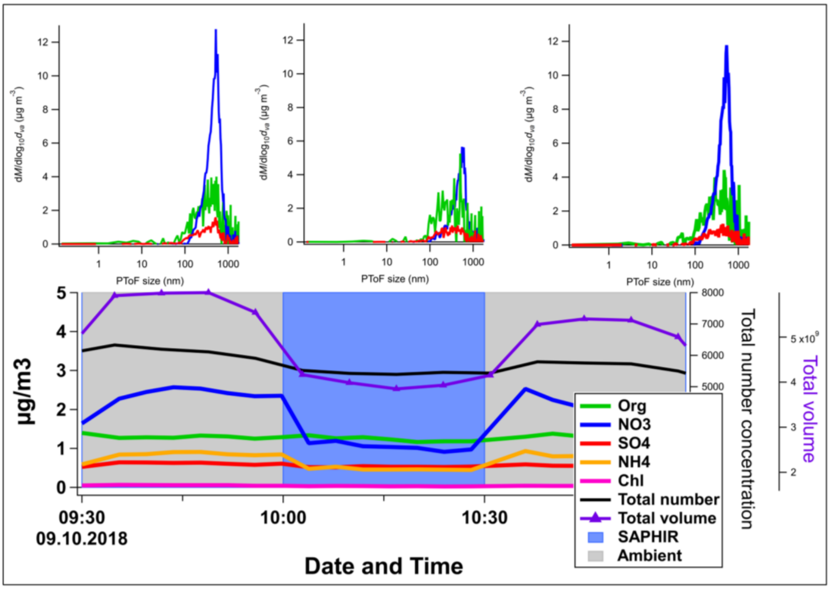

Figure A 2: Comparison of the size-dependent chemical composition of aerosol between 2 meters height ambient air measurement and SAPHIR measurement with the JULIAC setup

A. 2 Aerosol wall loss of the SAPHIR chamber

For well understanding of ambient aerosol level with data of the JULIAC campaign, wall loss of the SAPHIR chamber need to be considered in case underestimates ambient aerosol concentration. A set of batch mode SAPHIR experiments were done during the JULIAC break time slot, which had a smooth decay line of aerosol concentration after 5-8 hours sufficient reaction of injected reactants. The aerosol decay period of these batch-mode experiments was only related to synthetic air dilution and aerosol wall loss, and basic SAPHIR setup, like fans speed, is keeping with the JULIAC campaign. Therefore, four batch mode experiments were used to estimate aerosol wall loss during the JULIAC campaign and their detailed information were all listed in Table A 1.

Appendix

$$y = y_0 + Aexp\left\{\frac{-(x-x_0)}{\tau}\right\} \qquad \text{Eq. 25}$$

$$\frac{dy}{dx} = \frac{1}{\tau} * \ Aexp\left\{\frac{-(x-x_0)}{\tau}\right\} \qquad \text{Eq. 26}$$

$$\frac{dy}{dx} = -\frac{y}{\tau} + \frac{y_0}{\tau} \qquad \text{Eq. 27}$$

$$Dilution\ effect = \frac{dV*y}{\mathrm{dt*Vsaphir}} \qquad \text{Eq. 28}$$

As shown in Figure A left), the decay line of aerosol concentration during the SAPHIR chamber experiment under batch mode on July 5th, 2019 was given as an example. Exponential X-offset fitting (as Eq. 25) was applied from 12:00 (UTC) when the aerosol boosting experiment in the chamber was fully completed. Aerosol decay speed equation Eq. 27 was transformed from Eq. 25 and its derivation equation Eq. 26. Therefore, -1/ τ is equal to the rate constant (K) of aerosol decay, composed of wall loss and dilution effect. The dilution effect of the SAPHIR chamber could be evaluated based on Eq. 28, in which dV means the flow of supplement synthetic air ($20 m^3/h$) and Vsaphir means the size of the SAPHIR chamber ($270 m^3$). Therefore, the rate constant of dilution effect was determined as $-2.06e^{-5}$, and then the wall loss rate constant of SAPHIR could be estimated.

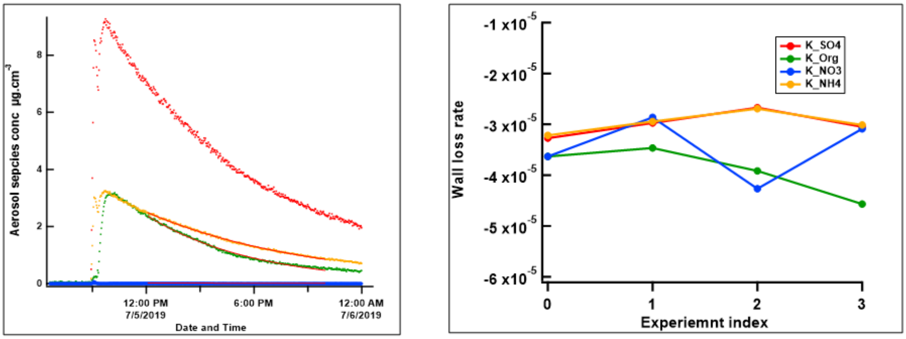

Figure A: Left), a data set example of aerosol decay time series caused by wall loss and synthetic air dilution with exponential X-offset fitting. Right) Variations of aerosol wall loss rate of sulfate, organics, nitrate, and ammonium among four independent bath-mode experiments in the SAPHIR chamber τ values of exponential X-offset fitting and rate constants (k) of aerosol species' decay for four independent bath-mode experiments in the SAPHIR chamber were listed in Table A 1. The good stability and comparable value of aerosol species' decay could be illustrated in Figure A right). After removing the dilution effect from the average value of the rate constant of aerosol decay, aerosol wall loss of the SAPHIR chamber was finally estimated as -0.99e^{-5} which is small enough to ignore.

Table A 1: Tau values of exponential X-offset fitting and calculated aerosol species wall loss rate constant of four independent bath-mode experiments in the SAPHIR chamber.

Index	**Date**	$\tau_{(SO4)}$	$k_{(SO4)}$	$\tau_{(Org)}$	$k_{(Org)}$	$\tau_{(NH4)}$	$k_{(NH4)}$	$\tau_{(NO3)}$	$k_{(NO3)}$
0	2019-06-27	30554	-3.27E-05	27530	-3.63E-05	31072	-3.22E-05	27512	-3.63E-05
1	2019- 06-28	33622	-2.97E-05	28856	-3.47E-05	33946	-2.95E-05	34917	-2.86E-05
2	2019-06-30	37423	-2.67E-05	25531	-3.92E-05	37122	-2.69E-05	23434	-4.27E-05
3	2019-07-05	32787	-3.05E-05	21891	-4.57E-05	33185	-3.01E-05	32386	-3.09E-05
AVERAGE			-2.99E-05		-3.90E-05		-2.97E-05		-3.46E-05

A. 3 Diagnostic and calibration parameters of AMS

Table A 2: diagnostic parameters and ionization calibration coefficient overview of two HR-ToF-AMS during the whole JULIAC campaign. Single ion (SI) value is used to convert MS signal intensity to units of mass concentration. In this study, airbeam means the ion intensity of 28 (N_2^+). Ionization Efficiency/ Airbeam (IE/AB) reflects the sensitivity of the instrument and is a key parameter to evaluate if an IE/AB correction is needed.

Date	Instrument	Single Ion before	Single Ion after	Ionization Efficiency	Airbeam_VMS/Hz	Airbeam_V-PTOF/ Hz	Ionization Efficiency/ Airbeam (IE/AB)
2019.01.14	AMS_1	12.3	12.9	4.59E-08	1.32E+05	2.60E+05	3.48E-13
2019.02.22	AMS_1	12.3	12.8	9.05E-08	2.03E+05	---	4.46E-13
2019.04.01	AMS_1	12.9	13.4	9.50E-08	2.04E+05	4.00E+05	4.66E-13
2019.04.05	AMS_1	12.9	12.1	7.50E-08	1.64E+05	3.30E+05	4.57E-13
2019.04.08	AMS_1	12.1	12.1	7.50E-08	2.03E+05	4.10E+05	3.69458E-13
2019.04.11	AMS_1	12.1	12.6	7.50E-08	2.31E+05	4.61E+05	3.24675E-13
2019.04.24	AMS_1	12.6	12.4	1.03E-07	2.32E+05	5.10E+05	4.43966E-13
2019.06.19	AMS_2	16.1	16.1	4.68E-08	5.99E+04	5.40E+04	7.81302E-13
2019.07.02	AMS_2	16.1	15.6	1.02E-07	1.09E+05	1.10E+05	9.3578E-13
2019.07.15	AMS_2	15.6	12	9.75E-08	1.03E+05	1.10E+05	9.46602E-13

2019.08.09	AMS_2	12.2	13.5	8.47E-08	9.54E+05	1.10E+05	8.87841E-14
2019.08.21	AMS_2	13.7	12.3	1.12E-07	1.62E+05	1.70E+05	6.93827E-13
2019.09.04	AMS_2	12.3	12.7	1.29E-07	1.67E+05	1.70E+05	7.69461E-13
2019.09.20	AMS_2	8.6	8.6	8.18E-08	1.02E+05	1.10E+05	8.01569E-13
2019.11.18	AMS_2	16.3	15.6	1.03E-07	1.39E+05	1.50E+10	7.38129E-13

A. 4 Aerosol composition overview during the JULIAC

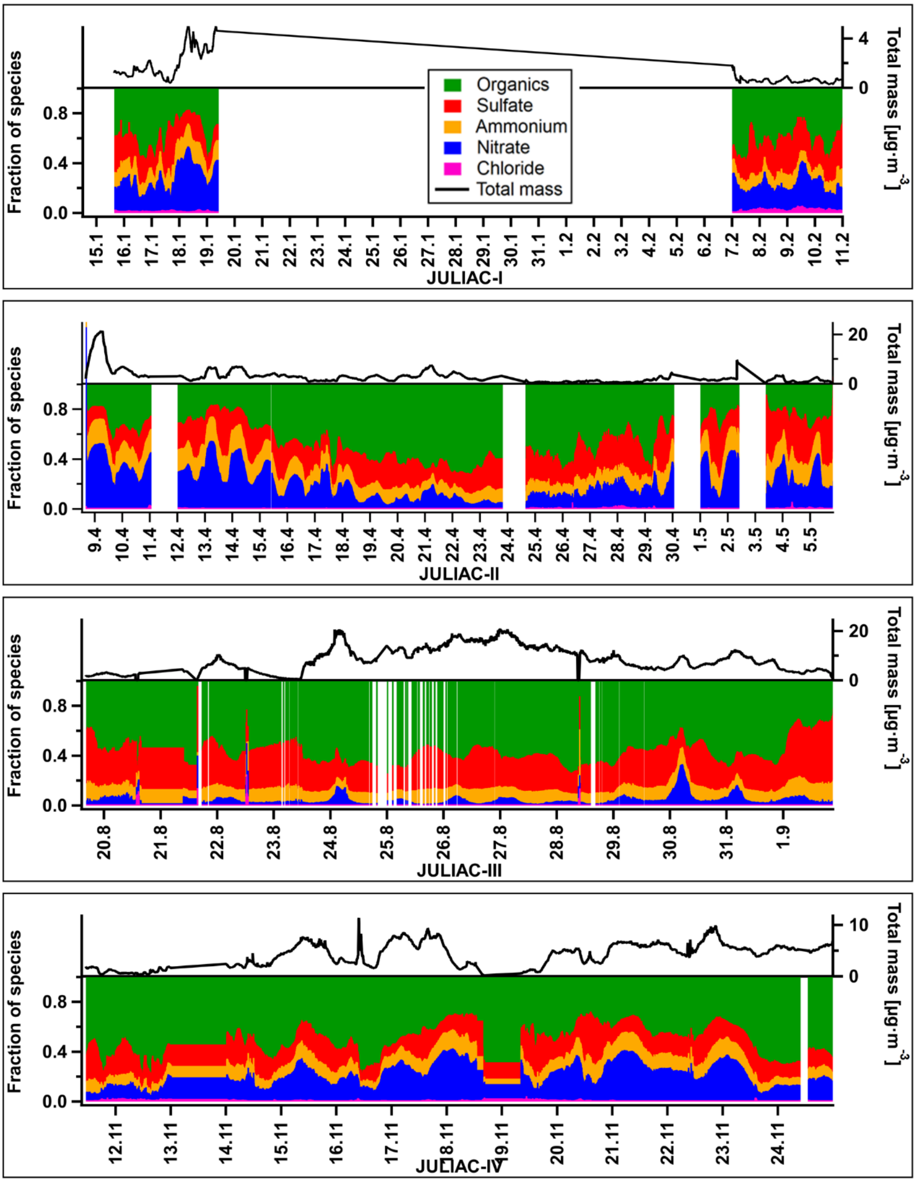

Figure A 3: the time-series of aerosol total mass concentration and aerosol species' fraction for all JULIAC intensive measurements.

A. 5 MSA-OA supplement

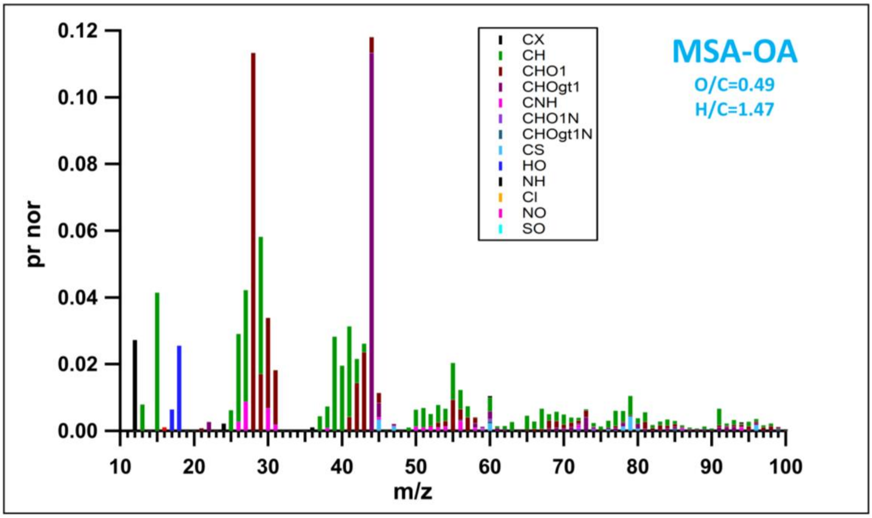

Figure A 4: MSA-OA factor profile separated by PMF during the JULIAC-III phase in this study. Normalized ions attribution in factor profile are colored by corresponding ion family groups, and elemental ratios (O/C. H/C) of MSA-OA factor are also marked in the graph. The y-axis presents the ion signal intensity fraction while the x-axis range is m/z (mass to charge) 10-100

Table A 3: the cross-correlation analysis (R^2 and theta angle) of MSA-OA spectrum among seasonal MSA-OA resolved in four JULIAC phases and MSA-OA factor reported in previous PMF studies.

R^2, Theta	MSA-OA_JULIAC-II	MSA-OA_JULIAC-III	Reference
MSA-OA_JULIAC-II	1, 0	0.60, 35.2	JULIAC-II
MSA-OA_JULIAC-III	0.60, 35.2	1, 0	JULIAC-III
MSA-OA_Schlag	0.84, 23.9	0.70, 30	(Schlag et al., 2017)
MSA-OA_schmale	0.25, 54.3	0,61.6	(Schmale et al., 2013)
MSA-OA_Mace_head	0.35, 53.2	0, 63.4	(Crippa et al., 2014)

A. 6 Ions list for AMS HR analysis

Table A 4: Manually chosen ions and their assign to families for the whole JULIAC campaign high-resolution AMS data treatment.

HR ions	Mass	Family	HR ions	Mass	Family	HR ions	Mass	Family
C	12	Cx	C5H2O	78.01056671	CHO1	C3H7O5	123.0294037	CHOgt1
j13C	13.00335979	Cx	j13CCH5O3	78.02722168	CHOgt1	C6H5NO2	123.0319977	CHOgt1N
CH	13.00782013	CH	C2H6O3	78.0316925	CHOgt1	C7H7O2	123.0446014	CHOgt1

N	14.00306988	Air	C6H6	78.04695129	CH	C8H11O	123.0810013	CHO1
j13CH	14.01117992	CH	j13CC2H9O2	78.06360626	CHOgt1	C9H15	123.1174011	CH
j15N	15.00010967	Air	Br	78.91832733	Other	j13CC5H3O3	124.0115738	CHOgt1
NH	15.01089954	NH	CHj34SO2	78.96552277	CS	C6H4O3	124.0159988	CHOgt1
CH3	15.02346992	CH	j13CH2SO2	78.98090363	CS	j13CC2H7O5	124.0326996	CHOgt1
O	15.99491978	Air	CH3SO2	78.98536682	CS	j13CC5H5NO2	124.0353928	CHOgt1N
NH2	16.01872063	NH	C2H4j34Sj17O	78.99829865	CS	C7H8O2	124.0523987	CHOgt1
j13CH3	16.02683067	CH	j13CC4H2O	79.01392365	CHO1	C8H12O	124.0887985	CHO1
HO	17.00274086	HO	C5H3O	79.01838684	CHO1	C9H16	124.1251984	CH
j15NH2	17.01576042	NH	j13CCH6O3	79.03504944	CHOgt1	C6H5O3	125.0239029	CHOgt1
NH3	17.02655029	NH	C6H7	79.05477142	CH	C3H7j18OO4	125.0335922	CHOgt1
j18O	17.99916077	Air	O2Ti	79.93777624	Other	C7H9O2	125.0603027	CHOgt1
H2O	18.01055908	HO	SO3	79.95681763	SO	C8H13O	125.0966034	CHO1
j15NH3	18.02358055	NH	CH2j34SO2	79.9733429	CS	C9H17	125.1330032	CH
NH4	18.03437042	NH	j13CH3SO2	79.98873138	CS	j126Xe	125.9042664	Other
F	18.99839973	Other	C4O2	79.98983002	CHOgt1	C6H6O3	126.0317001	CHOgt1
Hj18O	19.0069809	HO	j13CC4H3O	80.02174377	CHO1	C10H6	126.0469971	CH
j2HHO	19.01683998	HO	C5H4O	80.02620697	CHO1	C7H10O2	126.0681	CHOgt1
H3O	19.01839066	HO	C6H8	80.06259918	CH	C8H14O	126.1044998	CHO1
Arplus2	19.98118973	Air	j81Br	80.91629028	Other	C9H18	126.1408997	CH
H2j18O	20.01481056	HO	HSO3	80.96463776	SO	I	126.9044647	Other
j2HH2O	20.02466965	HO	CH3j34SO2	80.98117065	CS	C6H7O3	127.0394974	CHOgt1
HNe	21.00027084	Other	j13CC3O2	80.99318695	CHOgt1	C10H7	127.0548019	CH
N3plus2	21.00461006	Other	C4HO2	80.99765778	CHOgt1	C7H11O2	127.0758972	CHOgt1
C2H2Oplus2	21.00527954	CHO1	j13CC4H4O	81.02957153	CHO1	j13CC7H14O	127.1078186	CHO1
H3j18O	21.02264023	HO	C5H5O	81.03404236	CHO1	C8H15O	127.1122971	CHO1
CO2plus2	21.99492073	CHOgt1	C6H9	81.07042694	CH	C9H19	127.1486969	CH
Na	22.98977089	Other	CCl2	81.93771362	Other	j128Xe	127.9035339	Other
Hj22Ne	22.99921036	Other	j34SO3	81.9526062	SO	j13CC5H7O3	128.0428772	CHOgt1
OLi	23.01091872	Other	Hj33SO3	81.9640274	SO	C6H8O3	128.0473022	CHOgt1
SOplus2	23.98348999	SO	H2SO3	81.97247314	SO	j13CC9H7	128.058136	CH
C2	24	Cx	C4H2O2	82.00547791	CHOgt1	C10H8	128.0626068	CH
j34SOplus2	24.98139	SO	j13CC4H5O	82.03739166	CHO1	j13CC6H11O2	128.0792542	CHOgt1
j13CC	25.00336075	Cx	C5H6O	82.04186249	CHO1	C7H12O2	128.0836945	CHOgt1
C2H	25.00782967	CH	C6H10	82.07824707	CH	j13CC7H15O	128.1156464	CHO1
CN	26.00307083	CHN	j13CCl2	82.94106293	Other	j13CC8H19	128.1520233	CH
j13CCH	26.01118088	CH	Hj34SO3	82.96042633	SO	C4H3NO4	129.0061951	CHOgt1N
C2H2	26.0156498	CH	C4H3O2	83.01331329	CHOgt1	C9H5O	129.0339966	CHO1
Cj15N	27.00011063	CHN	C5H7O	83.04969025	CHO1	j13CC5H8O3	129.050705	CHOgt1
j13CN	27.00642967	CHN	C6H11	83.0860672	CH	C6H9O3	129.0552063	CHOgt1
CHN	27.0109005	CHN	Kr	83.91150665	Other	j13CC9H8	129.0659027	CH
j13CCH2	27.0189991	CH	j85Sr	83.91342926	Other	C10H9	129.0704041	CH
C2H3	27.02347946	CH	Cj37ClCl	83.93475342	Other	j13CC6H12O2	129.0870819	CHOgt1
N2	28.00614929	Air	C4H4O2	84.02113342	CHOgt1	C7H13O2	129.0915985	CHOgt1
j13CHN	28.0142498	CHN	C5H8O	84.05751801	CHO1	Te	129.9062195	Other
CHO	29.00274086	CHO1	C6H12	84.09390259	CH	j13CC3H3NO4	130.0095673	CHOgt1N
j15NN	29.00317955	Air	Rb	84.91178894	Other	j13CC8H5O	130.0373993	CHO1
C2H5	29.03912926	CH	C3HSO	84.97480774	CS	C9H6O	130.0419006	CHO1
NO	29.99798965	NO	C3H3NO2	85.01638031	CHOgt1N	j13CC5H9O3	130.0585175	CHOgt1
j13CHO	30.00609016	CHO1	C4H5O2	85.02895355	CHOgt1	j13CC9H9	130.0737762	CH
CH2O	30.01055908	CHO1	C5H9O	85.06533813	CHO1	C10H10	130.0782013	CH

Appendix

CH4N	30.03437042	CHN	C6H13	85.10172272	CH	j13CC6H13O2	130.0949097	CHOgt1
j13CCH5	30.04248047	CH	j86Sr	85.90926361	Other	C8H3O2	131.0133057	CHOgt1
j15NO	30.99501991	NO	Cj37Cl2	85.93180847	Other	j13CC8H6O	131.0452271	CHO1
HNO	31.00580978	NO	j13CC2HSO	85.97816467	CS	C9H7O	131.0496979	CHO1
CHj18O	31.0069809	CHO1	C3H2SO	85.9826355	CS	j13CC9H10	131.081604	CH
j13CH2O	31.01391983	CHO1	C7H2	86.01564789	CH	C10H11	131.0861053	CH
CH3O	31.01839066	CHO1	j13CC2H3NO2	86.01972961	CHOgt1N	Xe	131.9041595	Other
CH4j15N	31.03141022	CHN	C4H6O2	86.03678131	CHOgt1	j13CC7H3O2	132.0166626	CHOgt1
j13CH4N	31.03772926	CHN	C5H10O	86.07317352	CHO1	C8H4O2	132.0211029	CHOgt1
CH5N	31.04220009	CHN	C5H12N	86.09697723	CHN	j13CC8H7O	132.0529938	CHO1
O2	31.98983002	Air	C6H14	86.10955048	CH	C9H8O	132.0574951	CHO1
Nj18O	32.00223923	NO	j87Sr	86.90888214	Other	j13CC9H11	132.0894318	CH
CH2j18O	32.01480865	CHO1	j87Rb	86.90917969	Other	C10H12	132.0939026	CH
j13CH3O	32.02174377	CHO1	C3Hj34SO	86.97060394	CS	Cs	132.9054413	Other
CH5j15N	32.03923035	CHN	j13CC2H2SO	86.98599243	CS	C4H5O5	133.0137024	CHOgt1
j13CH5N	32.04555511	CHN	C3H3O3	87.00821686	CHOgt1	j13CC7H4O2	133.0244904	CHOgt1
HS	32.97990036	Other	C7H3	87.02348328	CH	C8H5O2	133.029007	CHOgt1
j17OO	32.99404907	Air	C4H7O2	87.04460144	CHOgt1	j13CC8H8O	133.0608673	CHO1
H3NO	33.02146912	NO	C5H11O	87.08099365	CHO1	C9H9O	133.0653076	CHO1
CH3j18O	33.02264023	CHO1	Sr	87.90561676	Other	j13CC9H12	133.0972595	CH
Hj33S	33.97927856	Other	C3Hj34Sj17O	87.974823	CS	C10H13	133.1016998	CH
j18OO	33.99407959	Air	C3H2j34SO	87.9784317	CS	C11H2	134.0157013	CH
H3j15NO	34.01850128	NO	j13CC2H3O3	88.01157379	CHOgt1	j13CC3H5O5	134.0170593	CHOgt1
Cl	34.96884918	Cl	C3H4O3	88.01603699	CHOgt1	j13CC7H5O2	134.0323029	CHOgt1
Hj34S	34.97568893	Other	j13CC6H3	88.02683258	CH	C8H6O2	134.0368042	CHOgt1
H3S	34.99554062	Other	C7H4	88.03130341	CH	j13CC8H9O	134.0686951	CHO1
H3Nj18O	35.02571106	NO	C4H8O2	88.0524292	CHOgt1	C9H10O	134.0731964	CHO1
HCl	35.97668076	Cl	j13CC4H11O	88.08434296	CHO1	j13CC9H13	134.1050873	CH
C3	36	Cx	C5H12O	88.08881378	CHO1	C10H14	134.1094971	CH
j37Cl	36.96590042	Cl	C3H2j34Sj17O	88.98265076	CS	C7H3O3	135.008194	CHOgt1
H3j34S	36.99134064	Other	C3H5O3	89.02387238	CHOgt1	C4H5j18OO4	135.0179443	CHOgt1
j13CC2	37.0033493	Cx	C7H5	89.03912354	CH	j13CC10H2	135.0190125	CH
C3H	37.00782013	CH	C4H9O2	89.06025696	CHOgt1	j13CC7H6O2	135.0401306	CHOgt1
Hj37Cl	37.97372818	Cl	j13CC4H12O	89.09217072	CHO1	C8H7O2	135.0446014	CHOgt1
C2N	38.00307083	CHN	C2H2O4	89.99530792	CHOgt1	j13CC8H10O	135.0765228	CHO1
j13CC2H	38.01118088	CH	j13CC2H5O3	90.02722168	CHOgt1	C9H11O	135.0809937	CHO1
C3H2	38.0156517	CH	C3H6O3	90.0316925	CHOgt1	j13CC9H14	135.1128998	CH
K	38.96371078	Other	C7H6	90.04695129	CH	C10H15	135.1174011	CH
C2j15N	39.00011063	CHN	C4H10O2	90.06807709	CHOgt1	j13CC6H3O3	136.0115814	CHOgt1
j13CCN	39.00643158	CHN	j182Wplus2	90.97411346	Tungsten	C7H4O3	136.0160065	CHOgt1
j13CC2H2	39.01900101	CH	j13CCH2O4	90.99866486	CHOgt1	j13CC7H7O2	136.0480042	CHOgt1
C3H3	39.02347946	CH	C6H3O	91.01838684	CHO1	C8H8O2	136.0523987	CHOgt1
Ar	39.96237946	Air	j13CC2H6O3	91.03504944	CHOgt1	j13CC8H11O	136.0843506	CHO1
C3H4	40.03129959	CH	C3H7O3	91.03952026	CHOgt1	C9H12O	136.0888062	CHO1
j41K	40.96183014	Other	C7H7	91.05477142	CH	j13CC9H15	136.1207275	CH
C2HO	41.00273895	CHO1	j183Wplus2	91.47511292	Tungsten	C10H16	136.1251984	CH
j13CC2H4	41.03466034	CH	j184Wplus2	91.97545624	Tungsten	j13CC6H4O3	137.0193939	CHOgt1
C3H5	41.03911972	CH	j13CC5H3O	92.02174377	CHO1	C7H5O3	137.0238953	CHOgt1
C2H2O	42.01055908	CHO1	C6H4O	92.02620697	CHO1	j13CC7H8O2	137.0557861	CHOgt1
j13CC2H5	42.04248047	CH	j13CC2H7O3	92.0428772	CHOgt1	C8H9O2	137.0603027	CHOgt1
C3H6	42.04695129	CH	C3H8O3	92.04734039	CHOgt1	j13CC8H12O	137.0921631	CHO1

C2Hj18O	43.0069809	CHO1	j13CC6H7	92.05812836	CH	C9H13O	137.0966034	CHO1
j13CCH2O	43.01391983	CHO1	C7H8	92.06259918	CH	j13CC9H16	137.1285553	CH
C2H3O	43.01839066	CHO1	j186Wplus2	92.97718048	Tungsten	C10H17	137.1329956	CH
C3H7	43.05477905	CH	C6H5O	93.03404236	CHO1	C3H6SO4	137.998703	CS
CO2	43.98983002	CHOgt1	j13CC2H8O3	93.05069733	CHOgt1	j13CC6H5O3	138.0272217	CHOgt1
C2H4O	44.02621078	CHO1	C3H9O3	93.05516815	CHOgt1	C7H6O3	138.0316925	CHOgt1
CHS	44.97990036	CS	C7H9	93.07042694	CH	C11H6	138.0469971	CH
j13CO2	44.99317932	CHOgt1	C2Cl2	93.93771362	Cx	j13CC7H9O2	138.0636139	CHOgt1
CHO2	44.99765015	CHOgt1	C5H2O2	94.00547791	CHOgt1	C8H10O2	138.0681	CHOgt1
C2H5O	45.03403854	CHO1	C6H6O	94.04186249	CHO1	j13CC8H13O	138.0999908	CHO1
C2H7N	45.05784988	CHN	j13CC2H9O3	94.05852509	CHOgt1	C9H14O	138.1045074	CHO1
j13CHS	45.98324966	CS	C6H8N	94.0656662	CHN	j13CC9H17	138.1363831	CH
NO2	45.99290085	NO	C7H10	94.07824707	CH	C10H18	138.1408997	CH
Cj18OO	45.99409866	CHOgt1	j13CCCl2	94.94106293	Cx	j13CC2H6SO4	139.0020294	CS
j13CCH7N	46.061203	CHN	C2HCl2	94.94553375	CH	C6H5NO3	139.0269012	CHOgt1N
CCl	46.96884918	Other	j13CC4H2O2	95.00883484	CHOgt1	j13CC6H6O3	139.0350494	CHOgt1
CHj34S	46.97569275	CS	C5H3O2	95.01331329	CHOgt1	j13CC10H6	139.0503082	CH
j15NO2	46.98994064	NO	C6H7O	95.04969025	CHO1	C11H7	139.0547943	CH
CH3S	46.99554062	CS	j13CC5H8N	95.06903076	CHN	j13CC7H10O2	139.0714417	CHOgt1
HNO2	47.00072861	NO	C7H11	95.0860672	CH	C8H11O2	139.0758972	CHOgt1
CH3O2	47.01330948	CHOgt1	C2j37ClCl	95.93475342	Cx	j13CC8H14O	139.1078186	CHO1
CH5NO	47.03710938	CHO1N	j13CCHCl2	95.94888306	CH	C9H15O	139.1123047	CHO1
SO	47.96697998	SO	SO4	95.95172882	SO	j13CC9H18	139.1442108	CH
j13CCl	47.97220612	Other	CH4SO3	95.9881134	CS	C10H19	139.1486969	CH
Nj18OO	47.99715042	NO	C5H4O2	96.02113342	CHOgt1	C3H6j34SO4	139.9944763	CS
j13CH3S	47.99890137	CS	C6H8O	96.05751801	CHO1	C6H4O4	140.0110016	CHOgt1
C4	48	Cx	C7H12	96.09390259	CH	j13CC5H5NO3	140.030304	CHOgt1N
j13CH3O2	48.01665878	CHOgt1	j13CCj37ClCl	96.93811035	Cx	C7H8O3	140.0473022	CHOgt1
j13CH5NO	48.04047012	CHO1N	HS2O2	96.94180298	SO	j13CC10H7	140.058136	CH
Cj37Cl	48.96590042	Other	C2Hj37ClCl	96.94258118	CH	C11H8	140.0626068	CH
j33SO	48.96636963	SO	j33SO4	96.95111847	SO	j13CC7H11O2	140.0792542	CHOgt1
HSO	48.97481155	SO	HSO4	96.95955658	SO	j13CC8H15O	140.1156464	CHO1
CH3j34S	48.99134064	CS	j13CH4SO3	96.99147034	CS	C9H16O	140.1201019	CHO1
HO3	48.99256897	HO	C4HO3	96.99256897	CHOgt1	j13CC9H19	140.1520233	CH
j13CC3	49.0033493	Cx	C8H	97.00782776	CH	C10H20	140.1564941	CH
C4H	49.00782013	CH	C5H5O2	97.02895355	CHOgt1	j13CC5H4O4	141.0143127	CHOgt1
j34SO	49.96278	SO	C6H9O	97.06533813	CHO1	C6H5O4	141.0187988	CHOgt1
Hj33SO	49.9742012	SO	C7H13	97.10172272	CH	j13CC6H8O3	141.050705	CHOgt1
C3N	50.00307083	CHN	C2j37Cl2	97.93180847	Cx	j13CC10H8	141.0659485	CH
j13CC3H	50.01118088	CH	H2S3	97.93186225	Other	C11H9	141.0704041	CH
C4H2	50.0156517	CH	Hj33SSO2	97.941185	SO	C8H13O2	141.0915985	CHOgt1
Hj34SO	50.97061157	SO	j13CCHj37ClCl	97.94593811	CH	j13CC8H16O	141.1234741	CHO1
j13CC2N	51.00642776	CHN	j34SO4	97.94753265	SO	j13CC9H20	141.1598511	CH
C3HN	51.01089859	CHN	Hj33SO4	97.9589386	SO	C10H21	141.1643066	CH
j13CC3H2	51.01900101	CH	H2SO4	97.96737671	SO	j13CC5H5O4	142.0221405	CHOgt1
C4H3	51.02347946	CH	CH4j34SO3	97.98390961	CS	C6H6O4	142.0265961	CHOgt1
C3O	51.99491882	CHO1	j13CC3HO3	97.9959259	CHOgt1	C7H10O3	142.0630035	CHOgt1
j13CC2HN	52.01425552	CHN	C4H2O3	98.00039673	CHOgt1	j13CC10H9	142.0737762	CH
C3H2N	52.01871872	CHN	j13CC7H	98.01117706	CH	C11H10	142.0782013	CH
j13CC3H3	52.02682877	CH	C8H2	98.01564789	CH	j13CC7H13O2	142.0948944	CHOgt1
C4H4	52.03129959	CH	C5H6O2	98.03678131	CHOgt1	j13CC9H21	142.1676788	CH

Appendix

j13CC2O	52.99826813	CHO1	C6H10O	98.07317352	CHO1	j13CC5H6O4	143.0299683	CHOgt1
C3HO	53.00273895	CHO1	C7H14	98.10955048	CH	C6H7O4	143.0343933	CHOgt1
j13CC2H2N	53.02207947	CHN	j99Ru	98.90593719	Other	j13CC6H10O3	143.0663452	CHOgt1
C3H3N	53.02655029	CHN	Hj34SSO2	98.93759155	SO	C7H11O3	143.0708008	CHOgt1
j13CC3H4	53.03466034	CH	C2Hj37Cl2	98.9396286	CH	j13CC10H10	143.081604	CH
C4H5	53.03911972	CH	Hj34SO4	98.95535278	SO	C11H11	143.0861053	CH
C3H2O	54.01055908	CHO1	H2j33SO4	98.96676636	SO	C9H4O2	144.0211029	CHOgt1
j13CC2H3N	54.02990341	CHN	j13CC3H2O3	99.00374603	CHOgt1	j13CC5H7O4	144.037796	CHOgt1
C3H4N	54.03437042	CHN	C4H3O3	99.00821686	CHOgt1	C10H8O	144.0574951	CHO1
C4H6	54.04695129	CH	C8H3	99.02348328	CH	j13CC6H11O3	144.074173	CHOgt1
C3H3O	55.01839066	CHO1	C4H5NO2	99.0320282	CHOgt1N	j13CC10H11	144.0894318	CH
j13CC2H4N	55.03772736	CHN	j13CC4H6O2	99.04013062	CHOgt1	C11H12	144.0939026	CH
C4H7	55.05477905	CH	C5H7O2	99.04460144	CHOgt1	j13CC8H4O2	145.0244904	CHOgt1
C2O2	55.98983002	CHOgt1	C6H11O	99.08099365	CHO1	C9H5O2	145.029007	CHOgt1
C3H4O	56.02621078	CHO1	j13CC6H14	99.11290741	CH	C6H9O4	145.0500946	CHOgt1
C3H6N	56.05002975	CHN	C7H15	99.11737823	CH	j13CC9H8O	145.0608978	CHO1
C4H8	56.06259918	CH	H2j34SO4	99.96317291	SO	C10H9O	145.0653076	CHO1
C3H5O	57.03403854	CHO1	C3O4	99.97966003	CHOgt1	j13CC10H12	145.0972595	CH
j13CC2H6N	57.05337906	CHN	j13CC3H3O3	100.0115738	CHOgt1	C11H13	145.1016998	CH
C4H9	57.07043076	CH	C4H4O3	100.0159988	CHOgt1	j13CC8H5O2	146.0323029	CHOgt1
C2H2O2	58.00548172	CHOgt1	j13CC7H3	100.0268021	CH	C9H6O2	146.0368042	CHOgt1
j13CC2H5O	58.03739929	CHO1	C8H4	100.0313034	CH	j13CC5H9O4	146.0534363	CHOgt1
C3H6O	58.04187012	CHO1	j13CC3H5NO2	100.0353928	CHOgt1N	j13CC9H9O	146.0686951	CHO1
C3H8N	58.06567001	CHN	C5H8O2	100.0523987	CHOgt1	C10H10O	146.0731964	CHO1
j13CC3H9	58.07378006	CH	C6H12O	100.0887985	CHO1	j13CC10H13	146.1050873	CH
C4H10	58.07825089	CH	j13CC6H15	100.120697	CH	C11H14	146.1094971	CH
COP	58.96868134	CHO1	C7H16	100.1251984	CH	j13CC8H6O2	147.0401306	CHOgt1
C2H3O2	59.01330948	CHOgt1	ORb	100.906707	Other	C9H7O2	147.0446014	CHOgt1
C2H5NO	59.03710938	CHO1N	j13CC2O4	100.983017	CHOgt1	j13CC9H10O	147.0765228	CHO1
C3H7O	59.04969025	CHO1	C3HO4	100.9875031	CHOgt1	C10H11O	147.0809937	CHO1
j13CC2H8N	59.06903076	CHN	j13CC3H4O3	101.0194016	CHOgt1	j13CC10H14	147.1128998	CH
C3H9N	59.07350159	CHN	C4H5O3	101.0239029	CHOgt1	C11H15	147.1174011	CH
j13CC3H10	59.08160019	CH	C8H5	101.0391006	CH	C8H4O3	148.0160065	CHOgt1
CSO	59.96697998	CS	j13CC4H8O2	101.0557938	CHOgt1	j13CC8H7O2	148.0479584	CHOgt1
j13COP	59.97203064	CHO1	C5H9O2	101.0603027	CHOgt1	C9H8O2	148.0523987	CHOgt1
CHOP	59.97650146	CHO1	j13CC5H12O	101.0922012	CHO1	j13CC9H11O	148.0843506	CHO1
C2HCl	59.97668076	CH	C6H13O	101.0966034	CHO1	C10H12O	148.0888062	CHO1
C5	60	Cx	j13CC6H16	101.1286011	CH	j13CC10H15	148.1207275	CH
CH2NO2	60.00854874	CHOgt1N	Ru	101.9043503	Other	C11H16	148.1251984	CH
C2H4O2	60.02112961	CHOgt1	j13CC2HO4	101.9908371	CHOgt1	C2HN2O6	148.9835052	CHOgt1N
j13CCH5NO	60.04047012	CHO1N	C3H4NO3	102.0190964	CHOgt1N	j13CC7H4O3	149.0193939	CHOgt1
C2H6NO	60.04494095	CHO1N	C4H6O3	102.0317001	CHOgt1	C8H5O3	149.0238953	CHOgt1
C3H8O	60.05751038	CHO1	C8H6	102.0469971	CH	C12H5	149.0391252	CH
j13CSO	60.97034073	CS	C5H10O2	102.0681	CHOgt1	j13CC8H8O2	149.0557861	CHOgt1
NOP	60.97174835	NO	j13CC5H13O	102.0999985	CHO1	j13CC9H12O	149.0921631	CHO1
j13CHOP	60.97985458	CHO1	C6H14O	102.1044998	CHO1	C10H13O	149.0966034	CHO1
j13CCHCl	60.98003387	CH	Rh	102.9055023	Other	j13CC10H16	149.1285553	CH
C2H2Cl	60.98450089	CH	C3H3O4	103.0030975	CHOgt1	C11H17	149.1330255	CH
j13CC4	61.0033493	Cx	C3H5NO3	103.0269012	CHOgt1N	j13CCHN2O6	149.9868164	CHOgt1N
C5H	61.00782013	CH	j13CC3H6O3	103.0350494	CHOgt1	j13CC7H5O3	150.0272064	CHOgt1
j13CH2NO2	61.01190948	CHOgt1N	C4H7O3	103.0394974	CHOgt1	C8H6O3	150.0316925	CHOgt1

C2H5O2	61.02894974	CHOgt1	C8H7	103.0548019	CH	C5H10O5	150.0527954	CHOgt1
j13CCH6NO	61.04829407	CHO1N	C5H11O2	103.0758972	CHOgt1	C9H10O2	150.0681	CHOgt1
Cj34SO	61.96278	CS	j13CC5H14O	103.1078033	CHO1	j13CC9H13O	150.0999908	CHO1
NSO	61.97005844	NO	j13CC2H3O4	104.0064774	CHOgt1	C10H14O	150.1045074	CHO1
C2Hj37Cl	61.97372818	CH	C3H4O4	104.0110016	CHOgt1	C2HN2j18OO5	150.9877014	CHOgt1N
NO3	61.98781967	NO	C7H4O	104.0261993	CHO1	C7H3O4	151.0030975	CHOgt1
j13CCH2Cl	61.98785782	CH	j13CC3H7O3	104.0428772	CHOgt1	j13CC7H6O3	151.0350494	CHOgt1
CH2O3	62.0003891	CHOgt1	C4H8O3	104.0473022	CHOgt1	C8H7O3	151.039505	CHOgt1
C5H2	62.0156517	CH	C8H8	104.0625992	CH	j13CC4H10O5	151.0561829	CHOgt1
C2H6O2	62.03678131	CHOgt1	j13CC2H4O4	105.0143127	CHOgt1	j13CC8H10O2	151.0714417	CHOgt1
Cu	62.92959976	Other	C3H5O4	105.0187988	CHOgt1	C9H11O2	151.0758972	CHOgt1
HNSO	62.97789001	NO	C3H7NO3	105.0426025	CHOgt1N	j13CC9H14O	151.1078186	CHO1
C2H2j37Cl	62.98155212	CH	C8H9	105.0703964	CH	C10H15O	151.1123047	CHO1
HNO3	62.9956398	NO	j13CC2H5O4	106.0221024	CHOgt1	C11H19	151.1486969	CH
j13CH2O3	63.00374985	CHOgt1	C7H6O	106.0419006	CHO1	j13CC6H3O4	152.006485	CHOgt1
C5H3	63.02347946	CH	j13CC2H7NO3	106.0459366	CHOgt1N	j13CC7H7O3	152.0428772	CHOgt1
SO2	63.9618988	SO	C8H10	106.0782013	CH	C8H8O3	152.0473022	CHOgt1
Nj34SO	63.96585464	NO	C3H7O4	107.0344009	CHOgt1	C5H10j18OO4	152.0570679	CHOgt1
C5H4	64.03130341	CH	C7H7O	107.0496979	CHO1	C12H8	152.0626068	CH
j65Cu	64.92780304	Other	C8H11	107.0860977	CH	j13CC8H11O2	152.0792542	CHOgt1
j33SO2	64.96128845	SO	C6H4O2	108.0211029	CHOgt1	j13CC9H15O	152.1156464	CHO1
HSO2	64.96972656	SO	C7H8O	108.0575027	CHO1	C10H16O	152.1201019	CHO1
HNj34SO	64.97367859	NO	j13CC7H11	108.0894012	CH	j13CC10H19	152.1520233	CH
C4HO	65.00273895	CHO1	C8H12	108.0939026	CH	C11H20	152.1564941	CH
C5H5	65.03912354	CH	C6H5O2	109.0289993	CHOgt1	C6H3NO4	153.0061951	CHOgt1N
j34SO2	65.95770264	SO	C7H9O	109.0653	CHO1	C7H5O4	153.0187988	CHOgt1
Hj33SO2	65.96911621	SO	C8H13	109.1016998	CH	j13CC7H8O3	153.050705	CHOgt1
H2SO2	65.97754669	SO	C5H2O3	110.0003967	CHOgt1	C8H9O3	153.0552063	CHOgt1
HNj34Sj17O	65.97789764	NO	C6H6O2	110.0367966	CHOgt1	j13CC11H8	153.0659485	CH
j13CC3HO	66.00610352	CHO1	C7H10O	110.0731964	CHO1	C12H9	153.0704041	CH
C4H2O	66.01056671	CHO1	C8H14	110.1095963	CH	C9H13O2	153.0915985	CHOgt1
C5H6	66.04695129	CH	j13CC4H2O3	111.0037537	CHOgt1	j13CC9H16O	153.1234741	CHO1
Hj34SO2	66.96552277	SO	C5H3O3	111.0082016	CHOgt1	j13CC10H20	153.1598511	CH
C4H3O	67.01838684	CHO1	C9H3	111.0234985	CH	C11H21	153.1643066	CH
j13CC4H6	67.05030823	CH	C6H7O2	111.0446014	CHOgt1	j13CC5H3NO4	154.0095673	CHOgt1N
C5H7	67.05477142	CH	C7H11O	111.0810013	CHO1	C6H4NO4	154.0140076	CHOgt1N
H2j34SO2	67.9733429	SO	C8H15	111.1174011	CH	j13CC6H5O4	154.0221405	CHOgt1
C3O2	67.98983002	CHOgt1	C5H4O3	112.0159988	CHOgt1	C7H6O4	154.0265961	CHOgt1
j13CC3H3O	68.02174377	CHO1	C6H8O2	112.0523987	CHOgt1	j13CC7H9O3	154.0585175	CHOgt1
C4H4O	68.02620697	CHO1	C7H12O	112.0887985	CHO1	C8H10O3	154.0630035	CHOgt1
C5H8	68.06259918	CH	C8H16	112.1251984	CH	j13CC11H9	154.0737762	CH
C3HO2	68.99765778	CHOgt1	C5H5O3	113.0239029	CHOgt1	C12H10	154.0782013	CH
C4H5O	69.03404236	CHO1	C9H5	113.0391006	CH	j13CC8H13O2	154.0949097	CHOgt1
j13CC4H8	69.06596375	CH	C6H9O2	113.0603027	CHOgt1	j13CC10H21	154.1676788	CH
C5H9	69.07042694	CH	C7H13O	113.0966034	CHO1	C11H22	154.1721039	CH
C3H2O2	70.00547791	CHOgt1	C8H17	113.1330032	CH	j13CC5H4NO4	155.017395	CHOgt1N
C4H6O	70.04186249	CHO1	C4H4NO3	114.0190964	CHOgt1N	j13CC6H6O4	155.0299683	CHOgt1
C5H10	70.07824707	CH	C5H6O3	114.0317001	CHOgt1	C7H7O4	155.0343933	CHOgt1
C3H3O2	71.01331329	CHOgt1	C9H6	114.0469971	CH	j13CC7H10O3	155.0663452	CHOgt1
C4H7O	71.04969025	CHO1	C6H10O2	114.0681	CHOgt1	j13CC11H10	155.081604	CH
C5H11	71.0860672	CH	j13CC6H13O	114.0999985	CHO1	C12H11	155.0861053	CH

C3H4O2	72.02113342	CHOgt1	C7H14O	114.1044998	CHO1	j13CC10H22	155.1755066	CH
C3H6NO	72.04493713	CHO1N	C8H18	114.1408997	CH	C11H23	155.1799927	CH
C4H8O	72.05751801	CHO1	C4H3O4	115.0030975	CHOgt1	j13CC6H7O4	156.037796	CHOgt1
C4H10N	72.08132172	CHN	C4H5NO3	115.0269012	CHOgt1N	C7H8O4	156.0422974	CHOgt1
C5H12	72.09390259	CH	C5H7O3	115.0394974	CHOgt1	C8H12O3	156.078598	CHOgt1
C6H	73.00782776	CH	C9H7	115.0548019	CH	j13CC11H11	156.0894318	CH
C3H5O2	73.02895355	CHOgt1	C7H15O	115.1122971	CHO1	C12H12	156.0939026	CH
j13CC2H6NO	73.04829407	CHO1N	j13CC7H18	115.1442032	CH	j13CC10H23	156.1833344	CH
C4H9O	73.06533813	CHO1	C8H4O	116.0261993	CHO1	C11H24	156.1878052	CH
j13CC3H10N	73.08467865	CHN	j13CC3H5NO3	116.0302963	CHOgt1N	C6H5O5	157.0137024	CHOgt1
C4H11N	73.08914948	CHN	j13CC4H7O3	116.0428772	CHOgt1	C6H7NO4	157.0375061	CHOgt1N
j13CC4H12	73.09725189	CH	C5H8O3	116.0473022	CHOgt1	j13CC6H8O4	157.0456085	CHOgt1
C2H2O3	74.00039673	CHOgt1	C9H8	116.0625992	CH	C7H9O4	157.0500946	CHOgt1
j13CC5H	74.01117706	CH	C6H12O2	116.0837021	CHOgt1	C11H9O	157.0653076	CHO1
C6H2	74.01564789	CH	j13CC7H4O	117.0295715	CHO1	j13CC7H12O3	157.0820007	CHOgt1
C3H6O2	74.03678131	CHOgt1	C8H5O	117.0339966	CHO1	j13CC11H12	157.0972595	CH
C3H8NO	74.06059265	CHO1N	j13CC4H8O3	117.0506973	CHOgt1	C12H13	157.1016998	CH
C4H10O	74.07317352	CHO1	C9H9	117.0703964	CH	j13CC10H24	157.1911621	CH
j13CC3H11N	74.09250641	CHN	C6H13O2	117.0915985	CHOgt1	j13CC5H5O5	158.0170593	CHOgt1
j13CCH2O3	75.00374603	CHOgt1	C4H6O4	118.0266037	CHOgt1	C10H6O2	158.0368042	CHOgt1
C2H3O3	75.00821686	CHOgt1	j13CC7H5O	118.0373917	CHO1	j13CC5H7NO4	158.040863	CHOgt1N
j13CC5H2	75.01899719	CH	C8H6O	118.0419006	CHO1	j13CC6H9O4	158.0534363	CHOgt1
C6H3	75.02348328	CH	C9H10	118.0782013	CH	j13CC10H9O	158.0686951	CHO1
C3H7O2	75.04460144	CHOgt1	C5H12NO2	118.0867996	CHOgt1N	C11H10O	158.0731964	CHO1
j13CC2H8NO	75.06394196	CHO1N	C7H3O2	119.013298	CHOgt1	j13CC11H13	158.1050873	CH
j13CC3H10O	75.07652283	CHO1	j13CC3H6O4	119.0299606	CHOgt1	C12H14	158.1094971	CH
CSO2	75.9618988	CS	C4H7O4	119.0344009	CHOgt1	C6H5j18OO4	159.0179443	CHOgt1
C2H4SO	75.99828339	CS	C8H7O	119.0496979	CHO1	j13CC9H6O2	159.0401306	CHOgt1
j13CCH3O3	76.01157379	CHOgt1	C5H11O3	119.0708008	CHOgt1	C10H7O2	159.0446014	CHOgt1
C2H4O3	76.01603699	CHOgt1	C9H11	119.0860977	CH	C7H11O4	159.0657043	CHOgt1
C6H4	76.03130341	CH	j13CC6H3O2	120.0166626	CHOgt1	j13CC10H10O	159.0765228	CHO1
C3H8O2	76.0524292	CHOgt1	C7H4O2	120.0211029	CHOgt1	C8H15O3	159.1020966	CHOgt1
j13CSO2	76.96525574	CS	C8H8O	120.0575027	CHO1	j13CC11H14	159.1128998	CH
CHSO2	76.96972656	CS	C9H12	120.0939026	CH	C12H15	159.1174011	CH
j13CCH4SO	77.00164032	CS	C7H5O2	121.0289993	CHOgt1	C9H4O3	160.0160065	CHOgt1
C5HO	77.00273895	CHO1	C8H9O	121.0653	CHO1	j13CC9H7O2	160.0479584	CHOgt1
C2H5O3	77.02387238	CHOgt1	C9H13	121.1016998	CH	C10H8O2	160.0523987	CHOgt1
C6H5	77.03912354	CH	C6H2O3	122.0003967	CHOgt1	j13CC6H11O4	160.0690918	CHOgt1
j13CC2H8O2	77.05578613	CHOgt1	C6H4NO2	122.0242004	CHOgt1N	C11H12O	160.0888062	CHO1
C3H9O2	77.06025696	CHOgt1	C7H6O2	122.0367966	CHOgt1	j13CC7H15O3	160.1054688	CHOgt1
Cj34SO2	77.95769501	CS	C8H10O	122.0731964	CHO1	j13CC11H15	160.1207275	CH
j13CHSO2	77.9730835	CS	C9H14	122.1095963	CH	C12H16	160.1251984	CH
CH2SO2	77.97754669	CS	j13CC5H2O3	123.0037537	CHOgt1	j13CC8H4O3	161.0193939	CHOgt1
C2H4j34SO	77.99407959	CS	C6H3O3	123.0082016	CHOgt1	j13CC9H8O2	161.0558014	CHOgt1
j13CC4HO	78.00610352	CHO1	j13CC5H4NO2	123.0275574	CHOgt1N	j13CC10H12O	161.0921631	CHO1
						j13CC11H16	161.1285553	CH

A. 7 Source factors supplement of organic PMF analysis

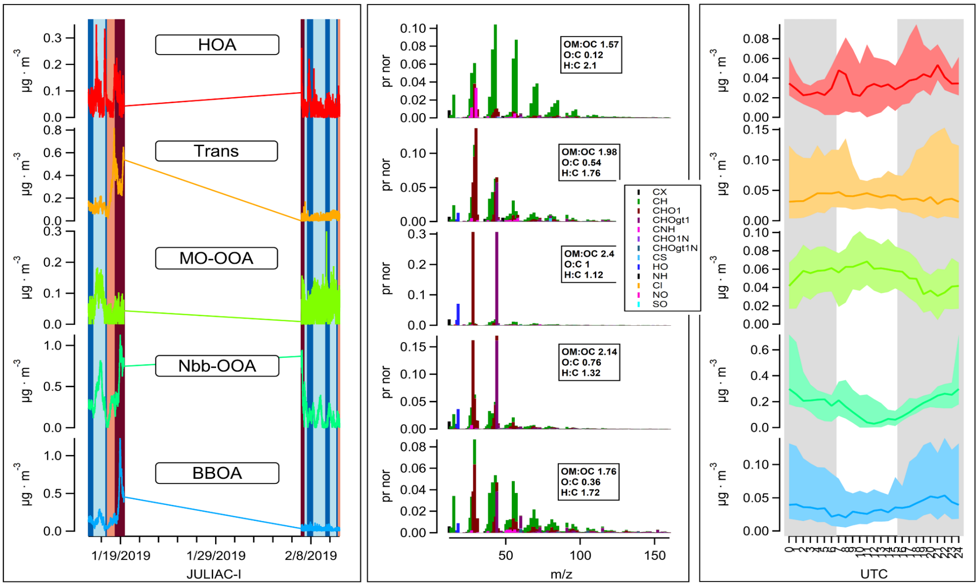

Figure A 5: The organic aerosol source apportionment results overview resolved by PMF for the JULIAC-I. From left to right, the overview of OA contribution variations of source factors, high-resolution source factors spectra colored by ions family group, and corresponding source factor contribution diurnal pattern (median+IQR). Elemental ratio (OM:OC, O:C, H:C) of all OA factors are marked in the graph.

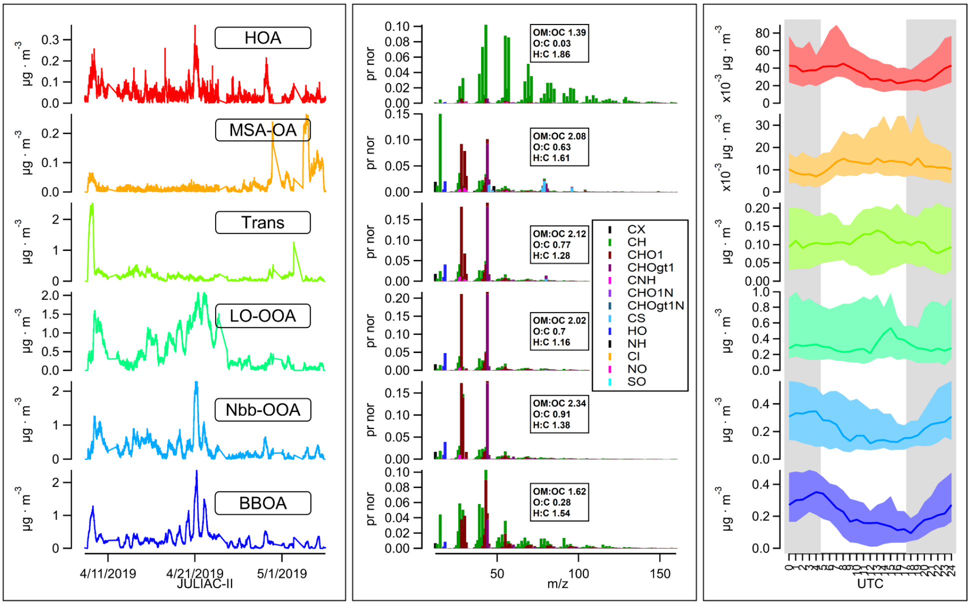

Figure A 6: The organic aerosol source apportionment results overview resolved by PMF for the JULIAC-II. From left to right, the overview of OA contribution variations of source factors, high-resolution source factors spectra colored by ions family group, and corresponding source factor contribution diurnal pattern (median+IQR). Elemental ratio (OM:OC, O:C, H:C) of all OA factors are marked in the graph.

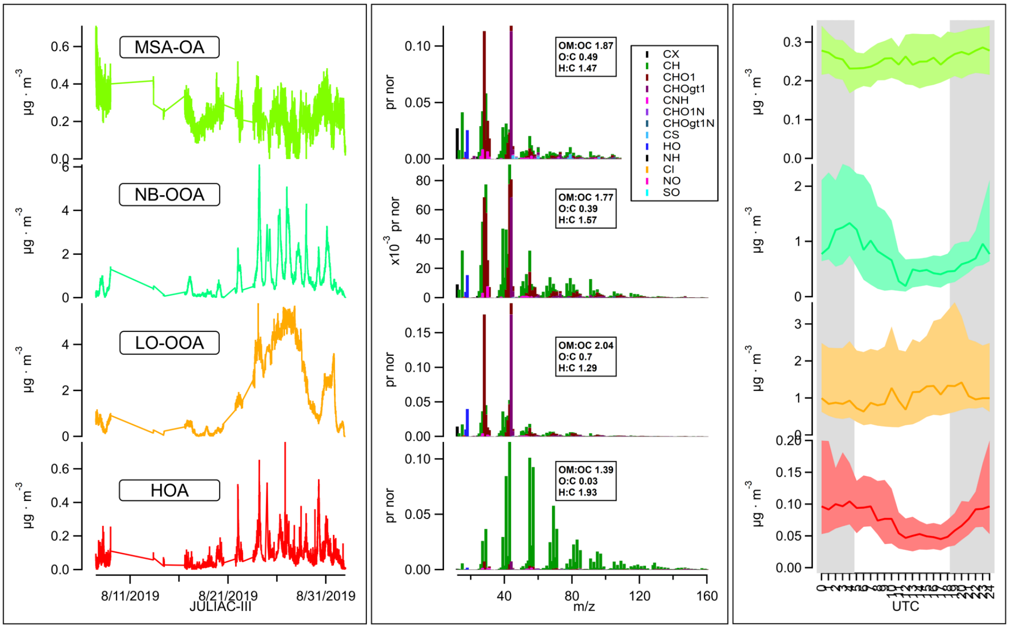

Figure A 7: The organic aerosol source apportionment results overview resolved by PMF for the JULIAC-III. From left to right, the overview of OA contribution variations of source factors, high-resolution source factors spectra colored by ions family group, and corresponding source factor contribution diurnal pattern (median+IQR). Elemental ratio (OM:OC, O:C, H:C) of all OA factors are marked in the graph.

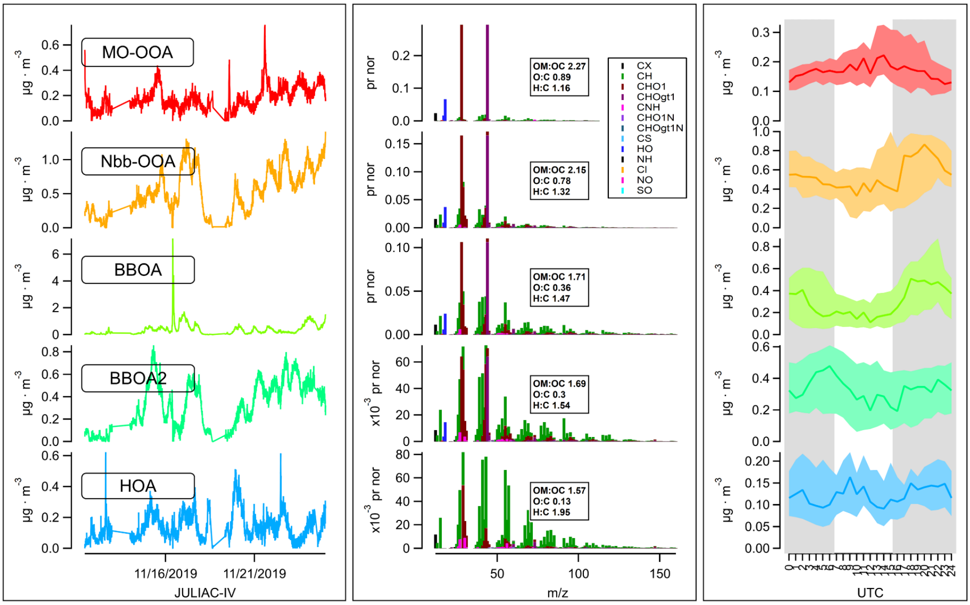

Figure A 8: The organic aerosol source apportionment results overview resolved by PMF for the JULIAC-IV. From left to right, the overview of OA contribution variations of source factors, high-resolution source factors spectra colored by ions family group, and corresponding source factor contribution diurnal pattern (median+IQR). Elemental ratio (OM:OC, O:C, H:C) of all OA factors are marked in the graph.

A. 8 Regional transport factor supplement

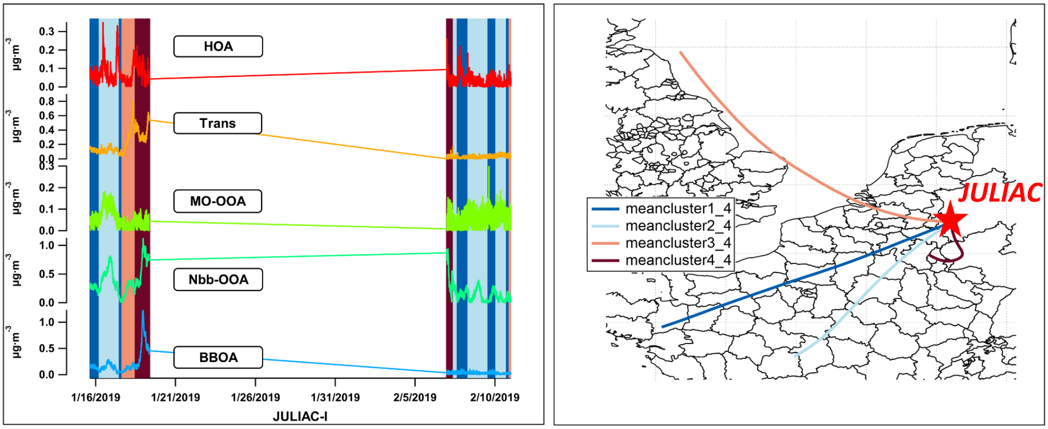

Figure A 9: left) Concentration time series of PMF source factors of the JULIAC-I phase with the background color of trajectory clusters; right) Four trajectory clusters of the JULIAC-I 24-hours back-trajectory simulated by HYSPLIT4.

A. 9 Temperature dependent rate constant

$$k(T) = A\ (T/298\ K)^n\ e^{-Ea/RT}$$

$$R = 8.314472E\text{-}03\ kJ\ /\ mole\ K$$

Table A 5: temperature dependent rate constant calculation

Reaction	JULIAC Phases	Averaged temperature K (UTC 18:00-5:00)	A	Ea kJ/mole	k(T) $cm^3\ molec^{-1}\ s^{-1}$	reference
Furan+ $NO_3\cdot$	JULIAC-I	278	1.30E-13	-5.82	1.51E-12	(Cabañas et al., 2004)
	JULIAC-II	283	1.30E-13	-5.82	1.47E-12	
	JULIAC-III	293	1.30E-13	-5.82	1.39E-12	
	JULIAC-IV	277	1.30E-13	-5.82	1.51E-12	
Furan+ O_3	JULIAC	298	2.42E-18		2.42E-18	(Atkinson et al., 1983)
Isoprene+ $NO_3\cdot$	JULIAC-I	278	3.02E-12	3.71	5.65E-13	(Atkinson 1991)
	JULIAC-II	283	3.02E-12	3.71	5.92E-13	
	JULIAC-III	293	3.02E-12	3.71	6.50E-13	
	JULIAC-IV	277	3.02E-12	3.71	5.62E-13	
Isoprene+ O_3	JULIAC-I	278	5.60E-15	15.05	7.73E-18	(Grosjean et al., 1996)
	JULIAC-II	283	5.60E-15	15.05	8.83E-18	
	JULIAC-III	293	5.60E-15	15.05	1.15E-17	
	JULIAC-IV	277	5.60E-15	15.05	7.62E-18	
alpha-pinene+ $NO_3\cdot$	JULIAC-I	278	1.19E-12	-4.07	6.46E-12	(Atkinson 1991)
	JULIAC-II	283	1.19E-12	-4.07	6.38E-12	
	JULIAC-III	293	1.19E-12	-4.07	6.21E-12	
	JULIAC-IV	277	1.19E-12	-4.07	6.47E-12	
BETA-pinene+ $NO_3\cdot$	JULIAC	298	2.51E-12		2.51E-12	(Atkinson 1991)
d-limonene+ $NO_3\cdot$	JULIAC	298	1.22E-11		1.22E-11	(Atkinson 1991)
alpha-pinene+ O_3	JULIAC-I	278	4.80E-16	4.41	6.63E-17	(Khamaganov et al., 2001)
	JULIAC-II	283	4.80E-16	4.41	6.98E-17	
	JULIAC-III	293	4.80E-16	4.41	7.75E-17	
	JULIAC-IV	277	4.80E-16	4.41	6.59E-17	
BETA-pinene+ O_3	JULIAC-I	278	1.74E-15	10.78	1.53E-17	(Khamaganov and Hites 2001)
	JULIAC-II	283	1.74E-15	10.78	1.69E-17	
	JULIAC-III	293	1.74E-15	10.78	2.06E-17	
	JULIAC-IV	277	1.74E-15	10.78	1.51E-17	
limonene+ O_3	JULIAC-I	278	2.95E-15	6.51	1.64E-16	(Khamaganov and Hites 2001)
	JULIAC-II	283	2.95E-15	6.51	1.76E-16	
	JULIAC-III	293	2.95E-15	6.51	2.01E-16	
	JULIAC-IV	277	2.95E-15	6.51	1.63E-16	
Naphthalene+ O_3	JULIAC	295	<3.01E-19		2.81E-19	(Atkinson et al., 1986)
Naphthalene+ $NO_3\cdot$	JULIAC	298	2.00E-11		2.00E-11	(Atkinson et al., 2007)

A. 10 Gas tracers and meteorological condition overview

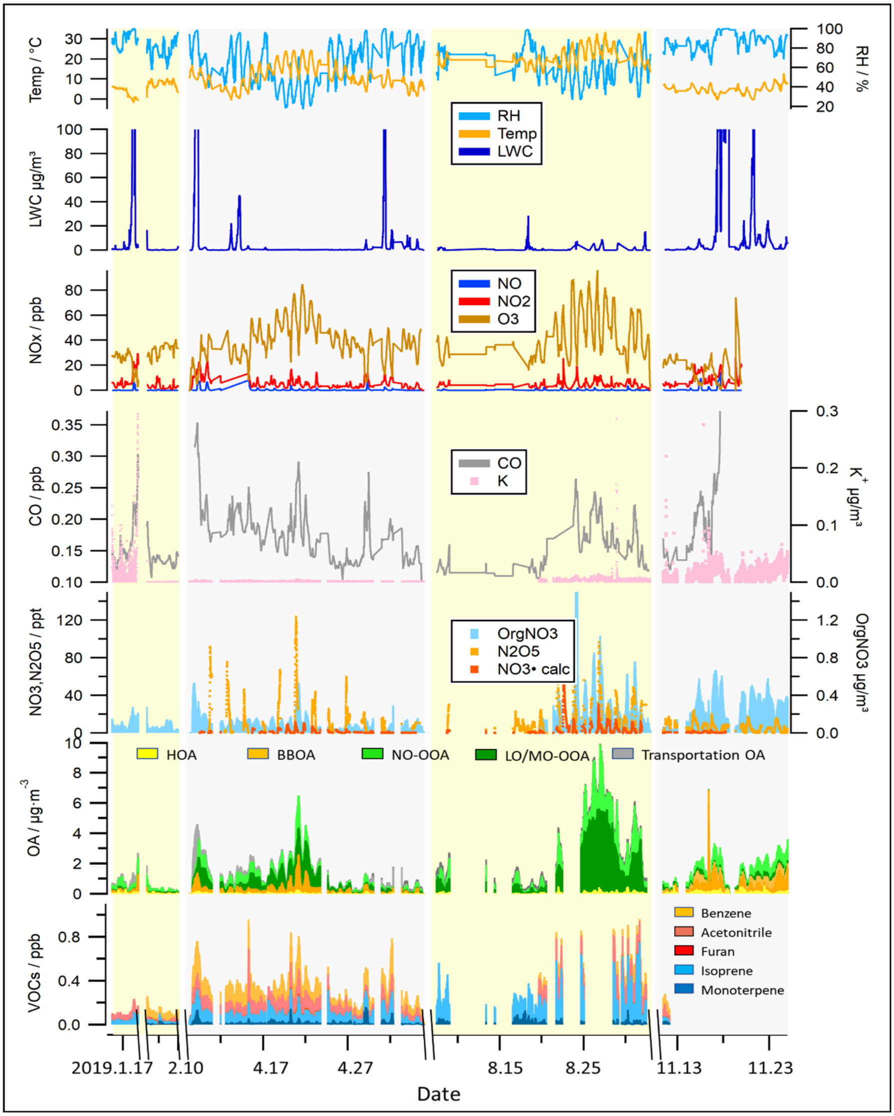

Figure A 10: Yearly overview of variation of organic aerosol source contribution, aerosol LWC, related gas tracers concentration (like VOCs, CO, O_3, NOx, N_2O_5, NO_3 radical) and meteorological condition (temperature and RH) during the whole JULIAC campaign.

A. 11 Source factors overview of NO_3 +Organics PMF analysis

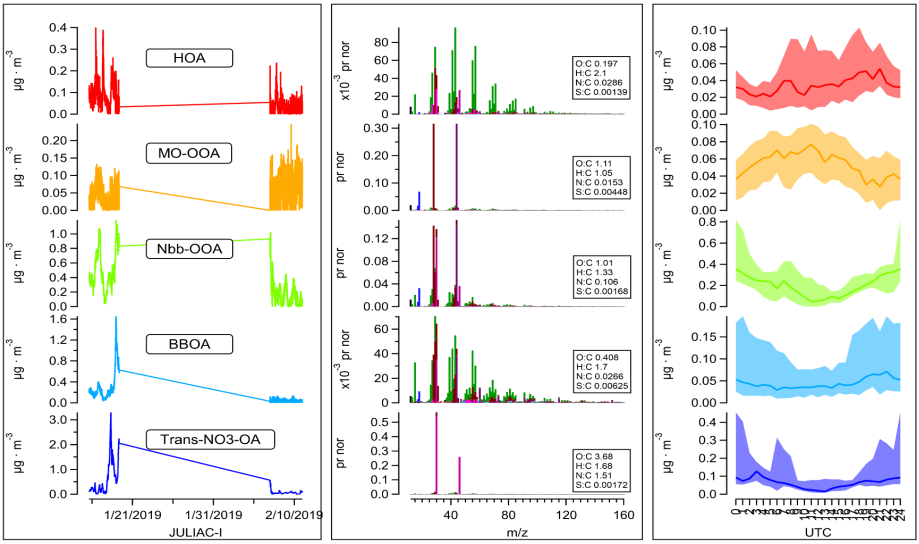

Figure A 11: The NO3+organic aerosol source apportionment results overview resolved by PMF for the JULIAC-I. From left to right, the overview of OA contribution variations of source factors, high-resolution source factors spectra colored by ions family group, and corresponding source factor contribution diurnal pattern (median+IQR). The elemental ratio (OM:OC, O:C, H:C) of all OA factors are marked in the graph.

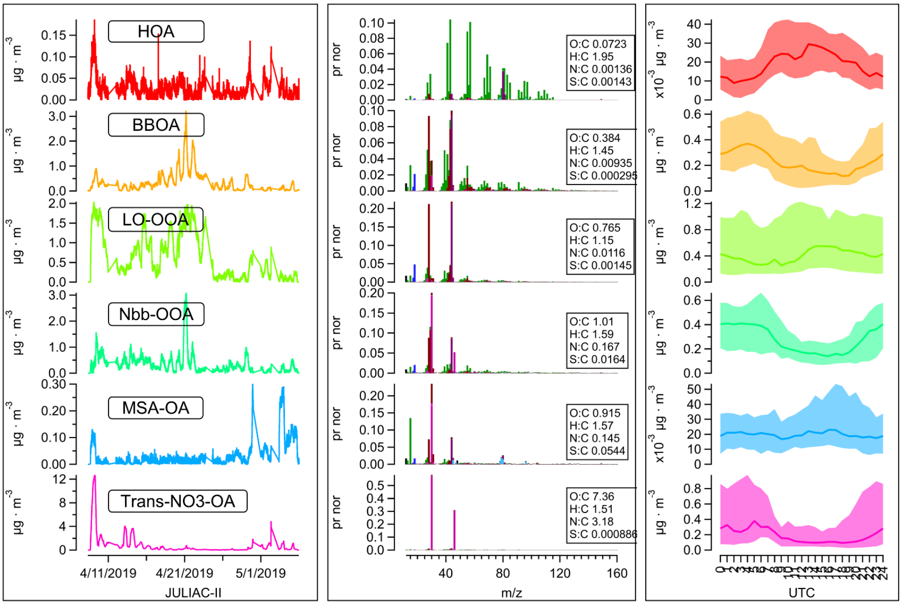

Figure A 12: The NO$_3$+organic aerosol source apportionment results overview resolved by PMF for the JULIAC-II. From left to right, the overview of OA contribution variations of source factors, high-resolution source factors spectra colored by ions family group, and corresponding source factor contribution diurnal pattern (median+IQR). The elemental ratio (OM:OC, O:C, H:C) of all OA factors are marked in the graph.

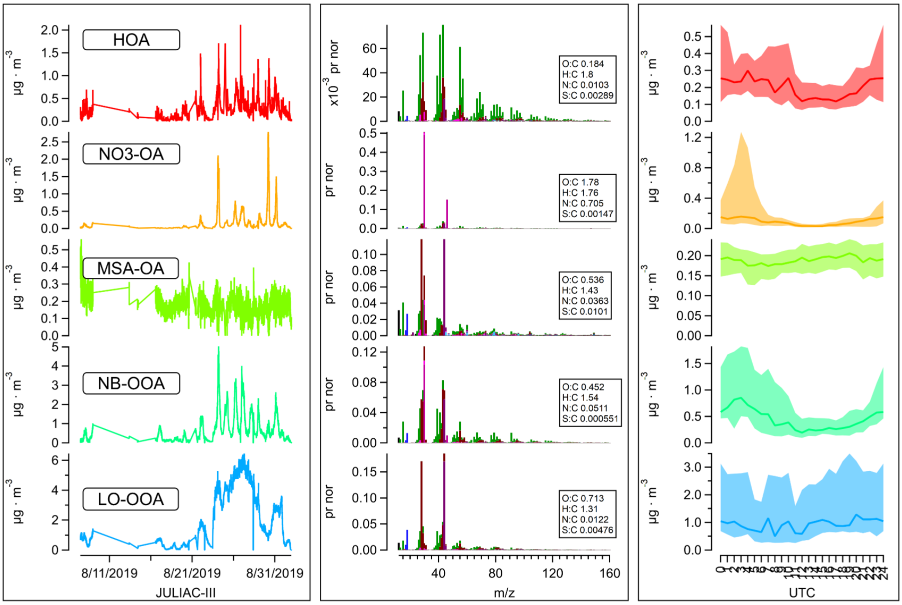

Figure A 13: The NO3+organic aerosol source apportionment results overview resolved by PMF for the JULIAC-III. From left to right, the overview of OA contribution variations of source factors, high-resolution source factors spectra colored by ions family group, and corresponding source factor contribution diurnal pattern (median+IQR). The elemental ratio (OM:OC, O:C, H:C) of all OA factors are marked in the graph.

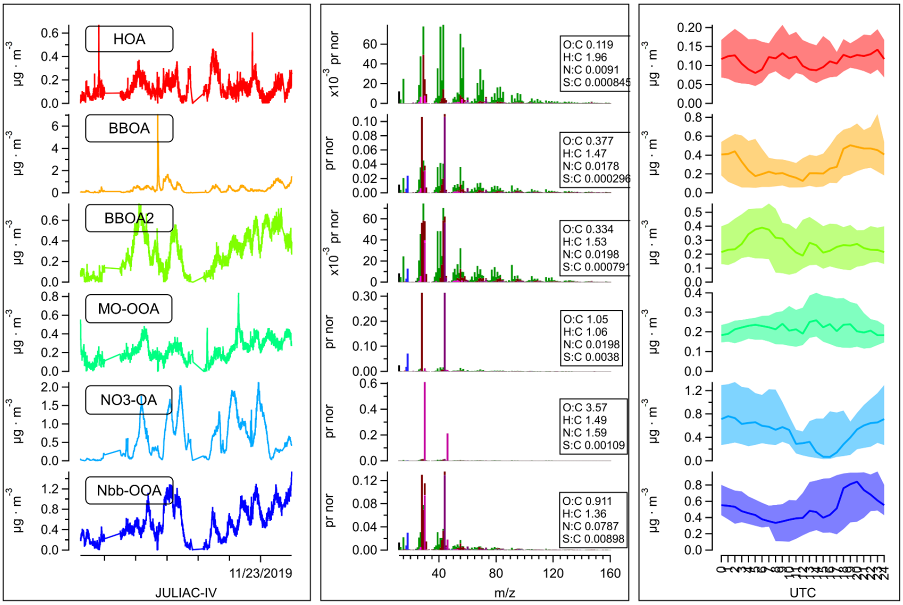

Figure A 14: The NO3+organic aerosol source apportionment results overview resolved by PMF for the JULIAC-IV. From left to right, the overview of OA contribution variations of source factors, high-resolution source factors spectra colored by ions family group, and corresponding source factor contribution diurnal pattern (median+IQR). The elemental ratio (OM:OC, O:C, H:C) of all OA factors are marked in the graph.

A. 12 Instruments and available data for the JULIAC campaign

Table A 6: Overview of instruments involved in the JULIAC campaign. Table including instrument name, measured atmospheric species, and key operation information. (Table credit: IEK-8, Forschungszentrum Jülich, 2019: Overview of available data files in the SAPHIR data archive).

	instrument	param	Measured parameters	Comment
Infrastructure	ASS_METEO	all_param	meteorological data from the ASS meteorological tower at different heights	600 s
	JULIAC_SPS	all_param	status data from the JULIAC inlet (temperatures, pressures, flows, rel. humidity etc.)	10 s, 60 s
	SAPHIR_SPS	all_param	status data from the SAPHIR chamber (temperatures, pressures, gas supply etc.)	10 s, 60 s
	SAPHIR_COLLECTED	all_param	status data from the SAPHIR chamber (temperatures, pressures, gas supply etc.) + some derived parameters	60 s
	PLUS_SPS	all_param	status data from the PLUS chamber (flow, environmental conditons inside PLUS)	
Radicals	LIF	ROx	OH, HO2, RO2	
	LP_LIF	kOH	OH reactivity	
	saphir_ohdoas	all_param	OH, HCHO, SO2, C10H8 (Naphthalene)	SO2 and C10H8 only during ambient air measurements

Nitrogen species + O3	SAPHIR.BRCIMS	HONO_relConc	HONO	
	LOPAP	HONO	HONO	
	CRDS	NO3_N2O5	NO3, N2O5	
	CRANOX	all_param	O3, NO, NO2, NOx	Operated by VOC group
	TR42	NO_NO2_NOx	NO , NO2 , NOx	CLD, ECO Physics type 780TR; operated by NOx group
	AN_41M	O3	O3	UV absorption, Environnement S.A./Ansyco type O341M; operated by NOx group
	AN_42M	O3	O3	UV absorption, Environnement S.A./Ansyco type O342M (borrowed from Mobilab); operated by NOx group
	AN_42M#2	O3	O3	UV absorption, Environnement S.A./Ansyco type O342M; operated by NOx group
	ESA_42e	O3	O3	UV absorption; ENVEA O3-42e operated by NOx group
	TS_49i	O3	O3	UV absorption; Thermo Scientific model 49i Ozonemonitor; operated by NOx group
	ICAD_1005	NO2	NO2	CEAS-DOAS, AIRYX typ ICAG HG; operated by NOx group
	ICAD_1005	NOx	NOx	CEAS-DOAS, AIRYX typ ICAG HG; operated by NOx group
	CAPS_Leicester	NO2	NO2	CAPS NO2 instrument from Leicester (Roberto Sommariva)
	ICIMS_Leicester	ClNO2	ClNO2	Iodide CIMS from Univ. of Leicester (Roberto Sommariva)
Multi components				
	PICARRO_CFKADS2290	all_param	CO, CO2, CH4, H2O	Operated by VOC group
	PICARRO_CFKADS2270	CO_CO2_CH4_H2O	CO, CO2, CH4, H2O	CRDS, Picarro typ G2401; operated by NOx group
	PICARRO_CFKADS2109	CO_CO2_CH4_H2O	CO, CO2, CH4, H2O	CRDS, Picarro typ G2401; operated by NOx group
	PICARRO_LBDS2006	HCHO_H2O_CH4	HCHO, H2O, CH4	CRDS, Picarro typ G2307; operated by NOx group
	PICARRO_CFHADS2042	CO2_CH4_H2O	CO2, CH4, H2O	CRDS 10Hz, Picarro typ G2311-f; operated by NOx group
Organic compounds				
	PTRTOFMS_H3O	VOC	VOC	PTRTOFMS operated in the H3O+-Mode
	VOCUS_H3O	VOC	VOC	VOCUS operated in the H3O+-Mode
	ICIMS_GAS	all_param	VOC	Gothenburg ICIMS Figaero
	HANTZSCH	HCHO	HCHO	
	GC_FID_GREEN	all_param	VOC	Green describes one of two GCMS-Systems in the GC-Container. Green uses a polar column

	GC_FID_RED	all_param	VOC	Red describes one of two GCMS-Systems in the GC-Container. Red uses a non polar column
	GC_MS_GREEN	all_param	VOC	Green describes one of two GCMS-Systems in the GC-Container. Green uses a polar column
	GC_MS_RED	all_param	VOC	Red describes one of two GCMS-Systems in the GC-Container. Red uses a non polar column
Aerosols				
	hetero-SMPS[ID]	all_param	aerosol size distribution, Aerosol total number concentration	the [ID] following "SMPS" is the identifier of the specific SMPS used for the measurements
	hetero-CPC[ID]	numb-conc	Number concentration	the [ID] following "CPC" is the identifier of the specific CPC used for the measurements
	hetero-TSI-CPC	numb-conc	Number concentration	different ID (TSI_CPC) which is a borrowed instrument from TSI because our needs repair
	ZAMS	all_param	chemical speciation (NH4, SO4, NO3, ORG, Chl, O/C, H/C, N/C etc.)	Zepplin-AMS
	TAMS	all_param	chemical speciation (NH4, SO4, NO3, ORG, Chl, O/C, H/C, N/C etc.)	TAG-AMS
	IAMS	all_param	chemical speciation (NH4, SO4, NO3, ORG, Chl, O/C, H/C, N/C etc.)	IUTA-AMS
	ICIMS_PARTICLE	all_param	VOC particle	Gothenburg ICIMS Figaero

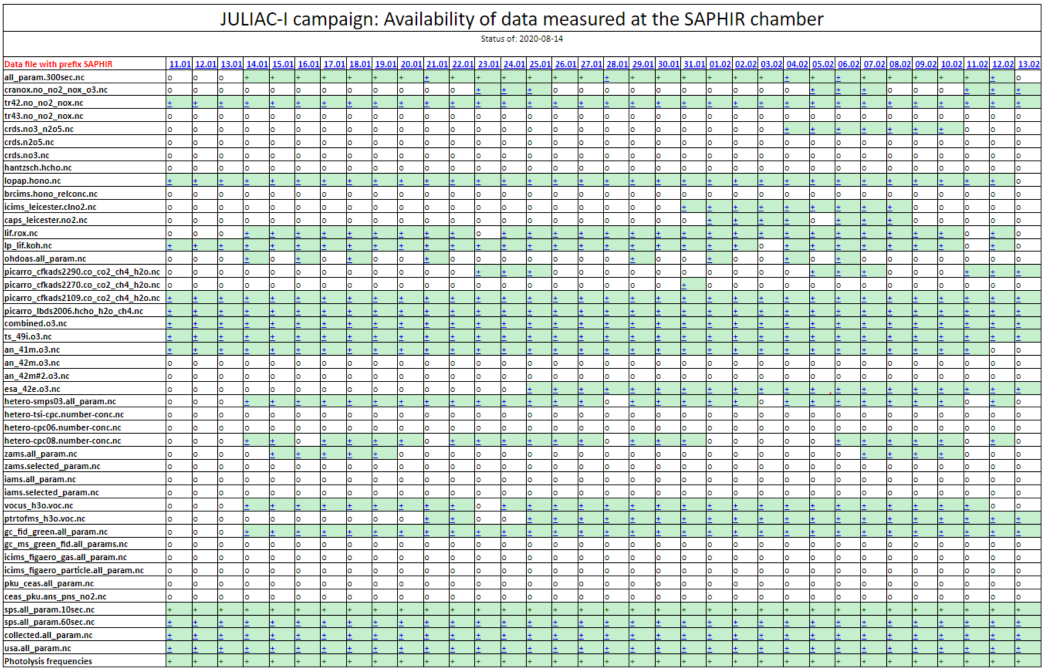

JULIAC-I campaign: Availability of data measured at the SAPHIR chamber

Status of: 2020-08-14

Data file with prefix SAPHIR	11.01	12.01	13.01	14.01	15.01	16.01	17.01	18.01	19.01	20.01	21.01	22.01	23.01	24.01	25.01	26.01	27.01	28.01	29.01	30.01	31.01	01.02	02.02	03.02	04.02	05.02	06.02	07.02	08.02	09.02	10.02	11.02	12.02	13.02
all_param.300sec.nc	o	o	o	+	+	+	+	+	+	+	+	+	+	+	+	+	+	+	+	+	+	+	+	+	+	+	+	+	+	+	+	+	+	o
cranox.no_no2_nox_o3.nc	o	o	o	o	o	o	o	o	o	o	o	o	+	+	+	o	o	o	o	o	o	o	o	o	o	+	+	+	o	o	o	+	+	+
tr42.no_no2_nox.nc	+	+	+	+	+	+	+	+	+	+	+	+	+	+	+	+	+	+	+	+	+	+	+	+	+	+	+	+	+	+	+	+	+	+
tr43.no_no2_nox.nc	o	o	o	o	o	o	o	o	o	o	o	o	o	o	o	o	o	o	o	o	o	o	o	o	o	o	o	o	o	o	o	o	o	o
crds.no3_n2o5.nc	o	o	o	o	o	o	o	o	o	o	o	o	o	o	o	o	o	o	o	o	o	o	o	o	+	+	+	+	+	+	+	o	o	o
crds.n2o5.nc	o	o	o	o	o	o	o	o	o	o	o	o	o	o	o	o	o	o	o	o	o	o	o	o	o	o	o	o	o	o	o	o	o	o
crds.no3.nc	o	o	o	o	o	o	o	o	o	o	o	o	o	o	o	o	o	o	o	o	o	o	o	o	o	o	o	o	o	o	o	o	o	o
hantzsch.hcho.nc	o	o	o	o	o	o	o	o	o	o	o	o	o	o	o	o	o	o	o	o	o	o	o	o	o	o	o	o	o	o	o	o	o	o
lopap.hono.nc	+	+	+	+	+	+	+	+	+	+	+	+	+	+	+	+	+	+	+	+	+	+	+	+	+	+	+	+	+	+	+	+	+	o
brcims.hono_relconc.nc	o	o	o	o	o	o	o	o	o	o	o	o	o	o	o	o	o	o	o	o	o	o	o	o	o	o	o	o	o	o	o	o	o	o
icims_leicester.clno2.nc	o	o	o	o	o	o	o	o	o	o	o	o	o	o	o	o	o	o	o	o	+	+	+	+	+	+	+	+	+	o	o	o	o	o
caps_leicester.no2.nc	o	o	o	o	o	o	o	o	o	o	o	o	o	o	o	o	o	o	o	o	o	+	+	+	+	o	+	+	+	o	o	o	o	o
lif.rox.nc	o	o	o	+	+	+	+	+	+	+	+	+	o	+	+	+	+	+	+	+	+	+	+	+	+	+	+	+	+	+	+	o	+	o
lp_lif.koh.nc	+	+	+	+	+	+	+	+	+	+	+	+	+	+	+	+	+	+	+	+	+	+	+	o	+	+	+	+	+	+	+	o	+	o
ohdoas.all_param.nc	o	o	o	+	o	+	o	+	o	o	+	o	o	o	o	o	o	o	+	o	o	+	o	o	+	o	+	o	o	o	o	o	o	o
picarro_cfkads2290.co_co2_ch4_h2o.nc	o	o	o	o	o	o	o	o	o	o	o	o	+	+	+	o	o	o	o	o	o	o	o	o	o	+	+	+	o	o	o	+	+	+
picarro_cfkads2270.co_co2_ch4_h2o.nc	o	o	o	o	o	o	o	o	o	o	o	o	o	o	o	o	o	o	o	o	+	o	o	o	o	o	o	o	o	o	o	o	o	o
picarro_cfkads2109.co_co2_ch4_h2o.nc	+	+	+	+	+	+	+	+	+	+	+	+	+	+	+	+	+	+	+	+	+	+	+	+	+	+	+	+	+	+	+	+	+	+
picarro_lbds2006.hcho_h2o_ch4.nc	+	+	+	+	+	+	+	+	+	+	+	+	+	+	+	+	+	+	+	+	+	+	+	+	+	+	+	+	+	+	+	+	+	+
combined.o3.nc	+	+	+	+	+	+	+	+	+	+	+	+	+	+	+	+	+	+	+	+	+	+	+	+	+	+	+	+	+	+	+	+	+	+
ts_49i.o3.nc	+	+	+	+	+	+	+	+	+	+	+	+	+	+	+	+	+	+	+	+	+	+	+	+	+	+	+	+	+	+	+	+	+	+
an_41m.o3.nc	+	+	+	+	+	+	+	+	+	+	+	+	+	+	+	+	+	+	+	+	+	+	+	+	+	+	+	+	+	+	+	+	o	o
an_42m.o3.nc	o	o	o	o	o	o	o	o	o	o	o	o	o	o	o	o	o	o	o	o	o	o	o	o	o	o	o	o	o	o	o	o	o	o
an_42m#2.o3.nc	o	o	o	o	o	o	o	o	o	o	o	o	o	o	o	o	o	o	o	o	o	o	o	o	o	o	o	o	o	o	o	o	o	o
esa_42e.o3.nc	o	o	o	o	o	o	o	o	o	o	o	o	o	o	+	+	+	+	+	+	+	+	+	+	+	+	+	+	+	+	+	+	+	+
hetero-smps03.all_param.nc	o	o	o	+	+	+	+	+	+	+	+	+	+	+	+	+	+	o	+	+	+	+	+	o	+	+	+	+	+	+	+	o	+	o
hetero-tsi-cpc.number-conc.nc	o	o	o	o	o	o	o	o	o	o	o	o	o	o	o	o	o	o	o	o	o	o	o	o	o	o	o	o	o	o	o	o	o	o
hetero-cpc06.number-conc.nc	o	o	o	o	o	o	o	o	o	o	o	o	o	o	o	o	o	o	o	o	o	o	o	o	o	o	o	o	o	o	o	o	o	o
hetero-cpc08.number-conc.nc	o	o	o	+	+	o	+	+	+	+	o	+	+	+	+	+	+	o	+	+	+	o	o	o	o	o	+	+	+	+	+	o	+	o
zams.all_param.nc	o	o	o	o	+	+	+	+	+	o	o	o	o	o	o	o	o	o	o	o	o	o	o	o	o	o	o	+	+	+	+	o	o	o
zams.selected_param.nc	o	o	o	o	o	o	o	o	o	o	o	o	o	o	o	o	o	o	o	o	o	o	o	o	o	o	o	o	o	o	o	o	o	o
iams.all_param.nc	o	o	o	o	o	o	o	o	o	o	o	o	o	o	o	o	o	o	o	o	o	o	o	o	o	o	o	o	o	o	o	o	o	o
iams.selected_param.nc	o	o	o	o	o	o	o	o	o	o	o	o	o	o	o	o	o	o	o	o	o	o	o	o	o	o	o	o	o	o	o	o	o	o
vocus_h3o.voc.nc	o	o	o	+	+	+	+	+	+	+	+	+	o	+	+	+	+	+	+	+	+	+	+	+	+	+	+	+	+	+	+	+	o	o
ptrtofms_h3o.voc.nc	o	o	o	o	o	o	o	o	o	o	+	+	o	o	+	+	+	+	+	+	+	+	+	+	+	+	+	+	+	+	+	+	+	+
gc_fid_green.all_param.nc	o	o	o	+	+	+	+	+	+	+	+	+	+	+	+	+	+	+	+	+	+	+	+	+	+	+	+	+	+	+	+	+	+	+
gc_ms_green_fid.all_params.nc	o	o	o	o	o	o	o	o	o	o	o	o	o	o	o	o	o	o	o	o	o	o	o	o	o	o	o	o	o	o	o	o	o	o
icims_figaero_gas.all_param.nc	o	o	o	o	o	o	o	o	o	o	o	o	o	o	o	o	o	o	o	o	o	o	o	o	o	o	o	o	o	o	o	o	o	o
icims_figaero_particle.all_param.nc	o	o	o	o	o	o	o	o	o	o	o	o	o	o	o	o	o	o	o	o	o	o	o	o	o	o	o	o	o	o	o	o	o	o
pku_ceas.all_param.nc	o	o	o	o	o	o	o	o	o	o	o	o	o	o	o	o	o	o	o	o	o	o	o	o	o	o	o	o	o	o	o	o	o	o
ceas_pku.ans_pns_no2.nc	o	o	o	o	o	o	o	o	o	o	o	o	o	o	o	o	o	o	o	o	o	o	o	o	o	o	o	o	o	o	o	o	o	o
sps.all_param.10sec.nc	+	+	+	+	+	+	+	+	+	+	+	+	+	+	+	+	+	+	+	+	+	+	+	+	+	+	+	+	+	+	+	+	+	+
sps.all_param.60sec.nc	+	+	+	+	+	+	+	+	+	+	+	+	+	+	+	+	+	+	+	+	+	+	+	+	+	+	+	+	+	+	+	+	+	+
collected.all_param.nc	+	+	+	+	+	+	+	+	+	+	+	+	+	+	+	+	+	+	+	+	+	+	+	+	+	+	+	+	+	+	+	+	+	+
usa.all_param.nc	+	+	+	+	+	+	+	+	+	+	+	+	+	+	+	+	+	+	+	+	+	+	+	+	+	+	+	+	+	+	+	+	+	+
Photolysis frequencies	+	+	+	+	+	+	+	+	+	+	+	+	+	+	+	+	+	+	+	+	+	+	+	+	+	+	+	+	+	+	+	+	+	+

Table A 7: Overview of all available data detected during JULIAC-I. The data file name is the combination of instrument and param inform listed in Table A 6. Green filling in table means data existence. (Table credit: IEK-8, Forschungszentrum Jülich, 2019: Overview of available data files in the SAPHIR data archive)

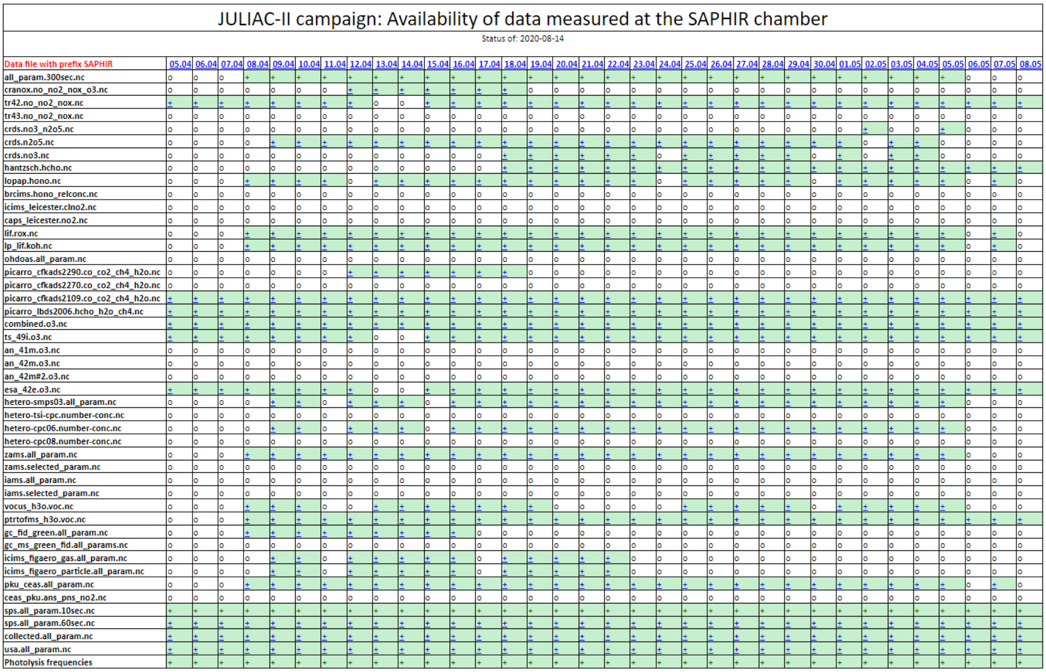

JULIAC-II campaign: Availability of data measured at the SAPHIR chamber

Status of: 2020-08-14

Data file with prefix SAPHIR	05.04	06.04	07.04	08.04	09.04	10.04	11.04	12.04	13.04	14.04	15.04	16.04	17.04	18.04	19.04	20.04	21.04	22.04	23.04	24.04	25.04	26.04	27.04	28.04	29.04	30.04	01.05	02.05	03.05	04.05	05.05	06.05	07.05	08.05
all_param.300sec.nc	o	o	o	+	+	+	+	+	+	+	+	+	+	+	+	+	+	+	+	+	+	+	+	+	+	+	+	+	+	+	+	o	o	o
cranox.no_no2_nox_o3.nc	o	o	o	o	o	o	o	+	+	+	+	+	+	+	o	o	o	o	o	o	o	o	o	o	o	o	o	o	o	o	o	o	o	o
tr42.no_no2_nox.nc	+	+	+	+	+	+	+	+	o	o	+	+	+	+	+	+	+	+	+	+	+	+	+	+	+	+	+	+	+	+	+	+	+	+
tr43.no_no2_nox.nc	o	o	o	o	o	o	o	o	o	o	o	o	o	o	o	o	o	o	o	o	o	o	o	o	o	o	o	o	o	o	o	o	o	o
crds.no3_n2o5.nc	o	o	o	o	o	o	o	o	o	o	o	o	o	o	o	o	o	o	o	o	o	o	o	o	o	o	o	+	o	o	+	o	o	o
crds.n2o5.nc	o	o	o	o	+	+	+	+	+	+	+	+	+	+	+	+	+	+	+	+	+	+	+	+	+	+	+	o	+	+	o	o	o	o
crds.no3.nc	o	o	o	o	o	o	o	o	o	o	o	o	o	+	+	+	+	+	+	o	+	+	+	+	+	o	+	o	+	+	o	o	o	o
hantzsch.hcho.nc	o	o	o	o	o	o	o	o	o	o	o	o	o	+	+	+	+	+	+	+	+	+	+	+	+	+	+	+	+	+	+	+	+	+
lopap.hono.nc	o	o	o	+	+	+	+	o	+	+	+	+	+	+	+	+	+	+	+	o	+	+	+	+	+	o	+	+	+	+	+	o	+	o
brcims.hono_relconc.nc	o	o	o	o	o	o	o	o	o	o	o	o	o	o	o	o	o	o	o	o	o	o	o	o	o	o	o	o	o	o	o	o	o	o
icims_leicester.clno2.nc	o	o	o	o	o	o	o	o	o	o	o	o	o	o	o	o	o	o	o	o	o	o	o	o	o	o	o	o	o	o	o	o	o	o
caps_leicester.no2.nc	o	o	o	o	o	o	o	o	o	o	o	o	o	o	o	o	o	o	o	o	o	o	o	o	o	o	o	o	o	o	o	o	o	o
lif.rox.nc	o	o	o	+	+	+	+	+	+	+	+	+	+	+	+	+	+	+	+	+	+	+	+	+	+	+	+	+	+	+	+	o	+	o
lp_lif.koh.nc	o	o	o	+	+	+	+	+	+	+	+	+	+	+	+	+	+	+	+	+	+	+	+	+	+	+	+	+	+	+	+	o	+	o
ohdoas.all_param.nc	o	o	o	o	o	o	o	o	o	o	o	o	o	o	o	o	o	o	o	o	o	o	o	o	o	o	o	o	o	o	o	o	o	o
picarro_cfkads2290.co_co2_ch4_h2o.nc	o	o	o	o	o	o	o	+	+	+	+	+	+	+	o	o	o	o	o	o	o	o	o	o	o	o	o	o	o	o	o	o	o	o
picarro_cfkads2270.co_co2_ch4_h2o.nc	o	o	o	o	o	o	o	o	o	o	o	o	o	o	o	o	o	o	o	o	o	o	o	o	o	o	o	o	o	o	o	o	o	o
picarro_cfkads2109.co_co2_ch4_h2o.nc	+	+	+	+	+	+	+	+	+	+	+	+	+	+	+	+	+	+	+	+	+	+	+	+	+	+	+	+	+	+	+	+	+	+
picarro_lbds2006.hcho_h2o_ch4.nc	+	+	+	+	+	+	+	+	+	+	+	+	+	+	+	+	+	+	+	+	+	+	+	+	+	+	+	+	+	+	+	+	+	+
combined.o3.nc	+	+	+	+	+	+	+	+	+	+	+	+	+	+	+	+	+	+	+	+	+	+	+	+	+	+	+	+	+	+	+	+	+	+
ts_49i.o3.nc	+	+	+	+	+	+	+	+	o	o	+	+	+	+	+	+	+	+	+	+	+	+	+	+	+	+	+	+	+	+	+	+	+	+
an_41m.o3.nc	o	o	o	o	o	o	o	o	o	o	o	o	o	o	o	o	o	o	o	o	o	o	o	o	o	o	o	o	o	o	o	o	o	o
an_42m.o3.nc	o	o	o	o	o	o	o	o	o	o	o	o	o	o	o	o	o	o	o	o	o	o	o	o	o	o	o	o	o	o	o	o	o	o
an_42m#2.o3.nc	o	o	o	o	o	o	o	o	o	o	o	o	o	o	o	o	o	o	o	o	o	o	o	o	o	o	o	o	o	o	o	o	o	o
esa_42e.o3.nc	+	+	+	+	+	+	+	+	o	o	+	+	+	+	+	+	+	+	+	+	+	+	+	+	+	+	+	+	+	+	+	+	+	+
hetero-smps03.all_param.nc	o	o	o	o	+	+	o	+	+	+	o	+	+	+	+	+	+	+	+	+	+	+	+	+	+	+	+	+	+	+	+	o	o	o
hetero-tsi-cpc.number-conc.nc	o	o	o	o	o	o	o	o	o	o	o	o	o	o	o	o	o	o	o	o	o	o	o	o	o	o	o	o	o	o	o	o	o	o
hetero-cpc06.number-conc.nc	o	o	o	o	+	+	o	+	+	+	o	+	+	+	+	+	+	+	+	+	+	+	+	+	+	+	+	+	+	+	+	o	o	o
hetero-cpc08.number-conc.nc	o	o	o	o	o	o	o	o	o	o	o	o	o	o	o	o	o	o	o	o	o	o	o	o	o	o	o	o	o	o	o	o	o	o
zams.all_param.nc	o	o	o	+	+	+	+	+	+	+	+	+	+	+	+	+	+	+	+	+	+	+	+	+	+	+	+	+	+	+	+	o	o	o
zams.selected_param.nc	o	o	o	o	o	o	o	o	o	o	o	o	o	o	o	o	o	o	o	o	o	o	o	o	o	o	o	o	o	o	o	o	o	o
iams.all_param.nc	o	o	o	o	o	o	o	o	o	o	o	o	o	o	o	o	o	o	o	o	o	o	o	o	o	o	o	o	o	o	o	o	o	o
iams.selected_param.nc	o	o	o	o	o	o	o	o	o	o	o	o	o	o	o	o	o	o	o	o	o	o	o	o	o	o	o	o	o	o	o	o	o	o
vocus_h3o.voc.nc	o	o	o	+	+	+	o	o	+	+	+	+	+	+	+	o	o	o	o	o	+	+	+	+	+	o	+	+	+	+	+	o	o	o
ptrtofms_h3o.voc.nc	o	o	o	+	+	+	+	+	+	+	+	+	+	+	+	+	+	+	+	+	+	+	+	+	+	+	+	+	+	+	+	+	+	+
gc_fid_green.all_param.nc	o	o	o	+	+	+	+	+	+	+	+	+	o	o	o	o	o	o	o	o	o	o	o	o	o	o	o	o	o	o	o	o	o	o
gc_ms_green_fid.all_params.nc	o	o	o	o	o	o	o	o	o	o	o	o	o	o	o	o	o	o	o	o	o	o	o	o	o	o	o	o	o	o	o	o	o	o
icims_figaero_gas.all_param.nc	o	o	o	o	+	+	o	+	+	+	+	+	o	+	+	+	+	+	o	o	o	o	o	o	o	o	o	o	o	o	o	o	o	o
icims_figaero_particle.all_param.nc	o	o	o	o	+	+	o	+	+	+	+	+	o	+	+	+	+	+	o	o	o	o	o	o	o	o	o	o	o	o	o	o	o	o
pku_ceas.all_param.nc	o	o	o	+	+	+	+	+	+	+	+	+	+	+	+	+	+	+	+	+	+	+	+	+	+	+	+	+	+	+	+	o	+	o
ceas_pku.ans_pns_no2.nc	o	o	o	o	o	o	o	o	o	o	o	o	o	o	o	o	o	o	o	o	o	o	o	o	o	o	o	o	o	o	o	o	o	o
sps.all_param.10sec.nc	+	+	+	+	+	+	+	+	+	+	+	+	+	+	+	+	+	+	+	+	+	+	+	+	+	+	+	+	+	+	+	+	+	+
sps.all_param.60sec.nc	+	+	+	+	+	+	+	+	+	+	+	+	+	+	+	+	+	+	+	+	+	+	+	+	+	+	+	+	+	+	+	+	+	+
collected.all_param.nc	+	+	+	+	+	+	+	+	+	+	+	+	+	+	+	+	+	+	+	+	+	+	+	+	+	+	+	+	+	+	+	+	+	+
usa.all_param.nc	+	+	+	+	+	+	+	+	+	+	+	+	+	+	+	+	+	+	+	+	+	+	+	+	+	+	+	+	+	+	+	+	+	+
Photolysis frequencies	+	+	+	+	+	+	+	+	+	+	+	+	+	+	+	+	+	+	+	+	+	+	+	+	+	+	+	+	+	+	+	+	+	+

Table A 8: Overview of all available data detected during JULIAC-II. Data file name is the combination of instrument and param inform listed in Table A 6. Green filling in table means data existence. (Table credit: IEK-8, Forschungszentrum Jülich , 2019: Overview of available data files in the SAPHIR data archive)

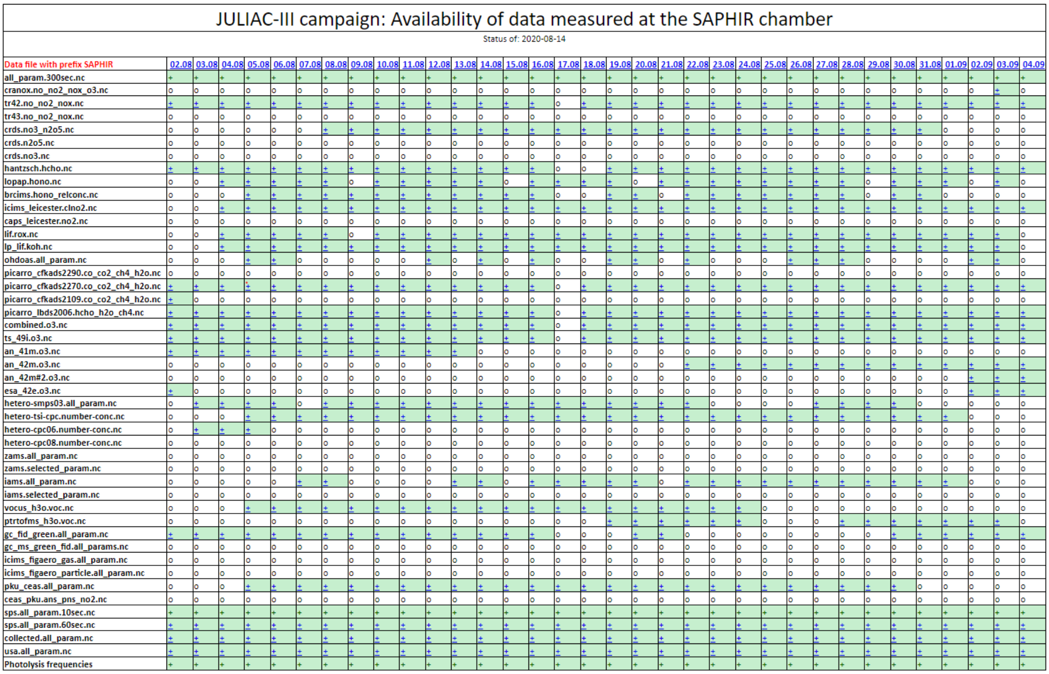

JULIAC-III campaign: Availability of data measured at the SAPHIR chamber

Status of: 2020-08-14

Data file with prefix SAPHIR	02.08	03.08	04.08	05.08	06.08	07.08	08.08	09.08	10.08	11.08	12.08	13.08	14.08	15.08	16.08	17.08	18.08	19.08	20.08	21.08	22.08	23.08	24.08	25.08	26.08	27.08	28.08	29.08	30.08	31.08	01.09	02.09	03.09	04.09
all_param.300sec.nc	+	+	+	+	+	+	+	+	+	+	+	+	+	+	+	+	+	+	+	+	+	+	+	+	+	+	+	+	+	+	+	+	+	+
cranox.no_no2_nox_o3.nc	o	o	o	o	o	o	o	o	o	o	o	o	o	o	o	o	o	o	o	o	o	o	o	o	o	o	o	o	o	o	o	o	+	o
tr42.no_no2_nox.nc	+	+	+	+	+	+	+	+	+	+	+	+	+	+	+	o	+	+	+	+	+	+	+	+	+	+	+	+	+	+	+	+	+	+
tr43.no_no2_nox.nc	o	o	o	o	o	o	o	o	o	o	o	o	o	o	o	o	o	o	o	o	o	o	o	o	o	o	o	o	o	o	o	o	o	o
crds.no3_n2o5.nc	o	o	o	o	o	o	+	+	+	+	+	+	+	+	+	+	+	+	+	+	+	+	+	+	+	+	+	+	+	+	o	o	o	o
crds.n2o5.nc	o	o	o	o	o	o	o	o	o	o	o	o	o	o	o	o	o	o	o	o	o	o	o	o	o	o	o	o	o	o	o	o	o	o
crds.no3.nc	o	o	o	o	o	o	o	o	o	o	o	o	o	o	o	o	o	o	o	o	o	o	o	o	o	o	o	o	o	o	o	o	o	o
hantzsch.hcho.nc	+	+	+	+	+	+	+	+	+	+	+	+	+	+	+	o	o	+	+	+	+	+	+	+	+	+	+	+	+	+	+	+	+	+
lopap.hono.nc	o	o	+	+	+	+	+	o	+	+	+	+	+	o	+	+	+	+	o	+	+	+	+	+	+	+	+	o	+	+	+	o	+	o
brcims.hono_relconc.nc	o	o	o	+	+	+	+	+	+	+	+	+	+	+	+	o	o	+	+	o	+	+	+	+	+	+	+	o	+	+	o	o	o	o
icims_leicester.clno2.nc	o	o	+	+	+	+	+	+	+	+	+	+	+	+	+	+	+	+	+	+	+	+	+	+	+	+	+	+	+	+	+	+	+	+
caps_leicester.no2.nc	o	o	o	o	o	o	o	o	o	o	o	o	o	o	o	o	o	o	o	o	o	o	o	o	o	o	o	o	o	o	o	o	o	o
lif.rox.nc	o	o	+	+	+	+	+	o	+	+	+	+	+	+	+	+	+	+	+	+	+	+	+	+	+	+	+	+	+	+	+	+	+	o
lp_lif.koh.nc	o	o	+	+	+	+	+	+	+	+	+	+	+	+	+	+	+	+	+	+	+	+	+	+	+	+	+	+	+	+	+	+	+	o
ohdoas.all_param.nc	o	o	o	+	+	o	o	o	o	o	+	o	+	o	+	o	o	+	+	o	+	o	o	o	+	+	+	o	o	o	o	+	+	o
picarro_cfkads2290.co_co2_ch4_h2o.nc	o	o	o	o	o	o	o	o	o	o	o	o	o	o	o	o	o	o	o	o	o	o	o	o	o	o	o	o	o	o	o	o	o	o
picarro_cfkads2270.co_co2_ch4_h2o.nc	+	+	+	+	+	+	+	+	+	+	+	+	+	+	+	o	+	+	+	+	+	+	+	+	+	+	+	+	+	+	+	+	+	+
picarro_cfkads2109.co_co2_ch4_h2o.nc	+	o	o	o	o	o	o	o	o	o	o	o	o	o	o	o	o	o	o	o	o	o	o	o	o	o	o	o	o	o	o	o	o	o
picarro_lbds2006.hcho_h2o_ch4.nc	+	+	+	+	+	+	+	+	+	+	+	+	+	+	+	o	+	+	+	+	+	+	+	+	+	+	+	+	+	+	+	+	+	+
combined.o3.nc	+	+	+	+	+	+	+	+	+	+	+	+	+	+	+	o	+	+	+	+	+	+	+	+	+	+	+	+	+	+	+	+	+	+
ts_49i.o3.nc	+	+	+	+	+	+	+	+	+	+	+	+	+	+	+	o	+	+	+	+	+	+	+	+	+	+	+	+	+	+	+	+	+	+
an_41m.o3.nc	+	+	+	+	+	+	+	+	+	+	+	+	o	o	o	o	o	o	o	o	o	o	o	o	o	o	o	o	o	o	o	o	o	o
an_42m.o3.nc	o	o	o	o	o	o	o	o	o	o	o	o	o	o	o	o	o	o	o	o	+	+	+	+	+	+	+	+	+	+	+	+	+	+
an_42m#2.o3.nc	o	o	o	o	o	o	o	o	o	o	o	o	o	o	o	o	o	o	o	o	o	o	o	o	o	o	o	o	o	o	o	+	+	+
esa_42e.o3.nc	+	o	o	o	o	o	o	o	o	o	o	o	o	o	o	o	o	o	o	o	o	o	o	o	o	o	o	o	o	o	o	+	+	+
hetero-smps03.all_param.nc	o	+	+	+	+	o	+	+	+	+	+	+	+	+	+	+	+	+	+	+	+	o	o	o	o	+	+	+	+	o	o	o	o	o
hetero-tsi-cpc.number-conc.nc	o	o	o	+	+	+	+	+	+	+	+	+	+	+	+	+	+	+	+	+	+	+	+	+	+	+	+	+	+	+	+	o	o	o
hetero-cpc06.number-conc.nc	o	+	+	+	o	o	o	o	o	o	o	o	o	o	o	o	o	o	o	o	o	o	o	o	o	o	o	o	o	o	o	o	o	o
hetero-cpc08.number-conc.nc	o	o	o	o	o	o	o	o	o	o	o	o	o	o	o	o	o	o	o	o	o	o	o	o	o	o	o	o	o	o	o	o	o	o
zams.all_param.nc	o	o	o	o	o	o	o	o	o	o	o	o	o	o	o	o	o	o	o	o	o	o	o	o	o	o	o	o	o	o	o	o	o	o
zams.selected_param.nc	o	o	o	o	o	o	o	o	o	o	o	o	o	o	o	o	o	o	o	o	o	o	o	o	o	o	o	o	o	o	o	o	o	o
iams.all_param.nc	o	o	o	o	o	+	+	o	o	o	o	+	+	o	+	+	+	+	+	o	+	+	+	+	+	+	+	+	+	+	+	o	o	o
iams.selected_param.nc	o	o	o	o	o	o	o	o	o	o	o	o	o	o	o	o	o	o	o	o	o	o	o	o	o	o	o	o	o	o	o	o	o	o
vocus_h3o.voc.nc	o	o	o	+	+	+	+	+	+	+	+	+	+	+	+	+	+	+	+	+	+	+	+	o	o	o	o	o	o	o	o	o	o	o
ptrtofms_h3o.voc.nc	o	o	o	o	o	o	o	o	o	o	o	o	o	o	o	o	o	+	+	+	+	+	+	o	o	o	+	+	+	+	+	+	+	o
gc_fid_green.all_param.nc	+	+	+	+	+	+	+	+	+	+	+	+	+	+	+	o	o	o	+	+	o	o	o	o	o	o	o	o	+	+	+	+	+	+
gc_ms_green_fid.all_params.nc	o	o	o	o	o	o	o	o	o	o	o	o	o	o	o	o	o	o	o	o	o	o	o	o	o	o	o	o	o	o	o	o	o	o
icims_figaero_gas.all_param.nc	o	o	o	o	o	o	o	o	o	o	o	o	o	o	o	o	o	o	o	o	o	o	o	o	o	o	o	o	o	o	o	o	o	o
icims_figaero_particle.all_param.nc	o	o	o	o	o	o	o	o	o	o	o	o	o	o	o	o	o	o	o	o	o	o	o	o	o	o	o	o	o	o	o	o	o	o
pku_ceas.all_param.nc	o	o	o	+	+	+	+	+	+	+	+	+	+	+	+	+	+	+	+	+	+	+	+	+	+	+	+	+	+	o	o	o	o	o
ceas_pku.ans_pns_no2.nc	o	o	o	o	o	o	o	o	o	o	o	o	o	o	o	o	o	o	o	o	o	o	o	o	o	o	o	o	o	o	o	o	o	o
sps.all_param.10sec.nc	+	+	+	+	+	+	+	+	+	+	+	+	+	+	+	+	+	+	+	+	+	+	+	+	+	+	+	+	+	+	+	+	+	+
sps.all_param.60sec.nc	+	+	+	+	+	+	+	+	+	+	+	+	+	+	+	+	+	+	+	+	+	+	+	+	+	+	+	+	+	+	+	+	+	+
collected.all_param.nc	+	+	+	+	+	+	+	+	+	+	+	+	+	+	+	+	+	+	+	+	+	+	+	+	+	+	+	+	+	+	+	+	+	+
usa.all_param.nc	+	+	+	+	+	+	+	+	+	+	+	+	+	+	+	+	+	+	+	+	+	+	+	+	+	+	+	+	+	+	+	+	+	+
Photolysis frequencies	+	+	+	+	+	+	+	+	+	+	+	+	+	+	+	+	+	+	+	+	+	+	+	+	+	+	+	+	+	+	+	+	+	+

Table A 9: Overview of all available data detected during the JULIAC-III. Data file name is the combination of instrument and param inform listed in Table A 6. Green filling in table means data existence. (Table credit : IEK-8, Forschungszentrum Jülich , 2019: Overview of available data files in the SAPHIR data archive).

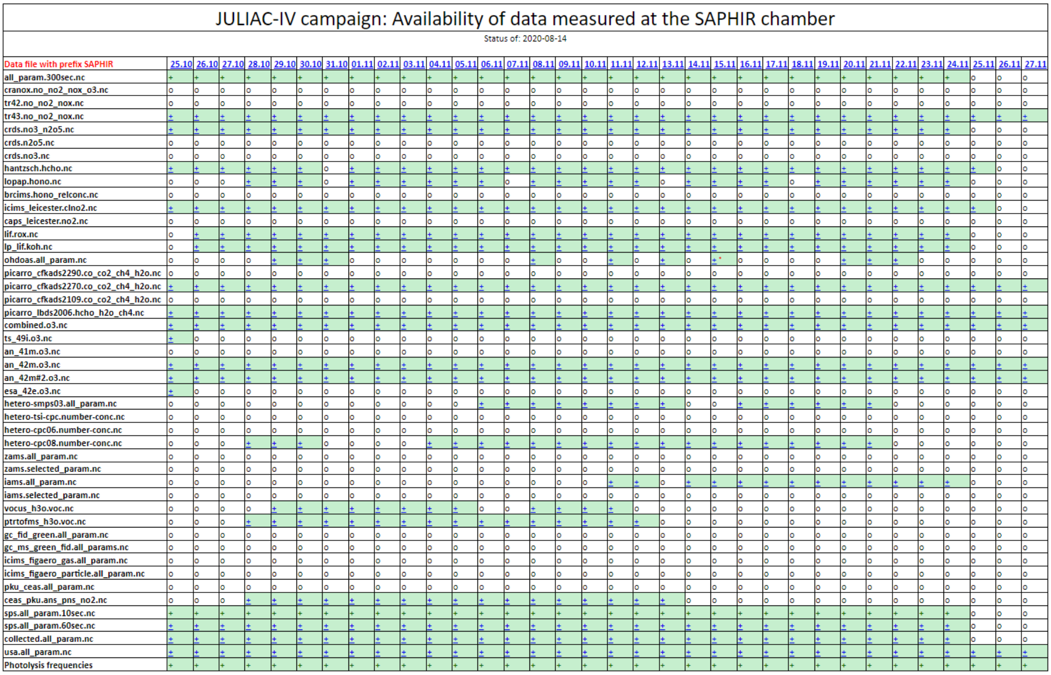

JULIAC-IV campaign: Availability of data measured at the SAPHIR chamber

Status of: 2020-08-14

Data file with prefix SAPHIR	25.10	26.10	27.10	28.10	29.10	30.10	31.10	01.11	02.11	03.11	04.11	05.11	06.11	07.11	08.11	09.11	10.11	11.11	12.11	13.11	14.11	15.11	16.11	17.11	18.11	19.11	20.11	21.11	22.11	23.11	24.11	25.11	26.11	27.11
all_param.300sec.nc	+	+	+	+	+	+	+	+	+	+	+	+	+	+	+	+	+	+	+	+	+	+	+	+	+	+	+	+	+	+	+	o	o	o
cranox.no_no2_nox_o3.nc	o	o	o	o	o	o	o	o	o	o	o	o	o	o	o	o	o	o	o	o	o	o	o	o	o	o	o	o	o	o	o	o	o	o
tr42.no_no2_nox.nc	o	o	o	o	o	o	o	o	o	o	o	o	o	o	o	o	o	o	o	o	o	o	o	o	o	o	o	o	o	o	o	o	o	o
tr43.no_no2_nox.nc	+	+	+	+	+	+	+	+	+	+	+	+	+	+	+	+	+	+	+	+	+	+	+	+	+	+	+	+	+	+	+	+	+	+
crds.no3_n2o5.nc	+	+	+	+	+	+	+	+	+	+	+	+	+	+	+	+	+	+	+	+	+	+	+	+	+	+	+	+	+	+	+	o	o	o
crds.n2o5.nc	o	o	o	o	o	o	o	o	o	o	o	o	o	o	o	o	o	o	o	o	o	o	o	o	o	o	o	o	o	o	o	o	o	o
crds.no3.nc	o	o	o	o	o	o	o	o	o	o	o	o	o	o	o	o	o	o	o	o	o	o	o	o	o	o	o	o	o	o	o	o	o	o
hantzsch.hcho.nc	+	+	+	+	+	+	o	+	+	+	+	+	+	+	+	+	+	+	+	+	+	+	+	+	+	+	+	+	+	+	+	+	o	o
lopap.hono.nc	o	o	o	+	+	+	o	+	+	+	+	+	+	o	+	+	+	+	+	o	+	+	+	+	o	+	+	+	+	+	+	o	o	o
brcims.hono_relconc.nc	o	o	o	o	o	o	o	o	o	o	o	o	o	o	o	o	o	o	o	o	o	o	o	o	o	o	o	o	o	o	o	o	o	o
icims_leicester.clno2.nc	+	+	+	+	+	+	+	+	+	+	+	+	+	+	+	+	+	+	+	+	+	+	+	+	+	+	+	+	+	+	+	+	o	o
caps_leicester.no2.nc	o	o	o	o	o	o	o	o	o	o	o	o	o	o	o	o	o	o	o	o	o	o	o	o	o	o	o	o	o	o	o	o	o	o
lif.rox.nc	o	+	+	+	+	+	+	+	+	+	+	+	+	+	+	+	+	+	+	+	+	+	+	+	+	+	+	+	+	+	+	o	o	o
lp_lif.koh.nc	o	+	+	+	+	+	+	+	+	+	+	+	+	+	+	+	+	+	+	+	+	+	+	+	+	+	+	+	+	+	+	o	o	o
ohdoas.all_param.nc	o	o	o	o	+	+	+	o	o	o	o	o	o	o	+	o	o	+	o	+	o	+ *	o	o	o	o	+	+	+	o	o	o	o	o
picarro_cfkads2290.co_co2_ch4_h2o.nc	o	o	o	o	o	o	o	o	o	o	o	o	o	o	o	o	o	o	o	o	o	o	o	o	o	o	o	o	o	o	o	o	o	o
picarro_cfkads2270.co_co2_ch4_h2o.nc	+	+	+	+	+	+	+	+	+	+	+	+	+	+	+	+	+	+	+	+	+	+	+	+	+	+	+	+	+	+	+	+	+	+
picarro_cfkads2109.co_co2_ch4_h2o.nc	o	o	o	o	o	o	o	o	o	o	o	o	o	o	o	o	o	o	o	o	o	o	o	o	o	o	o	o	o	o	o	o	o	o
picarro_lbds2006.hcho_h2o_ch4.nc	+	+	+	+	+	+	+	+	+	+	+	+	+	+	+	+	+	+	+	+	+	+	+	+	+	+	+	+	+	+	+	+	+	+
combined.o3.nc	+	+	+	+	+	+	+	+	+	+	+	+	+	+	+	+	+	+	+	+	+	+	+	+	+	+	+	+	+	+	+	+	+	+
ts_49i.o3.nc	+	o	o	o	o	o	o	o	o	o	o	o	o	o	o	o	o	o	o	o	o	o	o	o	o	o	o	o	o	o	o	o	o	o
an_41m.o3.nc	o	o	o	o	o	o	o	o	o	o	o	o	o	o	o	o	o	o	o	o	o	o	o	o	o	o	o	o	o	o	o	o	o	o
an_42m.o3.nc	+	+	+	+	+	+	+	+	+	+	+	+	+	+	+	+	+	+	+	+	+	+	+	+	+	+	+	+	+	+	+	+	+	+
an_42m#2.o3.nc	+	+	+	+	+	+	+	+	+	+	+	+	+	+	+	+	+	+	+	+	+	+	+	+	+	+	+	+	+	+	+	+	+	+
esa_42e.o3.nc	+	o	o	o	o	o	o	o	o	o	o	o	o	o	o	o	o	o	o	o	o	o	o	o	o	o	o	o	o	o	o	o	o	o
hetero-smps03.all_param.nc	o	o	o	o	o	o	o	o	o	o	o	o	+	+	+	+	+	+	+	+	o	o	+	+	+	+	+	+	o	o	o	o	o	o
hetero-tsi-cpc.number-conc.nc	o	o	o	o	o	o	o	o	o	o	o	o	o	o	o	o	o	o	o	o	o	o	o	o	o	o	o	o	o	o	o	o	o	o
hetero-cpc06.number-conc.nc	o	o	o	o	o	o	o	o	o	o	o	o	o	o	o	o	o	o	o	o	o	o	o	o	o	o	o	o	o	o	o	o	o	o
hetero-cpc08.number-conc.nc	o	o	o	+	+	+	o	o	o	o	+	+	+	+	+	+	+	+	+	+	+	+	+	+	+	+	+	+	o	o	o	o	o	o
zams.all_param.nc	o	o	o	o	o	o	o	o	o	o	o	o	o	o	o	o	o	o	o	o	o	o	o	o	o	o	o	o	o	o	o	o	o	o
zams.selected_param.nc	o	o	o	o	o	o	o	o	o	o	o	o	o	o	o	o	o	o	o	o	o	o	o	o	o	o	o	o	o	o	o	o	o	o
iams.all_param.nc	o	o	o	o	o	o	o	o	o	o	o	o	o	o	o	o	o	+	+	o	+	+	+	+	+	+	+	+	+	+	+	o	o	o
iams.selected_param.nc	o	o	o	o	o	o	o	o	o	o	o	o	o	o	o	o	o	o	o	o	o	o	o	o	o	o	o	o	o	o	o	o	o	o
vocus_h3o.voc.nc	o	o	o	o	+	+	+	+	+	+	+	+	o	o	+	+	+	+	o	o	o	o	o	o	o	o	o	o	o	o	o	o	o	o
ptrtofms_h3o.voc.nc	o	o	o	+	+	+	+	+	+	+	+	+	+	+	+	+	+	+	+	o	o	o	o	o	o	o	o	o	o	o	o	o	o	o
gc_fid_green.all_param.nc	o	o	o	o	o	o	o	o	o	o	o	o	o	o	o	o	o	o	o	o	o	o	o	o	o	o	o	o	o	o	o	o	o	o
gc_ms_green_fid.all_params.nc	o	o	o	o	o	o	o	o	o	o	o	o	o	o	o	o	o	o	o	o	o	o	o	o	o	o	o	o	o	o	o	o	o	o
icims_figaero_gas.all_param.nc	o	o	o	o	o	o	o	o	o	o	o	o	o	o	o	o	o	o	o	o	o	o	o	o	o	o	o	o	o	o	o	o	o	o
icims_figaero_particle.all_param.nc	o	o	o	o	o	o	o	o	o	o	o	o	o	o	o	o	o	o	o	o	o	o	o	o	o	o	o	o	o	o	o	o	o	o
pku_ceas.all_param.nc	o	o	o	o	o	o	o	o	o	o	o	o	o	o	o	o	o	o	o	o	o	o	o	o	o	o	o	o	o	o	o	o	o	o
ceas_pku.ans_pns_no2.nc	o	o	o	+	+	+	+	+	+	+	+	+	+	+	+	+	+	+	+	+	o	o	o	o	o	o	o	o	o	o	o	o	o	o
sps.all_param.10sec.nc	+	+	+	+	+	+	+	+	+	+	+	+	+	+	+	+	+	+	+	+	+	+	+	+	+	+	+	+	+	+	+	o	o	o
sps.all_param.60sec.nc	+	+	+	+	+	+	+	+	+	+	+	+	+	+	+	+	+	+	+	+	+	+	+	+	+	+	+	+	+	+	+	o	o	o
collected.all_param.nc	+	+	+	+	+	+	+	+	+	+	+	+	+	+	+	+	+	+	+	+	+	+	+	+	+	+	+	+	+	+	+	o	o	o
usa.all_param.nc	+	+	+	+	+	+	+	+	+	+	+	+	+	+	+	+	+	+	+	+	+	+	+	+	+	+	+	+	+	+	+	+	+	+
Photolysis frequencies	+	+	+	+	+	+	+	+	+	+	+	+	+	+	+	+	+	+	+	+	+	+	+	+	+	+	+	+	+	+	+	+	+	+

Table A 10: Overview of all available data detected during the JULIAC-IV. Data file name is the combination of instrument and param inform listed in Table A 6. Green filling in table means data existence. (Table credit : IEK-8, , Forschungszentrum Jülich , 2019: Overview of available data files in the SAPHIR data archive)

A. 13 Map of wildfire counts

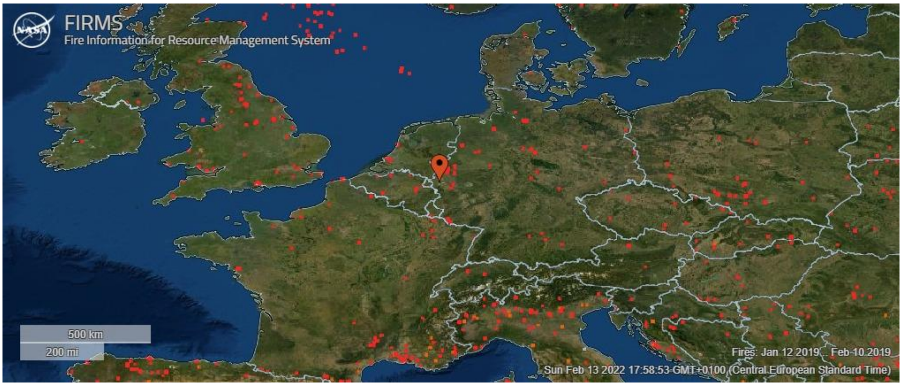

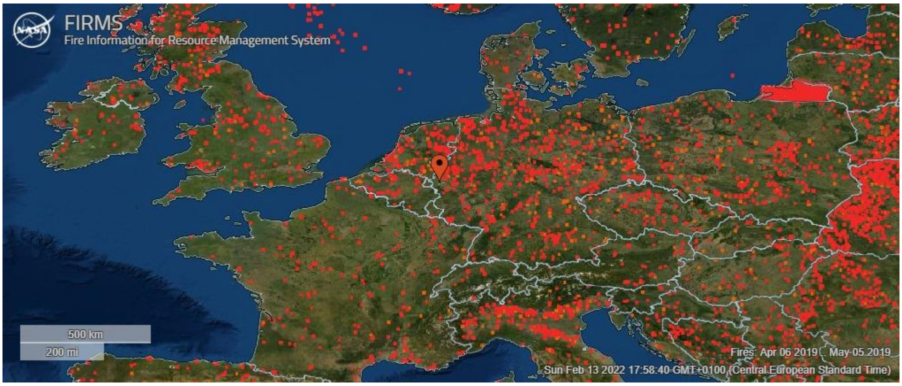

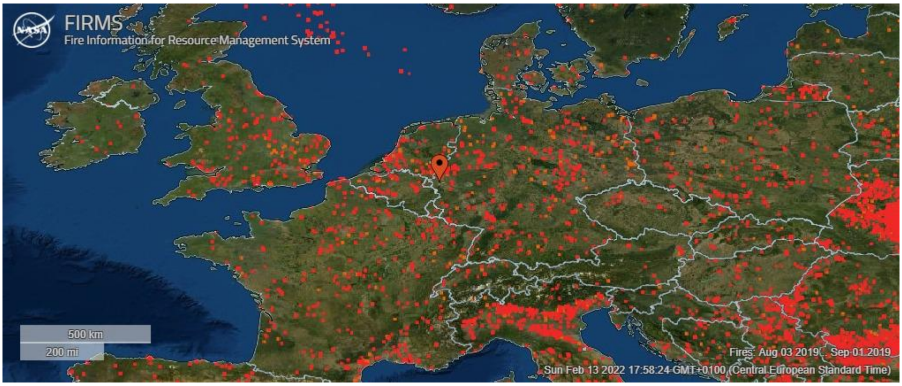

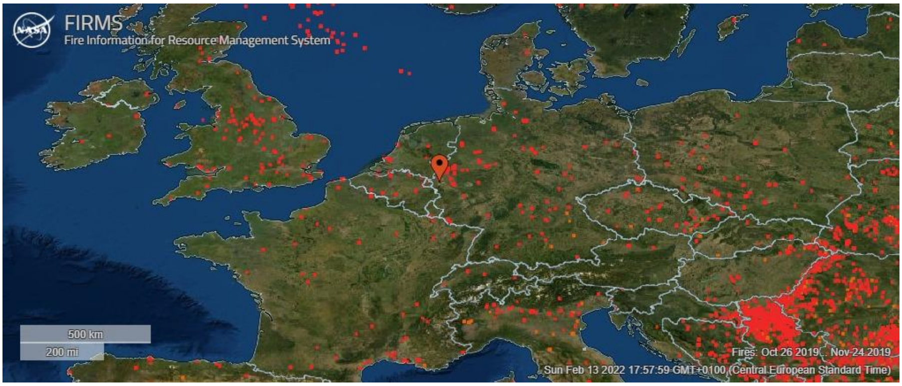

Figure A 15: Wildfire counts map during the JULIAC campaign, from top to bottom corresponding JULIAC-I to IV, supplied by Fire Information for Resource Management System (FIRMS) of NASA, https://firms.modaps.eosdis.nasa.gov/.

A. 14 NB-OOA diurnal variation supplement

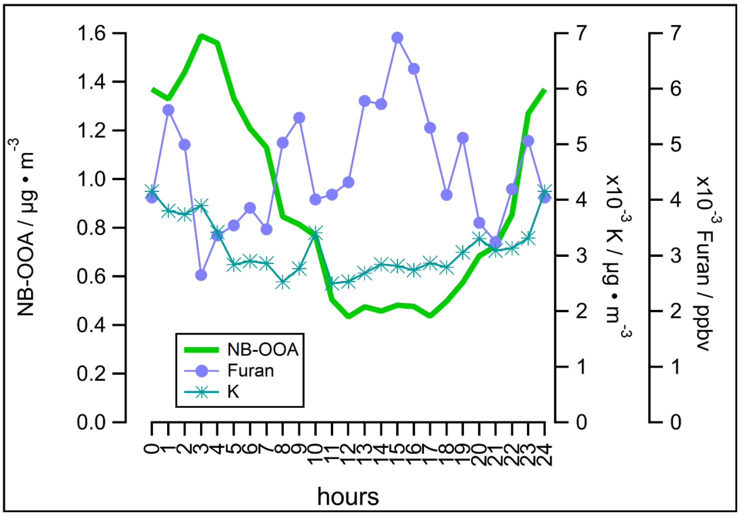

Figure A 16: Diurnal pattern of the averaged concentrations of NB-OOA factors and tracers for biomass burning (aerosol potassium, furan NB-OOA formation mechanism investigation.

List of Figures and Tables

List of Figures

List of Tables

Abbreviation

AMS	Aerosol Mass Spectrometer
BBOA	Biomass Burning Organic Aerosol
bbVOCs	Biomass Burning Volatile Organic Compounds
BLH	Boundary Layer Height
BVOCs	Biogenic Volatile Organic Compounds
CPC	Condensation Particle Counter
HOA	Hydrocarbon-Like Organic Aerosol
HR-TOF-AMS	High-Resolution Time-Of-Flight Aerosol Mass Spectrometer
HYSPLIT	Hybrid Single-Particle Lagrangian Integrated Trajectory
JULIAC	Jülich Atmospheric Chemistry Project
LO-OOA	Less Oxidized Oxygenated Organic Aerosol
MO-OOA	More Oxidized Oxygenated Organic Aerosol
MSA	Methanesulfonic Acid
MSA-OA	Methanesulfonic Acid-Containing Organic Aerosol
Nbb-OOA	Biomass Burning VOCs Dominated Nocturnal Oxidation Oxygenated Organic Aerosol
NBL	Nocturnal Boundary Layer
NB-OOA	Biogenic VOCs Dominated Nocturnal Oxidation Oxygenated Organic Aerosol
NF-PM1	Non-Refractory Submicron Particles
NO-OOA	Nocturnal Oxidation Oxygenated Organic Aerosol

NRW	Non-Parametric Wind Regressions
OA	Organic Aerosol
OOA	Oxygenated Organic Aerosol
PM1	Submicron Particles
PMF	Positive Matrix Factorization
POA	Primary Organic Aerosol
SAPHIR	Simulation of Atmospheric Photochemistry in a Large Reaction Chamber
SMPS	Scanning Mobility Particle Sizer
SOA	Secondary Organic Aerosol
Trans-OA	Continental Regional Transport Organic Aerosol
VOCs	Volatile Organic Compounds

References

Aiken, A.C., DeCarlo, P.F. and Jimenez, J.L. (2007). Elemental analysis of organic species with electron ionization high-resolution mass spectrometry. Analytical Chemistry **79**(21): 8350-8358.

Aiken, A.C., de Foy, B., Wiedinmyer, C., DeCarlo, P.F., Ulbrich, I.M., Wehrli, M.N., Szidat, S., Prevot, A.S.H., Noda, J., Wacker, L., Volkamer, R., Fortner, E., Wang, J., Laskin, A., Shutthanandan, V., Zheng, J., Zhang, R., Paredes-Miranda, G., Arnott, W.P., Molina, L.T., Sosa, G., Querol, X. and Jimenez, J.L. (2010). Mexico city aerosol analysis during milagro using high resolution aerosol mass spectrometry at the urban supersite (t0) – part 2: Analysis of the biomass burning contribution and the non-fossil carbon fraction. Atmos. Chem. Phys. **10**(12): 5315-5341.

Aiken, A.C., DeCarlo, P.F., Kroll, J.H., Worsnop, D.R., Huffman, J.A., Docherty, K.S., Ulbrich, I.M., Mohr, C., Kimmel, J.R., Sueper, D., Sun, Y., Zhang, Q., Trimborn, A., Northway, M., Ziemann, P.J., Canagaratna, M.R., Onasch, T.B., Alfarra, M.R., Prevot, A.S.H., Dommen, J., Duplissy, J., Metzger, A., Baltensperger, U. and Jimenez, J.L. (2008). O/c and om/oc ratios of primary, secondary, and ambient organic aerosols with high-resolution time-of-flight aerosol mass spectrometry. Environmental Science & Technology **42**(12): 4478-4485.

Aiken, A.C., Salcedo, D., Cubison, M.J., Huffman, J.A., DeCarlo, P.F., Ulbrich, I.M., Docherty, K.S., Sueper, D., Kimmel, J.R., Worsnop, D.R., Trimborn, A., Northway, M., Stone, E.A., Schauer, J.J., Volkamer, R.M., Fortner, E., de Foy, B., Wang, J., Laskin, A., Shutthanandan, V., Zheng, J., Zhang, R., Gaffney, J., Marley, N.A., Paredes-Miranda, G., Arnott, W.P., Molina, L.T., Sosa, G. and Jimenez, J.L. (2009). Mexico city aerosol analysis during milagro using high resolution aerosol mass spectrometry at the urban supersite (t0) – part 1: Fine particle composition and organic source apportionment. Atmos. Chem. Phys. **9**(17): 6633-6653.

Akherati, A., He, Y., Coggon, M.M., Koss, A.R., Hodshire, A.L., Sekimoto, K., Warneke, C., de Gouw, J., Yee, L., Seinfeld, J.H., Onasch, T.B., Herndon, S.C., Knighton, W.B., Cappa, C.D., Kleeman, M.J., Lim, C.Y., Kroll, J.H., Pierce, J.R. and Jathar, S.H. (2020). Oxygenated aromatic compounds are important precursors of secondary organic aerosol in biomass-burning emissions. Environmental Science & Technology **54**(14): 8568-8579.

Alfarra, M.R., Prevot, A.S.H., Szidat, S., Sandradewi, J., Weimer, S., Lanz, V.A., Schreiber, D., Mohr, M. and Baltensperger, U. (2007). Identification of the mass spectral signature of organic aerosols from wood burning emissions. Environmental Science & Technology **41**(16): 5770-5777.

Alfarra, M.R., Coe, H., Allan, J.D., Bower, K.N., Boudries, H., Canagaratna, M.R., Jimenez, J.L., Jayne, J.T., Garforth, A.A., Li, S.-M. and Worsnop, D.R. (2004). Characterization of urban and rural organic particulate in the lower fraser valley using two aerodyne aerosol mass spectrometers. Atmospheric Environment **38**(34): 5745-5758.

Allan, J.D., Jimenez, J.L., Williams, P.I., Alfarra, M.R., Bower, K.N., Jayne, J.T., Coe, H. and Worsnop, D.R. (2003). Quantitative sampling using an aerodyne aerosol mass spectrometer: 1. Techniques of data interpretation and error analysis (vol 108, art no 4090, 2003). Journal of Geophysical Research-Atmospheres **108**(D9).

Atkinson, R. (1991). Kinetics and mechanisms of the gas-phase reactions of the no3 radical with organic compounds. Journal of Physical and Chemical Reference Data **20**(3): 459-507.

Atkinson, R. and Aschmann, S.M. (1986). Kinetics of the reactions of naphthalene, 2-methylnaphthalene, and 2,3-dimethylnaphthalene with oh radicals and with o3 at 295 ± 1 k. International Journal of Chemical Kinetics **18**(5): 569-573.

Atkinson, R. and Arey, J. (2003). Gas-phase tropospheric chemistry of biogenic volatile organic compounds: A review. Atmospheric Environment **37**: 197-219.

Atkinson, R. and Arey, J. (2007). Mechanisms of the gas-phase reactions of aromatic hydrocarbons and pahs with oh and no 3 radicals. Polycyclic Aromatic Compounds **27**(1): 15-40.

Atkinson, R., Aschmann, S.M. and Carter, W.P.L. (1983). Kinetics of the reactions of o3 and oh radicals with furan and thiophene at 298 ± 2 k. International Journal of Chemical Kinetics **15**(1): 51-61.

Ayres, B.R., Allen, H.M., Draper, D.C., Brown, S.S., Wild, R.J., Jimenez, J.L., Day, D.A., Campuzano-Jost, P., Hu, W., de Gouw, J., Koss, A., Cohen, R.C., Duffey, K.C., Romer, P., Baumann, K., Edgerton, E., Takahama, S., Thornton, J.A., Lee, B.H., Lopez-Hilfiker, F.D., Mohr, C., Wennberg, P.O., Nguyen, T.B., Teng, A., Goldstein, A.H., Olson, K. and Fry, J.L. (2015). Organic nitrate aerosol formation via no₃ + biogenic volatile organic compounds in the southeastern united states. Atmos. Chem. Phys. **15**(23): 13377-13392.

Batchvarova, E. and Gryning, S.-E. (1994). An applied model for the height of the daytime mixed layer and the entrainment zone. Boundary-Layer Meteorology **71**(3): 311-323.

Bohn, B. and Zilken, H. (2005a). Model-aided radiometric determination of photolysis frequencies in a sunlit atmosphere simulation chamber. Atmos. Chem. Phys. **5**(1): 191-206.

Bohn, B., Rohrer, F., Brauers, T. and Wahner, A. (2005b). Actinometric measurements of no₂ photolysis frequencies in the atmosphere simulation chamber saphir. Atmos. Chem. Phys. **5**(2): 493-503.

Bolton, D. (1980). The computation of equivalent potential temperature. Monthly Weather Review **108**(7): 1046-1053.

Boucher, O., Randall, D., Artaxo, P., Bretherton, C., Feingold, G., Forster, P., Kerminen, V.M., Kondo, Y., Liao, H., Lohmann, U., Rasch, P., Satheesh, S.K., Sherwood, S., Stevens, B. and Zhang, X.Y. (2013). Clouds and aerosols. Climate change 2013: The physical science basis. Contribution of working group i to the fifth assessment report of the intergovernmental panel on climate change. T. F. Stocker , D. Qin , G. K. Plattner et al. Cambridge, UK, Cambridge University Press**:** 571-657.

Boyd, C.M., Nah, T., Xu, L., Berkemeier, T. and Ng, N.L. (2017). Secondary organic aerosol (soa) from nitrate radical oxidation of monoterpenes: Effects of temperature, dilution, and humidity on aerosol formation, mixing, and evaporation. Environmental Science & Technology **51**(14): 7831-7841.

Brown, S.S., Dubé, W.P., Osthoff, H.D., Wolfe, D.E., Angevine, W.M. and Ravishankara, A.R. (2007). High resolution vertical distributions of no₃ and n₂o₅ through the nocturnal boundary layer. Atmos. Chem. Phys. **7**(1): 139-149.

Brown, S.S., Stark, H., Ryerson, T.B., Williams, E.J., Nicks, D.K., Trainer, M., Fehsenfeld, F.C. and Ravishankara, A.R. (2003). Nitrogen oxides in the nocturnal boundary layer: Simultaneous in situ measurements of no3, n2o5, no2, no, and o3. Journal of Geophysical Research: Atmospheres **108**(D9): n/a-n/a.

Brown, S.S., deGouw, J.A., Warneke, C., Ryerson, T.B., Dubé, W.P., Atlas, E., Weber, R.J., Peltier, R.E., Neuman, J.A., Roberts, J.M., Swanson, A., Flocke, F., McKeen, S.A., Brioude, J., Sommariva, R., Trainer, M., Fehsenfeld, F.C. and Ravishankara, A.R. (2009). Nocturnal isoprene oxidation over the northeast united states in summer and its impact on reactive nitrogen partitioning and secondary organic aerosol. Atmos. Chem. Phys. **9**(9): 3027-3042.

Brown, S.S., Dubé, W.P., Bahreini, R., Middlebrook, A.M., Brock, C.A., Warneke, C., de Gouw, J.A., Washenfelder, R.A., Atlas, E., Peischl, J., Ryerson, T.B., Holloway, J.S., Schwarz, J.P., Spackman, R., Trainer, M., Parrish, D.D., Fehshenfeld, F.C. and Ravishankara, A.R. (2013). Biogenic voc oxidation and organic aerosol formation in an urban nocturnal boundary layer: Aircraft vertical profiles in houston, tx. Atmospheric Chemistry and Physics **13**(22): 11317-11337.

Brownwood, B., Turdziladze, A., Hohaus, T., Wu, R., Mentel, T.F., Carlsson, P.T.M., Tsiligiannis, E., Hallquist, M., Andres, S., Hantschke, L., Reimer, D., Rohrer, F., Tillmann, R., Winter, B., Liebmann, J., Brown, S.S., Kiendler-Scharr, A., Novelli, A., Fuchs, H. and Fry, J.L. (2021). Gas-particle partitioning and soa yields of organonitrate products from no3-initiated oxidation of isoprene under varied chemical regimes. ACS Earth Space Chem **5**(4): 785-800.

Budisulistiorini, S.H., Li, X., Bairai, S.T., Renfro, J., Liu, Y., Liu, Y.J., McKinney, K.A., Martin, S.T., McNeill, V.F., Pye, H.O.T., Nenes, A., Neff, M.E., Stone, E.A., Mueller, S., Knote, C., Shaw, S.L., Zhang, Z., Gold, A. and Surratt, J.D. (2015). Examining the effects of anthropogenic emissions on isoprene-derived secondary organic aerosol formation during the 2013 southern oxidant and aerosol study (soas) at the look rock, tennessee ground site. Atmospheric Chemistry and Physics **15**(15): 8871-8888.

Cabañas, B., Baeza, M.T., Salgado, S., Martín, P., Taccone, R. and Martínez, E. (2004). Oxidation of heterocycles in the atmosphere: Kinetic study of their reactions with no3 radical. The Journal of Physical Chemistry A **108**(49): 10818-10823.

Canagaratna, M.R., Onasch, T.B., Wood, E.C., Herndon, S.C., Jayne, J.T., Cross, E.S., Miake-Lye, R.C., Kolb, C.E. and Worsnop, D.R. (2010). Evolution of vehicle exhaust particles in the atmosphere. Journal of the Air & Waste Management Association **60**(10): 1192-1203.

Canagaratna, M.R., Jayne, J.T., Ghertner, D.A., Herndon, S., Shi, Q., Jimenez, J.L., Silva, P.J., Williams, P., Lanni, T., Drewnick, F., Demerjian, K.L., Kolb, C.E. and Worsnop, D.R. (2004). Chase studies of particulate emissions from in-use new york city vehicles. Aerosol Science and Technology **38**(6): 555-573.

Canagaratna, M.R., Jimenez, J.L., Kroll, J.H., Chen, Q., Kessler, S.H., Massoli, P., Hildebrandt Ruiz, L., Fortner, E., Williams, L.R., Wilson, K.R., Surratt, J.D., Donahue, N.M., Jayne, J.T. and Worsnop, D.R. (2015). Elemental ratio measurements of organic compounds using aerosol mass spectrometry: Characterization, improved calibration, and implications. Atmos. Chem. Phys. **15**(1): 253-272.

Canagaratna, M.R., Jayne, J.T., Jimenez, J.L., Allan, J.D., Alfarra, M.R., Zhang, Q., Onasch, T.B., Drewnick, F., Coe, H., Middlebrook, A., Delia, A., Williams, L.R., Trimborn, A.M., Northway, M.J., DeCarlo, P.F., Kolb, C.E., Davidovits, P. and Worsnop, D.R. (2007a). Chemical and microphysical characterization of ambient aerosols with the aerodyne aerosol mass spectrometer. Mass Spectrometry Reviews **26**(2): 185-222.

Canagaratna, M.R., Jayne, J.T., Jimenez, J.L., Allan, J.D., Alfarra, M.R., Zhang, Q., Onasch, T.B., Drewnick, F., Coe, H., Middlebrook, A., Delia, A., Williams, L.R., Trimborn, A.M., Northway, M.J., DeCarlo, P.F., Kolb, C.E., Davidovits, P. and Worsnop, D.R. (2007b). Chemical and microphysical characterization of ambient aerosols with the aerodyne aerosol mass spectrometer. Mass Spectrom Rev **26**(2): 185-222.

Canonaco, F., Slowik, J.G., Baltensperger, U. and Prévôt, A.S.H. (2015). Seasonal differences in oxygenated organic aerosol composition: Implications for emissions sources and factor analysis. Atmospheric Chemistry and Physics **15**(12): 6993-7002.

Canonaco, F., Crippa, M., Slowik, J.G., Baltensperger, U. and Prévôt, A.S.H. (2013). Sofi, an igor-based interface for the efficient use of the generalized multilinear engine (me-2) for the source apportionment: Me-2 application to aerosol mass spectrometer data. Atmos. Meas. Tech. **6**(12): 3649-3661.

Capes, G., Johnson, B., McFiggans, G., Williams, P.I., Haywood, J. and Coe, H. (2008). Aging of biomass burning aerosols over west africa: Aircraft measurements of chemical composition, microphysical properties, and emission ratios. Journal of Geophysical Research: Atmospheres **113**(D23).

Charlson, R.J., Lovelock, J.E., Andreae, M.O. and Warren, S.G. (1987). Oceanic phytoplankton, atmospheric sulphur, cloud albedo and climate. Nature **326**(6114): 655-661.

Chen, Q., Farmer, D.K., Rizzo, L.V., Pauliquevis, T., Kuwata, M., Karl, T.G., Guenther, A., Allan, J.D., Coe, H., Andreae, M.O., Pöschl, U., Jimenez, J.L., Artaxo, P. and Martin, S.T. (2015). Submicron particle mass concentrations and sources in the amazonian wet season (amaze-08). Atmospheric Chemistry and Physics **15**(7): 3687-3701.

Cheng, Y., Ma, Y. and Hu, D. (2021). Tracer-based source apportioning of atmospheric organic carbon and the influence of anthropogenic emissions on secondary organic aerosol formation in hong kong. Atmos. Chem. Phys. **21**(13): 10589-10608.

Chirico, R., DeCarlo, P.F., Heringa, M.F., Tritscher, T., Richter, R., Prévôt, A.S.H., Dommen, J., Weingartner, E., Wehrle, G., Gysel, M., Laborde, M. and Baltensperger, U. (2010). Impact of aftertreatment devices on primary emissions and secondary organic aerosol formation potential from in-use diesel vehicles: Results from smog chamber experiments. Atmos. Chem. Phys. **10**(23): 11545-11563.

Cho, C., Hofzumahaus, A., Fuchs, H., Dorn, H.-P., Glowania, M., Holland, F., Rohrer, F., Vardhan, V., Kiendler-Scharr, A., Wahner, A. and Novelli, A. (2021). Characterization of a chemical modulation reactor (cmr) for the measurement of atmospheric concentrations of hydroxyl radicals with a laser-induced fluorescence instrument. Atmospheric Measurement Techniques **14**(3): 1851-1877.

Clark, C.H., Kacarab, M., Nakao, S., Asa-Awuku, A., Sato, K. and Cocker, D.R. (2016). Temperature effects on secondary organic aerosol (soa) from the dark ozonolysis and photo-oxidation of isoprene. Environmental Science & Technology **50**(11): 5564-5571.

Cleaves, H.J. (2011). Branching ratio. Encyclopedia of astrobiology. M. Gargaud , R. Amils , J. C. Quintanilla et al. Berlin, Heidelberg, Springer Berlin Heidelberg**:** 218-218.

Coggon, M.M., Veres, P.R., Yuan, B., Koss, A., Warneke, C., Gilman, J.B., Lerner, B.M., Peischl, J., Aikin, K.C., Stockwell, C.E., Hatch, L.E., Ryerson, T.B., Roberts, J.M., Yokelson, R.J. and de Gouw, J.A. (2016). Emissions of nitrogen-containing organic compounds from the burning of herbaceous and arboraceous biomass: Fuel composition dependence and the variability of commonly used nitrile tracers. Geophysical Research Letters **43**(18): 9903-9912.

Cohen, M.D., Stunder, B.J.B., Rolph, G.D., Draxler, R.R., Stein, A.F. and Ngan, F. (2015). Noaa's hysplit atmospheric transport and dispersion modeling system. Bulletin of the American Meteorological Society **96**(12): 2059-2077.

Crippa, M., El Haddad, I., Slowik, J.G., DeCarlo, P.F., Mohr, C., Heringa, M.F., Chirico, R., Marchand, N., Sciare, J., Baltensperger, U. and Prévôt, A.S.H. (2013a). Identification of marine and continental aerosol sources in paris using high resolution aerosol mass spectrometry. Journal of Geophysical Research: Atmospheres **118**(4): 1950-1963.

Crippa, M., DeCarlo, P.F., Slowik, J.G., Mohr, C., Heringa, M.F., Chirico, R., Poulain, L., Freutel, F., Sciare, J., Cozic, J., Di Marco, C.F., Elsasser, M., Nicolas, J.B., Marchand, N., Abidi, E., Wiedensohler, A., Drewnick, F., Schneider, J., Borrmann, S., Nemitz, E., Zimmermann, R., Jaffrezo, J.L., Prévôt, A.S.H. and Baltensperger, U. (2013b). Wintertime aerosol chemical composition and source apportionment of the organic fraction in the metropolitan area of paris. Atmospheric Chemistry and Physics **13**(2): 961-981.

Crippa, M., Canonaco, F., Lanz, V.A., Äijälä, M., Allan, J.D., Carbone, S., Capes, G., Ceburnis, D., Dall'Osto, M., Day, D.A., DeCarlo, P.F., Ehn, M., Eriksson, A., Freney, E., Hildebrandt Ruiz, L., Hillamo, R., Jimenez, J.L., Junninen, H., Kiendler-Scharr, A., Kortelainen, A.M., Kulmala, M., Laaksonen, A., Mensah, A.A., Mohr, C., Nemitz, E., O'Dowd, C., Ovadnevaite, J., Pandis, S.N., Petäjä, T., Poulain, L., Saarikoski, S., Sellegri, K., Swietlicki, E., Tiitta, P., Worsnop, D.R., Baltensperger, U. and Prévôt, A.S.H. (2014). Organic aerosol components derived from 25 ams data sets across europe using a consistent me-2 based source apportionment approach. Atmos. Chem. Phys. **14**(12): 6159-6176.

Cross, E.S., Slowik, J.G., Davidovits, P., Allan, J.D., Worsnop, D.R., Jayne, J.T., Lewis †, D.K., Canagaratna, M. and Onasch, T.B. (2007). Laboratory and ambient particle density determinations using light scattering in conjunction with aerosol mass spectrometry. Aerosol Science and Technology **41**(4): 343-359.

Dai, Q., Schulze, B.C., Bi, X., Bui, A.A.T., Guo, F., Wallace, H.W., Sanchez, N.P., Flynn, J.H., Lefer, B.L., Feng, Y. and Griffin, R.J. (2019). Seasonal differences in formation processes of oxidized organic aerosol near houston, tx. Atmospheric Chemistry and Physics **19**(14): 9641-9661.

De Gouw, J. and Jimenez, J.L. (2009). Organic aerosols in the earth's atmosphere. Environmental Science & Technology **43**(20): 7614-7618.

de Gouw, J.A., Warneke, C., Parrish, D.D., Holloway, J.S., Trainer, M. and Fehsenfeld, F.C. (2003). Emission sources and ocean uptake of acetonitrile (ch3cn) in the atmosphere. Journal of Geophysical Research: Atmospheres **108**(D11).

Debevec, C., Sauvage, S., Gros, V., Salameh, T., Sciare, J., Dulac, F. and Locoge, N. (2021). Seasonal variation and origins of volatile organic compounds observed during 2 years at a western mediterranean remote background site (ersa, cape corsica). Atmos. Chem. Phys. **21**(3): 1449-1484.

Debevec, C., Sauvage, S., Gros, V., Sciare, J., Pikridas, M., Stavroulas, I., Salameh, T., Leonardis, T., Gaudion, V., Depelchin, L., Fronval, I., Sarda-Esteve, R., Baisnée, D., Bonsang, B., Savvides, C., Vrekoussis, M. and Locoge, N. (2017). Origin and variability in volatile organic compounds observed at an eastern mediterranean background site (cyprus). Atmos. Chem. Phys. **17**(18): 11355-11388.

DeCarlo, P.F., Ulbrich, I.M., Crounse, J., de Foy, B., Dunlea, E.J., Aiken, A.C., Knapp, D., Weinheimer, A.J., Campos, T., Wennberg, P.O. and Jimenez, J.L. (2010). Investigation of the sources and processing of organic aerosol over the central mexican plateau from aircraft measurements during milagro. Atmospheric Chemistry and Physics **10**(12): 5257-5280.

DeCarlo, P.F., Kimmel, J.R., Trimborn, A., Northway, M.J., Jayne, J.T., Aiken, A.C., Gonin, M., Fuhrer, K., Horvath, T., Docherty, K.S., Worsnop, D.R. and Jimenez, J.L. (2006). Field-deployable, high-resolution, time-of-flight aerosol mass spectrometer. Analytical Chemistry **78**(24): 8281-8289.

Dockery, D.W. and Stone, P.H. (2007). Cardiovascular risks from fine particulate air pollution. New England Journal of Medicine **356**(5): 511-513.

Dockery, D.W., Pope, C.A., Xu, X., Spengler, J.D., Ware, J.H., Fay, M.E., Ferris, B.G. and Speizer, F.E. (1993). An association between air pollution and mortality in six u.S. Cities. New England Journal of Medicine **329**(24): 1753-1759.

Drewnick, F., Hings, S.S., Curtius, J., Eerdekens, G. and Williams, J. (2006). Measurement of fine particulate and gas-phase species during the new year's fireworks 2005 in mainz, germany. Atmospheric Environment **40**(23): 4316-4327.

Drewnick, F., Hings, S.S., DeCarlo, P., Jayne, J.T., Gonin, M., Fuhrer, K., Weimer, S., Jimenez, J.L., Demerjian, K.L., Borrmann, S. and Worsnop, D.R. (2005). A new time-of-flight aerosol mass spectrometer (tof-ams)—instrument description and first field deployment. Aerosol Science and Technology **39**(7): 637-658.

Fanourgakis, G.S., Kanakidou, M., Nenes, A., Bauer, S.E., Bergman, T., Carslaw, K.S., Grini, A., Hamilton, D.S., Johnson, J.S., Karydis, V.A., Kirkevåg, A., Kodros, J.K., Lohmann, U., Luo, G., Makkonen, R., Matsui, H., Neubauer, D., Pierce, J.R., Schmale, J., Stier, P., Tsigaridis, K., van Noije, T., Wang, H., Watson-Parris, D., Westervelt, D.M., Yang, Y., Yoshioka, M., Daskalakis, N., Decesari, S., Gysel-Beer, M., Kalivitis, N., Liu, X., Mahowald, N.M., Myriokefalitakis, S., Schrödner, R., Sfakianaki, M., Tsimpidi, A.P., Wu, M. and Yu, F. (2019). Evaluation of global simulations of aerosol particle and cloud condensation nuclei number, with implications for cloud droplet formation. Atmos. Chem. Phys. **19**(13): 8591-8617.

Farina, S.C., Adams, P.J. and Pandis, S.N. (2010). Modeling global secondary organic aerosol formation and processing with the volatility basis set: Implications for anthropogenic secondary organic aerosol. Journal of Geophysical Research: Atmospheres **115**(D9).

Farmer, D.K., Matsunaga, A., Docherty, K.S., Surratt, J.D., Seinfeld, J.H., Ziemann, P.J. and Jimenez, J.L. (2010). Response of an aerosol mass spectrometer to organonitrates and organosulfates and implications for atmospheric chemistry. Proc Natl Acad Sci U S A **107**(15): 6670-6675.

Fisher, J.A., Jacob, D.J., Travis, K.R., Kim, P.S., Marais, E.A., Chan Miller, C., Yu, K., Zhu, L., Yantosca, R.M., Sulprizio, M.P., Mao, J., Wennberg, P.O., Crounse, J.D., Teng, A.P., Nguyen, T.B., St. Clair, J.M., Cohen, R.C., Romer, P., Nault, B.A., Wooldridge, P.J., Jimenez, J.L., Campuzano-Jost, P., Day, D.A., Hu, W., Shepson, P.B., Xiong, F., Blake, D.R., Goldstein, A.H., Misztal, P.K., Hanisco, T.F., Wolfe, G.M., Ryerson, T.B., Wisthaler, A. and Mikoviny, T. (2016). Organic nitrate chemistry and its implications for nitrogen budgets in an isoprene- and monoterpene-rich atmosphere: Constraints from aircraft (seac4rs) and ground-based (soas) observations in the southeast us. Atmos. Chem. Phys. **16**(9): 5969-5991.

Florou, K., Papanastasiou, D.K., Pikridas, M., Kaltsonoudis, C., Louvaris, E., Gkatzelis, G.I., Patoulias, D., Mihalopoulos, N. and Pandis, S.N. (2017). The contribution of wood burning and other pollution sources to wintertime organic aerosol levels in two greek cities. Atmospheric Chemistry and Physics **17**(4): 3145-3163.

Fountoukis, C. and Nenes, A. (2007). Isorropia ii: A computationally efficient thermodynamic equilibrium model for k⁺–ca²⁺–mg²⁺–nh₄⁺–na⁺–so₄^{2−}–no₃^{−}–cl^{−}–h₂o aerosols. Atmos. Chem. Phys. **7**(17): 4639-4659.

Fountoukis, C., Nenes, A., Sullivan, A., Weber, R., Van Reken, T., Fischer, M., Matías, E., Moya, M., Farmer, D. and Cohen, R.C. (2009). Thermodynamic characterization of mexico city aerosol during milagro 2006. Atmos. Chem. Phys. **9**(6): 2141-2156.

Fry, J.L., Draper, D.C., Barsanti, K.C., Smith, J.N., Ortega, J., Winkler, P.M., Lawler, M.J., Brown, S.S., Edwards, P.M., Cohen, R.C. and Lee, L. (2014). Secondary organic aerosol formation and organic nitrate yield from no3 oxidation of biogenic hydrocarbons. Environmental Science & Technology **48**(20): 11944-11953.

Fry, J.L., Kiendler-Scharr, A., Rollins, A.W., Wooldridge, P.J., Brown, S.S., Fuchs, H., Dubé, W., Mensah, A., dal Maso, M., Tillmann, R., Dorn, H.P., Brauers, T. and Cohen, R.C. (2009). Organic nitrate and secondary organic aerosol yield from no₃ oxidation of β-pinene evaluated using a gas-phase kinetics/aerosol partitioning model. Atmos. Chem. Phys. **9**(4): 1431-1449.

Fry, J.L., Draper, D.C., Zarzana, K.J., Campuzano-Jost, P., Day, D.A., Jimenez, J.L., Brown, S.S., Cohen, R.C., Kaser, L., Hansel, A., Cappellin, L., Karl, T., Hodzic Roux, A., Turnipseed, A., Cantrell, C., Lefer, B.L. and Grossberg, N. (2013). Observations of gas- and aerosol-phase organic nitrates at beachon-rombas 2011. Atmos. Chem. Phys. **13**(17): 8585-8605.

Fry, J.L., Brown, S.S., Middlebrook, A.M., Edwards, P.M., Campuzano-Jost, P., Day, D.A., Jimenez, J.L., Allen, H.M., Ryerson, T.B., Pollack, I., Graus, M., Warneke, C., de Gouw, J.A., Brock, C.A., Gilman, J., Lerner, B.M., Dubé, W.P., Liao, J. and Welti, A. (2018). Secondary organic aerosol (soa) yields from no3 radical + isoprene based on nighttime aircraft power plant plume transects. Atmos. Chem. Phys. **18**(16): 11663-11682.

Ge, X.L., Zhang, Q., Sun, Y.L., Ruehl, C.R. and Setyan, A. (2012). Effect of aqueous-phase processing on aerosol chemistry and size distributions in fresno, california, during wintertime. Environmental Chemistry **9**(3): 221-235.

Goldstein, A.H. and Galbally, I.E. (2007). Known and unknown organic constituents in the earth' s atmosphere. Environmental Science & Technology **41**(5): 1514-1521.

Griffin, R.J., Cocker III, D.R., Flagan, R.C. and Seinfeld, J.H. (1999). Organic aerosol formation from the oxidation of biogenic hydrocarbons. Journal of Geophysical Research: Atmospheres **104**(D3): 3555-3567.

Grosjean, E. and Grosjean, D. (1996). Rate constants for the gas-phase reaction of ozone with 1, 1-disubstituted alkenes. International Journal of Chemical Kinetics **28**(12): 911-918.

Guenther, A., Hewitt, C.N., Erickson, D., Fall, R., Geron, C., Graedel, T., Harley, P., Klinger, L., Lerdau, M., McKay, W.A., Pierce, T., Scholes, B., Steinbrecher, R., Tallamraju, R., Taylor, J. and Zimmerman, P. (1995). A global model of natural volatile organic compound emissions. Journal of Geophysical Research: Atmospheres **100**(D5): 8873-8892.

Guenther, A.B., Jiang, X., Heald, C.L., Sakulyanontvittaya, T., Duhl, T., Emmons, L.K. and Wang, X. (2012). The model of emissions of gases and aerosols from nature version 2.1 (megan2.1): An extended and updated framework for modeling biogenic emissions. Geosci. Model Dev. **5**(6): 1471-1492.

Hallquist, M., Wängberg, I., Ljungström, E., Barnes, I. and Becker, K. (1999). Aerosol and product yields from no3 radical-initiated oxidation of selected monoterpenes. Environmental Science & Technology **33**: 553-559.

Hallquist, M., Wenger, J.C., Baltensperger, U., Rudich, Y., Simpson, D., Claeys, M., Dommen, J., Donahue, N.M., George, C., Goldstein, A.H., Hamilton, J.F., Herrmann, H., Hoffmann, T., Iinuma, Y., Jang, M., Jenkin, M.E., Jimenez, J.L., Kiendler-Scharr, A., Maenhaut, W., McFiggans, G., Mentel, T.F., Monod, A., Prévôt, A.S.H., Seinfeld, J.H., Surratt, J.D., Szmigielski, R. and Wildt, J. (2009). The formation, properties and impact of secondary organic aerosol: Current and emerging issues. Atmos. Chem. Phys. **9**(14): 5155-5236.

Hayes, P.L., Ortega, A.M., Cubison, M.J., Froyd, K.D., Zhao, Y., Cliff, S.S., Hu, W.W., Toohey, D.W., Flynn, J.H., Lefer, B.L., Grossberg, N., Alvarez, S., Rappenglück, B., Taylor, J.W., Allan, J.D., Holloway, J.S., Gilman, J.B., Kuster, W.C., de Gouw, J.A., Massoli, P., Zhang, X., Liu, J., Weber, R.J., Corrigan, A.L., Russell, L.M., Isaacman, G., Worton, D.R., Kreisberg, N.M., Goldstein, A.H., Thalman, R., Waxman, E.M., Volkamer, R., Lin, Y.H., Surratt, J.D., Kleindienst, T.E., Offenberg, J.H., Dusanter, S., Griffith, S., Stevens, P.S., Brioude, J., Angevine, W.M. and Jimenez, J.L. (2013). Organic aerosol composition and sources in pasadena, california, during the 2010 calnex campaign. Journal of Geophysical Research: Atmospheres **118**(16): 9233-9257.

He, L.Y., Lin, Y., Huang, X.F., Guo, S., Xue, L., Su, Q., Hu, M., Luan, S.J. and Zhang, Y.H. (2010). Characterization of high-resolution aerosol mass spectra of primary organic aerosol emissions from chinese cooking and biomass burning. Atmos. Chem. Phys. **10**(23): 11535-11543.

Heberlein, J., Postel, O., Girshick, S., McMurry, P., Gerberich, W., Iordanoglou, D., Di Fonzo, F., Neumann, D., Gidwani, A., Fan, M. and Tymiak, N. (2001). Thermal plasma deposition of nanophase hard coatings. Surface and Coatings Technology **142-144**: 265-271.

Henry, R., Norris, G.A., Vedantham, R. and Turner, J.R. (2009). Source region identification using kernel smoothing. Environmental Science & Technology **43**(11): 4090-4097.

Henze, D.K., Seinfeld, J.H., Ng, N.L., Kroll, J.H., Fu, T.M., Jacob, D.J. and Heald, C.L. (2008). Global modeling of secondary organic aerosol formation from aromatic hydrocarbons: High- vs. Low-yield pathways. Atmos. Chem. Phys. **8**(9): 2405-2420.

Hildebrandt, L., Engelhart, G.J., Mohr, C., Kostenidou, E., Lanz, V.A., Bougiatioti, A., DeCarlo, P.F., Prevot, A.S.H., Baltensperger, U., Mihalopoulos, N., Donahue, N.M. and Pandis, S.N. (2010). Aged organic aerosol in the eastern mediterranean: The finokalia aerosol measurement experiment-2008. Atmospheric Chemistry and Physics **10**(9): 4167-4186.

Hodzic, A., Kasibhatla, P.S., Jo, D.S., Cappa, C.D., Jimenez, J.L., Madronich, S. and Park, R.J. (2016). Rethinking the global secondary organic aerosol (soa) budget: Stronger production, faster removal, shorter lifetime. Atmos. Chem. Phys. **16**(12): 7917-7941.

Hoyle, C.R., Berntsen, T., Myhre, G. and Isaksen, I.S.A. (2007). Secondary organic aerosol in the global aerosol – chemical transport model oslo ctm2. Atmos. Chem. Phys. **7**(21): 5675-5694.

Hu, W.W., Hu, M., Yuan, B., Jimenez, J.L., Tang, Q., Peng, J.F., Hu, W., Shao, M., Wang, M., Zeng, L.M., Wu, Y.S., Gong, Z.H., Huang, X.F. and He, L.Y. (2013). Insights on organic aerosol aging and the influence of coal combustion at a regional receptor site of central eastern china. Atmos. Chem. Phys. **13**(19): 10095-10112.

Hu, W.W., Campuzano-Jost, P., Palm, B.B., Day, D.A., Ortega, A.M., Hayes, P.L., Krechmer, J.E., Chen, Q., Kuwata, M., Liu, Y.J., de Sá, S.S., McKinney, K., Martin, S.T., Hu, M., Budisulistiorini, S.H., Riva, M., Surratt, J.D., St. Clair, J.M., Isaacman-Van Wertz, G., Yee, L.D., Goldstein, A.H., Carbone, S., Brito, J., Artaxo, P., de Gouw, J.A., Koss, A., Wisthaler, A., Mikoviny, T., Karl, T., Kaser, L., Jud, W., Hansel, A., Docherty, K.S., Alexander, M.L., Robinson, N.H., Coe, H., Allan, J.D., Canagaratna, M.R., Paulot, F. and Jimenez, J.L. (2015). Characterization of a real-time tracer for isoprene epoxydiols-derived secondary organic aerosol (iepox-soa) from aerosol mass spectrometer measurements. Atmospheric Chemistry and Physics **15**(20): 11807-11833.

Huang, D.D., Li, Y.J., Lee, B.P. and Chan, C.K. (2015). Analysis of organic sulfur compounds in atmospheric aerosols at the hkust supersite in hong kong using hr-tof-ams. Environmental Science & Technology **49**(6): 3672-3679.

Huang, S., Poulain, L., van Pinxteren, D., van Pinxteren, M., Wu, Z., Herrmann, H. and Wiedensohler, A. (2017). Latitudinal and seasonal distribution of particulate msa over the atlantic using a validated quantification method with hr-tof-ams. Environmental Science & Technology **51**(1): 418-426.

Jimenez, J.L., Jayne, J.T., Shi, Q., Kolb, C.E., Worsnop, D.R., Yourshaw, I., Seinfeld, J.H., Flagan, R.C., Zhang, X., Smith, K.A., Morris, J.W. and Davidovits, P. (2003). Ambient aerosol sampling using the aerodyne aerosol mass spectrometer. Journal of Geophysical Research: Atmospheres **108**(D7).

Jimenez, J.L., Canagaratna, M.R., Donahue, N.M., Prevot, A.S., Zhang, Q., Kroll, J.H., DeCarlo, P.F., Allan, J.D., Coe, H., Ng, N.L., Aiken, A.C., Docherty, K.S., Ulbrich, I.M., Grieshop, A.P., Robinson, A.L., Duplissy, J., Smith, J.D., Wilson, K.R., Lanz, V.A., Hueglin, C., Sun, Y.L., Tian, J., Laaksonen, A., Raatikainen, T., Rautiainen, J., Vaattovaara, P., Ehn, M., Kulmala, M., Tomlinson, J.M., Collins, D.R., Cubison, M.J., Dunlea, E.J., Huffman, J.A., Onasch, T.B., Alfarra, M.R., Williams, P.I., Bower, K., Kondo, Y., Schneider, J., Drewnick, F., Borrmann, S., Weimer, S., Demerjian, K., Salcedo, D., Cottrell, L., Griffin, R., Takami, A., Miyoshi, T., Hatakeyama, S., Shimono, A., Sun, J.Y., Zhang, Y.M., Dzepina, K., Kimmel, J.R., Sueper, D., Jayne, J.T., Herndon, S.C., Trimborn, A.M., Williams, L.R., Wood, E.C., Middlebrook, A.M., Kolb, C.E., Baltensperger, U. and Worsnop, D.R. (2009). Evolution of organic aerosols in the atmosphere. Science **326**(5959): 1525-1529.

Joo, T., Rivera-Rios, J.C., Takeuchi, M., Alvarado, M.J. and Ng, N.L. (2019). Secondary organic aerosol formation from reaction of 3-methylfuran with nitrate radicals. ACS Earth and Space Chemistry **3**(6): 922-934.

Kanakidou, M., Seinfeld, J.H., Pandis, S.N., Barnes, I., Dentener, F.J., Facchini, M.C., Van Dingenen, R., Ervens, B., Nenes, A., Nielsen, C.J., Swietlicki, E., Putaud, J.P., Balkanski, Y., Fuzzi, S., Horth, J., Moortgat, G.K., Winterhalter, R., Myhre, C.E.L., Tsigaridis, K., Vignati, E., Stephanou, E.G. and Wilson, J. (2005). Organic aerosol and global climate modelling: A review. Atmos. Chem. Phys. **5**(4): 1053-1123.

Karanasiou, A., Alastuey, A., Amato, F., Renzi, M., Stafoggia, M., Tobias, A., Reche, C., Forastiere, F., Gumy, S. and Mudu, P. (2021). Short-term health effects from outdoor exposure to biomass burning emissions: A review. Science of The Total Environment **781**: 146739.

Kelly, J.M., Doherty, R.M., O'Connor, F.M. and Mann, G.W. (2018). The impact of biogenic, anthropogenic, and biomass burning volatile organic compound emissions on regional and seasonal variations in secondary organic aerosol. Atmospheric Chemistry and Physics **18**(10): 7393-7422.

Khamaganov, V.G. and Hites, R.A. (2001). Rate constants for the gas-phase reactions of ozone with isoprene, α- and β-pinene, and limonene as a function of temperature. The Journal of Physical Chemistry A **105**(5): 815-822.

Kiendler-Scharr, A., Mensah, A.A., Friese, E., Topping, D., Nemitz, E., Prevot, A.S.H., Äijälä, M., Allan, J., Canonaco, F., Canagaratna, M., Carbone, S., Crippa, M., Dall Osto, M., Day, D.A., De Carlo, P., Di Marco, C.F., Elbern, H., Eriksson, A., Freney, E., Hao, L., Herrmann, H., Hildebrandt, L., Hillamo, R., Jimenez, J.L., Laaksonen, A., McFiggans, G., Mohr, C., O'Dowd, C., Otjes, R., Ovadnevaite, J., Pandis, S.N., Poulain, L., Schlag, P., Sellegri, K., Swietlicki, E., Tiitta, P., Vermeulen, A., Wahner, A., Worsnop, D. and Wu, H.C. (2016). Ubiquity of organic nitrates from nighttime chemistry in the european submicron aerosol. Geophysical Research Letters **43**(14): 7735-7744.

Kobayashi, Y. and Takegawa, N. (2022). A new method to quantify particulate sodium and potassium salts (nitrate, chloride, and sulfate) by thermal desorption aerosol mass spectrometry. Atmos. Meas. Tech. **15**(4): 833-844.

Kodros, J.K., Papanastasiou, D.K., Paglione, M., Masiol, M., Squizzato, S., Florou, K., Skyllakou, K., Kaltsonoudis, C., Nenes, A. and Pandis, S.N. (2020). Rapid dark aging of biomass burning as an overlooked source of oxidized organic aerosol. Proc Natl Acad Sci U S A **117**(52): 33028-33033.

Kostenidou, E., Lee, B.-H., Engelhart, G.J., Pierce, J.R. and Pandis, S.N. (2009). Mass spectra deconvolution of low, medium, and high volatility biogenic secondary organic aerosol. Environmental Science & Technology **43**(13): 4884-4889.

Kostenidou, E., Florou, K., Kaltsonoudis, C., Tsiflikiotou, M., Vratolis, S., Eleftheriadis, K. and Pandis, S.N. (2015). Sources and chemical characterization of organic aerosol during the summer in the eastern mediterranean. Atmospheric Chemistry and Physics **15**(19): 11355-11371.

Kulmala, M., Asmi, A., Lappalainen, H.K., Baltensperger, U., Brenguier, J.L., Facchini, M.C., Hansson, H.C., Hov, Ø., O'Dowd, C.D., Pöschl, U., Wiedensohler, A., Boers, R., Boucher, O., de Leeuw, G., Denier van der Gon, H.A.C., Feichter, J., Krejci, R., Laj, P., Lihavainen, H., Lohmann, U., McFiggans, G., Mentel, T., Pilinis, C., Riipinen, I., Schulz, M., Stohl, A., Swietlicki, E., Vignati, E., Alves, C., Amann, M., Ammann, M., Arabas, S., Artaxo, P., Baars, H., Beddows, D.C.S., Bergström, R., Beukes, J.P., Bilde, M., Burkhart, J.F., Canonaco, F., Clegg, S.L., Coe, H., Crumeyrolle, S., D'Anna, B., Decesari, S., Gilardoni, S., Fischer, M., Fjaeraa, A.M., Fountoukis, C., George, C., Gomes, L., Halloran, P., Hamburger, T., Harrison, R.M., Herrmann, H., Hoffmann, T., Hoose, C., Hu, M., Hyvärinen, A., Hõrrak, U., Iinuma, Y., Iversen, T., Josipovic, M., Kanakidou, M., Kiendler-Scharr, A., Kirkevåg, A., Kiss, G., Klimont, Z., Kolmonen, P., Komppula, M., Kristjánsson, J.E., Laakso, L., Laaksonen, A., Labonnote, L., Lanz, V.A., Lehtinen, K.E.J., Rizzo, L.V., Makkonen, R., Manninen, H.E., McMeeking, G., Merikanto, J., Minikin, A., Mirme, S., Morgan, W.T., Nemitz, E., O'Donnell, D., Panwar, T.S., Pawlowska, H., Petzold, A., Pienaar, J.J., Pio, C., Plass-Duelmer, C., Prévôt, A.S.H., Pryor, S., Reddington, C.L., Roberts, G., Rosenfeld, D., Schwarz, J., Seland, Ø., Sellegri, K., Shen, X.J., Shiraiwa, M., Siebert, H., Sierau, B., Simpson, D., Sun, J.Y., Topping, D., Tunved, P., Vaattovaara, P., Vakkari, V., Veefkind, J.P., Visschedijk, A., Vuollekoski, H., Vuolo, R., Wehner, B., Wildt, J., Woodward, S., Worsnop, D.R., van Zadelhoff, G.J., Zardini, A.A., Zhang, K., van Zyl, P.G., Kerminen, V.M., S Carslaw, K. and Pandis, S.N. (2011). General overview: European integrated project on aerosol cloud climate and air quality interactions (eucaari) – integrating aerosol research from nano to global scales. Atmos. Chem. Phys. **11**(24): 13061-13143.

Lalchandani, V., Kumar, V., Tobler, A., N, M.T., Mishra, S., Slowik, J.G., Bhattu, D., Rai, P., Satish, R., Ganguly, D., Tiwari, S., Rastogi, N., Tiwari, S., Mocnik, G., Prevot, A.S.H. and Tripathi, S.N. (2021). Real-time characterization and source apportionment of fine particulate matter in the delhi megacity area during late winter. Sci Total Environ **770**: 145324.

Lanz, V.A., Alfarra, M.R., Baltensperger, U., Buchmann, B., Hueglin, C., Szidat, S., Wehrli, M.N., Wacker, L., Weimer, S., Caseiro, A., Puxbaum, H. and Prevot, A.S.H. (2008). Source attribution of submicron organic aerosols during wintertime inversions by advanced factor analysis of aerosol mass spectra. Environmental Science & Technology **42**(1): 214-220.

Lanz, V.A., Prévôt, A.S.H., Alfarra, M.R., Weimer, S., Mohr, C., DeCarlo, P.F., Gianini, M.F.D., Hueglin, C., Schneider, J., Favez, O., D'Anna, B., George, C. and Baltensperger, U. (2010). Characterization of aerosol chemical composition with aerosol mass spectrometry in central europe: An overview. Atmospheric Chemistry and Physics **10**(21): 10453-10471.

Lathière, J., Hauglustaine, D.A., Friend, A.D., De Noblet-Ducoudré, N., Viovy, N. and Folberth, G.A. (2006). Impact of climate variability and land use changes on global biogenic volatile organic compound emissions. Atmos. Chem. Phys. **6**(8): 2129-2146.

Lee, B.H., Mohr, C., Lopez-Hilfiker, F.D., Lutz, A., Hallquist, M., Lee, L., Romer, P., Cohen, R.C., Iyer, S., Kurtén, T., Hu, W., Day, D.A., Campuzano-Jost, P., Jimenez, J.L., Xu, L., Ng, N.L., Guo, H., Weber, R.J., Wild, R.J., Brown, S.S., Koss, A., de Gouw, J., Olson, K., Goldstein, A.H., Seco, R., Kim, S., McAvey, K., Shepson, P.B., Starn, T., Baumann, K., Edgerton, E.S., Liu, J., Shilling, J.E., Miller, D.O., Brune, W., Schobesberger, S., D'Ambro, E.L. and Thornton, J.A. (2016). Highly functionalized organic nitrates in the southeast united states: Contribution to secondary organic aerosol and reactive nitrogen budgets. Proc Natl Acad Sci U S A **113**(6): 1516-1521.

Lelieveld, J., Evans, J.S., Fnais, M., Giannadaki, D. and Pozzer, A. (2015). The contribution of outdoor air pollution sources to premature mortality on a global scale. Nature **525**(7569): 367-371.

Li, J., Pósfai, M., Hobbs, P.V. and Buseck, P.R. (2003). Individual aerosol particles from biomass burning in southern africa: 2, compositions and aging of inorganic particles. Journal of Geophysical Research: Atmospheres **108**(D13).

Li, Y.J., Lee, B.P., Su, L., Fung, J.C.H. and Chan, C.K. (2015). Seasonal characteristics of fine particulate matter (pm) based on high-resolution time-of-flight aerosol mass spectrometric (hr-tof-ams) measurements at the hkust supersite in hong kong. Atmospheric Chemistry and Physics **15**(1): 37-53.

Lovelock, J.E., Maggs, R.J. and Rasmussen, R.A. (1972). Atmospheric dimethyl sulphide and the natural sulphur cycle. Nature **237**(5356): 452-453.

Mahilang, M., Deb, M.K. and Pervez, S. (2021). Biogenic secondary organic aerosols: A review on formation mechanism, analytical challenges and environmental impacts. Chemosphere **262**: 127771.

Martin, S.T., Andreae, M.O., Althausen, D., Artaxo, P., Baars, H., Borrmann, S., Chen, Q., Farmer, D.K., Guenther, A., Gunthe, S.S., Jimenez, J.L., Karl, T., Longo, K., Manzi, A., Müller, T., Pauliquevis, T., Petters, M.D., Prenni, A.J., Pöschl, U., Rizzo, L.V., Schneider, J., Smith, J.N., Swietlicki, E., Tota, J., Wang, J., Wiedensohler, A. and Zorn, S.R. (2010). An overview of the amazonian aerosol characterization experiment 2008 (amaze-08). Atmospheric Chemistry and Physics **10**(23): 11415-11438.

McGrath-Spangler, E.L. and Denning, A.S. (2013). Global seasonal variations of midday planetary boundary layer depth from calipso space-borne lidar. Journal of Geophysical Research: Atmospheres **118**(3): 1226-1233.

Middlebrook, A.M., Bahreini, R., Jimenez, J.L. and Canagaratna, M.R. (2012). Evaluation of composition-dependent collection efficiencies for the aerodyne aerosol mass spectrometer using field data. Aerosol Science and Technology **46**(3): 258-271.

Mohr, C., DeCarlo, P.F., Heringa, M.F., Chirico, R., Slowik, J.G., Richter, R., Reche, C., Alastuey, A., Querol, X., Seco, R., Peñuelas, J., Jiménez, J.L., Crippa, M., Zimmermann, R., Baltensperger, U. and Prévôt, A.S.H. (2012). Identification and quantification of organic aerosol from cooking and other sources in barcelona using aerosol mass spectrometer data. Atmospheric Chemistry and Physics **12**(4): 1649-1665.

Moore, D.J.T. (1999). Isentropic analysis techniques: Basic concepts.

Mutzel, A., Zhang, Y., Böge, O., Rodigast, M., Kolodziejczyk, A., Wang, X. and Herrmann, H. (2021). Importance of secondary organic aerosol formation of <i>α</i>-pinene, limonene, and <i>m</i>-cresol comparing day- and nighttime radical chemistry. Atmospheric Chemistry and Physics **21**(11): 8479-8498.

Myhre, G., Samset, B.H., Schulz, M., Balkanski, Y., Bauer, S., Berntsen, T.K., Bian, H., Bellouin, N., Chin, M., Diehl, T., Easter, R.C., Feichter, J., Ghan, S.J., Hauglustaine, D., Iversen, T., Kinne, S., Kirkevåg, A., Lamarque, J.F., Lin, G., Liu, X., Lund, M.T., Luo, G., Ma, X., van Noije, T., Penner, J.E., Rasch, P.J., Ruiz, A., Seland, Ø., Skeie, R.B., Stier, P., Takemura, T., Tsigaridis, K., Wang, P., Wang, Z., Xu, L., Yu, H., Yu, F., Yoon, J.H., Zhang, K., Zhang, H. and Zhou, C. (2013). Radiative forcing of the direct aerosol effect from aerocom phase ii simulations. Atmos. Chem. Phys. **13**(4): 1853-1877.

NG, N.L. (2011). Real-time methods for estimating organic component mass concentrations from aerosol mass spectrometer data. Environmental Science & Technology.

Ng, N.L., Canagaratna, M.R., Jimenez, J.L., Chhabra, P.S., Seinfeld, J.H. and Worsnop, D.R. (2011). Changes in organic aerosol composition with aging inferred from aerosol mass spectra.

Ng, N.L., Kwan, A.J., Surratt, J.D., Chan, A.W.H., Chhabra, P.S., Sorooshian, A., Pye, H.O.T., Crounse, J.D., Wennberg, P.O., Flagan, R.C. and Seinfeld, J.H. (2008). Secondary organic aerosol (soa) formation from reaction of isoprene with nitrate radicals (no₃). Atmos. Chem. Phys. **8**(14): 4117-4140.

Ng, N.L., Canagaratna, M.R., Zhang, Q., Jimenez, J.L., Tian, J., Ulbrich, I.M., Kroll, J.H., Docherty, K.S., Chhabra, P.S., Bahreini, R., Murphy, S.M., Seinfeld, J.H., Hildebrandt, L., Donahue, N.M., DeCarlo, P.F., Lanz, V.A., Prévôt, A.S.H., Dinar, E., Rudich, Y. and Worsnop, D.R. (2010). Organic aerosol components observed in northern hemispheric datasets from aerosol mass spectrometry. Atmos. Chem. Phys. **10**(10): 4625-4641.

Ng, N.L., Brown, S.S., Archibald, A.T., Atlas, E., Cohen, R.C., Crowley, J.N., Day, D.A., Donahue, N.M., Fry, J.L., Fuchs, H., Griffin, R.J., Guzman, M.I., Herrmann, H., Hodzic, A., Iinuma, Y., Jimenez, J.L., Kiendler-Scharr, A., Lee, B.H., Luecken, D.J., Mao, J., McLaren, R., Mutzel, A., Osthoff, H.D., Ouyang, B., Picquet-Varrault, B., Platt, U., Pye, H.O.T., Rudich, Y., Schwantes, R.H., Shiraiwa, M., Stutz, J., Thornton, J.A., Tilgner, A., Williams, B.J. and Zaveri, R.A. (2017). Nitrate radicals and biogenic volatile organic compounds: Oxidation, mechanisms, and organic aerosol. Atmos. Chem. Phys. **17**(3): 2103-2162.

Nowak, J.B., Huey, L.G., Russell, A.G., Tian, D., Neuman, J.A., Orsini, D., Sjostedt, S.J., Sullivan, A.P., Tanner, D.J., Weber, R.J., Nenes, A., Edgerton, E. and Fehsenfeld, F.C. (2006). Analysis of urban gas phase ammonia measurements from the 2002 atlanta aerosol nucleation and real-time characterization experiment (anarche). Journal of Geophysical Research: Atmospheres **111**(D17).

Organization, W.H. and Environment, W.E.C.f. (2021). Who global air quality guidelines: Particulate matter (pm2. 5 and pm10), ozone, nitrogen dioxide, sulfur dioxide and carbon monoxide, World Health Organization.

Ortega, A.M., Day, D.A., Cubison, M.J., Brune, W.H., Bon, D., de Gouw, J.A. and Jimenez, J.L. (2013). Secondary organic aerosol formation and primary organic aerosol oxidation from biomass-burning smoke in a flow reactor during flame-3. Atmos. Chem. Phys. **13**(22): 11551-11571.

Paatero, P. (1999). The multilinear engine: A table-driven, least squares program for solving multilinear problems, including the n-way parallel factor analysis model. Journal of Computational and Graphical Statistics **8**(4): 854-888.

Paatero, P. and Tapper, U. (1994). Positive matrix factorization: A non-negative factor model with optimal utilization of error estimates of data values. Environmetrics **5**(2): 111-126.

Paatero, P. and Hopke, P.K. (2003). Discarding or downweighting high-noise variables in factor analytic models. Analytica Chimica Acta **490**(1): 277-289.

Paatero, P., Hopke, P.K., Song, X.-H. and Ramadan, Z. (2002). Understanding and controlling rotations in factor analytic models. Chemometrics and Intelligent Laboratory Systems **60**(1): 253-264.

Paciga, A., Karnezi, E., Kostenidou, E., Hildebrandt, L., Psichoudaki, M., Engelhart, G.J., Lee, B.H., Crippa, M., Prevot, A.S.H., Baltensperger, U. and Pandis, S.N. (2016). Volatility of organic aerosol and its components in the megacity of paris. Atmospheric Chemistry and Physics **16**(4): 2013-2023.

Paglione, M., Kiendler-Scharr, A., Mensah, A.A., Finessi, E., Giulianelli, L., Sandrini, S., Facchini, M.C., Fuzzi, S., Schlag, P., Piazzalunga, A., Tagliavini, E., Henzing, J.S. and Decesari, S. (2014). Identification of humic-like substances (hulis) in oxygenated organic aerosols using nmr and ams factor analyses and liquid chromatographic techniques. Atmos. Chem. Phys. **14**(1): 25-45.

Parworth, C., Fast, J., Mei, F., Shippert, T., Sivaraman, C., Tilp, A., Watson, T. and Zhang, Q. (2015). Long-term measurements of submicrometer aerosol chemistry at the southern great plains (sgp) using an aerosol chemical speciation monitor (acsm). Atmospheric Environment **106**: 43-55.

Petit, J.E., Amodeo, T., Meleux, F., Bessagnet, B., Menut, L., Grenier, D., Pellan, Y., Ockler, A., Rocq, B., Gros, V., Sciare, J. and Favez, O. (2017). Characterising an intense pm pollution episode in march 2015 in france from multi-site approach and near real time data: Climatology, variabilities, geographical origins and model evaluation. Atmospheric Environment **155**: 68-84.

Pope, C.A. and Dockery, D.W. (2006). Health effects of fine particulate air pollution: Lines that connect. Journal of the Air & Waste Management Association **56**(6): 709-742.

Pratt, K.A. and Prather, K.A. (2012). Mass spectrometry of atmospheric aerosols—recent developments and applications. Part ii: On-line mass spectrometry techniques. Mass Spectrometry Reviews **31**(1): 17-48.

Pye, H.O.T., Chan, A.W.H., Barkley, M.P. and Seinfeld, J.H. (2010). Global modeling of organic aerosol: The importance of reactive nitrogen (no_x and no₃). Atmospheric Chemistry and Physics **10**(22): 11261-11276.

Pye, H.T., Luecken, D., Xu, L., Boyd, C., Ng, N., Baker, K., Ayres, B., Bash, J., Baumann, K., Carter, W., Edgerton, E., Fry, J., Hutzell, W., Schwede, D. and Shepson, P. (2015). Modeling the current and future roles of particulate organic nitrates in the southeastern united states. Environmental Science & Technology **49 24**: 14195-14203.

Raatikainen, T., Vaattovaara, P., Tiitta, P., Miettinen, P., Rautiainen, J., Ehn, M., Kulmala, M., Laaksonen, A. and Worsnop, D.R. (2010). Physicochemical properties and origin of organic groups detected in boreal forest using an aerosol mass spectrometer. Atmospheric Chemistry and Physics **10**(4): 2063-2077.

Ramanathan, V., Crutzen, P.J., Kiehl, J.T. and Rosenfeld, D. (2001). Aerosols, climate, and the hydrological cycle. Science **294**(5549): 2119.

Riva, M., Healy, R.M., Tomaz, S., Flaud, P.-M., Perraudin, E., Wenger, J.C. and Villenave, E. (2016). Gas and particulate phase products from the ozonolysis of acenaphthylene. Atmospheric Environment **142**: 104-113.

Rollins, A.W., Kiendler-Scharr, A., Fry, J.L., Brauers, T., Brown, S.S., Dorn, H.P., Dubé, W.P., Fuchs, H., Mensah, A., Mentel, T.F., Rohrer, F., Tillmann, R., Wegener, R., Wooldridge, P.J. and Cohen, R.C. (2009). Isoprene oxidation by nitrate radical: Alkyl nitrate and secondary organic aerosol yields. Atmos. Chem. Phys. **9**(18): 6685-6703.

Russell, M. (2005). Predicting secondary organic aerosol formation rates in southeast texas. Journal of Geophysical Research **110**(D7).

Saarikoski, S., Carbone, S., Decesari, S., Giulianelli, L., Angelini, F., Canagaratna, M., Ng, N.L., Trimborn, A., Facchini, M.C., Fuzzi, S., Hillamo, R. and Worsnop, D. (2012). Chemical characterization of springtime submicrometer aerosol in po valley, italy. Atmospheric Chemistry and Physics **12**(18): 8401-8421.

Schauer, J.J., Kleeman, M.J., Cass, G.R. and Simoneit, B.R.T. (1999). Measurement of emissions from air pollution sources. 2. C1 through c30 organic compounds from medium duty diesel trucks. Environmental Science & Technology **33**(10): 1578-1587.

Schauer, J.J., Kleeman, M.J., Cass, G.R. and Simoneit, B.R.T. (2001). Measurement of emissions from air pollution sources. 3. C1−c29 organic compounds from fireplace combustion of wood. Environmental Science & Technology **35**(9): 1716-1728.

Schlag, P., Kiendler-Scharr, A., Blom, M.J., Canonaco, F., Henzing, J.S., Moerman, M., Prévôt, A.S.H. and Holzinger, R. (2016). Aerosol source apportionment from 1-year measurements at the cesar tower in cabauw, the netherlands. Atmospheric Chemistry and Physics **16**(14): 8831-8847.

Schlag, P., Rubach, F., Mentel, T.F., Reimer, D., Canonaco, F., Henzing, J.S., Moerman, M., Otjes, R., Prevot, A.S.H., Rohrer, F., Rosati, B., Tillmann, R., Weingartner, E. and Kiendler-Scharr, A. (2017). Ambient and laboratory observations of organic ammonium salts in pm1. Faraday Discuss **200**: 331-351.

Schmale, J., Schneider, J., Nemitz, E., Tang, Y.S., Dragosits, U., Blackall, T.D., Trathan, P.N., Phillips, G.J., Sutton, M. and Braban, C.F. (2013). Sub-antarctic marine aerosol: Dominant contributions from biogenic sources. Atmospheric Chemistry and Physics **13**(17): 8669-8694.

Seibert, P., Kromp-Kolb, H., Baltensperger, U., Jost, D.T. and Schwikowski, M. (1994). Trajectory analysis of high-alpine air pollution data.

Shilling, J.E., Chen, Q., King, S.M., Rosenoern, T., Kroll, J.H., Worsnop, D.R., McKinney, K.A. and Martin, S.T. (2008). Particle mass yield in secondary organic aerosol formed by the dark ozonolysis of α-pinene. Atmos. Chem. Phys. **8**(7): 2073-2088.

Shrivastava, M., Easter, R.C., Liu, X., Zelenyuk, A., Singh, B., Zhang, K., Ma, P.-L., Chand, D., Ghan, S., Jimenez, J.L., Zhang, Q., Fast, J., Rasch, P.J. and Tiitta, P. (2015). Global transformation and fate of soa: Implications of low-volatility soa and gas-phase fragmentation reactions. Journal of Geophysical Research: Atmospheres **120**(9): 4169-4195.

Simoneit, B.R.T., Schauer, J.J., Nolte, C.G., Oros, D.R., Elias, V.O., Fraser, M.P., Rogge, W.F. and Cass, G.R. (1999). Levoglucosan, a tracer for cellulose in biomass burning and atmospheric particles. Atmospheric Environment **33**(2): 173-182.

Stefels, J., Steinke, M., Turner, S., Malin, G. and Belviso, S. (2007). Environmental constraints on the production and removal of the climatically active gas dimethylsulphide (dms) and implications for ecosystem modelling. Biogeochemistry **83**(1-3): 245-275.

Steiner, W.E., Clowers, B.H., Fuhrer, K., Gonin, M., Matz, L.M., Siems, W.F., Schultz, A.J. and Hill Jr, H.H. (2001). Electrospray ionization with ambient pressure ion mobility separation and mass analysis by orthogonal time-of-flight mass spectrometry. Rapid Communications in Mass Spectrometry **15**(23): 2221-2226.

Stocker, T.F., Qin, D., Plattner, G.-K., Tignor, M., Allen, S.K., Boschung, J., Nauels, A., Xia, Y., Bex, B. and Midgley, B. (2013). Ipcc, 2013: Climate change 2013: The physical science basis. Contribution of working group i to the fifth assessment report of the intergovernmental panel on climate change. Cambridge, United Kingdom and New York, NY, USA, Cambridge University Press.

Sueper, D. and collaborators. (2009). "Tof-ams data analysis software webpage." from http://cires1.colorado.edu/jimenez-group/wiki/index.php/ToF-AMS_Analysis_Software.

Sun, Y., Du, W., Fu, P., Wang, Q., Li, J., Ge, X., Zhang, Q., Zhu, C., Ren, L., Xu, W., Zhao, J., Han, T., Worsnop, D.R. and Wang, Z. (2016). Primary and secondary aerosols in beijing in winter: Sources, variations and processes. Atmospheric Chemistry and Physics **16**(13): 8309-8329.

Sun, Y.L., Zhang, Q., Schwab, J.J., Yang, T., Ng, N.L. and Demerjian, K.L. (2012). Factor analysis of combined organic and inorganic aerosol mass spectra from high resolution aerosol mass spectrometer measurements. Atmospheric Chemistry and Physics **12**(18): 8537-8551.

Sun, Y.L., Zhang, Q., Schwab, J.J., Demerjian, K.L., Chen, W.N., Bae, M.S., Hung, H.M., Hogrefe, O., Frank, B., Rattigan, O.V. and Lin, Y.C. (2011). Characterization of the sources and processes of organic and inorganic aerosols in new york city with a high-resolution time-of-flight aerosol mass apectrometer. Atmospheric Chemistry and Physics **11**(4): 1581-1602.

Tao, J., Gao, J., Zhang, L., Zhang, R., Che, H., Zhang, Z., Lin, Z., Jing, J., Cao, J. and Hsu, S.C. (2014). Pm_{2.5} pollution in a megacity of southwest china: Source apportionment and implication. Atmos. Chem. Phys. **14**(16): 8679-8699.

Tasoglou, A. and Pandis, S.N. (2015). Formation and chemical aging of secondary organic aerosol during the β-caryophyllene oxidation. Atmos. Chem. Phys. **15**(11): 6035-6046.

Tsigaridis, K., Krol, M., Dentener, F.J., Balkanski, Y., Lathière, J., Metzger, S., Hauglustaine, D.A. and Kanakidou, M. (2006). Change in global aerosol composition since preindustrial times. Atmos. Chem. Phys. **6**(12): 5143-5162.

Tsigaridis, K., Daskalakis, N., Kanakidou, M., Adams, P.J., Artaxo, P., Bahadur, R., Balkanski, Y., Bauer, S.E., Bellouin, N., Benedetti, A., Bergman, T., Berntsen, T.K., Beukes, J.P., Bian, H., Carslaw, K.S., Chin, M., Curci, G., Diehl, T., Easter, R.C., Ghan, S.J., Gong, S.L., Hodzic, A., Hoyle, C.R., Iversen, T., Jathar, S., Jimenez, J.L., Kaiser, J.W., Kirkevåg, A., Koch, D., Kokkola, H., Lee, Y.H., Lin, G., Liu, X., Luo, G., Ma, X., Mann, G.W., Mihalopoulos, N., Morcrette, J.J., Müller, J.F., Myhre, G., Myriokefalitakis, S., Ng, N.L., O'Donnell, D., Penner, J.E., Pozzoli, L., Pringle, K.J., Russell, L.M., Schulz, M., Sciare, J., Seland, Ø., Shindell, D.T., Sillman, S., Skeie, R.B., Spracklen, D., Stavrakou, T., Steenrod, S.D., Takemura, T., Tiitta, P., Tilmes, S., Tost, H., van Noije, T., van Zyl, P.G., von Salzen, K., Yu, F., Wang, Z., Wang, Z., Zaveri, R.A., Zhang, H., Zhang, K., Zhang, Q. and Zhang, X. (2014). The aerocom evaluation and intercomparison of organic aerosol in global models. Atmos. Chem. Phys. **14**(19): 10845-10895.

Ulbrich, I.M., Canagaratna, M.R., Zhang, Q., Worsnop, D.R. and Jimenez, J.L. (2009). Interpretation of organic components from positive matrix factorization of aerosol mass spectrometric data. Atmos. Chem. Phys. **9**(9): 2891-2918.

Vester, B.P., Ebert, M., Barnert, E.B., Schneider, J., Kandler, K., Schutz, L. and Weinbruch, S. (2007). Composition and mixing state of the urban background aerosol in the rhein-main area (germany). Atmospheric Environment **41**(29): 6102-6115.

Visser, S., Slowik, J.G., Furger, M., Zotter, P., Bukowiecki, N., Canonaco, F., Flechsig, U., Appel, K., Green, D.C., Tremper, A.H., Young, D.E., Williams, P.I., Allan, J.D., Coe, H., Williams, L.R., Mohr, C., Xu, L., Ng, N.L., Nemitz, E., Barlow, J.F., Halios, C.H., Fleming, Z.L., Baltensperger, U. and Prévôt, A.S.H. (2015). Advanced source apportionment of size-resolved trace elements at multiple sites in london during winter. Atmos. Chem. Phys. **15**(19): 11291-11309.

Volkamer, R., San Martini, F., Molina, L.T., Salcedo, D., Jimenez, J.L. and Molina, M.J. (2007). A missing sink for gas-phase glyoxal in mexico city: Formation of secondary organic aerosol. Geophysical Research Letters **34**(19).

Wagner, N.L., Dubé, W.P., Washenfelder, R.A., Young, C.J., Pollack, I.B., Ryerson, T.B. and Brown, S.S. (2011). Diode laser-based cavity ring-down instrument for no₃, n₂o₅, no, no₂ and o₃ from aircraft. Atmos. Meas. Tech. **4**(6): 1227-1240.

Wang, G., Cheng, S., Wei, W., Zhou, Y., Yao, S. and Zhang, H. (2016). Characteristics and source apportionment of vocs in the suburban area of beijing, china. Atmospheric Pollution Research **7**(4): 711-724.

Wang, Y., Chen, Y., Wu, Z., Shang, D., Bian, Y., Du, Z., Schmitt, S.H., Su, R., Gkatzelis, G.I., Schlag, P., Hohaus, T., Voliotis, A., Lu, K., Zeng, L., Zhao, C., Alfarra, M.R., McFiggans, G., Wiedensohler, A., Kiendler-Scharr, A., Zhang, Y. and Hu, M. (2020). Mutual promotion between aerosol particle liquid water and particulate nitrate enhancement leads to severe nitrate-dominated particulate matter pollution and low visibility. Atmos. Chem. Phys. **20**(4): 2161-2175.

Weber, R. (2003). Short-term temporal variation in pm2.5 mass and chemical composition during the atlanta supersite experiment, 1999. Journal of the Air & Waste Management Association **53**(1): 84-91.

Wu, R., Vereecken, L., Tsiligiannis, E., Kang, S., Albrecht, S.R., Hantschke, L., Zhao, D., Novelli, A., Fuchs, H., Tillmann, R., Hohaus, T., Carlsson, P.T.M., Shenolikar, J., Bernard, F., Crowley, J.N., Fry, J.L., Brownwood, B., Thornton, J.A., Brown, S.S., Kiendler-Scharr, A., Wahner, A., Hallquist, M. and Mentel, T.F. (2021). Molecular composition and volatility of multi-generation products formed from isoprene oxidation by nitrate radical. Atmospheric Chemistry and Physics **21**(13): 10799-10824.

Xu, L., Suresh, S., Guo, H., Weber, R.J. and Ng, N.L. (2015a). Aerosol characterization over the southeastern united states using high-resolution aerosol mass spectrometry: Spatial and seasonal variation of aerosol composition and sources with a focus on organic nitrates. Atmos. Chem. Phys. **15**(13): 7307-7336.

Xu, L., Guo, H., Boyd, C.M., Klein, M., Bougiatioti, A., Cerully, K.M., Hite, J.R., Isaacman-VanWertz, G., Kreisberg, N.M., Knote, C., Olson, K., Koss, A., Goldstein, A.H., Hering, S.V., de Gouw, J., Baumann, K., Lee, S.-H., Nenes, A., Weber, R.J. and Ng, N.L. (2015b). Effects of anthropogenic emissions on aerosol formation from isoprene and monoterpenes in the southeastern united states. Proceedings of the National Academy of Sciences **112**(1): 37.

Yan, J.P., Jung, J.Y., Zhang, M.M., Xu, S.Q., Lin, Q., Zhao, S.H. and Chen, L.Q. (2019). Significant underestimation of gaseous methanesulfonic acid (msa) over southern ocean. Environmental Science & Technology **53**(22): 13064-13070.

Young, D.E., Kim, H., Parworth, C., Zhou, S., Zhang, X., Cappa, C.D., Seco, R., Kim, S. and Zhang, Q. (2016). Influences of emission sources and meteorology on aerosol chemistry in a polluted urban environment: Results from discover-aq california. Atmos. Chem. Phys. **16**(8): 5427-5451.

Yu, J., Cocker, D.R., Griffin, R.J., Flagan, R.C. and Seinfeld, J.H. (1999). Gas-phase ozone oxidation of monoterpenes: Gaseous and particulate products. Journal of Atmospheric Chemistry **34**(2): 207-258.

Yu, J., Yan, C., Liu, Y., Li, X., Zhou, T. and Zheng, M. (2018). Potassium: A tracer for biomass burning in beijing? Aerosol and Air Quality Research **18**(9): 2447-2459.

Zhang, H., Yee, L.D., Lee, B.H., Curtis, M.P., Worton, D.R., Isaacman-VanWertz, G., Offenberg, J.H., Lewandowski, M., Kleindienst, T.E., Beaver, M.R., Holder, A.L., Lonneman, W.A., Docherty, K.S., Jaoui, M., Pye, H.O.T., Hu, W., Day, D.A., Campuzano-Jost, P., Jimenez, J.L., Guo, H., Weber, R.J., de Gouw, J., Koss, A.R., Edgerton, E.S., Brune, W., Mohr, C., Lopez-Hilfiker, F.D., Lutz, A., Kreisberg, N.M., Spielman, S.R., Hering, S.V., Wilson, K.R., Thornton, J.A. and Goldstein, A.H. (2018). Monoterpenes are the largest source of summertime organic aerosol in the southeastern united states. Proc Natl Acad Sci U S A **115**(9): 2038-2043.

Zhang, J., Huff Hartz, K.E., Pandis, S.N. and Donahue, N.M. (2006). Secondary organic aerosol formation from limonene ozonolysis: Homogeneous and heterogeneous influences as a function of nox. The Journal of Physical Chemistry A **110**(38): 11053-11063.

Zhang, J., Wang, Y., Huang, X., Liu, Z., Ji, D. and Sun, Y. (2015a). Characterization of organic aerosols in beijing using an aerodyne high-resolution aerosol mass spectrometer. Advances in Atmospheric Sciences **32**(6): 877-888.

Zhang, Q., Jimenez, J.L., Worsnop, D.R. and Canagaratna, M. (2007a). A case study of urban particle acidity and its influence on secondary organic aerosol. Environmental Science & Technology **41**(9): 3213-3219.

Zhang, Q., Jimenez, J.L., Canagaratna, M.R., Ulbrich, I.M., Ng, N.L., Worsnop, D.R. and Sun, Y. (2011). Understanding atmospheric organic aerosols via factor analysis of aerosol mass spectrometry: A review. Anal Bioanal Chem **401**(10): 3045-3067.

Zhang, Q., Jimenez, J.L., Canagaratna, M.R., Allan, J.D., Coe, H., Ulbrich, I., Alfarra, M.R., Takami, A., Middlebrook, A.M., Sun, Y.L., Dzepina, K., Dunlea, E., Docherty, K., DeCarlo, P.F., Salcedo, D., Onasch, T., Jayne, J.T., Miyoshi, T., Shimono, A., Hatakeyama, S., Takegawa, N., Kondo, Y., Schneider, J., Drewnick, F., Borrmann, S., Weimer, S., Demerjian, K., Williams, P., Bower, K., Bahreini, R., Cottrell, L., Griffin, R.J., Rautiainen, J., Sun, J.Y., Zhang, Y.M. and Worsnop, D.R. (2007b). Ubiquity and dominance of oxygenated species in organic aerosols in anthropogenically-influenced northern hemisphere midlatitudes. Geophysical Research Letters **34**(13).

Zhang, R., Jing, J., Tao, J., Hsu, S.C., Wang, G., Cao, J., Lee, C.S.L., Zhu, L., Chen, Z., Zhao, Y. and Shen, Z. (2013). Chemical characterization and source apportionment of pm_{2.5} in beijing: Seasonal perspective. Atmos. Chem. Phys. **13**(14): 7053-7074.

Zhang, X., Hecobian, A., Zheng, M., Frank, N.H. and Weber, R.J. (2010). Biomass burning impact on pm_{2.5} over the southeastern us during 2007: Integrating chemically speciated frm filter measurements, modis fire counts and pmf analysis. Atmos. Chem. Phys. **10**(14): 6839-6853.

Zhang, X., Smith, K.A., Worsnop, D.R., Jimenez, J., Jayne, J.T. and Kolb, C.E. (2002). A numerical characterization of particle beam collimation by an aerodynamic lens-nozzle system: Part i. An individual lens or nozzle. Aerosol Science and Technology **36**(5): 617-631.

Zhang, Y.J., Tang, L.L., Wang, Z., Yu, H.X., Sun, Y.L., Liu, D., Qin, W., Canonaco, F., Prévôt, A.S.H., Zhang, H.L. and Zhou, H.C. (2015b). Insights into characteristics, sources, and evolution of submicron aerosols during harvest seasons in the yangtze river delta region, china. Atmospheric Chemistry and Physics **15**(3): 1331-1349.

Zhao, D.F., Kaminski, M., Schlag, P., Fuchs, H., Acir, I.H., Bohn, B., Häseler, R., Kiendler-Scharr, A., Rohrer, F., Tillmann, R., Wang, M.J., Wegener, R., Wildt, J., Wahner, A. and Mentel, T.F. (2015). Secondary organic aerosol formation from hydroxyl radical oxidation and ozonolysis of monoterpenes. Atmospheric Chemistry and Physics **15**(2): 991-1012.

Zhou, S., Collier, S., Jaffe, D.A., Briggs, N.L., Hee, J., Sedlacek Iii, A.J., Kleinman, L., Onasch, T.B. and Zhang, Q. (2017). Regional influence of wildfires on aerosol chemistry in the western us and insights into atmospheric aging of biomass burning organic aerosol. Atmospheric Chemistry and Physics **17**(3): 2477-2493.

Zhu, Q., Huang, X.-F., Cao, L.-M., Wei, L.-T., Zhang, B., He, L.-Y., Elser, M., Canonaco, F., Slowik, J.G., Bozzetti, C., El-Haddad, I. and Prévôt, A.S.H. (2018). Improved source apportionment of organic aerosols in complex urban air pollution using the multilinear engine (me-2). Atmospheric Measurement Techniques **11**(2): 1049-1060.

Zorn, S.R., Drewnick, F., Schott, M., Hoffmann, T. and Borrmann, S. (2008). Characterization of the south atlantic marine boundary layer aerosol using an aerodyne aerosol mass spectrometer. Atmospheric Chemistry and Physics **8**(16): 4711-4728.

Schriften des Forschungszentrums Jülich
Reihe Energie & Umwelt / Energy & Environment

Band / Volume 582
Closed Carbon Cycle Mobility –
Klimaneutrale Kraftstoffe für den Verkehr der Zukunft
F. Schorn, J. Häusler, J. L. Breuer, S. Weiske, J. Pasel, R. C. Samsun, R. Peters (2022), 220 pp
ISBN: 978-3-95806-636-6

Band / Volume 583
Machine learning for monitoring groundwater resources over Europe
Y. Ma (2022), viii, 125 pp
ISBN: 978-3-95806-638-0

Band / Volume 584
Mechanical properties of single and dual phase proton conducting membranes
W. Zhou (2022), IV, VI, 133 pp
ISBN: 978-3-95806-645-8

Band / Volume 585
Improvements to gravity wave physics from an observational perspective
M. Geldenhuys (2022), vii, 136 pp
ISBN: 978-3-95806-647-2

Band / Volume 586
Impact of severe convection on the water vapor mixing ratio in the extra-tropical stratosphere
D. Khordakova (2022), ii, 136 pp
ISBN: 978-3-95806-648-9

Band / Volume 587
Effects of salt precipitation during evaporation on porosity and permeability of porous media
J. Piotrowski (2022), xxvii, 139 pp
ISBN: 978-3-95806-650-2

Band / Volume 588
IEK-14 Report 2022
Forschung für die Energiewende und den Wandel im Rheinischen Revier
B. Emonts (Hrsg.) (2022)
ISBN: 978-3-95806-652-6

Band / Volume 589
Oxidation of monoterpenes studied in atmospheric simulation chambers
L. L. Hantschke (2022), 188 pp
ISBN: 978-3-95806-653-3

Band / Volume 590
NiFe Layered Double Hydroxide Catalysts for Oxygen Evolution Reaction in Alkaline Water Electrolysis
W. Jiang (2022), 165 pp
ISBN: 978-3-95806-658-8

Band / Volume 591
Optimizing Cross-linked Infrastructure for Future Energy Systems
L. Welder (2022), xxiii, 360 pp
ISBN: 978-3-95806-659-5

Band / Volume 592
Evaluation von Reaktorkonzepten für die CO_2-basierte Methanolsynthese aus Wasserstoff und Kohlendioxid mithilfe von CFD-Simulationen
S. Weiske (2022), x, 369 pp
ISBN: 978-3-95806-661-8

Band / Volume 593
Spectral Induced Polarization of Biochar in Soil
Z. Gao (2022), XXVI, 155 pp
ISBN: 978-3-95806-662-5

Band / Volume 594
Eignung von nickelhaltigen Katalysatorsystemen in sauren Medien zur Nutzung im Betrieb von Brennstoffzellen
A. Karaca (2022), iv, 249 pp
ISBN: 978-3-95806-663-2

Band / Volume 595
Seasonal Comparison of the Chemical Composition and Source Apportionment of Aerosols during the Year-Long JULIAC Campaign
L. Liu (2022), VIII, 189 pp
ISBN: 978-3-95806-668-7

Weitere ***Schriften des Verlags im Forschungszentrum Jülich*** unter
http://wwwzb1.fz-juelich.de/verlagextern1/index.asp

Energie & Umwelt / Energy & Environment
Band / Volume 595
ISBN 978-3-95806-668-7

Mitglied der Helmholtz-Gemeinschaft

JÜLICH
Forschungszentrum